NBSIR 82-1667

TECHNICAL REPORTS

MATERIALS STUDIES FOR MAGNETIC FUSION ENERGY APPLICATIONS AT LOW TEMPERATURES - V

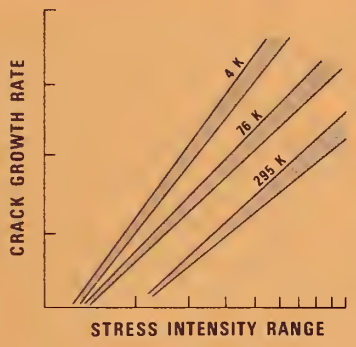

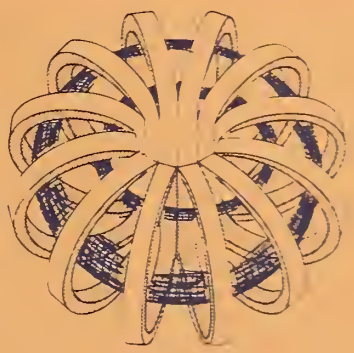

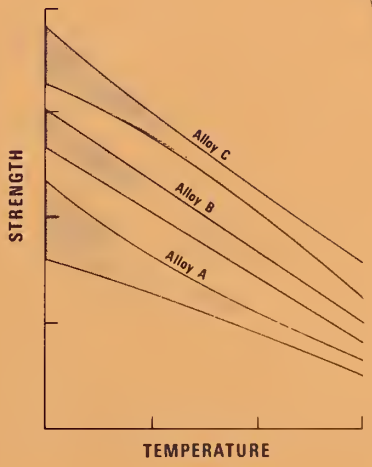

To
Department of Energy
Office of Fusion Energy
Washington, D.C. 20545

By
Fracture and Deformation Division
National Bureau of Standards
Boulder, CO 80303

NBSIR 82-1667

TECHNICAL REPORTS

MATERIALS STUDIES FOR MAGNETIC FUSION ENERGY APPLICATIONS AT LOW TEMPERATURES - V

Edited By

R.P. Reed and N.J. Simon
Fracture and Deformation Division
National Bureau of Standards
Boulder, Colorado 80303

May 1982

Sponsored By

Department of Energy
Office of Fusion Energy
Washington, D.C. 20545

U.S. DEPARTMENT OF COMMERCE, Malcolm Baldrige, Secretary

NATIONAL BUREAU OF STANDARDS, Ernest Ambler, Director

CONTENTS

CONTENTS (Cont'd)

SUMMARY

This report contains results of a research program to produce material property data that will facilitate design and development of cryogenic structures for the superconducting magnets of magnetic fusion energy power plants and prototypes. The program was conceived and developed jointly by the staffs of the National Bureau of Standards and the Office of Fusion Energy of the Department of Energy; it is managed by NBS and sponsored by DoE. Research is conducted at NBS and at various other laboratories through subcontracts with NBS.

The reports presented here summarize the fifth year of work on the low temperature materials research program. Highlights of the results are presented first. Research results are given for the four main program areas: structural alloys, weldings and castings, nonmetallics, and technology transfer. Objectives, approaches, and achievements are summarized in an introduction to each program area.

The major portion of the program has been the evaluation of the low temperature mechanical and physical properties of stainless steel base metals, welds, and castings, with particular emphasis on the nitrogen-strengthened stainless steels. Stainless steels with manganese additions and other high manganese steels have also been investigated. Work has been done on the production and standardization of nonmetallics, primarily industrial laminates, for low temperature applications and on the measurement of their properties at cryogenic temperatures. A brief summary is given of the fifth NBS/DoE Vail Workshop held in October 1981.

Note: Certain commercial equipment, instruments, or materials are identified in this paper to specify the experimental procedure adequately. In no case does such identification imply recommendation or endorsement by the National Bureau of Standards, nor does it imply that the material or equipment identified is necessarily the best available for the purpose. Papers by non-NBS authors have not been reviewed or edited by NBS. Therefore, the National Bureau of Standards accepts no responsibility for comments or recommendations contained therein.

ORGANIZATIONAL CONTACTS

The people responsible for the various major aspects of the program are listed below so that specific technical questions may be directed to them.

Department of Energy, Office of Fusion Energy, Washington, D.C. 20545

Program Monitor	D. Beard	(301) 353-4958 (FTS) 233-4958

National Bureau of Standards, Boulder, Colorado 80303

Program Manager	R. P. Reed	(303) 497-3870 (FTS) 320-3870
Structural Alloys	R. P. Reed	(303) 497-3870
	R. L. Tobler	(303) 497-3421
	J. M. Arvidson	(303) 497-3424
Elastic Properties	H. M. Ledbetter	(303) 497-3443
Welding and Casting	H. I. McHenry	(303) 497-3268
	T. A. Whipple	(303) 497-5795
	C. M. Fortunko	(303) 497-3523
Nonmetallics	M. B. Kasen	(303) 497-3558
	H. M. Ledbetter	(303) 497-3443
	R. D. Kriz	(303) 497-3547
Technology Transfer	N. J. Simon	(303) 497-3687

University of Wisconsin, Engineering Research Building, Madison, Wisconsin 53706

Program Manager	D. Larbalestier	(608) 263-2194

University of Colorado, Mechanical Engineering Department, Boulder, Colorado 80309

	S. K. Datta	(303) 492-7750

PROGRAM DESCRIPTION

The overall objective of the program is to assist in the design, construction, and safe operation of low temperature magnetic fusion energy (MFE) systems, especially superconducting magnets, through effective materials research and materials technology transfer. The specific steps taken to achieve this objective are: (1) evaluation of low temperature materials research needs specific to MFE devices; (2) development and monitoring of a research program to acquire the necessary data; and (3) rapid dissemination of the data to potential users through personal contacts, publications, and workshops.

Efforts directed at the first specific objective began with the publication of the Survey of Low Temperature Materials for Magnetic Fusion Energy in March 1977. A recent publication updating part of this survey, entitled Structural Alloys for Superconducting Magnets in Fusion Energy Systems, was included in volume IV (1981) of this series. Through continuous interactions with all low temperature design, construction, and measurement programs, such as the Large Coil Project, we are aware of new problems as they arise. This year's contribution to the second objective is described in Table 1 in the form of an outline of the research projects. The results appear later in this report. The third objective is satisfied, in part, by these annual reports and by the series of NBS-DoE Workshops on Materials at Low Temperatures, which are held each fall in Vail, Colorado. Starting with this annual report, handbook pages presenting the available data for specific materials will be distributed with the annual report.

Table 1. Outline of the NBS/DoE Program on Material Studies for Magnetic Fusion Energy Applications at Low Temperatures.

Program Area	Organization	Program Description
	A. Structural Alloys	
1. Characterization and development of strong, tough alloys	NBS	Assessment of low temperature properties of selected austenitic alloys containing varying concentrations of C, N, and Mn with a Fe-Cr-base. Assessment of Japanese austenitic alloys with Fe-Mn base.
2. Characterization and development of strong, fatigue-resistant alloys	NBS	Assessment of fatigue and fatigue crack growth rates of candidate structural alloys, including 300 series steels, Fe-Mn base alloys, and age-hardened alloys.
3. Characterization	NBS	Measurement of elastic, tensile, fracture toughness, and fatigue crack growth rate properties as a function of temperature for selected austenitic stainless steels and aluminum alloys. Study of effects of grain size, martensitic transformations, and alloying on low temperature behavior.
4. Characterization and modeling of martensitic start temperatures	University of Wisconsin	Study to assess, empirically, the relation between alloy content and the temperature at which martensite forms on cooling for commercial grades of AISI 300 series stainless steels.

Program Area	Organization	Program Description
	B. Welds and Castings	
1. Stainless steel welds and castings	NBS	Investigation of the metallurgical factors that affect the mechanical properties of stainless steel weldments and castings at cryogenic temperatures. Involves metallographic observations of duplex austenite/delta ferrite microstructures. in deformed and fractured stainless steels. Effects of ferrite and nitrogen content on the strength and toughness at 4 K are being studied in stainless steel castings; this work will be extended to weldments.
2. Stainless steel welds	NBS	Study of effects of oxygen and delta-ferrite content on submerged arc weldments at 4 K. Investigation of the effects of weld reinforcement and austenite stability on weld strength. Improvement of methods of ultrasonic testing.
3. Testing program	NBS	Continuation of mechanical property testing at 4 K of welds and plate material, in support of superconducting magnet design and construction.
	C. Nonmetallics for Magnet Structures	
1. Standardization	NBS	Continuing cooperation with industry to establish and refine cryogenic-grade specifications for insulating laminates and coding systems for laminates.

Program Area	Organization	Program Description
2. Characterization	NBS	Thermal conductivity measurements of composite components at cryogenic temperatures to aid in establishing models for predicting the thermal conductivity of a variety of laminates. Investigation of failure modes of laminates under compression at cryogenic temperatures.
3. Property determination and modeling	NBS	Development of dynamic methods of determining elastic properties of laminated composites. For a woven glass-fiber/epoxy composite, experimental determination of the complete nine-component elastic-constant tensor. Study of the local-stress distribution in a glass-fiber/epoxy composite "unit cell" using finite-element methods.
D. Technology Transfer		
1. NBS/DoE Workshop	NBS	An annual workshop to present research results to the fusion community, to discuss new problems, and to promote interaction between interested parties.
2. Handbook	NBS	Handbook data pages on mechanical and physical properties of AISI 316 stainless steels are published as an addendum to this report. Data pages on 21-6-9 stainless steel and AISI 304 stainless steels will be prepared for the next annual report.

HIGHLIGHTS OF RESULTS

HIGHLIGHTS OF RESULTS

STRUCTURAL ALLOYS:

Tensile and Fracture Properties of Austenitic Stainless Steels

A series of experiments on AISI 310, AISI 304N, manganese-modified AISI 304, and nitrogen-strengthened AISI 304 are reported with emphasis on the analyses of fracture and stress-strain characteristics. For analysis, stress-strain curves of metastable austenitic steel alloys were divided into three sections; the stress and strain parameters associated with each section were related to composition and martensitic transformation effects. The addition of manganese to Fe-Cr-Ni metastable steels increased the fracture toughness at 4 K, while maintaining or slightly increasing the tensile yield strength.

Measurement methodology continues to be emphasized. A review paper is included on tensile, fracture toughness, and fatigue low temperature measurements. The AISI 310 J-integral fracture toughness measurements were interpreted; here the alloy exhibited multiple serrations during testing of compact-tensile specimens, yet the crack extension was by ductile tearing.

Preliminary data on the effect of magnetic fields on deformation of austenitic steels at 4 K are reported. In particular, no effect on flow strength of AISI 304 and 310 alloys was observed for continuously applied 7-T fields at 4 K. Cycling of the fields on and off during testing at 4 K also produced no change of flow strength.

WELDING AND CASTING:

Stainless Steel Weldments

Nitrogen-strengthened austenitic Cr-Ni stainless steels are commonly considered for use as structural alloys in superconducting magnets because

they have a good combination of strength, stiffness, and toughness at 4 K. However, these nitrogen-strengthened stainless steels do not have good welding properties because of the difficulties in finding a matching strength filler alloy with sufficient toughness. Consequently, a new high-manganese austenitic steel, 25Mn-5Cr-1Ni, was evaluated and found to have a favorable combination of strength, toughness, and fatigue crack growth resistance at 4 K for both base plate and welds.

A new approach to ultrasonic inspection of welds has been developed using horizontally polarized shear waves that are transmitted and received by electromagnetic acoustic transducers (EMATs). Higher sensitivity than previously available is attained with this system. Ultrasonic techniques were also used to measure the elastic properties of a series of 316L stainless steel weldments with varying ferrite content. The results showed strong elastic anisotropy in the welds and little sensitivity of the elastic constants to ferrite content.

Stainless Steel Castings

CF8M castings are being studied for two reasons: (a) there is interest in their use as structural elements for superconducting magnets and (b) the factors affecting fracture and deformation modes are more easily observed because their duplex austenite/delta ferrite structure is coarser than that of weldments. Fracture toughness results show a decrease in toughness with increasing delta-ferrite content up to about 15 percent, followed by essentially constant fracture toughness at higher ferrite content. Metallographic studies have provided an explanation for this behavior: a continuous fracture path through the ferrite is established at about 15 percent delta-ferrite.

NONMETALLICS:

Standardization

Work continued on refining the specification for the G-10CR grade of cryogenic high-pressure industrial laminate. A revised draft incorporating input and suggestions from the fabricators has been completed and distributed to the fabricators for comment. Major additions were specifications for the cure cycle and minimum specifications for mechanical and physical properties.

Two additional laminators have joined three other manufacturers as producers of G-10CR.

Characterization

The thermal conductivity at cryogenic temperatures has been determined for two glass-fabric-reinforced epoxy-matrix laminates having different reinforcement-to-resin ratios in an attempt to determine the individual contribution of each to the total conductivity.

A polyimide-matrix variant of G-10CR has been characterized for mechanical properties down to 4 K. The mechanical performance of this variant, which ORNL found to have good radiation resistance, was found to be substantially inferior to that of conventional G-10CR.

The cryogenic performance of G-10CR produced by two companies that have recently started production of the material was screened to 76 K.

Property Determination and Modeling

1. At the first Japan-U.S. Conference on Composite Materials (Tokyo, January 1981), Ledbetter presented a review of NBS studies of anisotropic elastic constants and internal friction of fiber-reinforced composites. Materials that were studied include: boron-aluminum, boron-epoxy, graphite-epoxy, glass-epoxy, and aramid-epoxy. In all cases, elastic-constant direction dependence

could be described by a relationship developed for single crystals of homogeneous materials. Elastic stiffness was found to vary inversely with internal friction.

2. At the same conference, Datta, Ledbetter, and Kinra presented a theoretical-experimental study of wave propagation and elastic constants in particulate and fibrous composites. For two types of composites--particulate and fiber-reinforced--dynamic elastic properties were studied both theoretically and experimentally. The two composites contained, respectively, randomly distributed spherical inclusions and aligned continuous fibers, both in a homogeneous matrix. The theory described aligned, identical ellipsoidal inclusions. The theory applies to both spherical inclusions and short fibers as special cases. Previously Bose and Mal presented a similar theory for continuous fibers. The theories estimate the effective propagation speed of a plane harmonic wave, average the scattered field by the Waterman-Truell procedure, and use the Lax quasi-crystalline approximation. Theory and observation agree quite well. Particulate composites were studied in a through-transmission water-immersion tank, while the fiber composite was studied by both pulse-echo-overlap and resonance methods.

3. Datta and Ledbetter completed a critical comparison of observation and theory. Elastic constants, both the C_{ij}'s and the S_{ij}'s, were measured and calculated for a laminated, uniaxially fiber-reinforced boron-aluminum composite. Three theoretical models were considered: square-array, hexagonal-array, and random-distribution. By combining several existing theoretical studies on randomly distributed fibers, a full set of elastic constants can be predicted for this

model. The random-distribution model agrees best with observation, especially for off-diagonal elastic constants. Considering all nine elastic constants, observation and theory differ on the average by six percent.

4. During his NRC-NBS postdoctoral appointment in our laboratory, Kriz studied ply cracks and fracture strengths of graphite/epoxy laminates at 76 K. Quasi-isotropic laminates with a ply-stacking sequence of $[0/\pm45/90]_s$ and $[0/90/\pm45]_s$ were fabricated from T300/5208 graphite/epoxy and quasi-statically loaded in tension at 76 K. Fibers in the 0° plies, which are oriented unidirectionally parallel to the load axis, carry the largest portion of the tensile load; the weaker 90° and ±45° plies crack at loads much lower than the fracture strength. From a fractographic viewpoint, at 76 K, laminate ply cracks dominate the fracture process in adjacent plies. To understand better how defects affect laminate strength, we examined the effect of ply cracks on the fracture of the load-bearing 0° plies. An idealized linear-elastic finite-element model was used to predict the distribution of stress in the 0° ply near the crack tip. Variations in the residual-stress state caused by large temperature changes and absorbed moisture were included in the analysis. Experiment indicated that absorbed moisture significantly alters the fracture strength and fracture surface of a dehydrated $[0/90/°45]_s$ laminate tested at 76 K. The fracture surfaces of dehydrated laminates illustrate that the 0° ply fractures along several 90° ply cracks. When absorbed moisture saturates a $[0/90/\pm45]_s$ laminate, a single 90° ply crack dominates the fracture of the 0° ply, and the laminate fracture strength decreases by eight percent. A population of 37

samples statistically verified that moisture decreases strength; furthermore, skewness of the population to low strengths indicated a weak-link phenomenon that is indicated by a Weibull distribution. The Weibull shape parameter for fracture of the dehydrated laminates is 17.6, which increases to 19.0 when saturation causes a single ply crack to dominate the final fracture. A chi-squared confidence test for both dehydrated and saturated populations yielded confidence limits better than 90 percent. Similar fractographic and statistical investigations on $[0/\pm45/90]_s$ and $[0_8]$ laminates were considered.

A manuscript is now in preparation for presentation at the ASTM Symposium on Effects of Defects in Composite Materials (13 December 1982, San Francisco, California).

5. Dr. Kriz, as part of his NRC-NBS postdoctoral studies, also completed a study to monitor elastic-stiffness degradation. In particular, he studied degradation due to moisture absorption in graphite/epoxy. However, the method applied, in principle, to any elastically anisotropic material that degrades by any mechanism: moisture, mechanical fatigue, irradiation, et cetera. The method is based on the change in direction of the energy-flux vector (Poynting vector). Two short manuscripts have been submitted for publication in Composites Technology Reviews and in the proceedings of the ASNT spring conference (22-25 March 1982, Boston, Massachusetts).

TECHNOLOGY TRANSFER:

The annual NBS/DoE Workshop on Materials at Low Temperatures at Vail, Colorado in October 1981 was attended by about sixty representatives of the

materials and magnet design communities. Again, the meeting was viewed constructively; it served as a focal point to identify and discuss magnet construction or design problems related to materials. For a few who have become recently involved in cryogenic applications, the workshop was educational.

Handbook pages and supporting documentation have been prepared for AISI 316 stainless steels and are published as an addendum to this report. Properties covered include: tensile strength, yield strength, elongation, reduction of area, stress-strain curves, elastic constants, impact energy, fracture toughness, stress and strain controlled fatigue life, and fatigue crack growth rate. These pages will also be submitted to the advisory committee of the Materials Handbook for Fusion Energy Systems.

STRUCTURAL ALLOYS

STRUCTURAL ALLOYS PROGRAM

LEADER: R. P. Reed, NBS
STAFF: R. L. Tobler, J. M. Arvidson, NBS
CONTRACTS: Prof. D. Larbalestier, U. Wisconsin, Madison, WI.

OBJECTIVES:

(1) Development and characterization of strong, tough, structural alloys for use at 4 K in superconducting magnets.
(2) Development and characterization of strong, fatigue-resistant structural alloys for use at 4 K in pulsed superconducting magnets.
(3) Development of effective codes and standards related to low temperature property measurements and structural design.

RESEARCH PAST YEAR (1981):

(1) J-integral fracture toughness assessment of AISI 310 (4-300 K).
(2) Review of low temperature mechanical property test procedures.
(3) Assessment of CF8 stainless steel castings.
(4) Characterization of stress-strain behavior of metastable austenitic steels.
(5) Measurement of tensile and fracture properties of manganese-modified Fe-Cr-Ni base steels.
(6) Preliminary assessment of influence of magnetic fields on deformation of austenitic steels at 4 K.
(7) Study of prediction of martensitic start temperatures in Fe-Cr-Ni austenitic steels.

RESEARCH THIS YEAR (1982):

(1) Continued research on effects of magnetic-fields on 4-K deformation of austenitic steels.
(2) Construction of 500,000-N (110,000-lbf) capacity tensile-fatigue testing facility for the temperature range 4-300 K.
(3) Characterization of selected Japanese Fe-Mn base austenitic steels.
(4) Initiation of fatigue testing program in the temperature range 4-300 K.
(5) Study of the temperature dependence of the flow strength of austenitic steels.
(6) Continuation of study of martensitic-start temperatures in Fe-Cr-Ni austenitic steels.

DEFORMATION OF METASTABLE AUSTENITIC STEELS AT LOW TEMPERATURES*+

R. P. Reed and R. L. Tobler
Fracture and Deformation Division
National Bureau of Standards
Boulder, Colorado

ABSTRACT

Commercial grades of Fe-Cr-Ni austenitic stainless steels are metastable at low temperatures. Most of these steels do not transform on cooling, but do transform during deformation. Stress-strain curves reflect the transformation characteristics. There are typically three distinct stages of the stress-strain curve of polycrystalline Fe-Cr-Ni alloys at low temperatures. The stress-strain characteristics are discussed with respect to martensitic transformation.

*Work supported by Office of Fusion Energy, Department of Energy.
+To be published in Advances in Cryogenic Engineering--Materials Vol. 28, R. P. Reed and A. F. Clark, Eds, Plenum Press, New York (1982).

INTRODUCTION

The reaction of a solid to continuously increasing applied tensile load is portrayed using a stress-versus-strain curve. From stress-strain curves the Young's modulus, yield strength, ultimate tensile strength, percent elongation and work hardening characteristics can be obtained. Typically, following the elastic deformation region, a metal or alloy work hardens at a decreasing rate until localized specimen necking initiates and the ultimate strength of the specimen has been reached.

The stress-strain characteristics at low temperatures of commercial grades of polycrystalline austenitic stainless steels containing about 18 wt% chromium and 8 wt% nickel are not conventional. The anomalous behavior is thought to be caused by the martensitic transformation of face-centered-cubic austenite to body-centered-cubic (α') and hexagonal close-packed phases. This paper suggests that the plastic deformation of metastable austenites is composed of three stages, and uses a series of Fe-18Cr-8Ni-1-6Mn, 0.1-0.2N alloys, tested at 4 K, to demonstrate the usefulness of this characterization.

EXPERIMENTAL PROCEDURES

The tensile tests were conducted in liquid helium using a strain rate of 0.02 min^{-1}. Strain was recorded using a clamp-on strain-gage extensometer. Strains larger than about 0.10 were

*Work supported by Office of Fusion Energy, Department of Energy.

computed using load-time graphs of each test. Other experimental details, alloy compositions, and alloy hardness and grain size are discussed by Tobler and Reed [1,2].

TENSILE STRESS-STRAIN CURVES

Typical stress-strain curves of metastable polycrystalline austenitic stainless steels at temperatures between 4 and 295 K are illustrated in Fig. 1 for an Fe-18Cr-8Ni alloy. Compositions refer to weight percent. Alloys of this type remain ductile at

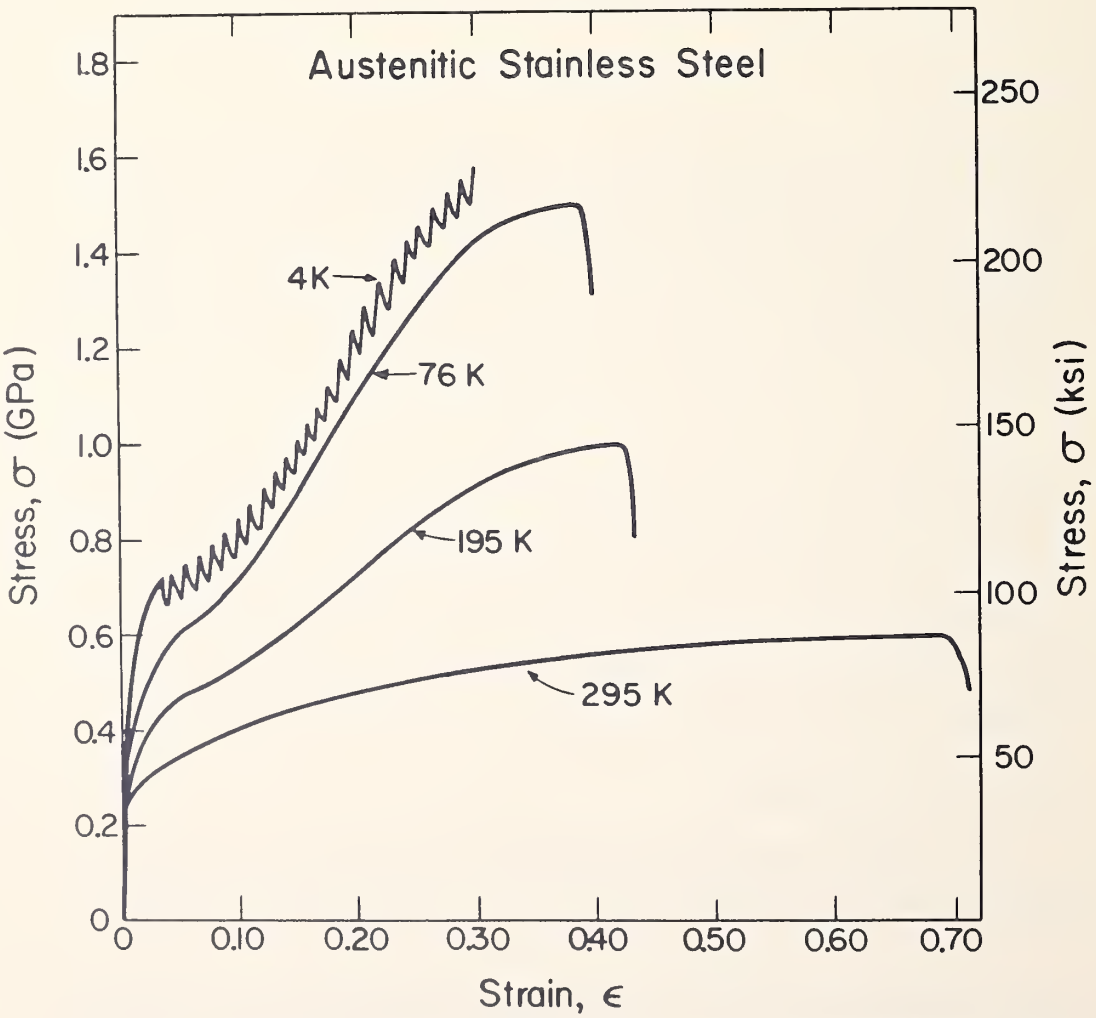

Figure 1. Typical stress versus strain curves (engineering) for polycrystalline Fe-18Cr-8Ni austenitic stainless steel.

low temperatures, exhibit considerable work hardening, have a region of low work hardening at 195, 76 and 4 K, and have discontinuous yielding at 4 K. The stress-strain curves for a series of Fe-18Cr-8Ni-1-6Mn with 0.1 and 0.2N are presented in Figs. 2 and 3, respectively. For purposes of clarity, the discontinuous yielding serrations have been deleted; instead only the maximum flow stress values are plotted and the load drops are omitted. The presence of an easy glide region is very apparent, followed by a region of high work hardening.

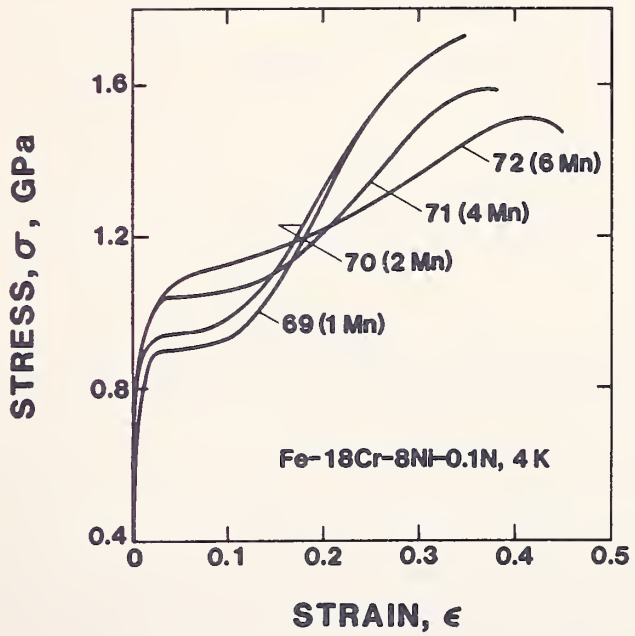

Figure 2. Stress-strain curves at 4 K for series of Fe-18Cr-8Ni-0.1N alloys with 1-6 wt% Mn.

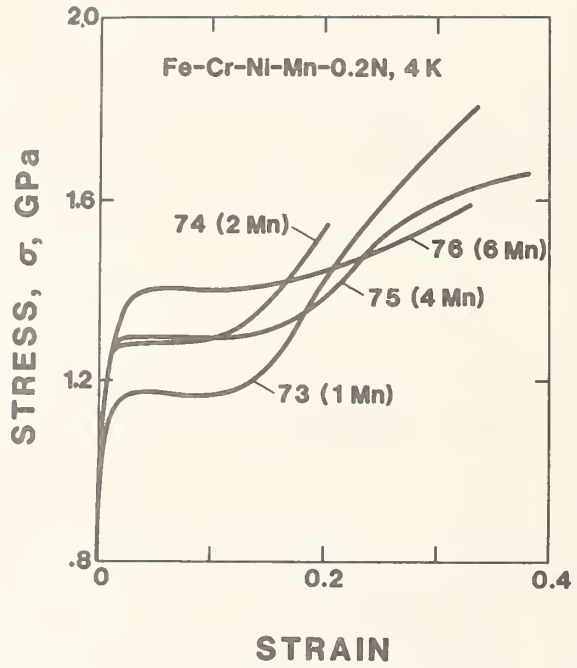

Figure 3. Stress-strain curves at 4 K for series of Fe-18Cr-8Ni-0.2N alloys with 1-6 wt% Mn.

DISCUSSION

For characterization and analysis, the stress-strain curves of such metastable polycrystalline austenitic alloys can be considered to have three stages of plastic deformation. These will be referred to as stages I, II and III. The stress-strain curve in Fig. 4 identifies these stages and (following single crystal nomenclature) assigns stress and strain symbols for the onset of the three stages. Stage I represents the first stage of plastic deformation, beginning at the elastic limit and ending at the onset of easy glide (usually about $\varepsilon = 0.02$). The yield strength is included in this stage. Stage II is the easy glide region. Stage III represents the region of high work hardening.

Since stable austenitic steels do not exhibit the stages of the stress-strain curves discussed above, it is likely that these stages are associated with martensitic transformation. The remainder of this paper concerns correlations between the stresses and strains of the three stages with parameters, such as composition, that affect austenite stability or represent martensite concentration.

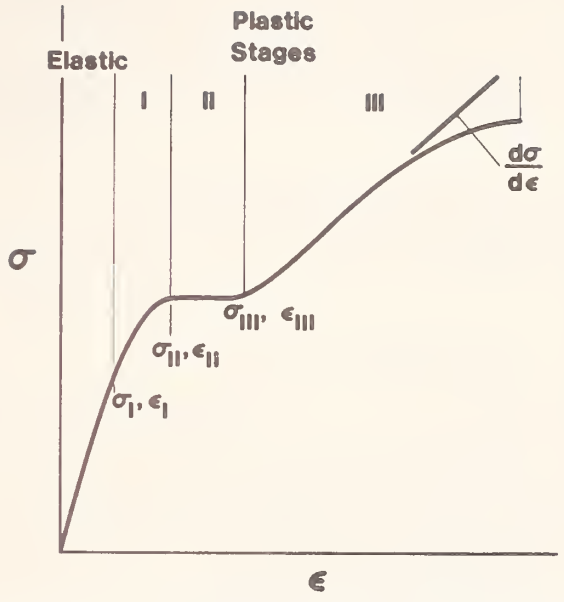

Figure 4. Identification of three stages of plastic deformation in austenitic stainless steels at low temperatures.

Stage I: In our study sufficiently accurate measurements were not obtained of the onset of Stage I, ε_I and σ_I. It is likely that only very small amounts (< 1%) of martensite form in this stage. Suzuki, et al [3], from studies on an 18Cr-9Ni steel, suggest hexagonal close-packed (hcp) martensite formation. Olsen and Azrin [4], using a TRIP steel (Fe-9Cr-8Ni-4Mo-2Si) that is less stable than a normal austenitic stainless steel suggest that stress-assisted body-centered-cubic martensite formations contribute substantially to early austenite deformation. Within the sensitivity of our x-ray (> 2% hexagonal close-packed, > 2% α') and magnetometer ($\geq$ 0.2% α') measurements, no marteniste formation was detected. In any case, the initial martensite formation is thought to contribute to the observed decrease of flow strength at decreasing temperatures below about 200 K [3,4,5].

The yield strength (σ_y, flow strength at plastic strain = 0.002) is within stage I. As shown in Fig. 5, σ_y is linearly dependent on Mn content, increasing with increasing Mn. The linear dependence matches that of σ_{II}, the stress at which Stage II begins. The increase of σ_y with Mn is considerable, about 33 MPa/wt% Mn, but not as high as the increase of σ_y from nitrogen addition. From Fig. 5, it is shown that an addition of 0.1 wt% N increases σ_y about 50%. Note that the dependence of σ_y on wt% Mn is independent of N content. The strength increases from N and Mn additions may arise from two sources: (1) Increased austenite stability [6,7]. This results in less martensitic

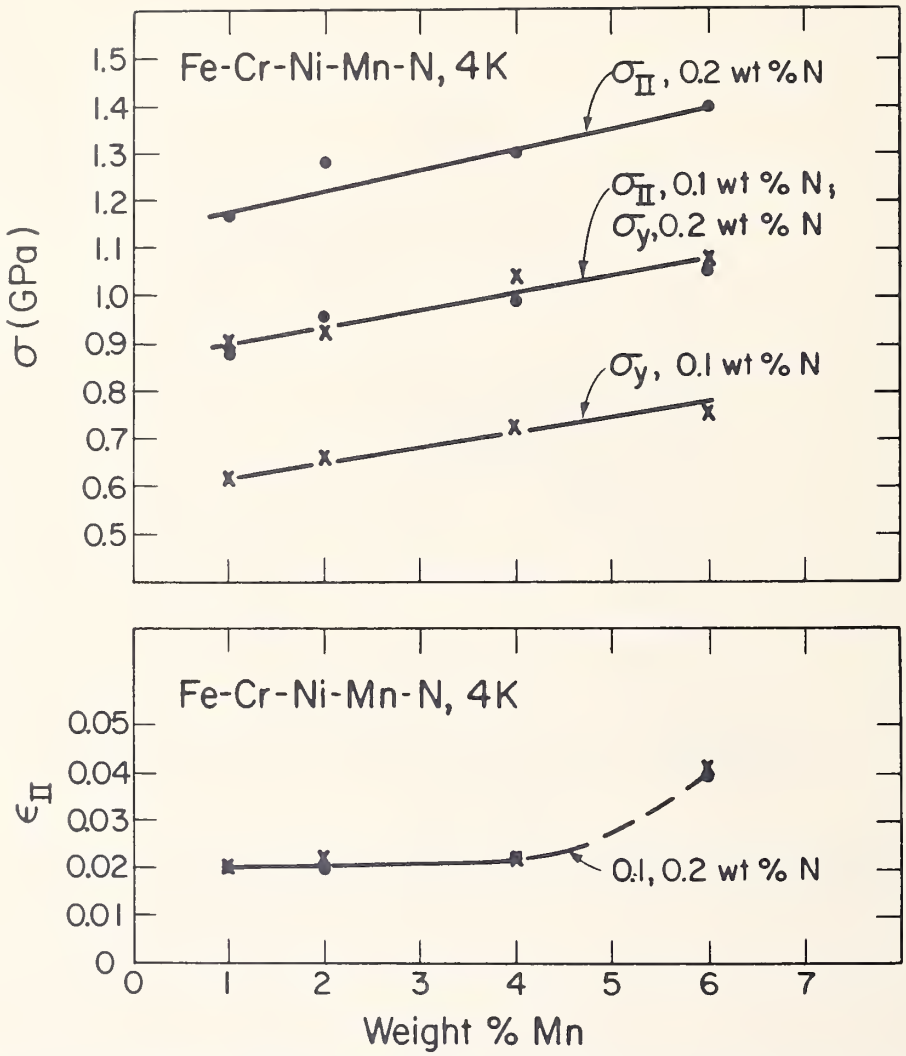

Figure 5. Tensile yield strength and stage II σ_{II} and ϵ_{II} at 4 K as a function of wt% Mn.

transformation, and, consequently, less work hardening and (2) Solid-solution strengthening. Approximately 0.1 wt% N is equivalent to 8 wt% Mn in contribution to strengthening.

Stage II: The stress to initiate stage II (σ_{II}) linearly increases with Mn content (see Fig. 5), but ϵ_{II} is essentially independent of Mn until 6% Mn is added (Fig. 5); at this concentration ϵ_{II} is larger. Similarly to σ_y, N addition has a much stronger influence on σ_{II}, compared to Mn. The strain, ϵ_{II}, is independent of N content. In this stage, there is little work hardening. Work softening has been reported [8] and this stage has been termed "easy glide" [9]. Reed and Gunter [9], noting the easy glide region and measuring (using x-rays) the increase

of hcp martensite in the region, suggested that Stage II was caused by hcp formation in slip bands. Suzuki, et al, observed bcc formation at slip band intersections using transmission electron microscopy and proposed that these martensite laths act as "windows," promoting dislocation mobility at slip-band intersections.

Stage III: The transition to the region of high work hardening rates, stage III, is denoted by a strain, ε_{III}, and a stress, σ_{III}. These are plotted in Fig. 6. The strain, ε_{III},

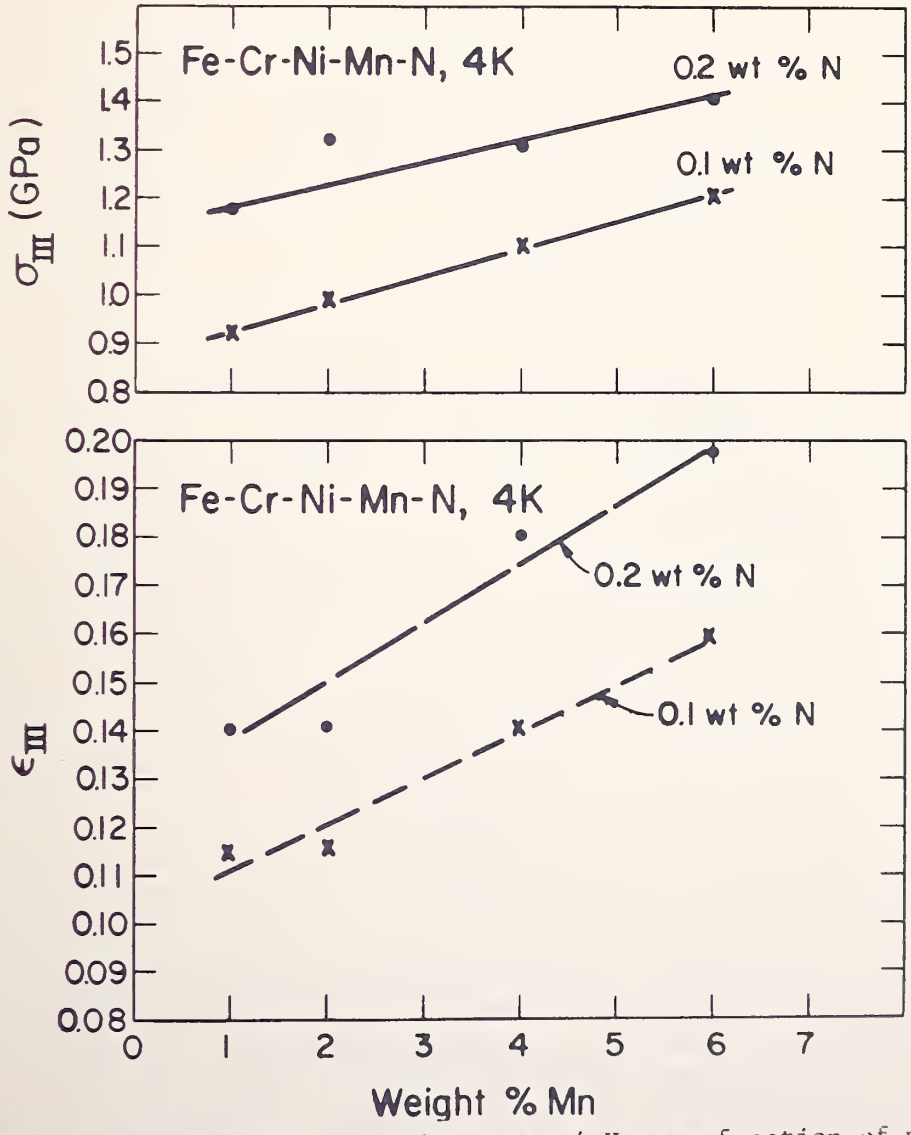

Figure 6. Stage III σ_{III} and ε_{III} at 4 K as a function of wt% Mn.

has greater scatter and apparently increases with increasing Mn. The stress, σ_{III}, increases mildly and linearly with increasing Mn content. In contrast to Stage II, the dependence of ε_{III} and σ_{III} on Mn appears to be conditioned by the N content. Stage III begins at lower stresses and lower strains for 0.1 wt% N, compared to 0.2 wt% N. The rate of work hardening, $d\sigma/d\varepsilon$, decreases with increasing Mn, as shown in Fig. 7. The addition of N also lowers the rate of work hardening and slightly affects the dependence of Mn content. N contributes to the reduction of $d\sigma/d\varepsilon$ about ten times more strongly (on the basis of wt% addition) than Mn.

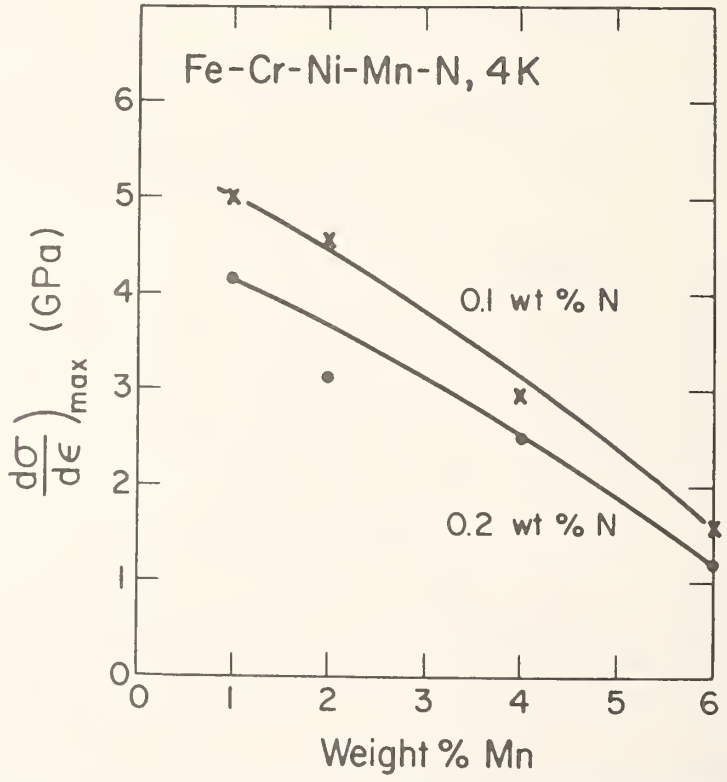

Figure 7. Rate of work hardening versus wt% Mn for alloy series at 4 K.

In Fig. 4 of the Tobler and Reed paper [1] in this volume, the "normalized" percent α' martensite (divided by the percent uniform elongation within the measurement length) is plotted as a function of composition [Mn + Ni + 10 (C+N)]. Using these data and Fig. 7, the dependence of work hardening rate in stage III on percent α' martensite per unit elongation is shown in Fig. 8. Clearly, there is a strong linear correlation, and the rate of

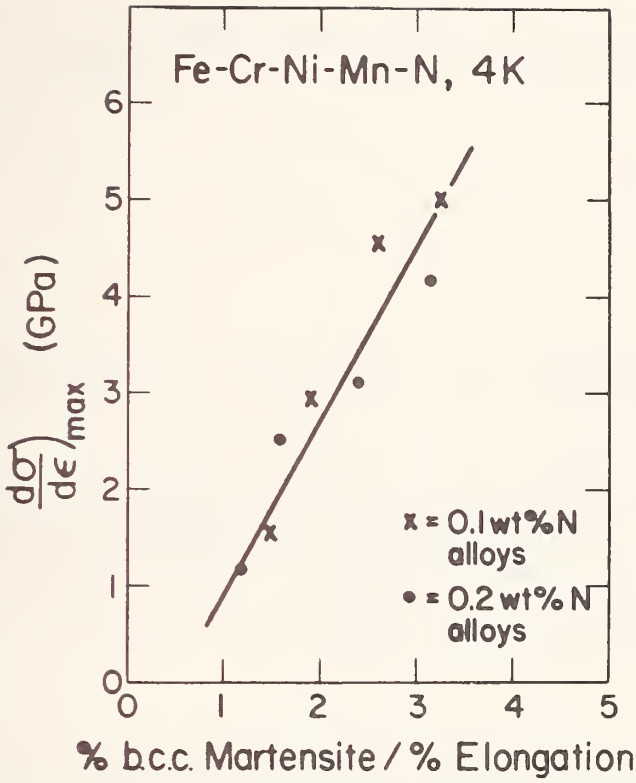

Figure 8. Rate of work hardening versus "normalized" martensite function (wt% α' martensite divided by % elongation) for alloy series at 4 K.

work hardening can be regarded as a function of austenite stability with respect to α' formation as determined by composition. This dependence may imply that α' formation in stage III is distinct from stage II (and possibly stage I) formation at slip band intersections. A second possibility is that sizable α' formation produces sufficient accommodation deformation, resulting from the associated $\gamma \rightarrow \alpha'$ volume expansion, to increase the defect concentration (and work hardening) sufficiently more than the transformation strains serve to produce specimen strain.

The fracture toughness variation with composition is difficult to assess (see Ref. 1). Typically, at 4 K for a series of stable and metastable austenitic alloys, the toughness ($K_{Ic}(J)$) varies as the reciprocal of the σ_y (1). Since the stability of the alloys has been demonstrated to affect the stress-strain characteristics, one may expect that the plastic zone at the crack tip of the specimens may also be affected. The extent of easy glide in stage II may influence the shape of the zone of crack-tip plasticity; more easy glide may result in more planar and local extension of the plastic zone ahead of the crack tip.

Such net-section yielding phenomena would be expected to result in lower effective fracture toughness. Indeed, a linear relationship is obtained if one assumes that $K_{Ic}(J) \sim a(\varepsilon_{III}-\varepsilon_{II}) + b(\frac{1}{\sigma_y})$ where the proportionally constants a and b are related by $a \simeq \frac{1}{10} b$ with the units of $K_{Ic}(J)$ in $MPa\sqrt{m}$ and σ_y in MPa.

SUMMARY

We have suggested that stress-strain curves of metastable austenitic stainless steels have three stages of plastic deformation. Using stress-strain curves for a series of Fe-18Cr-8Ni alloys with varying Mn (1-6 wt%) and N (0.1, 0.2 wt%) contents the parameters of stress and strain associated with the onset of the three stages have been demonstrated to correlate very well with alloy content. Alloy content affects austenite stability. Correlations of thermodynamic stability, elastic-plastic fracture toughness, and solid solution strengthening with the parameters of the three stages will be explored in future papers.

REFERENCES

1. R. L. Tobler and R. P. Reed, "Tensile and Fracture Properties of Manganese-Modified AISI 304 Type Stainless Steel," Advances in Cryogenic Engineering (Materials), Vol. 28, Plenum Press, New York (1981), pp.

2. R. L. Tobler and R. P. Reed, "Tensile and Fracture Properties of Manganese-Modified AISI 304 Type Stainless Steel," in: Materials Studies for Magnetic Fusion Energy Applications at Low Temperatures IV, NBSIR 81-1645, R. P. Reed and N. J. Simon, eds., National Bureau of Standards, Boulder, Colorado, pp. 77-100 (1981).

3. T. Suzuki, H. Kujima, K. Suzuki, T. Hashimoto, S. Koite, and M. Ichihara, "Plastic Deformation and Martensitic Transformation in an Iron-Base Alloy," Scripta Met., 10:353-358 (1976).

4. G. B. Olson and M. Azrin, "Transformation Behavior in Trip Steels," Metall. Trans. A, 9A:713-721 (1978).

5. R. L. Tobler, R. P. Reed, and D. S. Burkhalter, "Temperature Dependence of Yielding in Austenitic Stainless Steels," in: Materials Studies for Magnetic Fusion Energy Applications at Low Temperatures III, NBSIR 80-1627, R. P. Reed, ed., National Bureau of Standards, Boulder, Colorado, pp. 51-78 (1980).

6. G. H. Eichelman and F. C. Hull, "The Effect of Composition on the Temperature of Sponteneous Transformation of Austenite to Martensite in 18-8-Type Stainless Steel," Trans. Am. Soc. Met., 45:77-104 (1953).

7. I. Williams, R. G. Williams, and R. C. Capellero, "Stability of Austenitic Stainless Steels Between 4 K and 373 K," Proc. Sixth Int'l. Cryogenic Eng. Conf., IPC Science and Technology Press, Guildford, Surrey, England, pp. 337-341 (1976).

8. R. P. Reed and C. J. Guntner, "Stress-Induced Martensitic Transformations in 18Cr-8Ni-Steel," Trans. AIME, 230:1713-1720 (1964).

9. C. J. Guntner and R. P. Reed, "The Effect of Experimental Variables Including the Martensitic Transformation on the Low-Temperature Mechanical Properties of Austenitic Stainless Steels, Trans. ASM, 55:399-419 (1962).

TEMPERATURE DEPENDENCE OF FLOW STRENGTH OF Fe-20Cr-16Ni-6Mn-0.2N AND Fe-18Cr-10Ni-1.5Mn-0.1N (304LN) AUSTENITIC STEELS*

R. P. Reed, R. L. Tobler, and J. W. Elmer
Fracture and Deformation Division
National Bureau of Standards
Boulder, Colorado

ABSTRACT

Recent studies have suggested the possibility of three anomalies in the temperature dependence of the flow strength Fe-Cr-Ni and Fe-Cr-Ni-Mn austenitic stainless steels. Reduction of flow strength at decreasing temperature may be associated with the onset of martensite transformation, the magnetic transition at the Neel temperature, and low temperature dislocation dynamics. The tensile flow strength was investigated in the temperature range 4 to 295 K for two annealed polycrystalline alloys: Fe-20Cr-16Ni-6Mn-0.2N steel (produced in the USSR) and Fe-18Cr-10Ni-0.1N steel (AISI 304LN). The former alloy is stable with repect to strain-induced martensitic transformations, the latter metastable.

Major conclusions are: (1) The temperature dependence of the flow strength of the two alloys is best characterized by a linear dependence of log σ versus T. The more stable Fe-20Cr-16Ni-6Mn-0.2N alloy exhibits a linear slope (log σ-T) over the entire temperature test range. The less stable Fe-18Cr-10Ni-1.5Mn-0.1N alloy exhibits two linear ranges on a log σ versus T plot. (2) Temperature change experiments at constant specimen strain indicate reversibility of flow strength at temperatures below about 100 K. (3) The reported anomalous low temperature decreases of the flow strength associated with the Neel transition temperature and very low temperatures for austenitic steels were not confirmed by this study.

*Work supported by Department of Energy, Office of Magnetic Fusion Energy, and the National Science Foundation.

INTRODUCTION

Austenitic stainless steels are used extensively as the structural materials in cryogenic systems, and knowledge of the dependence of their strength on temperature is sometimes essential for proper design. This study addresses the temperature dependence of the tensile flow strength in the range 4 K to room temperature.

Recent studies [1-3] of Fe-Cr-Ni and Fe-Cr-Ni-Mn austenitic stainless steels have reported three anomalies in the temperature dependence of the flow strength. These anomalies consist of sharp decreases of strength on the order of 100 MPa occurring over narrow temperature intervals between room temperature and 4 K. One type occurs only in metastable steels and is associated with the onset of austenite-to-martensite transformation, usually at about 200 K. For both stable and metastable steel compositions, two additional anomalies are reported at temperatures between 60 and 35 K and between 20 and 4 K. The flow strength decrease in the temperature interval 60 to 35 K has been attributed to the paramagnetic-to-antiferromagnetic transition at the Neel temperature, where the elastic constants are known to decrease 1 to 2 percent. It has been suggested that flow strength reductions below 20 K result from possible dislocation tunneling mechanisms [2]. Studies in our laboratory [4-6] have identified the decrease in flow strength associated with austenite instability with respect to martensitic transformations. However, we have not been successful in detecting the other two anomalies. The observations of different investigators are discussed in this paper. Data are presented for an Fe-20Cr-16Ni-6Mn-0.2N steel (produced in the USSR and independently tested by two research laboratories) and for an Fe-18Cr-10Ni-1.5Mn-0.1N steel (AISI 304LN). The former alloy was expected to be stable with respect to martensitic transformations, the latter metastable.

MATERIAL

The test material was a 25-mm plate of nitrogen-strengthened austenitic stainless steel, obtained from the Paton Institute of Electrowelding, Kiev, USSR. The material was tested in the as-received condition, which is characterized as follows:

Composition (wt.%): Fe-20.3Cr-16.4Ni-6.1Mn-0.19N-0.06C-0.21Mo-0.26Si-0.025P-0.026S-0.09Cu.

Hardness: Rockwell B88, at 295 K after machining tensile specimens.

Microstructure: Equiaxed austenitic grains, free of carbonitride precipitation when viewed at 400X.

Grain size: Average grain diameter of 39 μm (ASTM No. 6.4).

The AISI 304LN material was received from a commercial U.S. supplier. It was one of nine alloys produced from three 136-kg vacuum-induction-melted heats, split with respect to carbon level, and teemed into 76 cm x 200 cm x 360-cm hot-topped cast-iron ingot molds. The ingots were then reheated and soaked at 1561 K, hot-rolled to 25-mm-thick plates and air cooled. The plate was final annealed at 1332 K for one hour and water quenched.

Composition (wt.%): Fe-18.0Cr-9.91Ni-1.50Mn-0.016P-0.017S-0.57Si-0.205Mo-0.197Cu-0.037C-0.12N.

Hardness: Rockwell B79 at 295 K after machining tensile specimens.

Microstructure: Equiaxed austenitic grains.

Grain Size: Average grain diameter of 105 μm.

PROCEDURE

In a previous study, unpolished, longitudinally oriented specimens were used to measure tensile yield and ultimate strengths, as well as ductility, at selected temperatures [6]. In this study, transverse-oriented specimens were

used for yield strength measurements at variable temperatures. These specimens were 6.25 mm in diameter and 25 mm in gage length. The specimens were electropolished in perchloric acid solution (70 percent methanol, 25 percent glycerol, 5 percent perchloric acid) to remove scratches and cold-worked material from machining operations. A total of 0.1 mm (4 mils) was removed from the diameter, which is about four times the scratch depth.

Tensile tests used a screw-driven machine at a crosshead velocity of 8.5×10^{-3} mm/s, with apparatus previously described [7]. Variable temperatures were achieved using controlled thermal conduction from cryogenic fluid reservoirs attached to the load train and electric heaters on the specimen grips. The automatic regulators used in this study are capable of maintaining specified temperatures to ± 0.2 K, with an estimated absolute uncertainty of ± 1 K [6]. A Chromel-constantan thermocouple was attached to the center of the gage length of one calibration specimen to check the temperature control.

A strain-gage extensometer was clipped on to the specimen between two set screws at a gage length of 25 mm. Calibrations were performed using a vertically mounted micrometer at 295, 76, and 4 K. Sensitivity varied from 69 mV/cm at 295 K to 72 mV/cm at 4 K. Indirect calibration was also performed at intermediate temperatures. This was done by elastically loading a dummy specimen at selected temperatures; the extensometer sensitivity was inferred from apparent specimen compliance after correction for the temperature dependence of Young's modulus. The ratio of recorder pen travel in mm to specimen extension in mm was about 300.

Specimen-to-specimen scatter of the temperature dependence of the flow strength was eliminated by performing temperature change tests on some specimens. To test a single specimen at three to five temperatures, the procedure in Figure 1 was used. A specimen was loaded to a strain within the range

0.0005 to 0.002 at T_1, then unloaded, cooled to T_2, and reloaded until plastic flow resumed. Cooling to the lower temperature usually took 10 to 20 minutes. Additional loadings at lower temperatures were also performed, and the flow strength obtained by extrapolating to the original strain at the first loading.

RESULTS AND DISCUSSION

Magnetic measurements [6] at 295 K after low temperature (76, 4 K) deformation confirmed that the Fe-20Cr-16Ni-6Mn-0.2N alloy does not exhibit any α' (body-centered cubic) martensitic transformation and that the Fe-18Cr-10Ni-1.5Mn-0.1N alloy is metastable and partially transformed to α' martensite. This was expected since calculations listed in Table 1 of T_{ms} [8] (the temperature at which α' martensite is expected to begin to transform on cooling), and T_{md} [9] (the highest temperature of deformation-induced α' martensite) are both quite low for the Fe-20Cr-16Ni-6Mn-0.2N alloy and T_{md} for the Fe-18Cr-10Ni-1.5Mn-0.1N alloy is sufficiently high. Stacking fault energy (SFE) calculations listed also in Table 1, indicate that the Fe-20Cr-16Ni-6Mn-0.2N alloy is relatively more stable with respect to the face-centered cubic to hexagonal close-packed (ε) strain-induced transformation.

Alloy Fe-20Cr-16Ni-6Mn-0.2N:

Tensile test results for unpolished specimens are presented in Figure 2 for the Fe-20Cr-16Ni-6Mn-0.2N alloy. Yield and flow strengths increased strongly as temperature was lowered, while ductility decreased moderately. Between 295 and 4 K the yield strength rose from 338 to 1120 MPa, a factor of 3.3. The ultimate strength increased by a factor of 2.3, reaching 1611 MPa at 4 K. Despite one specimen which had an exceptionally low elongation (14 percent), the average elongation and reduction of area at 4 K remain high

(30 and 42 percent, respectively). These trends are typical for nitrogen-strengthened, fully austenitic, stable stainless steels.

The elastic constants for Fe-20Cr-16Ni-6Mn-0.2N steel [12] are shown in Figure 3. The E (Young's) and G (shear) moduli show a regular, nearly linear increase as temperature is reduced from 300 K, until a plateau is approached below about 76 K. In the 60 to 48 K range, the E and G moduli decrease by about ½ percent. This decrease marks the Neel temperature, T_N, at which there is a change in magnetic ordering from paramagnetic to antiferromagnetic conditions. The midpoint of the transition is about 54 K. These data were used to guide the choice of temperatures for the yield strength measurements near T_N.

The yield strength data near T_N are of special interest. Since a decrease of the shear modulus occurs at T_N, it has been suggested that the magnetic ordering phenomenon might have a measurable effect on resistance to dislocation movement, and, hence, tensile flow strength. As indicated below, we were unable to detect any effect, and so our data do not support the conclusions of other investigators testing a similar heat of the same steel [1].

The yield strength results are presented in Figure 4, which compares data from this study (Table 2) with those of our previous study (Table 3) and with USSR data (Table 4). Between 300 and 4 K, the results show approximate conformation to an exponential function given as follows:

$$\sigma_y = 1170 \exp (4.2 \times 10^{-3} T) \qquad (1)$$

Most of the data fit this equation to within about 6 percent, although two points deviate by larger amounts (-10 percent at 295 K, +8 percent at 60 K).

Figure 5 shows only the data at test temperatures between 4 and 100 K. For these results, combined with our previous data, the data spread for five tests at 4 K is ± 55 MPa, owing primarily to specimen-to-specimen variability. The previously tested specimens [6] were longitudinal and unpolished (28 finish), but the results are indistinguishable from the electropolished transverse specimens. It appears that the scatter at 76 and 4 K is similar. Therefore, the anomalous 7-percent drop of σ_y at T_N, as reported by Yushchenko et al. [1], falls well within specimen-to-specimen variability determined in our study. This suggests either that the anomaly reported at T_N is not a real material effect or that the work of Yushchenko et al. [1] is more precise, reflecting a superior testing technique or less material variability.

To eliminate the obscuring effect of specimen-to-specimen variability, single-specimen temperature-change tests were performed. The results from these tests tend to support the conclusion that no anomalous decreases of strength occurred. In Figure 5, the multiple data points from single specimens are linked with straight lines. These trend lines have nearly equivalent slopes and do not cross over one another. One specimen was tested first at 60 K, then at 50 K, but the strength did not decrease, as would have been expected from the trend line drawn by Yushchenko et al. [1] through this temperature interval.

In the temperature-change tests, it was assumed that strain history effects are negligible, e.g., that the pattern of the dislocation movement is physically unchanged by the temperatures involved. A flow stress increase on reloading at the second (lower) temperature is then just the measure of stress needed to continue plastic deformation for the same dislocation mechanism at a lower temperature.

The flow strength (σ_f) is proportional to the shear modulus (G) and the dislocation density (P) through the relationship

$$\sigma_f = \alpha \, Gb \, p^{\frac{1}{2}}$$

where α usually has a value between 0.2 and 0.5 (e.g., Conrad [13]). The ½ percent decrease of G measured at T_N for the Fe-20Cr-16Ni-6Mn-0.2N alloy would not alone be sufficient to account for the 7-percent decrease of σ_y, as reported by Yushchenko et al. Indeed, the ½-percent effect is indistinguishable from experimental scatter in σ_y measurements. The single-specimen change test conducted at 60 and 50 K shows an increase of σ_y with a magnitude equivalent to that expected from the exponential function of Eq. (1).

Finally, it should be pointed out that in addition to the Neel temperature anomaly, Soviet authors have also reported a 15-percent decrease of σ_y for other Fe-Cr-Ni stainless steels at temperatures between 20 and 4 K [2,3]. This has not been explained completely, but dislocation tunnelling process is a possible explanation [2,3]. However, the present data for Fe-20Cr-16Ni-6Mn-0.2N steel indicate no anomaly at this temperature either. Yushchenko et al. [1] do not present data below 20 K for this particular steel, so confirmation is lacking.

Alloy Fe-18Cr-10Ni-1.5Mn-0.1N: Tensile flow strength data at strain offsets of 0.0005 and 0.002 (yield strength) are plotted as a function of temperature in Figure 6 and listed in Table 5. Plotted linearly versus temperature, the dependence of flow strength is slightly concave upwards with decreasing temperature. The difference between the 0.002 and 0.0005 strain flow strengths is also plotted versus temperature in Figure 6. Approximately, the

difference doubles at 4 K, compared to room temperature, indicating that at low strains the rate of work hardening increases at lower temperatures.

The ratio of the flow strength at 0.0005 plastic strain at 76 and 4 K to 295 K is 2.3 and 2.9, respectively. At a strain of 0.002, the ratios of 76 and 4 K flow strengths to room temperature flow strength are 2.2 and 2.8, respectively. Cottrell and Stokes [14] originally suggested that these ratios are a constant, independent of strain. But, within the strain range measured, there is a slight trend for the ratio to decrease at higher strains.

Temperature-change experiments were also performed on the Fe-18Cr-10Ni alloy. In Figure 7, the measurements from seven specimens are plotted. In all of these measurements, the temperature was lowered after reaching strains between 0.0005 and 0.002. The temperature dependence found from single-specimen tests is plotted as a smooth curve in Figure 7. All specimens exhibited normally rising flow strength with a decrease in temperature, with the possible exception of the specimen originally strained at 295 K. The change of strength achieved from the changing of temperature matches that obtained from individual tests at the two temperatures. Thus, the flow strength contributions are reversible with temperature (in the range 4 to 190 K) for these alloys at the low strain levels at which measurements were obtained. This implies that there was no change in deformation mechanism for this alloy at temperatures below 190 K.

Our data and data for a similar Fe-18.25Cr-9.7Ni-0.91Mn-0.01S-0.29Si-0.01C alloy [3] are presented for comparison in Figure 8. Whereas all three of the anomalies were reported in the USSR steel, none of them were evident in our steel, which is similar in base composition and in total interstitial content.

The temperature dependence of the flow strength of the Fe-20Cr-16Ni-6Mn-0.2N alloy is included in the linear plot of σ_y-T of Figure 6 and that of the Fe-18Cr-10Ni-1.5Mn-0.1N is included in the log σ-T plot of Figure 4. Clearly the temperature dependences of the flow strength of the two alloys are different and cannot be characterized by the same equation form. From Figure 4 one may suggest that the dependence of the flow strength on temperature of the Fe-18Cr-10Ni-1.5Mn-0.1N alloy may be characterized by a change of deformation mechanism below about 200 K, producing two linear regions (4 to 200 K, 200 to 300 K) in the log σ-T graph. The temperature change experiments (Figure 7) do not conflict with this characterization. The austenite of the Fe-20Cr-16Ni-6Mn-0.2N alloy is relatively very stable and is expected to have higher stacking fault energy [10,11] and lower M_s (below 0 K) than the Fe-18Cr-10Ni-1.5Mn-0.1N alloy, owing to the higher concentrations of nickel, nitrogen, and manganese. Furthermore, α transformation was detected in Fe-18Cr-10Ni-1.5Mn-0.1N specimens deformed to 0.002 strains at 76 and 4 K, and the estimated T_{md} for this alloy is calculated to be about 179 K (Table 1).

The temperature dependences of the two alloys, normalized with respect to the shear modulus, are plotted in Figure 9; they are not identical. The Fe-20Cr-16Ni-6Mn-0.2N alloy, considered to have a higher stacking fault energy, (Table 1) has a steeper temperature dependence. This corresponds to the form of the temperature dependence as a function of stacking fault energy found for several face-centered cubic elements [13].

SUMMARY

Two austenitic stainless steel alloys were measured in tension between 4 and 300 K and compared with other data for identical or similar alloys. One alloy contains 20Cr, 16Ni, 6Mn, and 0.2N; the other contains 18Cr, 10Ni, 1.5Mn, and 0.1N and is an AISI 304LN.

1. The reported anomalous low temperature dependences of the flow strength associated with the Neel transition temperature and very low temperatures ($\lesssim$20 K) for austenitic steels were not confirmed by this study.
2. Temperature change experiments indicate reversibility of flow strength at temperatures below about 100 K. This implies that the deformation mechanisms do not change at low temperatures for these alloys.
3. The temperature dependence of the flow strength of the two alloys is best characterized by a linear dependence of log σ versus T. The more stable Fe-20Cr-16Ni-6Mn-0.2N alloy exhibits a linear slope of log σ versus T over the entire temperature test range (4 to 295 K). The less stable Fe-18Cr-10Ni-1.5Mn-0.1N alloy, partially transforming to body-centered cubic martensite at low temperatures, exhibits two linear ranges on a log σ versus T plot, one from 4 to about 200 K, the other from about 200 to 295 K.

REFERENCES

1. Yushchenko, K. A., Verkin, B. I., Ilichev, V. Ya., and Klimenko, I. N., "The Influence of Magnetic Structure on Temperature Dependence of the Yield Strength of 20Cr-16Ni-6Mn Steel at Low Temperatures," in Advances in Cryogenic Engineering-Materials, Vol. 28, Plenum Press, New York, 67-72 (1982).

2. Ilichev, V. Ya., Medvedev, Ya. M., Shapovalov, I. A., and Klimenko, I. N. "Low Temperature Anomaly of the Temperature Dependence of the Flow Stresses in Iron-Chromium-Nickel Alloys," Fizika Metallov i Metallovedenie 44, No. 2, 173-176 (1980).

3. Verkin, B. I., Ilichev, V. Ya., and Klimenko, I. N., "The Low Temperature Change of the Magnetic Structure and Plastic Properties of Fe-Cr-Ni Alloys," in Advances in Cryogenic Engineering-Materials, Vol. 26, Plenum Press, New York, 120-125 (1980).

4. Reed, R. P. and Simon, N. J., editors, "Material Studies for Magnetic Fusion Energy Applications at Low Temperatures - IV, National Bureau of Standards, Boulder, CO, NBSIR 81-1645, (1981).

5. Tobler, R. L., Beekman, D. H., and Reed, R. P., "Low-Temperature Dependence of Yielding in AISI 316 Stainless Steels," unpublished, National Bureau of Standards, Boulder, CO (1981).

6. Reed, R. P., Tobler, R. L., Elmer, J. W., McHenry, H. I., and Yushchenko, K. A., "Strength and Toughness of USSR Fe-20Cr-16Ni-6Mn-0.2N Weldments at Cryogenic Temperatures, in Proceedings of the Eighth International Cryogenic Engineering Conference, IPC Science and Technology Press, Guildford, Surrey, England, 797-801 (1980).

7. Read, D. T. and Tobler, R. L., "Mechanical Property Measurements at Low Temperatures," in Advances in Cryogenic Engineering-Materials, Vol. 28, Plenum Press, New York, 17-28, (1982).

8. Eichelman, G. H. and Hull, F. C., "The Effect of Composition on the Temperature of Spontaneous Transformation of Austenite to Martensite in 18-8-Type Stainless Steel," Transactions of the American Society for Metals 45, 77-104 (1953).

9. Williams, I., Williams, R. G., and Capellero, R. C., "Stability of Austenitic Stainless Steels between 4 K and 373 K," in Proceedings of the Sixth International Cryogenic Engineering Conference, IPC Science and Technology Press, Guildford, Surrey, England, 337-341 (1976).

10. Schramm, R. E. and Reed, R. P., "Stacking Fault Energies of Seven Commercial Austenitic Stainless Steels," Metallurgical Transactions 6A 1345-1351, (1975).

11. Rhodes, C. G. and Thompson, A. W., "The Composition Dependence of Stacking Fault Energy in Austenitic Stainless Steels," Metallurgical Transactions 8A, 1901-1906 (1977).

12. Ledbetter, H. M. and Austin, M. W., "Low-temperature elastic properties of an Fe-20-16Ni-6Mn alloy," in Material Studies for Magnetic Fusion Energy Applications at Low Temperatures - V, R. P. Reed and N. N. Simon, editors, National Bureau of Standards, Boulder, CO, NBSIR (1982).

13. Conrad, H., "The Cryogenic Properties of Metals," in High-Strength Materials, V. F. Zackay, Editor, John Wiley & Sons, NY, 436-509 (1965).

14. Cottrell, A. H. and Stokes, R. J., "Effects of Temperature on the Plastic Properties of Aluminum Crystals," Proceedings of the Royal Society A233, 17-34 (1955).

Table 1. Calculations of Stacking Fault Energy and Austenite Stability.

Alloy	T_{ms} [8] (K)	T_{md} [9] (K)	SFE [10] (10^{-5} J/m^2)	SFE [11] (10^{-5} J/m^2)
Fe-20Cr-15N-6Mn-0.2N	-898	-5	84	36
Fe-18Cr-10Ni-1.5Mn-0.1N	-106	179	28	23

Table 2. Yield Strength Measurements for Fe-20Cr-16Ni-6Mn-0.2N Stainless Steel (Transverse, Electropolished).

Specimen	Temperature (K)	Yield Strength, σ_y (MPa)
1	38	1029
2	45	993
3	295	356
4	4	1190
5	76	886
6	20.5	1034
7-1	57	898
7-2	41.5	958
8-1	67	896
8-2	30.5	1040
8-3	4	1151
9-1	59.5	955
9-2	50	1000
9-3	10	1167

Table 3. Yield Strength Measurements for Fe-20Cr-16Ni-6Mn-0.2N Stainless Steel.*

Specimen No.	Temperature (K)	Yield Strength, σ_y (MPa)
1C B3	-	343
2C B3	-	333
2C B2	-	465
7	-	525
4	153	609
2-1	100	765
1C B1	76	832
2C B2	76	878
1	76	838
8	76	823
6	60	979
2-3	58	951
4	40	1028
3	18	1069
5	15	1082
2	4	1077
B2	4	1096
B4	4	1186

* Longitudinal specimens, as machined, 28 finish.

Table 4. Yield Strength Measurements* for Fe-20Cr-16Ni-6Mn-0.2N Steel.

Temperature (K)	Yield Strength, σ_y (MPa)
20	1122
31	1008
42	946
51	904
57	880
58	923
62	934
68	893
72	863
80	848
102	770
108	769
114	748
123	700
162	595
184	550
300	~340?

* USSR data [1-3]; taken using ruler and interpolation from published graphs.

Table 5. Tensile Results, Fe-18Cr-10Ni-1.5Mn-0.1N Steel.

Specimen No.	Temperature K	Flow Strength $\sigma_{0.0005}$ MPa	$\sigma_{0.0002}$ MPa	$\sigma_{0.002}-\sigma_{0.0005}$ MPa
4	295	230	262	32
3	190	350	408	48
17	150	400	458	58
5	145	418	460	42
1	120	448	490	42
2	83	482	569	87
6	72	530	614	84
10	70	536	*	--
8	57	553	619	66
11	35	561	*	--
7	29	603	670	67
9	4	593	685	92
12	4	657	736	79
16	4	662	750	88

*Multiple straining started at 0.0005 strain.

LIST OF FIGURES

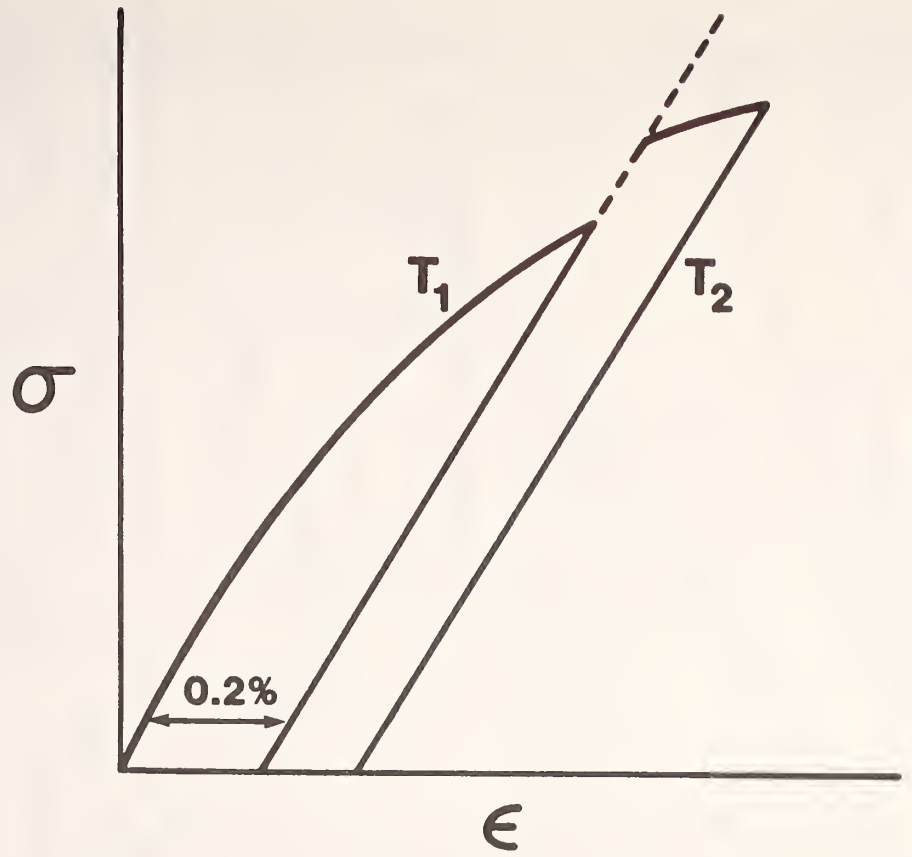

Figure 1. Temperature change test procedure to obtain reversible change of flow strength at two temperatures.

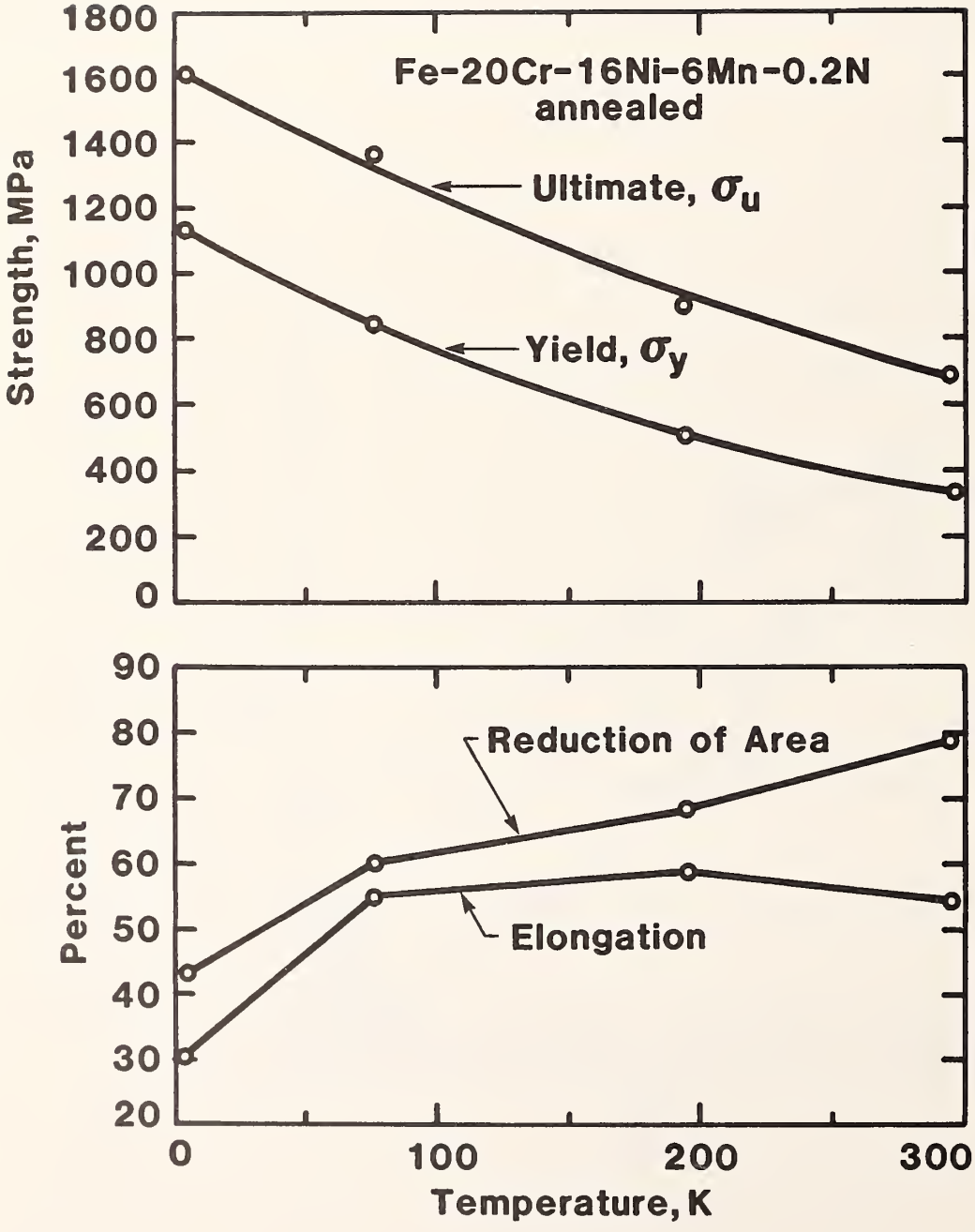

Figure 2. Tensile properties at 295, 195, 76, and 4 K of alloy Fe-20Cr-16Ni-6Mn-0.2N.

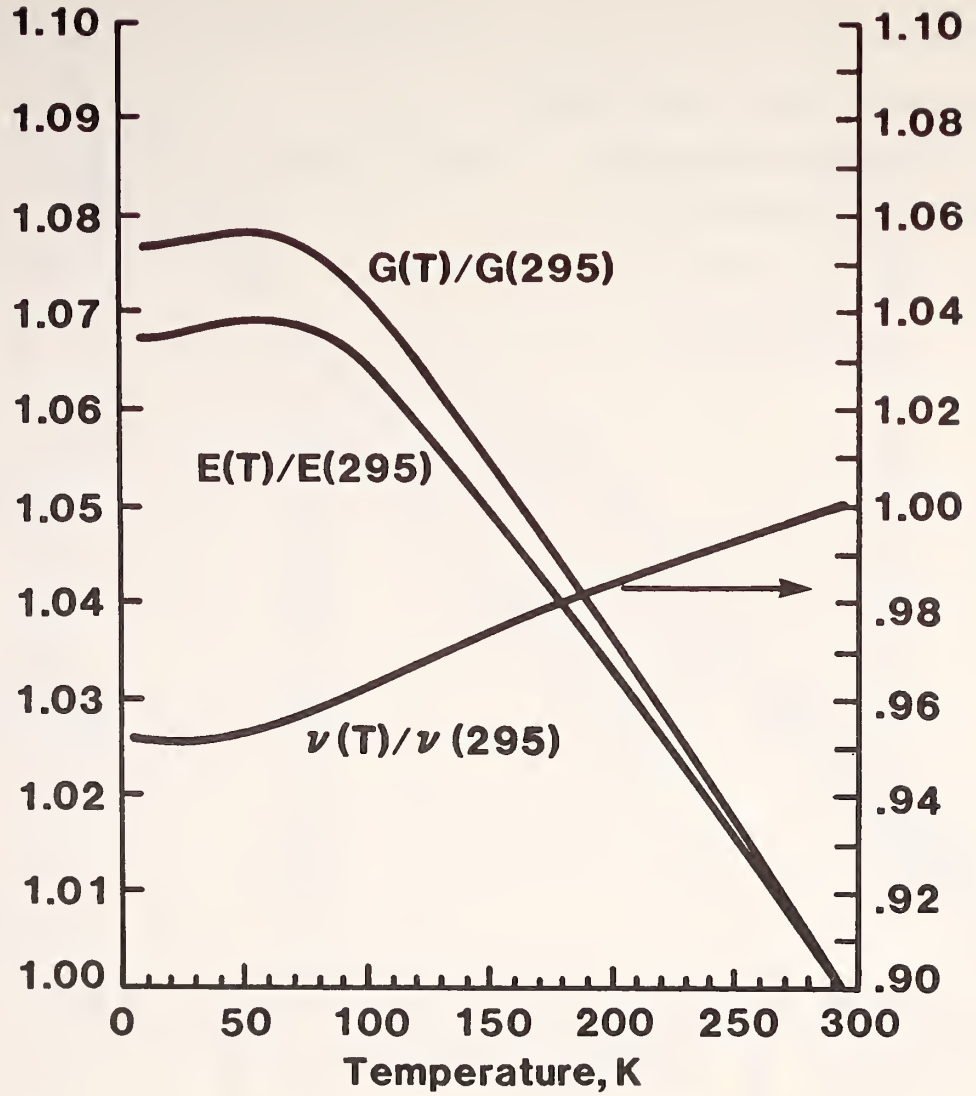

Figure 3. Elastic properties of Fe-20Cr-16Ni-6Mn-0.2N steel (G = shear modulus, E = Young's modulus, ν = Poisson's ratio [12]).

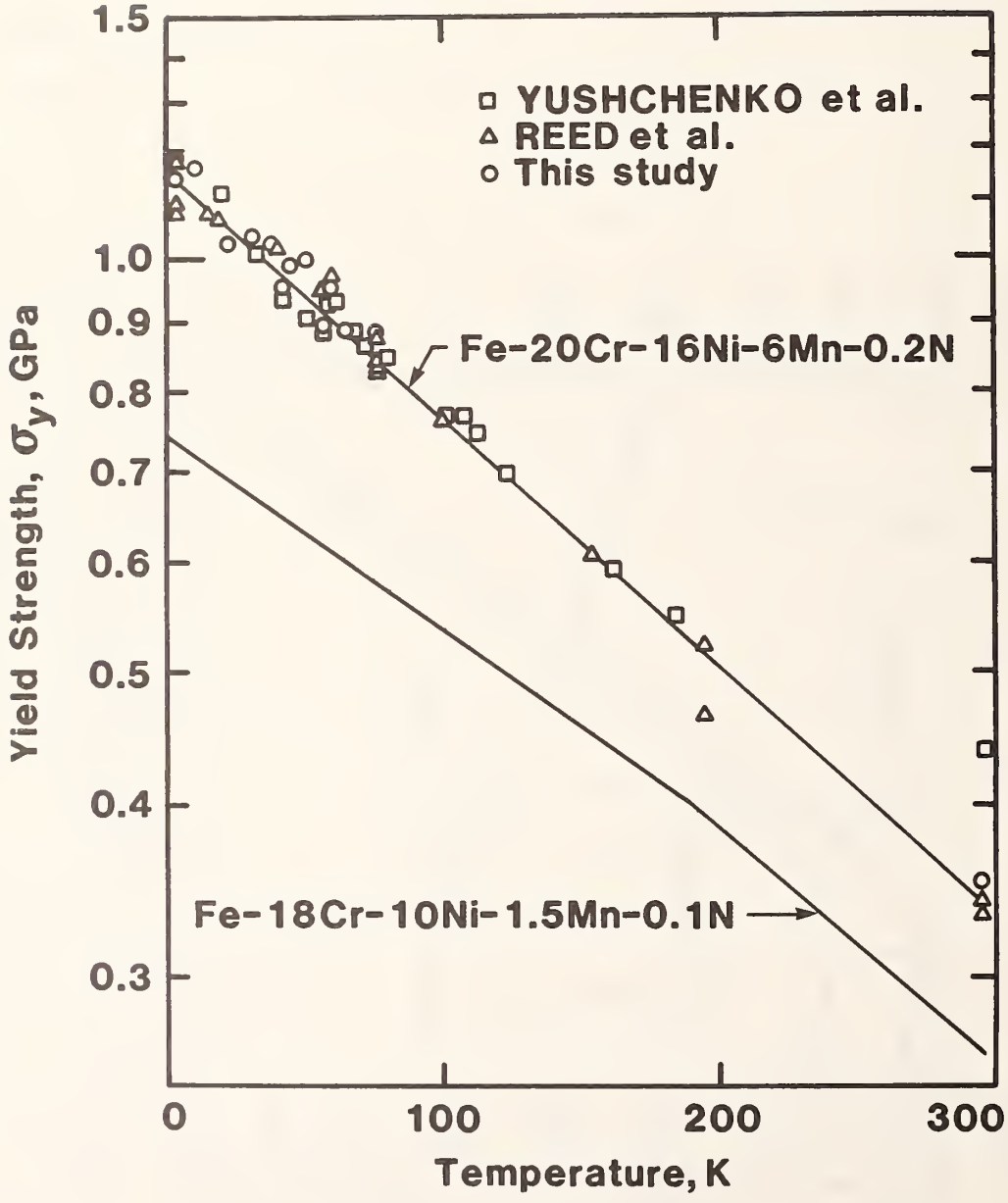

Figure 4. Yield strength versus temperature for Fe-20Cr-16Ni-6Mn-0.2N steel, summarizing data from this study and other studies [1-3,6]. Also included are average data of Fe-18Cr-10Ni-1.5Mn-0.1N alloy.

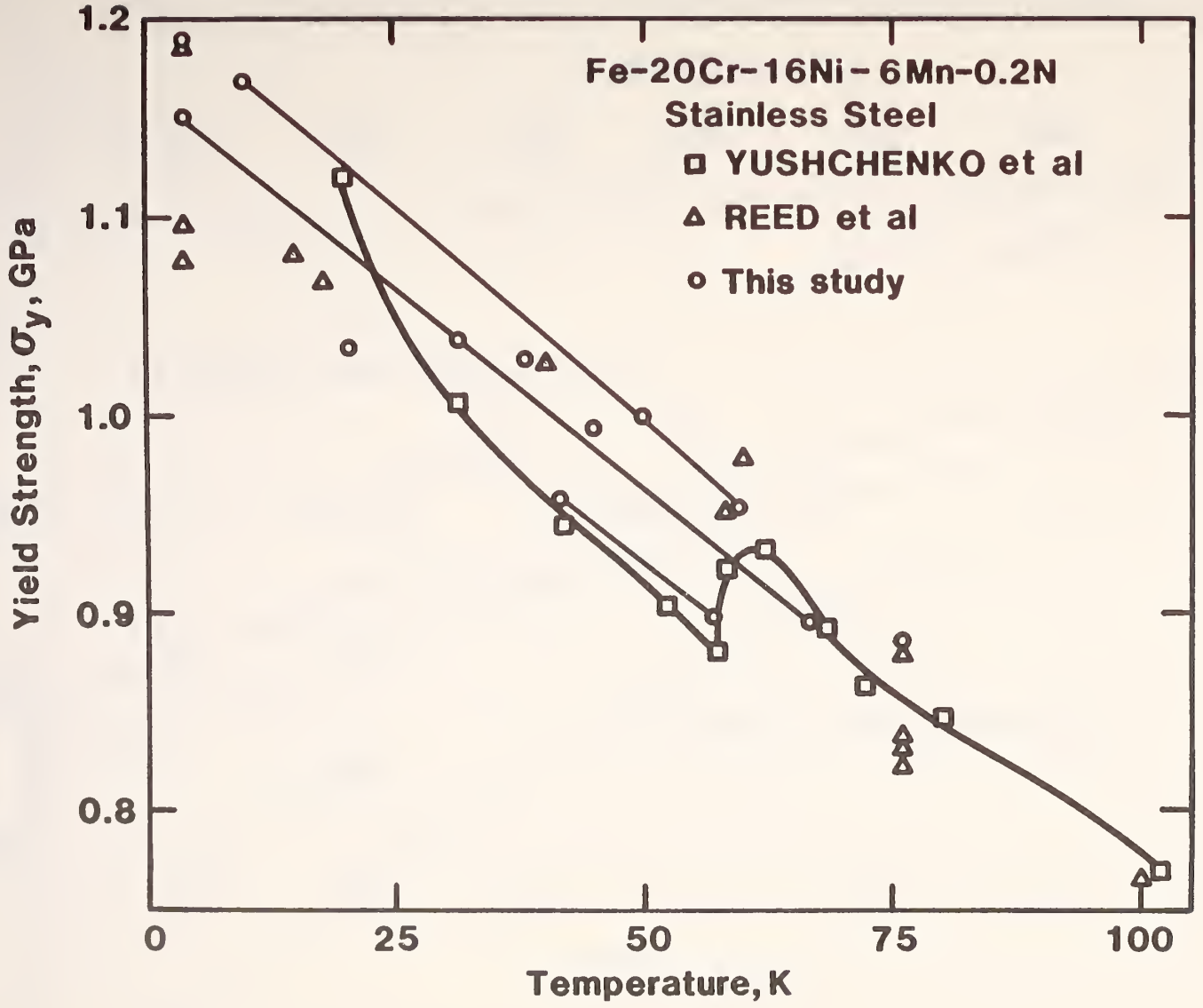

Figure 5. Yield strength data at cryogenic temperatures, showing specimen-to-specimen variability and trend, as reported by other studies [1-3].

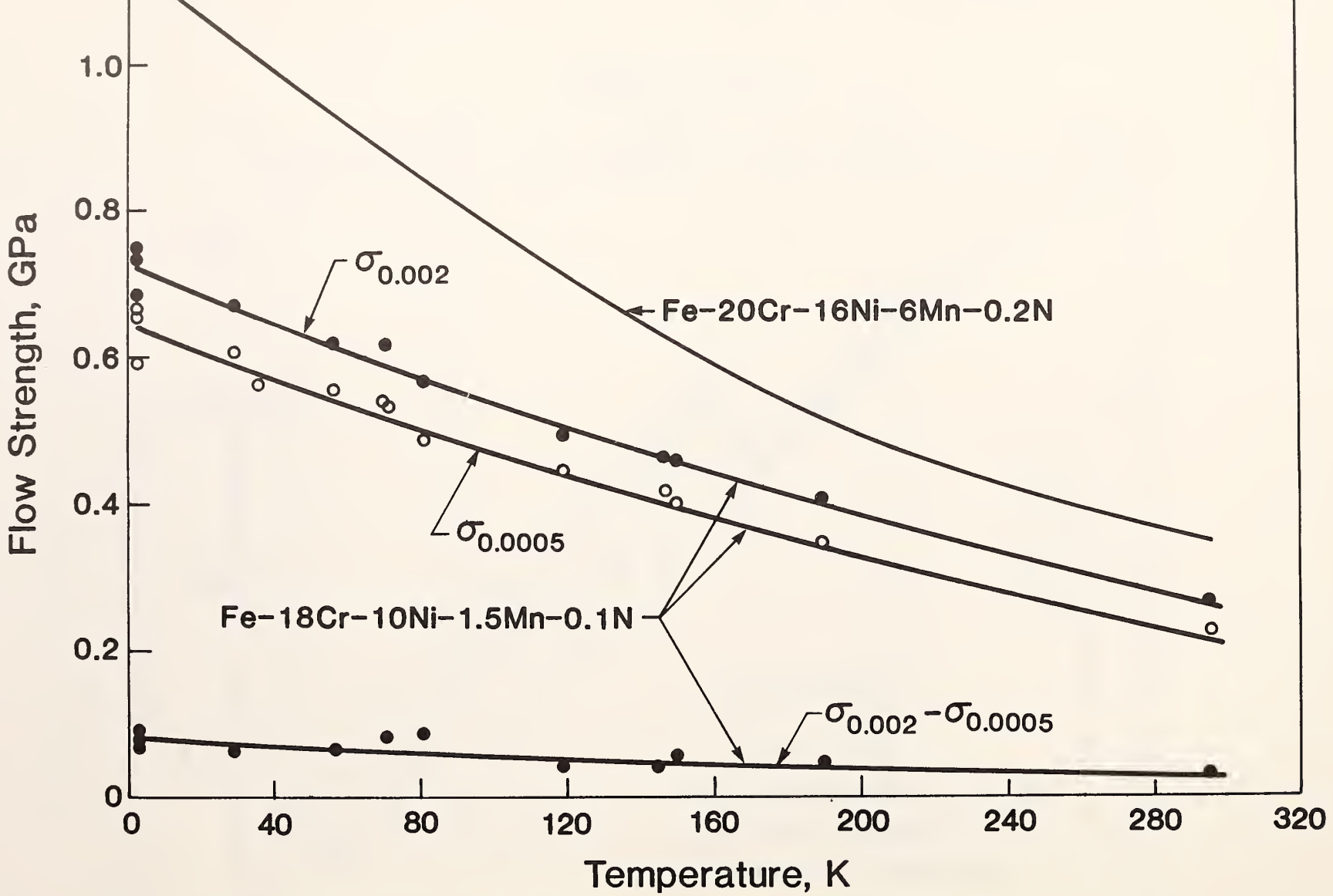

Figure 6. Flow strength at strains of 0.0005 and 0.002 as a function of temperature for Fe-18Cr-10Ni-1.5Mn-0.1N alloy. Also included are average data of Fe-20Cr-16Ni-6Mn-0.2N alloy.

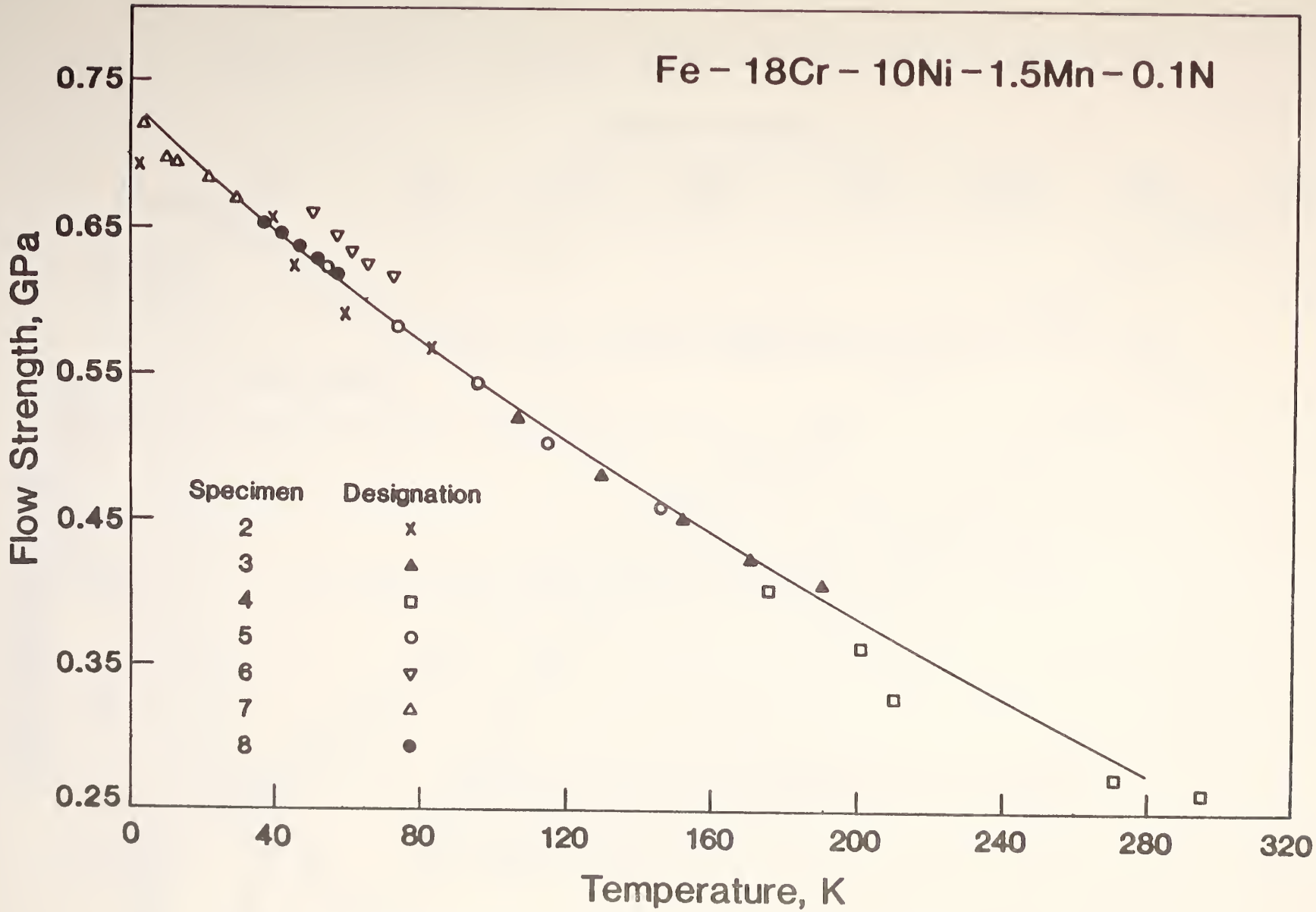

Figure 7. Flow strength of Fe-18Cr-10Ni-1.5Mn-0.1N alloy at strain of 0.002 (yield strength) measured from specimens sequentially cooled and strained.

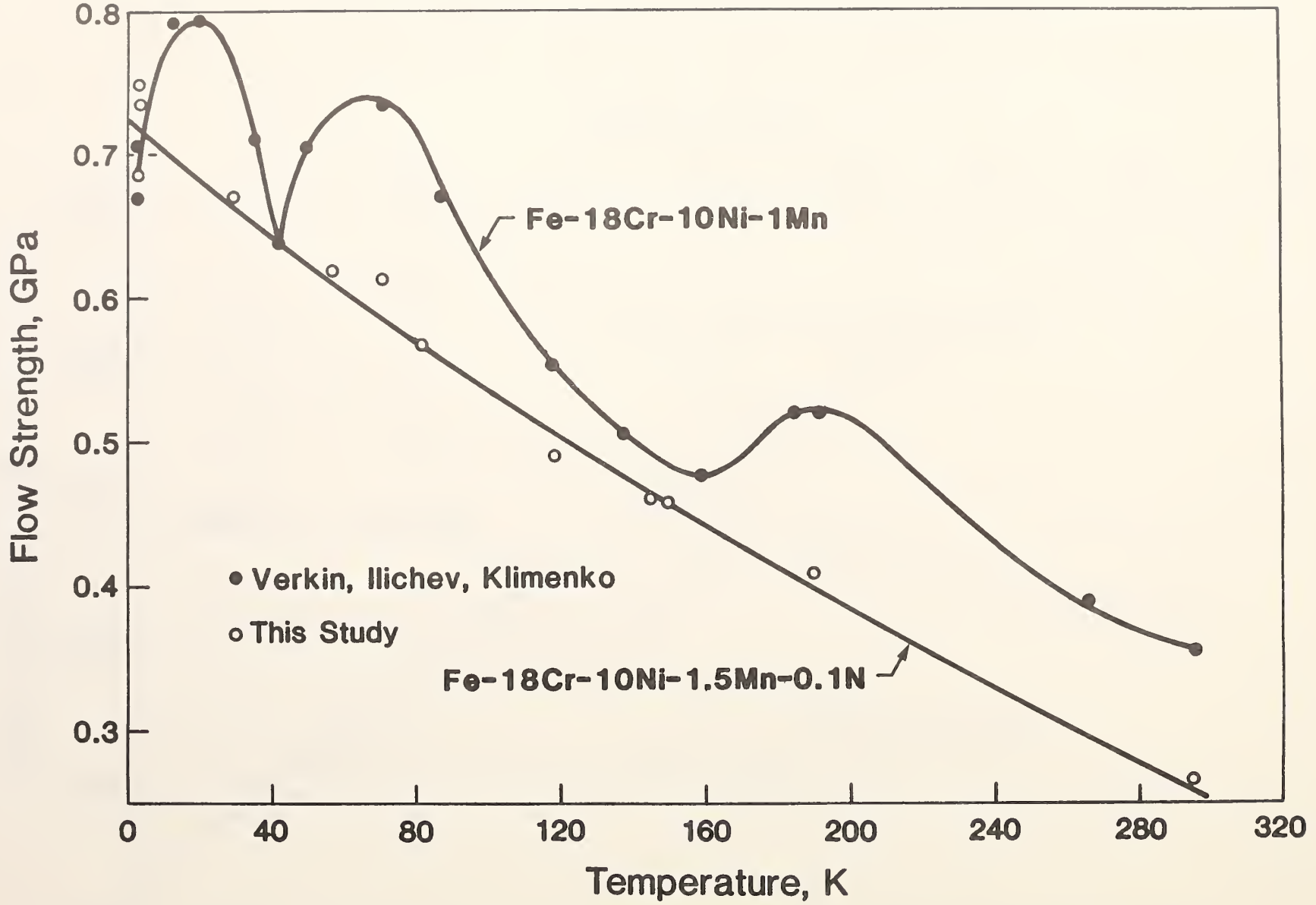

Figure 8. Comparison of data from Verkin et al. [3] and this study for Fe-18Cr-10Ni alloys.

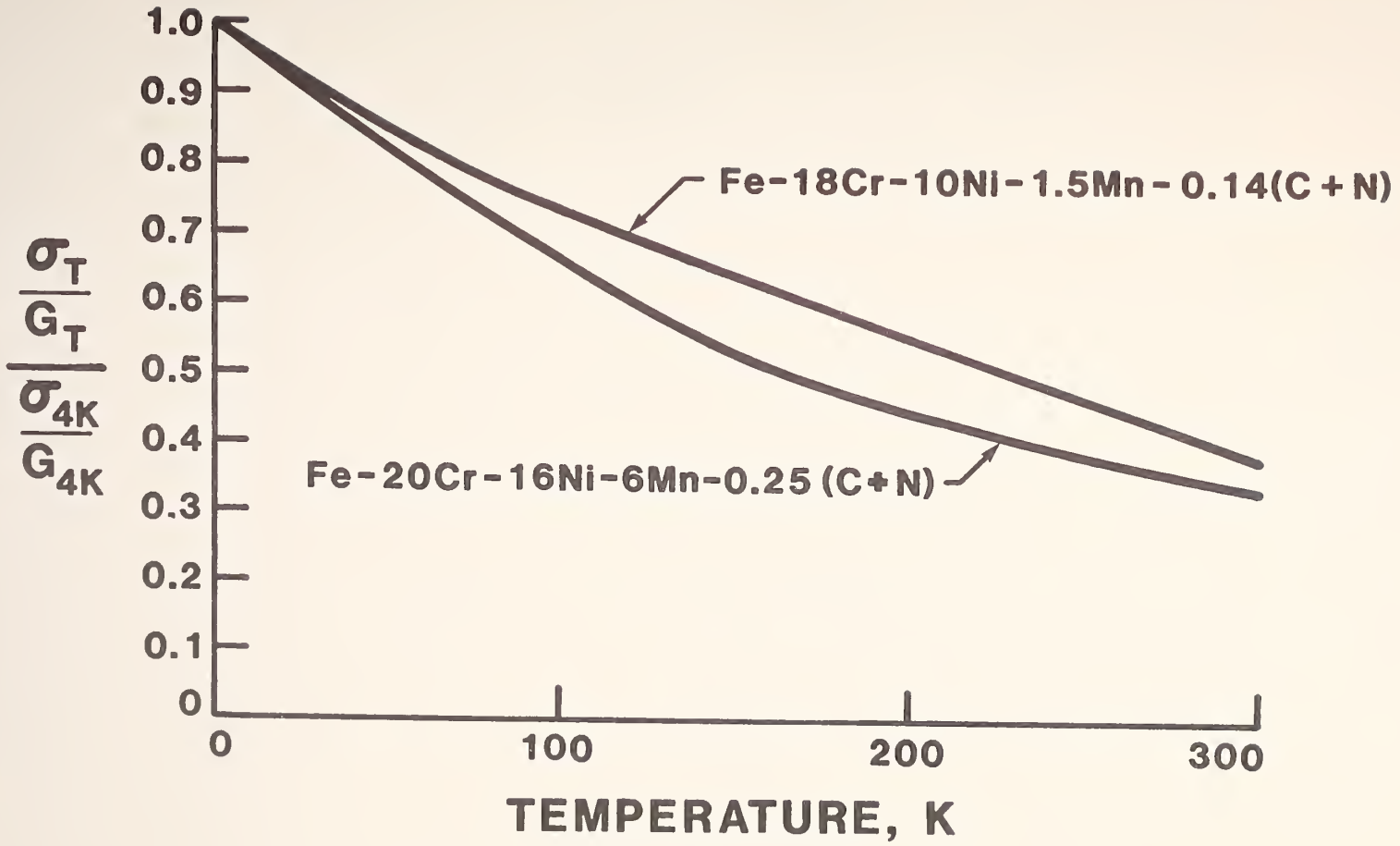

Figure 9. Normalized temperature dependence of the flow strength at 0.0002 strain for both alloys.

TENSILE AND FRACTURE PROPERTIES OF MANGANESE-MODIFIED AISI 304 TYPE STAINLESS STEEL*

R. L. Tobler and R. P. Reed
Fracture and Deformation Division
National Bureau of Standards
Boulder, Colorado

ABSTRACT

A series of ten low-carbon AISI-304-type austenitic stainless steels having 1 to 6% Mn and 0.1 to 0.2% N were produced and tested to determine the effect of these elements on properties at 4 K. Tensile tests (at 295, 76, and 4 K) and J-integral fracture toughness tests (at 4 K) were conducted on developmental steels containing 18.25 to 19.50% Cr, 7.9 to 8.75% Ni, and 0.02 to 0.03% C. All steels were hot-rolled at 1450 K (2150°F) from ingots to 25.4-mm (1-in) plates. The 4-K yield strengths ranged from 620 MPa (90 ksi) to 1068 MPa (155 ksi), increasing strongly with nitrogen content. Unacceptably low toughness was observed in the low manganese compositions, whereas the fracture toughnesses of alloys containing 6% Mn were equivalent to those of conventional AISI 304 stainless steels.

+To be published in Advances in Cryogenic Engineering-Materials, Vol. 28, R. P. Reed and A. F. Clark, Eds, Plenum Press, New York (1982).

INTRODUCTION

The AISI-300 series stainless steels are austenitic Fe-Cr-Ni alloys offering relatively low strength but excellent cryogenic ductility and toughness. Recently, nitrogen-strengthened grades, such as AISI 304 N or AISI 304 LN, have attracted attention as possible substitutes for applications demanding higher strength. Nitrogen is a relatively inexpensive strengthener, and it stabilizes the austenitic structure with respect to martensitic phase transformation. A disadvantage of the nitrogen strengthened grades is that they are more difficult to fabricate. To overcome this disadvantage, manganese additions (greater than the normal 1 or 2 wt.%) have been recommended. The potential advantages of manganese-modified type AISI 304 LN steels are: (1) consistent fabricability, (2) consistent weldability, and (3) reliable supply in all product forms[1]. Other studies[2–4] have reported potential advantages with manganese additions. It was the purpose of this study to investigate the effects of manganese on the 4 K mechanical properties of nitrogen strengthened AISI 304 L type alloys. Therefore, a series of steels containing 1-6% Mn and 0.1-0.2% N were prepared, tested, and compared with previous results for Fe-18Cr-10Ni stainless steels[5,6].

MATERIALS

Ten stainless steel plates were obtained from a commercial steel manufacturer. These steels had chemical compositions as listed in Table 1. Heats 69, 70, 73 and 74 have compositions corresponding to AISI 304 LN; the other heats are modifications. Grain size ranged randomly from 49 to 57 μm diameter and hardness

Table 1. Compositions of normal (Mn = 2% or less) and modified (greater than 2% Mn) type 304 LN stainless steel.

Heat No.	Weight Percent									
	C	Mn	P	S	Si	Cr	Ni	Mo	Cu	N
69	0.025	1.02	0.022	0.013	0.53	18.19	8.68	0.32	0.30	0.11
70	0.028	2.00	0.021	0.013	0.63	18.10	8.66	0.31	0.28	0.11
71	0.025	3.85	0.023	0.013	0.59	18.22	8.70	0.31	0.29	0.11
72	0.021	5.81	0.023	0.014	0.64	18.06	8.62	0.33	0.30	0.11
73	0.025	1.19	0.023	0.015	0.60	19.36	7.81	0.32	0.28	0.19
74	0.022	2.01	0.023	0.013	0.64	19.35	7.89	0.32	0.30	0.19
75	0.024	3.85	0.022	0.014	0.65	19.25	7.84	0.31	0.31	0.21
76	0.033	5.79	0.024	0.014	0.61	19.48	7.83	0.31	0.31	0.21
77	0.026	4.03	0.023	0.014	0.62	18.71	8.22	0.31	0.30	0.15
78	0.031	5.80	0.024	0.014	0.62	18.42	8.29	0.31	0.30	0.15

from R_B 82 to 94. No precipitation at grain boundaries was observed from careful light microscopy examination of the microstructures for all heats.

All steels were produced from ingots (12.7 x 12.7 x 17.8 cm) which were hot-rolled at 1450 K to plates approximately 25 mm thick. The plates were annealed at 1340 K for one-half hour, then water quenched and acid pickled. Grain boundary segregation was suspected in the lower Mn alloys. Solution treatments at 1560 K for one hour with a water quench were made on heats 69 and 78. Following this anneal, compact fracture specimens were machined.

EXPERIMENTAL PROCEDURE

Tensile tests were conducted using equipment, procedures, and specimen geometry previously described[5]. The specimens were machined in the transverse orientation. The load-vs-deflection curves were recorded using the outputs from a commercial load cell and strain-gauge extensometer. The crosshead rate was 8.5 μms^{-1}.

Single-specimen J-integral tests were used to measure fracture toughness. The technique incorporates a computer to enable digital data acquisition and J-resistance curve plotting during the tests, as described previously[5,6]. The compact fracture toughness specimen was 24.6 mm thick and 50.8 mm wide. The notch was machined in the TL orientation, as defined in ASTM E-399-78a[7].

The fracture specimens were fatigue cracked at 76 K to a crack length, a, between 27.25 and 31.44 mm (a/W ≃ 0.535 to 0.620). The maximum load used in fatigue precracking was 22 kN. The specimens were then loaded in displacement control. As the load increased, partial unloadings (10%) were performed periodically. Using a crack-length-vs-compliance correlation, the crack length at each unloading was inferred and used to obtain the crack extension increment (Δa) from the difference of the initial precrack length. The J value at each unloading point was calculated using the expression: $J = \lambda A/Bb$, where λ is the Merkle-Corten factor, A is the area under the load-vs-deflection curve at the unloading point, and b is the specimen ligament ($b = W - a$).

Scatter in the J-resistance curves led to uncertainties of ± 15% in the values of J_{Ic}.

The J_{Ic} values were converted to K_{Ic} estimates, denoted $K_{Ic}(J)$, using a Young's modulus value of 206.8 GPa, a Poisson's ratio of 0.30, and the standard formula relating the elastic J to K_{Ic}[5].

Magnetic measurements, using a bar magnet, torsion balance were used to estimate the percent bcc (ferromagnetic) martensite that formed during deformation. A calibration had previously been made relating data obtained from the torsion balance device to volume percent bcc martensite[8]. The measurements were all made within the gage length, in the uniform elongation section.

X-ray techniques previously described[8], (measurement and computation of integrated peak intensities of fcc, bcc, and hcp structures) were used to estimate the amount of bcc martensite on the fracture surface of compact tension specimens. The area of the specimens examined was restricted to near the pre-crack tip to ensure some relationship to the plastic-zone at initiation of crack growth. In all x-ray measurements no hcp phase was ever detected on the crack surface.

Hardness measurements were made using a diamond pyramid indentor and a 10 g load. Hardness traverses on annealed specimens with polished surfaces were conducted to attempt to detect segregation effects at grain boundaries.

RESULTS AND DISCUSSION

Tensile Properties

The tensile properties of the steels tested in this study are plotted in Figs. 1 through 3 and tabulated in Ref. 5. In these figures comparison is made with trend lines from a previous study[6]. As shown in Fig. 1, the yield strength (σ_y) data for the

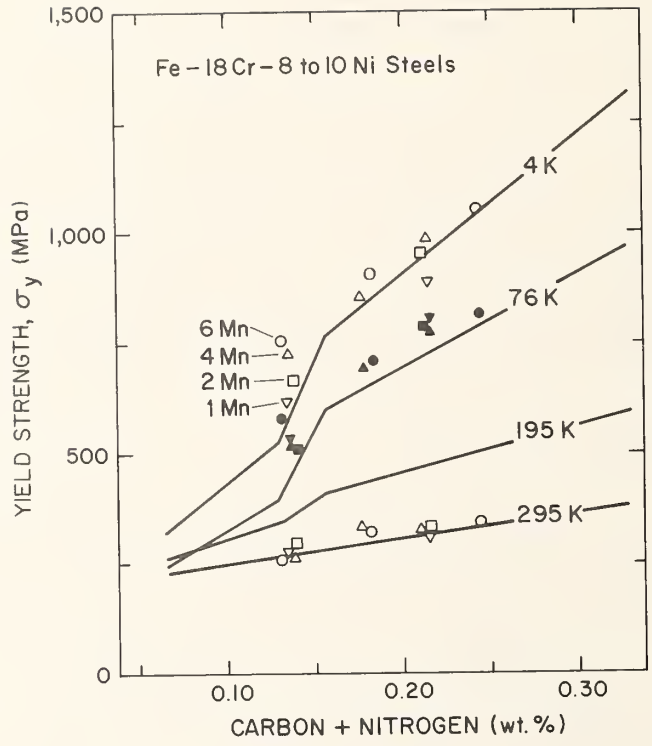

Fig. 1 Effect of carbon plus nitrogen content on yield strength of stainless steels, at various temperatures.

present Fe-18.25-19.5Cr-7.90-8.75Ni steels (open symbols) agree well with previous data trends for Fe-18Cr-10Ni steels (solid lines). The 295 K data confirm a previous conclusion: the yield strength is a linear function of C+N content[6], for the composition range studied. The 4 K data also confirm the existence of a kink in the σ_y-vs-C+N plot at C+N contents between 0.127 and 0.157 wt.%. In our previous study[6], this kink was attributed to the structural instability of the austenitic phase at lower interstitial contents. In the present study at 4 K there is a clear trend of increasing σ_y values with higher Mn contents at C+N contents from 0.131 to 0.138 wt.%. Apparently, the kink at 4 K is removed by the stabilizing effect of Mn additions at this critical interstitial content with respect to the martensitic transformation.

The ultimate tensile strength results of the present study, shown in Fig. 2, are also in general agreement with expected trends. The data at room temperature fall on the same trend line that was previously reported for the Fe-18Cr-10Ni stainless steels. The 4 K data show a minor variation, probably owing to the austenite stabilizing effect of Mn modifications. As more manganese is added at a given interstitial concentration level,

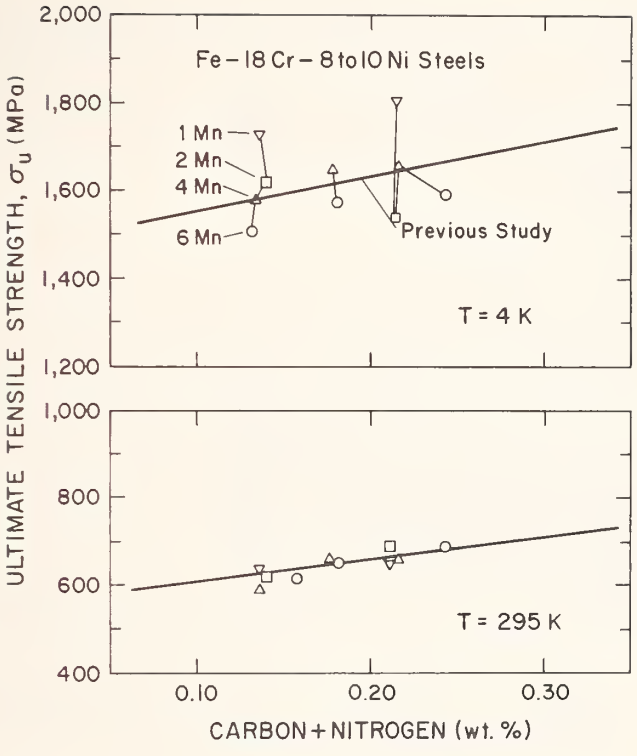

Fig. 2 Effect of carbon plus nitrogen interstitials on ultimate strength at two test temperatures.

the austentite is progressively more stable during tests at 4 K; as a result, less martensite is formed during testing and ultimate tensile strength is reduced as Mn concentration is increased to 6%.

Figure 3 shows the spread of the elongation and reduction of area measurements for the ten steels. Not all of the ductility values are typical of commercial stainless steels. In particular, the reduction of area values for the developmental steels containing 1-4% Mn are lower compared with values previously reported for Fe-18Cr-10Ni steels[6] or other commercially available AISI 304 LN steels. Only the 6% Mn-modified steels possess ductility values at the expected levels.

Magnetic measurements made on the fractured tensile specimens were converted to percent martensite, and "normalized" by dividing by the strain corresponding to the uniform elongation where the measurements were made. This procedure assumes a linear dependence of martensite formation with strain. The data are plotted versus Mn + Ni + 10(C+N) concentration in weight percent in Fig. 4. At higher solute concentrations the amount of martensite per unit strain is reduced. A ratio of the relative alloying contributions was chosen to provide a good fit to the data, and the result

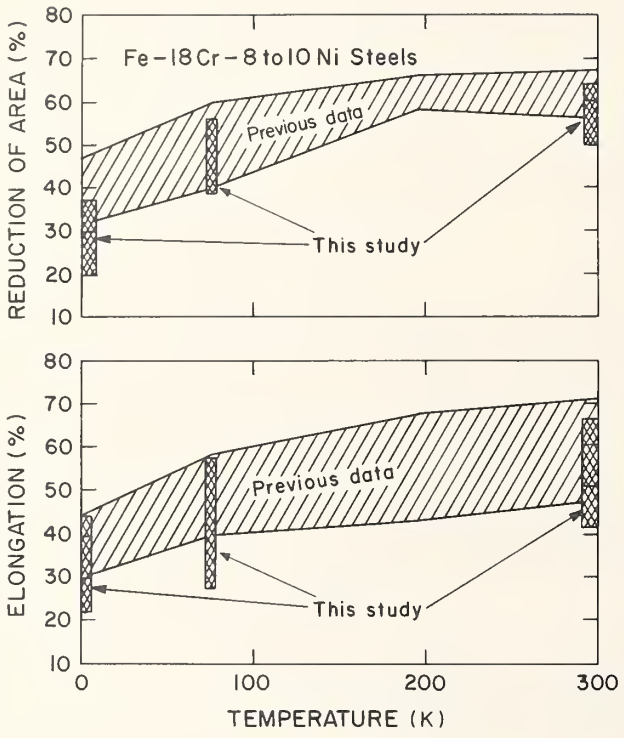

Fig. 3 Ductility of stainless steels.

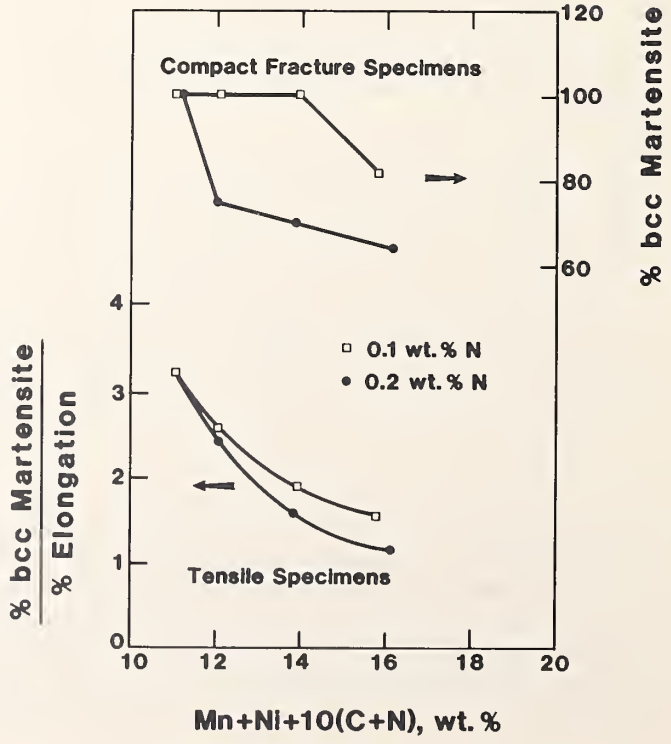

Fig. 4 The effect of alloy content on martensite formation at 4 K at the crack tip in compact tensile specimens and within uniform elongation section of tensile specimens.

follows approximately the prediction of the dependence of M_d temperature found by Williams[9] for compression of Fe-Cr-Ni alloys at low temperatures. However, from Fig. 4, it appears that the dependence on N content is not linear with Mn + Ni content. Also, the dependence of bcc martensite at compact specimen fracture surfaces is not linear with solute alloying concentration.

Fracture Toughness

The J_{Ic} results obtained for one specimen of each of the ten different steel compositions tested are tabulated[5] and the K_{Ic} (J) values are plotted in Fig. 5. The K_{Ic} (J) data follow regular trends depending on Mn and N content. Solid lines have been drawn to connect data representing constant Mn contents; for each Mn content the 0.1 N composition is represented by the symbol at the lowest yield strength, whereas the 0.2 N composition is represented by the higher yield strength, and 0.15 N is intermediate. From Fig. 5 it is clear that higher N at a given Mn content lowers the K_{Ic} (J) value. It is also clear that Mn has a favorable effect, raising both the strength and the toughness of these developmental alloys.

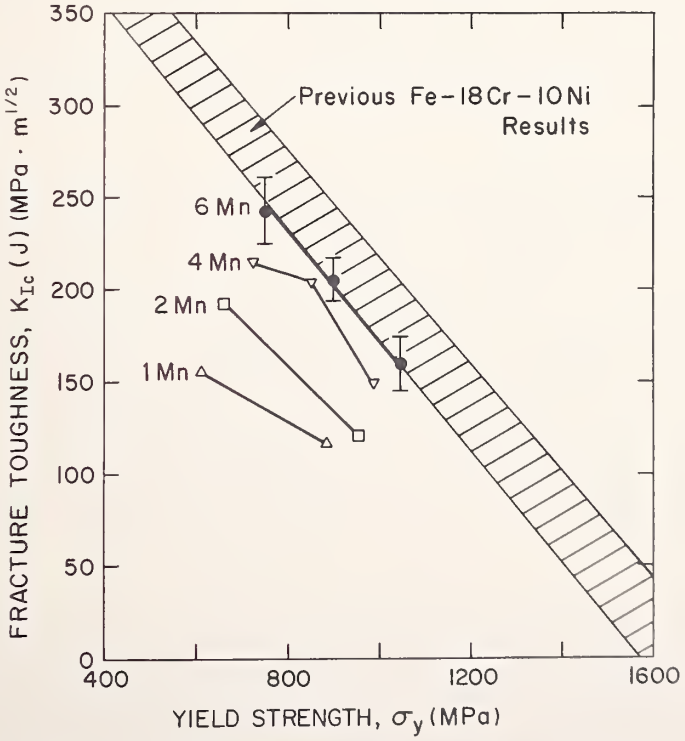

Fig. 5 Fracture toughness-vs-yield strength results for Mn-N modified steels of the present study, as compared with previous results for AISI 304 type stainless steels.

The major observation is that the 6%-Mn-modified steels have acceptable fracture toughness, whereas the modifications containing 1-4% Mn display inferior properties. The 1 and 2% Mn steels are particularly poor, having estimated K_{Ic} values as low as 117 $MPa \cdot m^{1/2}$. Their load-deflection fracture toughness test records showed a nearly linear-elastic behavior, with regions of instability (serrations). This evaluation is based on comparison with the previous results for a series of nine Fe-18Cr-10Ni stainless steels containing variable C+N contents. As shown in Fig. 5, the 6% Mn-modified steels exhibit an inverse $K_{Ic}(J)$ vs. σ_y relationship at 4 K and, within the measurement error indicated by the error bars shown in the figure, the inverse-linear trend falls along the lower bound of the scatter band of data for the Fe-18Cr-10Ni steels.

The cause of the unexpected low $K_{Ic}(J)$ values of the 1-4% Mn grades is not clear and we have examined several possibilities. The nominal compositional variations between the 1-2% Mn steels of this study and the Fe-18Cr-10Ni-1.5Mn steels of the previous study include a 1.25-2.5% difference in nickel content which may be significant. Metallurgical factors, such as interstitial segregation, may also contribute to the low fracture toughness of the 1-4% Mn steels of the present study. However, light microscopy revealed no evidence of sensitization or other obvious microstructural differences. Microhardness traverses across grain boundaries and centers failed to detect any hardness variations.

Evidence of an abnormal condition in the 1, 2, and 4% Mn steels was obtained by scanning electron microscopy performed on the fracture surfaces of the compact specimens subsequent to J_{Ic} testing at 4 K. Figure 6 presents typical results. Specimens containing 4% Mn or less exhibited unusual features consisting of isolated facets (probably intercrystalline fracture) surrounded by a matrix of numerous very fine dimples. In contrast, the three heats containing 6% Mn (heats 72, 76, and 78) all showed a more completely dimpled fracture mode, with relatively large dimples; this type of fracture was also observed in the Fe-18Cr-10Ni steels of our previous study, which had good fracture toughness. The only apparent distinction between thermal-mechanical treatments of the two alloy series was the temperature of hot-working of the billet. The hot-rolling temperature of the initial 304 LN alloy series was 1560 K (2350°F) and the rolling temperature of the 1-6 wt.% Mn alloy series was 1450 K (2150°F). In addition, plates from heats 69 and 78 were re-solution annealed at a higher temperature, machined into compact-tensile specimens, and tested at 4 K. The values of $K_{Ic}(J)$ (heat 69-133 $MPa \cdot m^{1/2}$; heat 78-172 $MPa \cdot m^{1/2}$) were about 15% lower than those reported in Fig. 5. This decrease was presumably caused by the increased grain size. In any case, the re-solution treatment failed to eliminate the problem of low toughness.

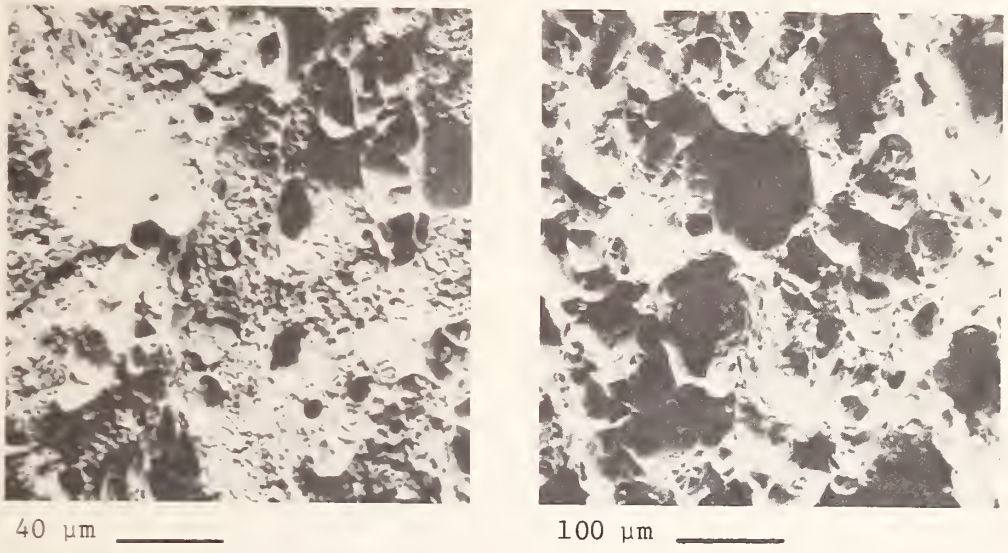

Fig. 6 Micrographs of fracture surfaces of low- (heat 69, left) and high toughness (heat 72, right) austenitic stainless steels.

X-ray diffractometer measurement data of the amount of martensitic transformation phases on the fracture surface near the crack tip of compact tensile specimens, tested at 4 K, are also shown in Fig. 4. As the alloy stability increases the amount of transformation during early crack formation is reduced. However, in all heats and tests the amount of transformation was extensive (> 64%), indicating large amounts of local plastic deformation in the region of the crack tip. We have also detected large amounts of transformation in the tough Fe-18Cr-10Ni austenitic steels[6]. In Fig. 4 notice that a tough alloy (heat 72) exhibited more crack tip martensite (81%) than two of the alloys (heats 74, 75) that exhibited marginal toughness. Therefore, it is difficult to argue that martensitic transformation, per se, results in reduced toughness. The rate of transformation per unit strain and the mechanisms of transformation must be considered. A possibility remains that the martensitic transformation which influences the stress-strain characteristics, produces a modified plastic zone. This modified zone in turn may influence J-integral measurements.

CONCLUSION

The data of this study show that 6% Mn-modified AISI 304 LN stainless steel can be produced, having conventional tensile and fracture toughness properties equivalent to standard AISI 304 LN stainless steel when tested at 4 K. However, the 1-4% Mn heats tested in this study displayed some unusual apparently brittle fracture features in association with relatively low fracture toughness. The cause of this behavior has not yet been established, but the problem deserves a full investigation.

ACKNOWLEDGMENTS

The stainless steel plates were produced by Armco, under the direction of R. H. Espy of Armco's Research and Technology Division. E. L. Brown, now at the Colorado School of Mines, contributed metallographic assistance, and D. Baxter of NBS conducted many of the tensile and fracture toughness tests. The work was sponsored by the Department of Energy, Office of Fusion Energy.

REFERENCES

1. R. H. Espy, "Stainless Steel Alloy Development," presented at NBS/DoE Workshop on Materials at Low Temperatures, Vail, Colorado, October 16-18, 1979.
2. T. Kato, M. Fujikura, T. Soh, and K. Ishida, "Effects of Alloying Elements on the Austenite Stability and Mechanical Properties of Austenitic Stainless Cast Steels at Cryogenic Temperatures," Denki Seiko, 48 (3):179-190 (1977).
3. J. Hochmann, "Le role des additions demanganese dans les aciers inoxydables austenitiques," Materiaux et Techniques, Spec. Issue 65:69-87 (1977).
4. A. B. Meade and R. Oppenheim, "Tieftemperatureigen schaftor stickstofflegierter austenitische chrom-nickel-(Molybdan)-sonie Chrom-Mangan-Nickel-Stakle und deren Eignung als Kaltzahe Stahle," DEW-Technische Berichte, 12:13-19 (1972).
5. R. L. Tobler and R. P. Reed, "Tensile and Fracture Properties of Manganese-Modified Fe-18Cr-8Ni Type Austenitic Stainless Steels," in: Materials Studies for Magnetic Fusion Energy Applications at Low Temperatures - IV, NBSIR 81-1645, R. P. Reed and N. J. Simon, eds., National Bureau of Standards, Boulder, Colorado, pp. 77-100 (1980).
6. R. L. Tobler, D. T. Read, and R. P. Reed, "Strength and Toughness Relationship for Interstitially Strengthened AISI 304 Stainless Steels at 4 K," in: Materials Studies for Magnetic Fusion Energy Applications at Low Temperatures - IV, NBSIR 81-1645, R. P. Reed and N. J. Simon, eds., National Bureau of Standards, Boulder, Colorado, pp. 37-76 (1981).
7. Standard Method of Test for Plane Strain Fracture Toughness of Metallic Materials (Designation E399-74), in: 1974 Annual Book of ASTM Standards, Part 10, American Society for Testing and Materials, Philadelphia, Pennsylvania pp. 432-451 (1974).
8. R. P. Reed and C. J. Guntner, "Stress-Induced Martensitic Transformations in 18Cr-8Ni Steel," Trans. AIME, 230:1713-1720 (1964).
9. I. Williams, R. G. Williams, and R. C. Capellero, "Stability of Austenitic Stainless Steels Between 4 K and 373 K," Proc. Sixth Int'l. Cryogenic Eng. Conf., IPC Science and Technology Press, Guildford, Surrey, England pp. 337-341 (1976).

MAGNETIC FIELD EFFECTS ON TENSILE BEHAVIOR OF ALLOYS 304 AND 310 AT 4 K*

R. P. Reed and J. M. Arvidson
Fracture and Deformation Division
J. W. Ekin and R. H. Schoon
Electromagnetic Technology Division
National Bureau of Standards
Boulder, Colorado

ABSTRACT

Our experiments were conducted to assess the effects of a steady magnetic field on the austenite stress-strain characteristics at 4 K. Wire specimens (0.64 mm dia.) of both a stable Fe-26Cr-20Ni (AISI 310) and metastable Fe-18Cr-9Ni (AISI 304) were measured. A 7-T magnetic field was produced by a split-pair NbTi superconducting magnet with radial access ports and the field was applied perpendicular to the tensile specimen axis. Tests were conducted at 4 K with the field off, with the field on, and with the field switched on and off after prescribed amounts of plastic deformation. The Young's modulus, tensile yield strength and tensile stress-strain curves were measured. The results are summarized here: (1) During magnetic field on/off experiments, no change in austenite flow strength of either alloy was observed from the application or absence of a 7-T field and (2) There was no detectable affect of a constant 7-T magnetic field on the yield strength and Young's modulus of either alloy. However, the specimen-to-specimen yield strength data scatter was large and the application of magnetic field would not necessarily produce changes of flow strength in excess of the data scatter. Discussion is also presented on magnetic field effects on discontinuous yielding and cold worked alloys.

*Work supported by Department of Energy, Office of Magnetic Fusion Energy.

INTRODUCTION

The application of magnetic fields has been demonstrated to enhance body-centered cubic (bcc) martensitic transformations in ferrous alloys. Korenko and Cohen[1] have recently reported research on an Fe-22.5Ni-4Mn alloy at 6-T fields demonstrating that the magnitude of the applied field significantly influences transformation kinetics; higher fields raise the temperature of possible transformation and increase the amount of transformation. There has been an abundance of USSR papers discussing the use of strong (up to 35 T) pulsed fields to enhance transformation in Fe-Ni, Fe-Ni-Cr and Fe-Mn steels (e.g., Voronchikin, Romashev, Fakidov).[2]

Bolshutkin, Desnenko, and Ilichev[3] have studied the plastic deformation of a series of Fe-18Cr, 8-25Ni alloys at 4 K exposed to steady-state and transient magnetic fields and found small changes of flow strength that have been attributed to magnetostriction and Joule heating effects. They found that the flow strength of Fe, 18Cr, 8-15Ni alloys decreased on application of a 3.4 T magnetic field. The amount of strength decrease was between 1.0 and 5.0 MPa, reaching about 0.6% of the flow strength. The flow strength decrease only became detectable after plastic strains of about 0.05 and increased rapidly with increasing strain to a limiting strain of about 0.10. However, Bolshutkin, et al.[3] found that in more stable alloys (Fe, 18Cr, 20-25Ni) the flow strength increased (instead of decreased) with application of 3.4-T field. In these steels, the increase of flow strength varied from 2.0 to 3.0 MPa, beginning at strains near 0.01 and saturating at strains near 0.02.

These experiments were conducted to begin assessment of the effects of magnetic fields on austenite flow characteristics at 4 K. Many experiments

have shown that strain-induced martensitic transformations in Fe-Cr-Ni stainless steels affect the low temperature flow strength. At low strains, transformation apparently enhances strain and/or reduces the rate of work hardening. However, at larger strains, b.c.c. martensitic transformation correlates excellently with increased work hardening.[4] Therefore, two questions need to be answered: (1) Do applied fields up to 7 T enhance strain-induced martensite transformation in Fe-18Cr-8Ni steels? and (2) Does an enhanced martensite transformation result in higher or lower flow strengths under an applied magnetic field?

MATERIALS

Two stainless steels, AISI 304 and AISI 310, were selected for this test series. One steel (AISI 304) is metastable with respect to austenite-to-martensite transformation and transforms during plastic deformation at temperatures below about 200 K; the other steel (AISI 310) is completely stable with respect to martensitic transformation. Both were purchased as 0.64-mm-diameter wire in cold-drawn condition. Annealing times of 7.5, 15, and 30 min at 1340 K (1950 °F) produced yield strength reductions from 400 to 305, 285, and 290 MPa, respectively, at room temperature for the AISI 310 alloy. Annealing of AISI 304 at 1340 K (1950 °F) for 30 min resulted in a yield strength reduction from 321 to 233 MPa at room temperature. Thereafter, all annealed wire specimens were produced by vacuum annealing at 1340 K (1950 °F) for 30 min.

EXPERIMENTAL PROCEDURE

The apparatus has been described previously by Ekin.[5] Tensile load and a perpendicular magnetic field were simultaneously applied to wire specimens at 4 K. The magnetic field was produced by a 7-T split-pair NbTi magnet with radial access ports, allowing perpendicular application of the field to

the specimen. A schematic of the apparatus is shown in Fig. 1. These specimens were tested in straight sections, each with a 27.5-cm-long gage length. The magnet produces a 7-T field perpendicular to a 6.3-cm length of the specimen at its center. On each side of this central section, the field strength decreased linearly over an 8 cm length to 0 T. Therefore, while only about ½ of the specimen is exposed to 7 T, the entire specimen is exposed to some magnetic field. Magnetic field accuracy was ± 1.0%, and homogeneity over the sample central section was of the order of ± 1.0%.

The specimens were gripped at either end by soft silver soldering into copper channels, one fixed and one attached to the load train through a self-aligning universal joint. Strain was measured by taking the vertical displacement of the pull rod, as indicated by an LVDT electronic displacement sensor, and dividing by the gage length. The stiffness of the load train, relative to the sample, yields an accuracy in these measurements of ± 0.04%. Load was applied by a 2-kN servohydraulic testing system and measured by a compatible load cell in series with the pull rod. Load was measured to within ± 0.2%.

The specimens were strained at a constant rate of 0.002 cm/cm/min using the testing system's interval function generator and a linear ramp wave form. All of the specimens were strained between 0.025 and 0.040 at 4 K. Some experiments were conducted by sequentially turning the magnetic field on and off during the test. In such tests, the specimen was unloaded, but kept at 4 K, prior to field change. A schematic of the stress-strain curve during these tests is shown in Fig. 2.

EXPERIMENTAL RESULTS

All experimental data for AISI 310 are tabulated in Table I, and the experimental data for AISI 304 are summarized in Table II. In these tables, ANN

refers to annealed, and CD refers to cold drawn (as received). To determine the percent (bcc, α') martensite in the specimens at room temperature following deformation, a bar-magnet with a torsion spring was used. This apparatus has been previously described and calibrated.[6] Martensite was detected in all AISI 304 specimens strained at 76 and 4 K, but not in the AISI 304 specimens strained at room temperature. No martensite was detected in AISI 310 specimens.

DISCUSSION

Magnetic-field on/off measurements

Experiments in switching the magnetic field while the 304 or 310 specimens were held at 4 K did not reveal any change of flow strength. That is, after application of field, there was no accompanying increase or decrease of flow strength at 4 K. This implies, of course, that any attendant increase of martensitic transformation in alloy 304 (not definitively detected) did not measurably affect flow strength.

Constant-field measurements

There was no detectable effect of a 7-T magnetic field on the yield strength at 4 K of either the 304 or 310 alloys. However, the data scatter is large and the application of the magnetic field would not necessarily produce changes of flow strength in excess of the scatter of yield strength values.

The magnetic field did not affect the initiation of discontinuous yielding in the cold-drawn 310 alloy. No discontinuous yielding was observed in the annealed 310 alloy to strains of 0.04. In contrast to the 310 alloy behavior, serrated yielding was observed at lower strains for annealed alloy 304, compared with a cold-drawn condition. Data from Table II on the influence of magnetic field on strain to initiate discontinuous yielding in alloy 304 are not definitive. In the cold-drawn condition, the application of field may

slightly reduce the strain necessary for discontinuous yielding to begin; in the annealed condition the trend is apparently reversed.

CONCLUSIONS

The experiments reported here have produced no evidence that the application of a transverse magnetic field of 7 T at 4 K affects the tensile stress-strain characteristics of AISI 310 and 304 alloy wire.

Other variables that need to be considered include the effects of (1) pulsing fields, (2) longitudinal fields, (3) higher fields, and (4) larger specimen strain.

REFERENCES

1. Korenko, M. K. and Cohen, M., "Martensitic Transformation in High Magnetic Fields," Proc. Conf. on Martensitic Transformations, ICOMAT 1979, 24-29 June 1979, Massachusetts Institute of Technology, Cambridge, Massachusetts, 388-393 (1981).

2. Voronchikin, L. D., Romashev, L. N., and Fakidov, I. G., "Influence of the Initial State of Austenitic Steel on the Martensitic Transformation in a Strong Magnetic Field." Fizika Metallov i Metallovedenie, 26, No. 5, 948-951 (1968).

3. Bolshutkin, D. N., Desnenko, V. A., and Ilichev, V. Ya., "Low Temperature Plastic Deformation of Fe-Cr-Ni Steels in Magnetic Fields to 2.71 x 10^6 Am^{-1}," Cryogenics, 19, 231-234 (1979).

4. Reed, R. P. and Tobler, R. L., "Deformation of Metastable Austenitic Steels at Low Temperatures," in Advances in Cryogenic Engineering-Materials, Vol. 28, Plenum Press, New York (1982).

5. Ekin, J. W., "Fatigue and Stress Effects in NbTi and Nb_3Sn Multifilamentary Superconductors," in Advances in Cryogenic Engineering-Materials, Vol. 24, Plenum Press, New York, 306-316 (1978).

6. Reed, R. P. and Guntner, C. J., "Stress-Induced Martensitic Transformations in 18Cr-8Ni Steel," Trans. AIME, 230, 1713-1720 (1964).

Table I

AISI 310 Stainless Steel Wire*

Specimen No.	Test Temperature, K	Magnetic Field, T	Specimen Condition	Young's Modulus, GPa	Proportional Limit, MPa	Yield Strength (0.2% Offset), MPa	Strain† at Onset of Discontinuous Yield
3	295	0	CD	186	86	400	--
4	"	0	‡	174	134	305	--
5	"	0	§	162	114	285	--
6	"	0	ANN	168	97	290	--
1	4.2	0	CD	206	345	1,120	1.26
2	"	0	CD	206	610	1,230	1.45
11	"	7	CD	202	386	1,200	1.21
7	"	0	ANN	174	252	1,030	--
8	"	7	ANN	171	252	1,110	--
9	"	7	ANN	186	478	1,000	--
10	"	7	ANN	187	478	1,000	--
12	"	7	ANN	180	455	1,070	--

* 0.64-mm diameter.

‡ Annealed at 1339 K (1950 °F) for 7.5 min.

§ Annealed at 1339 K (1950 °F) for 15 min.

† Total strain (elastic/plastic).

Table II

AISI 304 Stainless Steel Wire*

Specimen No.	Test Temperature, K	Magnetic Field, T	Specimen Condition†	Young's Modulus,‡ GPa	Proportional Limit, MPa	Yield Strength (0.2% Offset), MPa	Strain§ at Onset of Discontinuous Yield
5	295	0	CD	196	104	321	--
9	"	1	ANN	208	91	233	--
8	76	0	ANN	194	86	387	--
6	4.2	0	CD	206	138	448	1.60
7	"	7	CD	213	138	460	1.56
12	"	7	CD	192	124	470	1.10
11	"	0	ANN	217	124	623	0.39
1	"	0	ANN	212	145	575	0.55
2	"	0	ANN	212	145	538	0.63
3	"	7	ANN	209	107	480	0.86
4	"	7	ANN	217	121	529	0.90
10	"	7	ANN	214	169	614	0.53
14	"	0/7/0...#	ANN	230	148	523	0.71
13	"	7/0/7...	ANN	229	169	483	0.81

* 0.64-mm diameter.

† ANN: annealed at 1339 K (1950 °F) for 30 min; CD: Cold Drawn (in as-received condition).

‡ All values of Young's modulus were taken at 0.5 - 1.0% strain by unloading and loading.

Initially the test commenced with field off - at approximately every 0.5% elongation the field condition was alternated between on and off.

LIST OF FIGURES

LIST OF TABLES

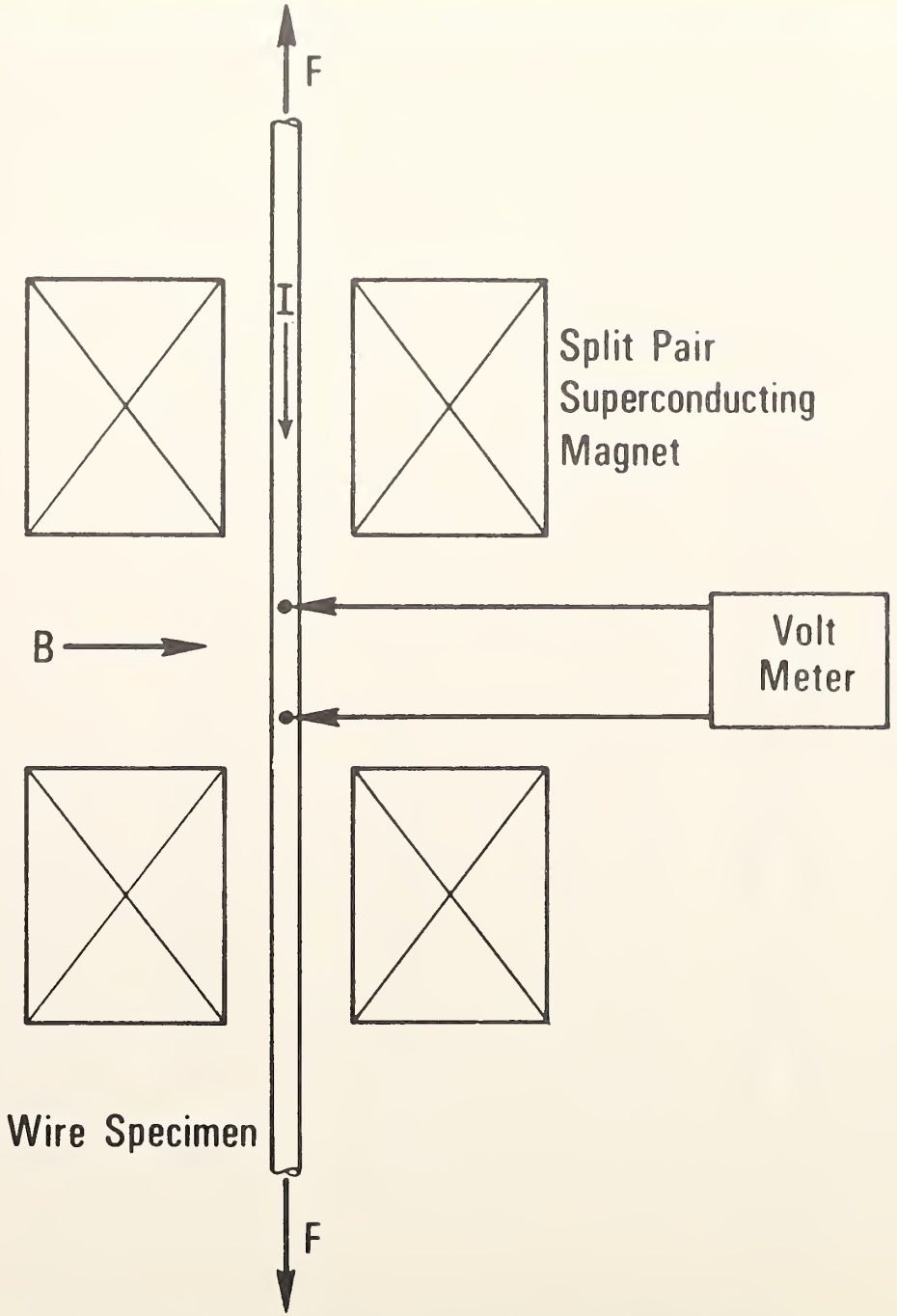

Figure 1. Schematic of apparatus to apply tensile force and magnetic field to wire specimens.

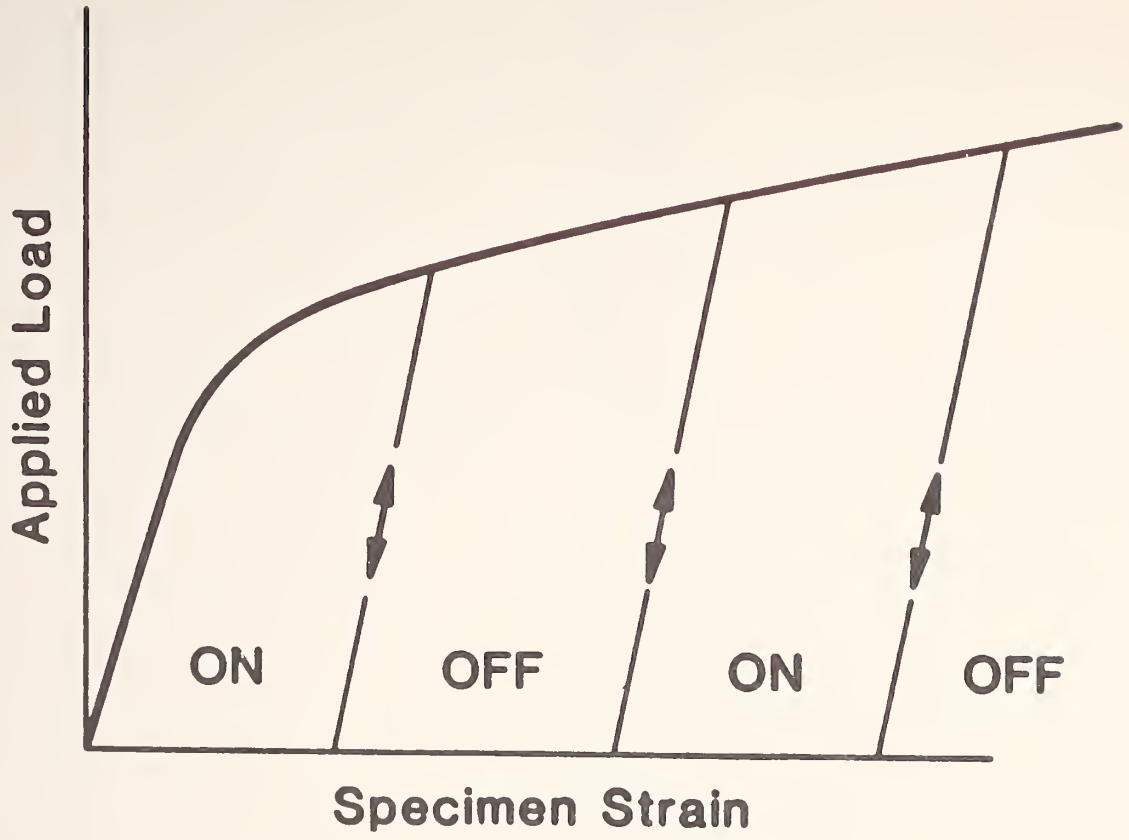

Figure 2. Schematic of applied tensile load versus specimen strain with magnetic field applied "on", then "off".

MARTENSITIC TRANSFORMATIONS IN TYPE 304 AUSTENITIC STAINLESS STEELS

F.J. Lamelas, D. C. Larbalestier and H. W. King*
Materials Science Center
University of Wisconsin-Madison
(*Department of Engineering Physics, Dalhousie University)

The following is a progress report for the period June 1980 to December 1981 on contract #NB80RAC0031. Further characterisation of these alloys is in progress and some of the conclusions presented here are to be regarded as tentative.

Introduction

The problem of martensitic transformations in the common austenitic stainless steels is well-known and frequently met[1,2]. Surprisingly, many features of the transformation remain unclear. Some of these features are the question of the mode of transformation: a) whether austenite (γ) breaks down directly to α' martensite or through the intermediate martensite (ε), b) whether ε is a true phase with the hcp structure or whether it is faulted γ , and c) whether and how the morphology of the martensites varies when produced spontaneously on exposure to low temperatures or under the simultaneous action of plastic flow and low temperatures.

The significance of these structural questions has acquired a more practical aspect with recent investigations of the low temperature mechanical properties of the austenitic steels such as 304 and 304N. Dalder[3] for example, finds that the 4K yield strengths of the 304N steels are about 20ksi less than expected. Reed[1] has noted that there is an anomalous decrease in yield strength with decreasing temperature in some unstable steels. This behavior appears to result from slip induced transformations to martensite (both ε and α'.) The reductions in yield strength are practically significant in that current designs of fusion reactor systems could usefully use extra yield strength without running into fracture toughness limitations.

The principal scope of the present work was to develop an equation for the temperature M_s at which martensite first forms on cooling in the absence of externally applied stress. An equation, due originally to Eichelman and Hull[4], does already exist. Rearranged into degree Kelvin and weight percent form with an added Mo factor, it is(2):

$$M_s(K) = 1578 - 61.1\,[Ni] - 41.7\,[Cr] - 33.3[Mn]$$

$$- 27.8[Si] - 1667\,[C+N] - 36.1[Mo]$$

This equation was originally developed for lower alloy steels than the AISI 300 steels and extensive studies by two of the present authors have shown that

the equation is only an approximate guide to the behavior of the 300 steels at cryogenic temperatures[2,5,6].

The present report is an interim progress report on the characterisation of some thirty specially melted steels in and around the 304 stainless steel specification.

Experimental Procedures

1) Alloy Preparation

Alloys were prepared by the addition of pure chromium, iron, and nickel to a base alloy of type 304 stainless steel. A base alloy was used in order to provide the special steels with a typical range of tramp elements in addition to the basic Fe-Cr-Ni elements, e.g. Mn, Si, Mo, Cu, C, N. (See ternary diagram, Fig. 1) The alloys were arc-melted in an argon atmosphere, homogenized for 24 hours at 1050 C, rolled and/or swaged to approximately 80% area reduction, and then annealed for 1/2 hour at 1050 C. All heat treatments were done in quartz tubes with sufficient argon to balance atmospheric pressure at 1050 C. Samples were protected with a wrapping of Nb foil to prevent interactions between the quartz and the samples during the heat treatment. Multiple samples were cut from each heat for further examination.

The stated chemical compositions in this report are those calculated from a special analysis of the base alloy (see Table 1) and a knowledge of the added weights of pure Fe, Cr or Ni. In no case was the weight change on melting >1%. Sample chemical analyses will be performed at the conclusion of the programme. It is interesting to note that the C content of our alloys makes them barely out of the low C grade but that the N content is about twice as large.

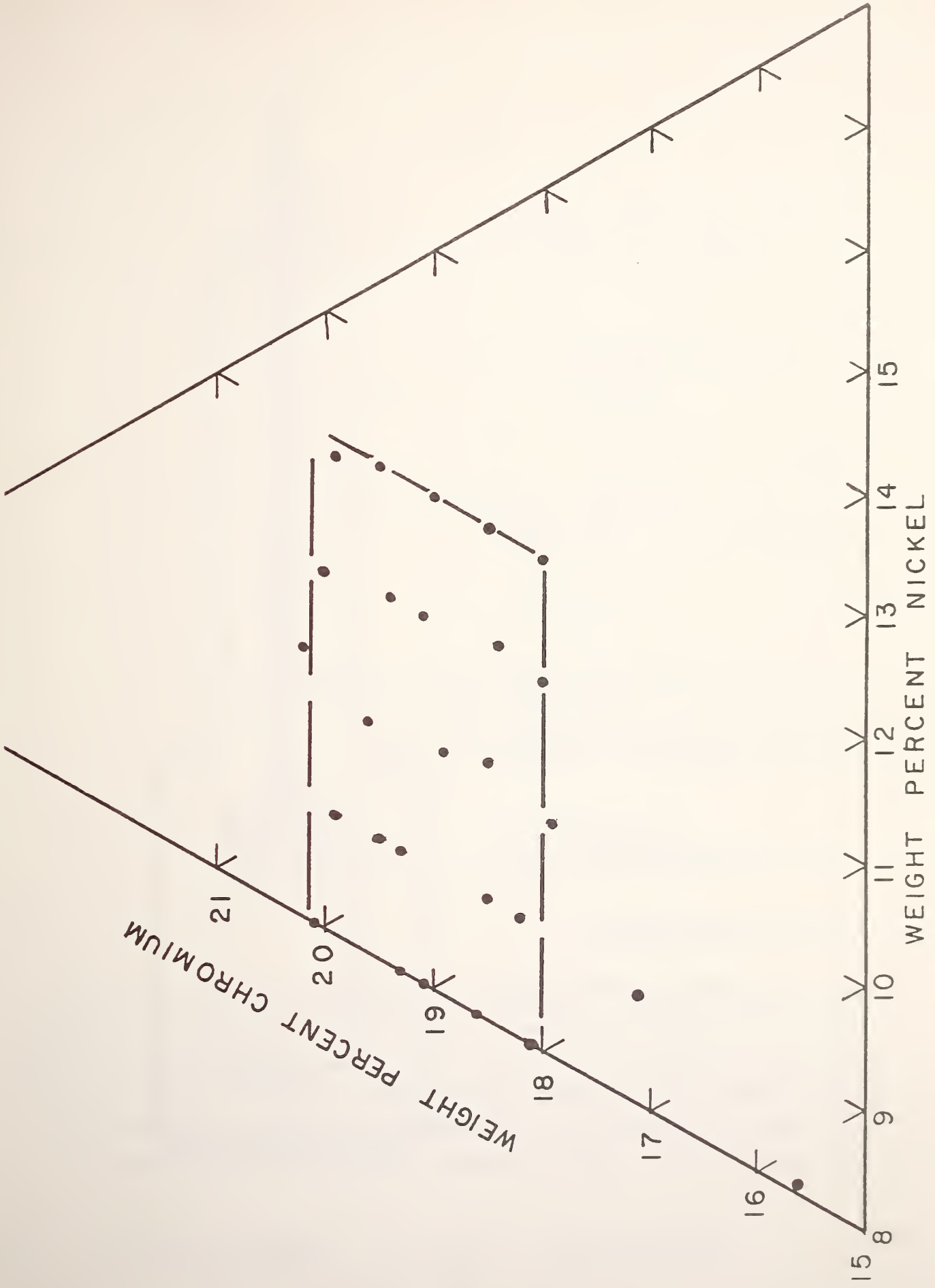

FIGURE 1. Alloys under investigation.

Table 1

Elements	Wt.%
N	0.079
C	0.034
S	0.006
P	0.031
Ni	9.78
Cr	18.76
Mn	1.71
Si	0.52
Mo	0.47
Cu	0.29
Sn	0.017
Co	0.21

Composition of stainless steel base alloy as analysed by National Spectrographic Laboratories

2. Resistivity Measurements

a) Continuous Measurements

Continuous measurements of resistance vs. temperature were made by means of a 4 terminal resistance rig mounted on the base of an Oxford Instrument Company continuous flow cryostat. (See Fig. 2 and 3). Resistance was measured with a Keithley Model 503 milliohmmeter with the analog voltage output fed into the Y-axis input of an XY recorder. Temperature measurement was obtained with a CLTS (cryogenic linear temperature sensor) mounted next to the sample. A

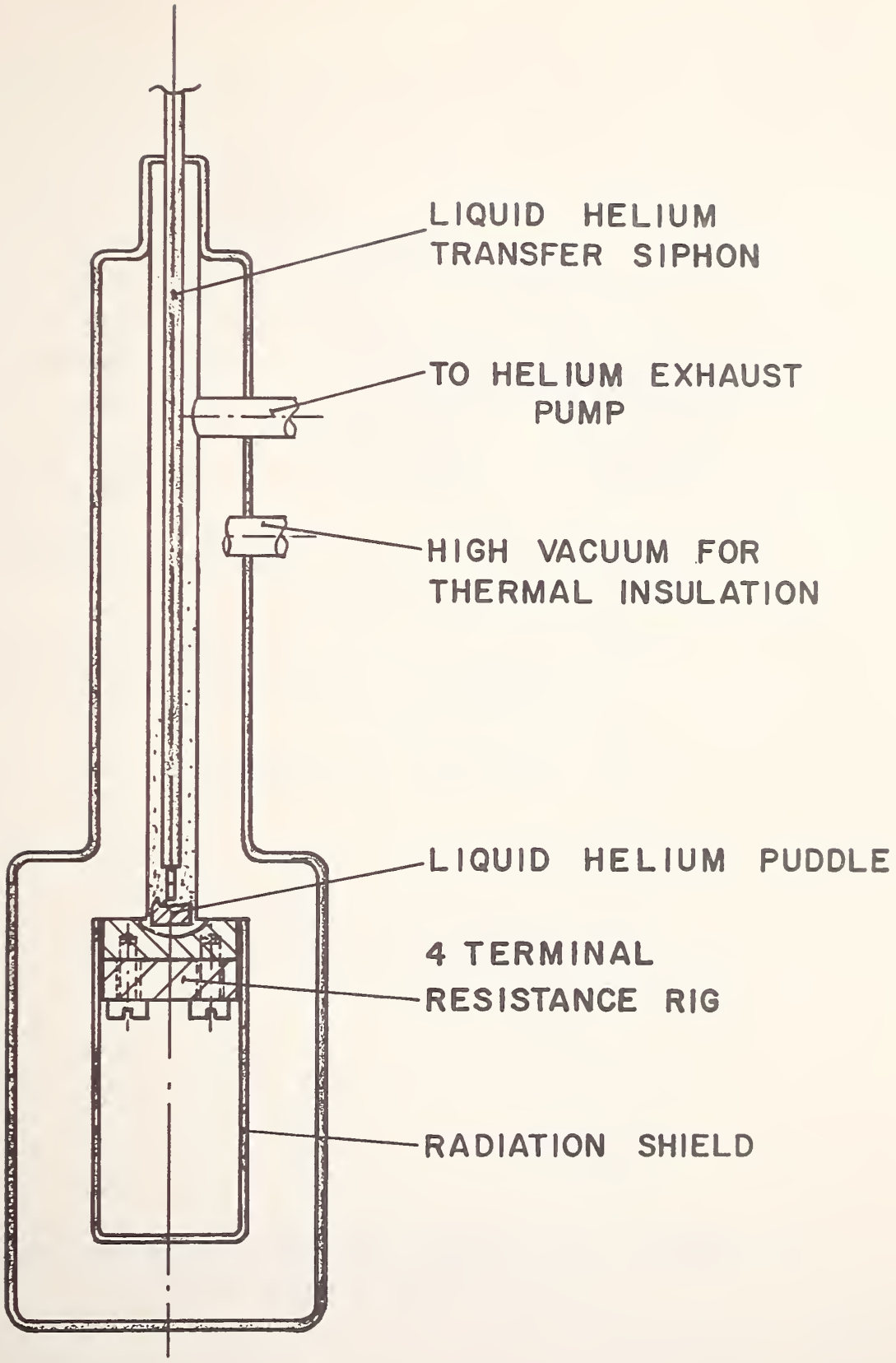

CONTINUOUS FLOW CRYOSTAT

FIGURE 2

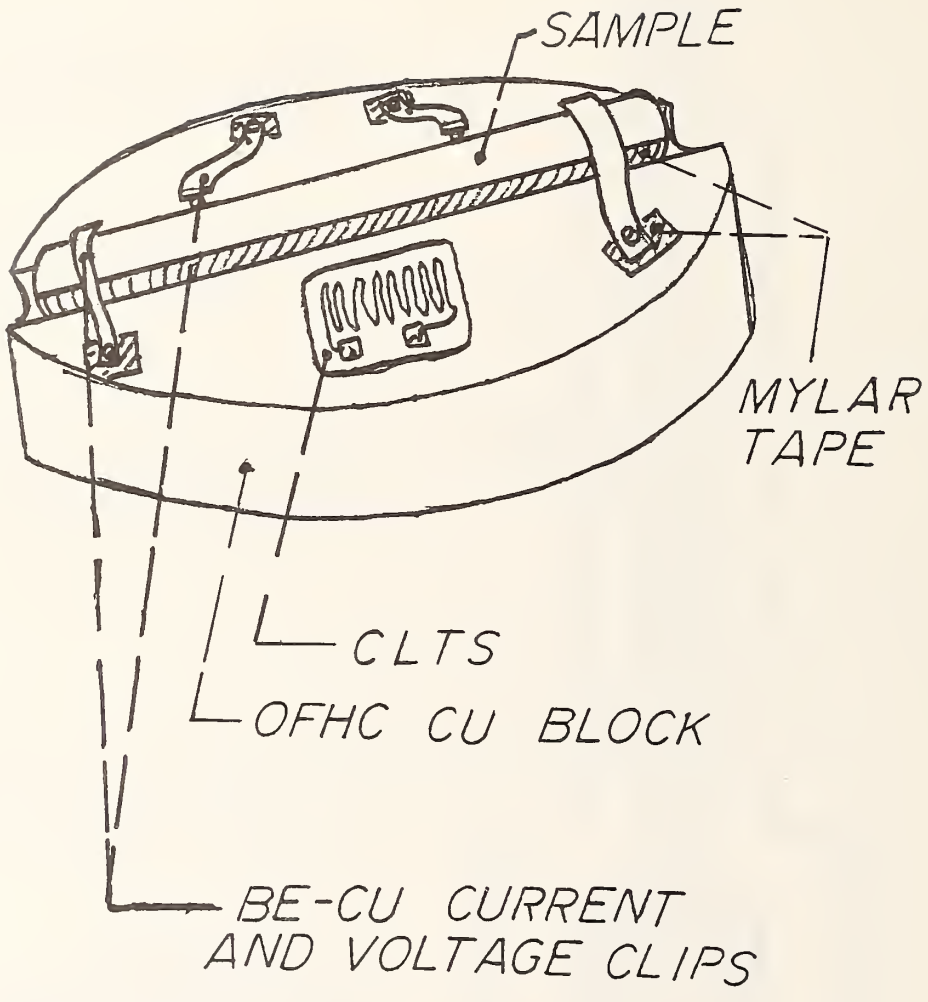

FIGURE 3. Four terminal resistance rig mounted on OFHC block for thermal stability.

constant current of 10 μA was passed through the CLTS, and the voltage across it (linearly proportional to temperature) was measured with a DVM whose analog output was fed into the X axis of the XY recorder. The samples were cooled at about 5K per minute to less than 10K. Faster rates tended to produce a temperature differential between sample and thermometer. The permissible cooling and heating rates were established by experiments with a fully stable steel for which the cooling and heating curves coincided. Transformation to martensite produced an irreversible increase in resistivity (see figures 8, 9 and 10.) Below about 40K all samples show a reversible increase in resistivity and this is believed to be due to the anti-ferromagnetic ordering occuring at these temperatures.

b) Fixed Temperature Measurements

Samples were also quenched to various temperatures between 273K and 4K using a variety of fixed temperature baths (Table 2).

TABLE 2

T(Kelvin)	BATH
273	H_2O at ice point
227	Chlorobenzene m.p.
196	Dry ice & methanol
156	Ethanol m.p.
113	Isopentane m.p.
77	Liquid N
4	Liquid He

Resistivity measurements were made with a standard 4 terminal apparatus.

3. Magnetisation Measurements

M vs. H curves were obtained with a DC integration magnetometer. The magnetisation rig consists of two sensing coils, each of approximately 20,000 turns, connected in a series opposed configuration. One coil is intentionally wound with more turns than the other so that its output can be potted down to balance the coil set when the empty coil pair output is integrated during a field sweep. Most measurements were performed in a liquid nitrogen cooled 0.5 Tesla copper solenoid fitted with a R.T. bore. Measurements were also made at 4K in fields up to 19 Tesla in order to assess the stability of some of the less stable steels in high magnetic fields.

The potentiometric balancing technique described above produces a baseline which is essentially zero in comparison to a sizeable magnetisation, e.g. that produced by a sample that has undergone substantial martensitic transformation. However this baseline is not negligible in comparison to the magnetisation of the paramagnetic γ phase or in fact samples consisting of γ and a very small (<.1%) amount of α' martensite. In order to measure paramagnetic susceptibilities of the order of 10^{-4} we used a ballistic measurement technique: the sample was repeatedly withdrawn and inserted into the sensing coil as the field was ramped. The difference in integrator output voltage with the sample in and out of the coil is proportional to the sample magnetisation (Fig. 6).

The volume % of transformation to α' martensite was calculated by measuring the saturation magnetisation of the sample and expressing this magnetisation as a percentage of the calculated saturation magnetisation of a totally transformed alloy of the same composition. The saturation magnetisation of the fully transformed alloy was calculated using a common band model[7].

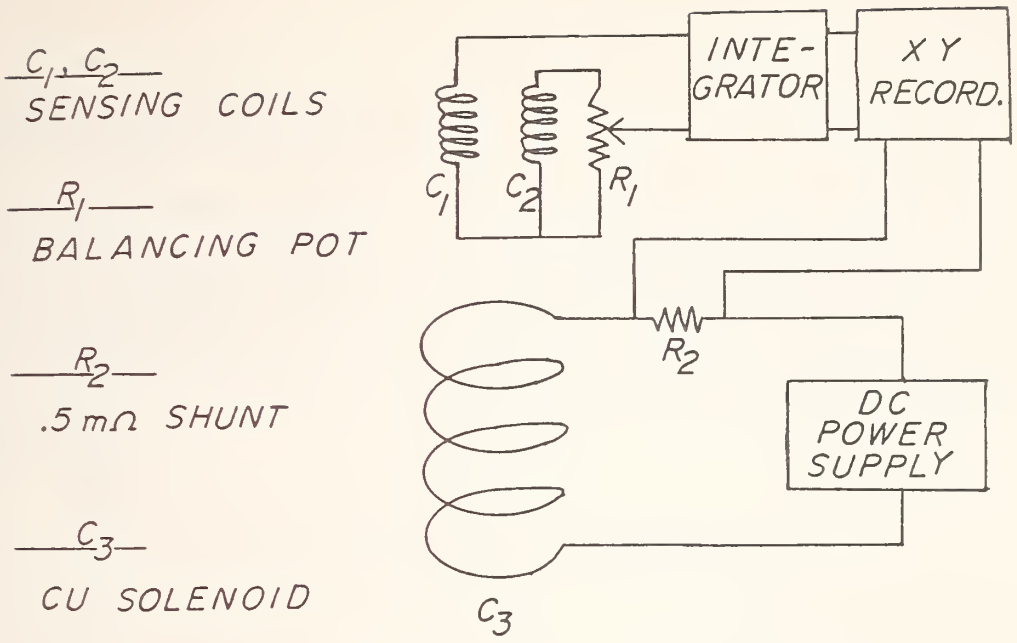

MAGNETOMETER CIRCUIT

FIGURE 4

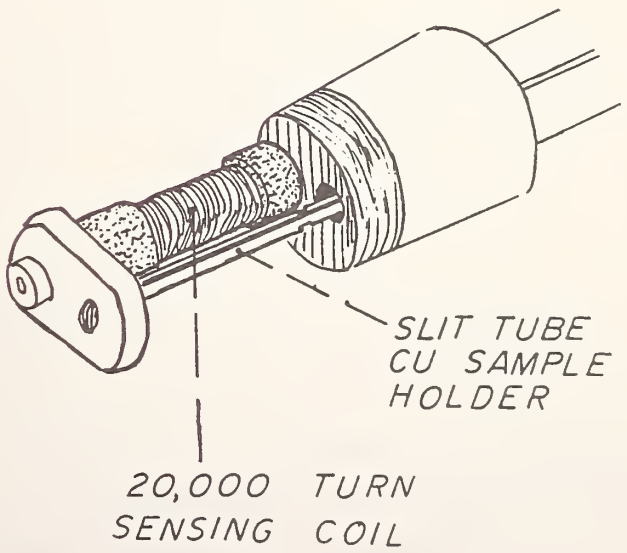

DC MAGNETOMETER

WITH ONE COIL REMOVED
TO SHOW SAMPLE HOLDER

FIGURE 5

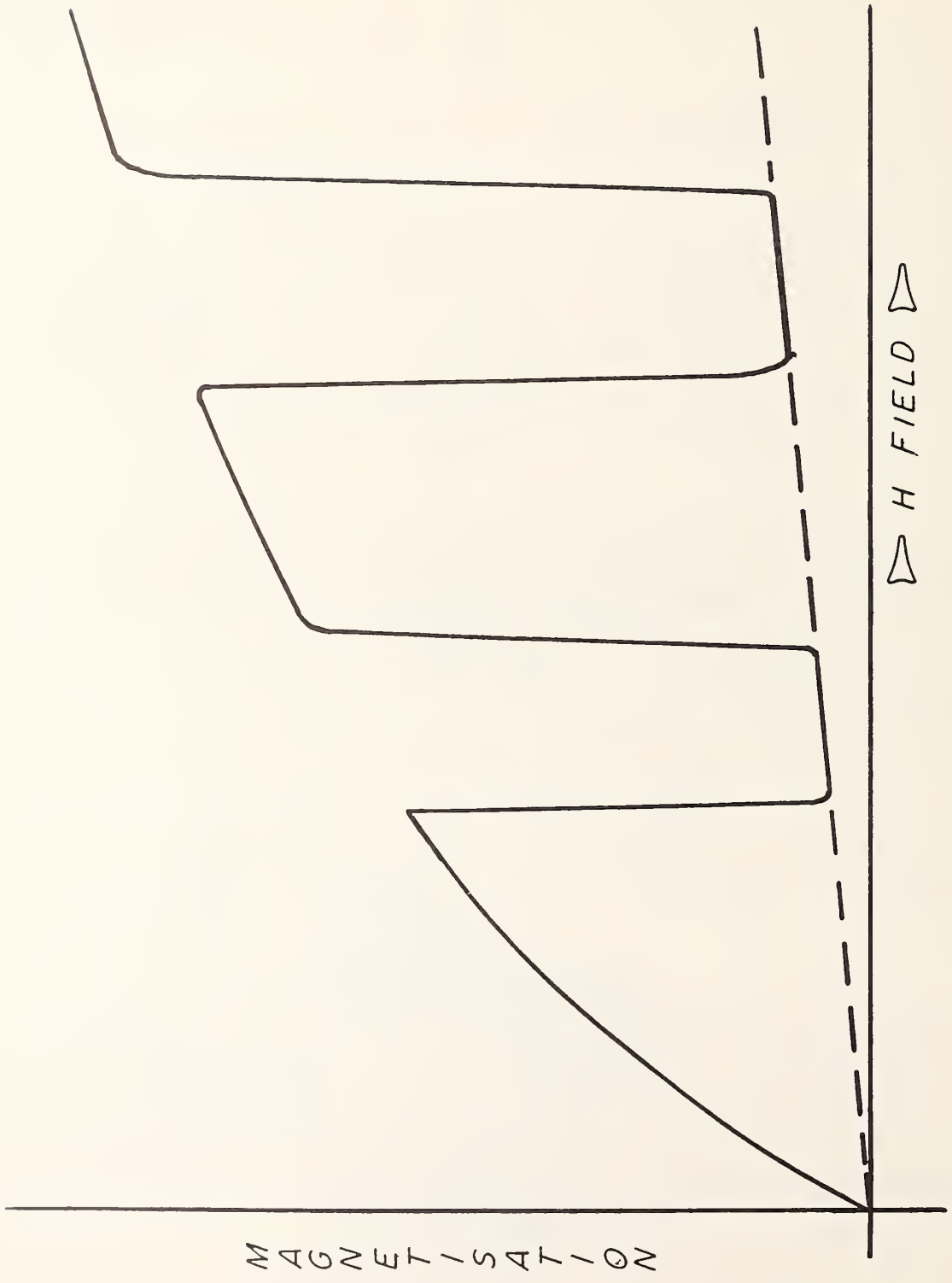

FIGURE 6. Typical M vs. H curve with non-zero baseline indicated by ballistic technique.

4. Metallography and Light Microscopy

Samples were prepared for observation using standard metallographic techniques: grinding with successive grades of silicon carbide, polishing with diamond paste, and finally electropolishing with an acetic acid-chromium trioxide solution. Grain boundary etching was performed by electroetching in oxalic acid solution and a glycerol /HCl/HNO_3 solution was used to reveal the α' martensite.

Results

The raw data available for the interpretation of the low temperature behaviour of these steels generally consists of:

1. A resistance-temperature trace from RT to about 10K

2. The magnetisation of the sample used in 1. both before and after cooling
3. The resistivity, magnetisation and light metallographic observation of one face of the sample used in quenching experiments.

An overview of the data is shown in Table 3 and examples of the 3 types of R/T curve observed are shown in figures 8, 9 and 10. Stable steels of high alloy content showed no transition to ε or α', having an R/T curve with no hysteresis, as shown in figure 8. The low temperature cusp seen in this and all traces is believed to be due to antiferromagnetic ordering. This type of behaviour has been designated type 1 or stable behavior.

Figure 9 portrays a gradual transition, the increase in resistance being rather progressive and occurring over a range of temperature, sometimes 20 to 50 K. This is named a type 2 or weak transition and is obtained for many steels of intermediate alloy content.

Figure 10 shows a sharp form of transition in which there is a marked irreversible increase in resistance which occurs over a rather narrow temperature range (< 5K). This is called a type 3 or strong transition. This is found for low alloy steels.

The behaviour of the steels is further summarised in figure 7. Although not all steels have yet been examined it appears that there is a gradual change in behaviour from the higher alloy steels which are quite stable, through those exhibiting a weak transition, to those having a strong instability. The dividing line between the stable and unstable steels appears to be drawn from about 20Cr/8Ni to 18Cr/11Ni, while only the leanest 18Cr/8Ni steel shows a strong transition.

An examination of Table 3 reveals a number of interesting features:

(i) The calculated M_s (M_s*) is always lower than the experimental M_s. Four of the seven unstable steels have values of $M_s - M_s$* between 110 and 135K, the three other values falling significantly outside this range. Additional samples remain to be tested, and individual sample analyses must be performed before this observation should be regarded as confirmed.

(ii) Fiedler, Averbach and Cohen[8] reported that 1% of α' martensite produced a resistivity increase of about 0.5%. Our measurements indicate some variation about this figure and clearly show the magnetic measurements as more sensitive. The quenching experiments (in which resistance and magnetisation were measured and one end face of the sample observed) are in all cases in accord with the continuous cooling R/T traces, although in the case of the 19.1 Cr/8Ni alloy no transition was observable in the R/T trace while a transformation to 1-2% α' could be detected magnetically.

(iii) The morphology of the martensite was always that of α' laths within sheets of stacking faults or ε. Since X-ray measurements have so far been inconclusive it is not certain whether the sheets are truly ε or faulted γ. In at least 3 alloys (15.6 Cr/8.1Ni, 17.1Cr/8.9Ni and 18.5Cr/8Ni) the sheets were visible before the α' could be detected, while for other alloys (18.1Cr/8Ni, 18.5Cr/9Ni) both sheets and α' appeared between the same pair of quench temperatures and it could not be determined whether M_s (ε) was indeed greater than M_s (α')

(iv) A suprising result is the highly non-linear response of alloys to cooling. All the steels which transformed had M_s values which were determined to be > 170K. Marginally higher alloy steels with M_s* values of 25 to 50K lower in fact showed no transformation to α', even though experimental values in the 100 to 170K range would have been expected. This behaviour is consistent, however, with the result that martensite is formed less easily in steels plastically deformed at 4K than 77K[2].

Summary

A series of some 30 steels in the 304 range have been made and characterisation of their spontaneous martensite breakdown on cooling is in progress. The most important interim results appear to be

(i) Experimental M_s values in unstable steels are consistently higher, by about 120K, than the values predicted from the Eichelman and Hull equation.

(ii) The behaviour of the 304 steels is highly non-linear, there being a marked change in the extent of the transformation as the alloy content increases. M_s values of <170K have not been found, although they are predicted by the Eichelman and Hull equation.

(iii) The mode of transformation in these steels is always consistent with previous workers who observed α' as laths occurring in sheets of ε or faulted γ .

Acknowledgements

We are grateful to undergraduate senior project students Sarah Helfrich and John Krebsbach for help and Dr. R. P. Reed for helpful discussions on a number of points.

References

1. R. P. Reed, Martensitic Phase Transformations, National Bureau of Standards, to be published.

2. D. C. Larbalestier and H. W. King, Cryogenics, 13, 160, (1973).

3. E.N.C. Dalder, Lawrence Livermore Laboratory, Paper at 1981 Vail Meeting on Low Temperature Constructional Materials.

4. G. H. Eichelman and F. C. Hull, TASM, 45, 77-104, (1953).

5. D. C. Larbalestier and H. W. King, Proc Int Cryogenic Eng Conf ICEC-4, IPC Science and Technology Press (1975) 338.

6. H. W. King and D. C. Larbalestier, Cryogenics 21, 521, (1981).

7. C. J. Curtis and F.C. Sherwin, Brit. J.A.P., 12, 344, (1961).

8. H. C. Fiedler, B.L. Averbach, and M. Cohen, TASM, 47, 267 (1955).

TABLE 3

Composition (Cr/Ni)*	Resisitivity Transition M_s (K)	Resisitivity Transition type of behavior	M_s (α') determined by magnetic measurements on quenched samples	% α' after a 4.2K quench	M_s (K) predicted by Eichelman & Hull Equation	Alloy Type	Observations of ε or faulted γ Formation
15.6/8.1	262	strong	196-273	32	197	3	-
15.6/8.1	-	-	196-227	6	197	2	ε visible at 273K
15.6/8.1	-	-	196-273	39	197	3	-
17.1/8.9	-	-	196-273	12	72	2/3	-
17.1/8.9	192	strong	-	13	72	2/3	-
17.1/8.9	-	-	196-227	12	72	2/3	ε visible at 273
18.1/8	224	strong	-	>22	105	3	-
18.1/8	-	-	196-227	18	105	3	a lot of ε at 226
18.2/9	262	weak	-	8	16	2	-
18/11	None	stable	-	0	-111	1	-
18/12	None	stable	-	0	-173	1	-
18.6/8	190,215	both weak	196-273	15	88	2	-
18.6/8	-	-	196-227	11	88	2	ε at 226
18.6/8	198	weak/strong	-	-	88	2	-
18.5/9	170	weak	196-273	4	-1	2	none apparent at 226
18.5/9	-	-	196-227	5	-1	2	both ε + α at 196
18.4/11.1	-	-	<4	0	-139	1	-

Composition (Cr/Ni)*	Resisitivity Transition M_s (K)	Resisitivity Transition type of behavior	M_s (α') determined by magnetic measurements on quenched samples	% α' after a 4.2K quench	M_s (K) predicted by Eichelman & Hull Equation	Alloy Type	Observations of ε or faulted γ Formation
18.5/12	-	-	<4	0	-200	1	
19.1/8	None	stable	-	1	62	2	
19.1/8	None	stable	196-227	2	62	2	ε at 196
19.1/11	-	-	<4	0	-161	1	
19/12	-	-	<4	0	-217	1	
19.3/8	188	weak	-	4	55	2	
19.3/8	-	-	157-196	4	55	2	ε visible at 196
19.6/9.9	-	-	<4	0	-116	1	
19.4/11	-	-	<4	0	-177	1	
19.5/12	-	-	<4	0	-236	1	
20.1/8	None	stable	-	7**	25	1	
20.1/8	-	-	196-273	5**	25	1/2	
20/10.2	-	-	<4	0	-156	1	
20/10.9	-	-	<4	0	-190	1	
19/9/11/9	-	-	<4	0	-244	1	

* These are nominal compositions - full analysis will be reported later.

** These measurements are thought to be due to δFerrite because

i) these alloys lie very close to the 1000°C δ phase field.

ii) there was no change in M after quenching to 4.2 K from the as-annealed condition.

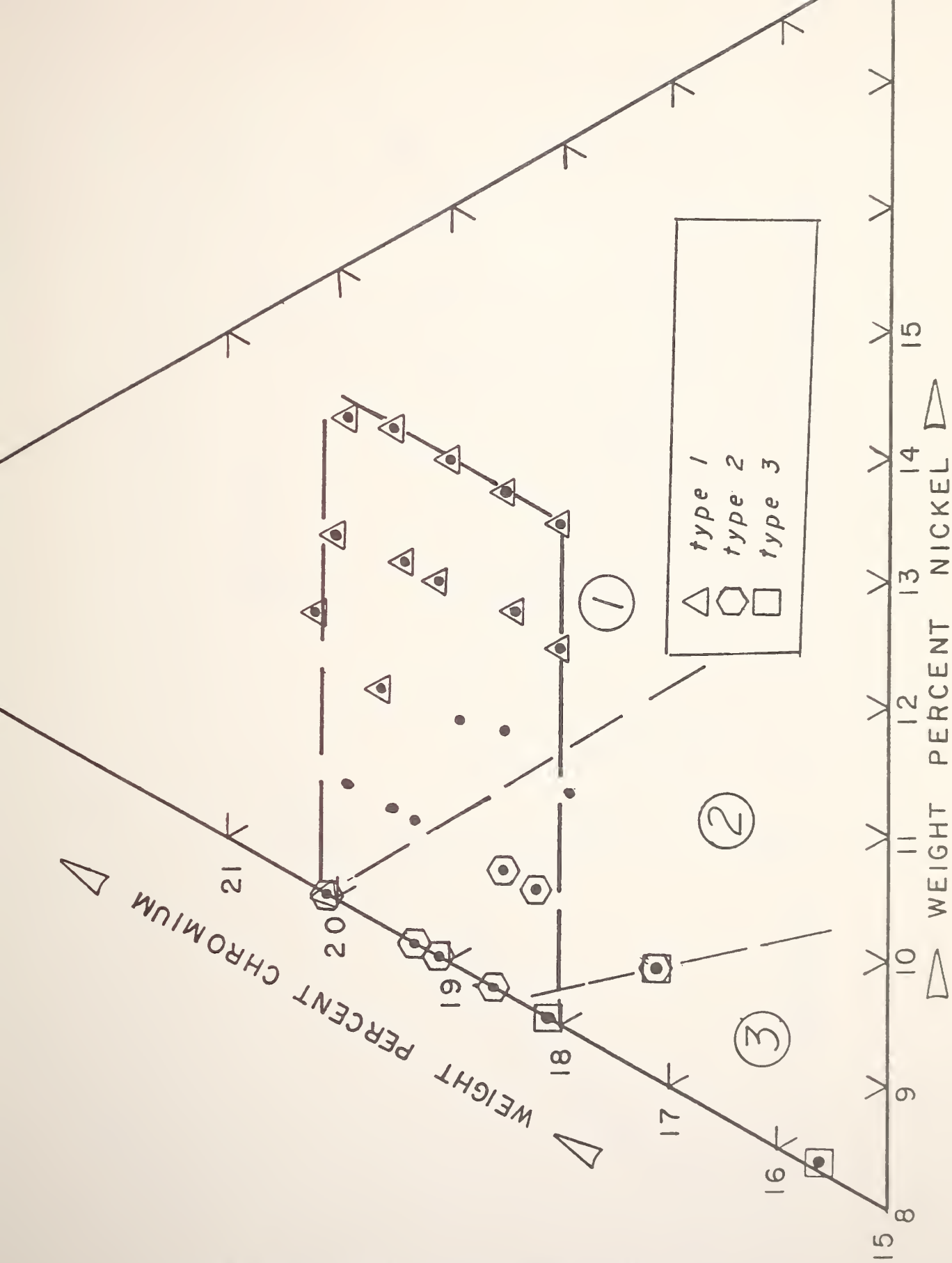

FIGURE 7. Alloy classification based on resistive and magnetic measurements.

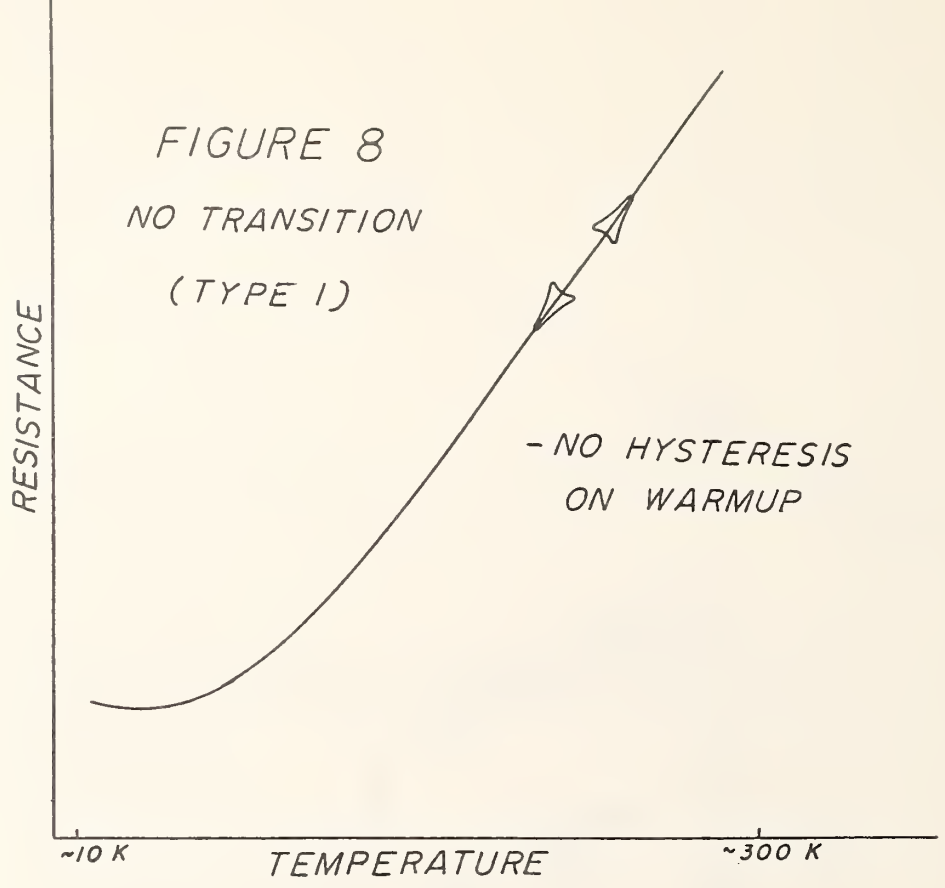
FIGURE 8
NO TRANSITION
(TYPE 1)
- NO HYSTERESIS
ON WARMUP
RESISTANCE
~10 K
TEMPERATURE
~300 K

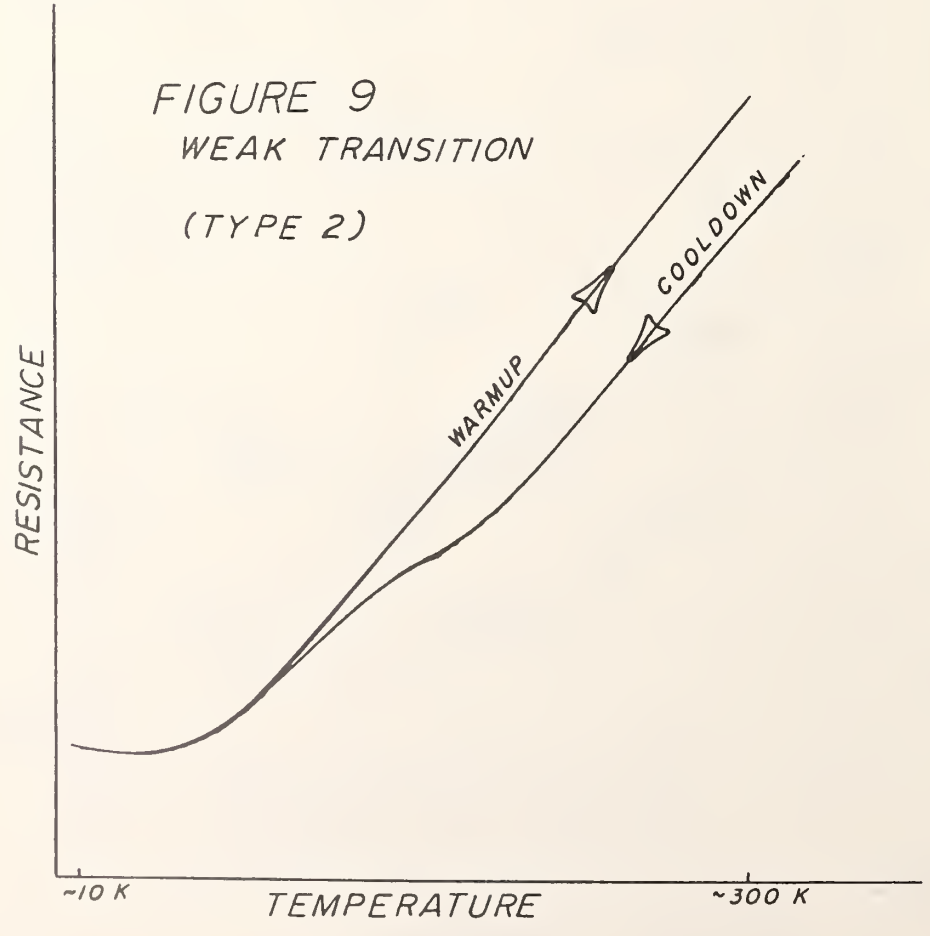
FIGURE 9
WEAK TRANSITION
(TYPE 2)
WARMUP
COOLDOWN
RESISTANCE
~10 K
TEMPERATURE
~300 K

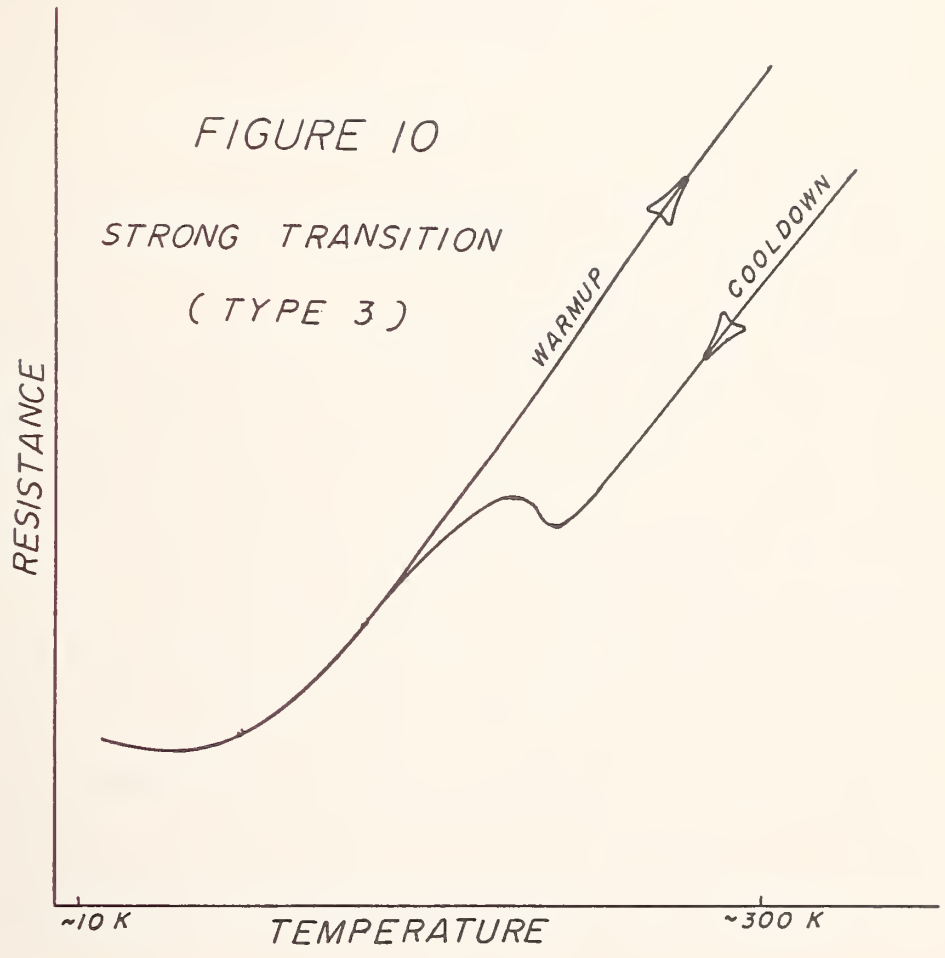
FIGURE 10
STRONG TRANSITION
(TYPE 3)
WARMUP
COOLDOWN
RESISTANCE
~10 K
TEMPERATURE
~300 K

FRACTURE TOUGHNESS OF CF8 STAINLESS STEEL CASTINGS IN LIQUID HELIUM*

E. L. Brown, T. A. Whipple, and R. L. Tobler
Fracture and Deformation Division
National Bureau of Standards
Boulder, Colorado 80303

ABSTRACT

Fracture toughness measurements for CF8 stainless steel castings in liquid helium at 4 K are reported. Single-phase (austenite) and duplex (austenite + δ-ferrite) castings were tested. On the basis of estimates from J-integral data, the plane-strain fracture toughness (K_{Ic}) of castings containing 3.2 to 14.5% δ-ferrite ranged from 84 to 179 MPa·$m^{1/2}$ at 4 K. In contrast, a fully austenitic casting (0% δ-ferrite) exhibited a K_{Ic} value of 331 MPa·$m^{1/2}$, which is nearly equivalent to the toughness of a wrought AISI 304 stainless steel of a similar strength. Optical and scanning electron microscopy studies indicate that the inferior toughness of castings containing δ-ferrite may be chiefly attributed to the brittleness of this body-centered-cubic phase at cryogenic temperatures and its distribution in the microstructure.

Key Words: Cast stainless steel; cryogenic properties of materials; fracture toughness; J-integral tests; low-temperature properties; stainless steels

*Work supported by Brookhaven National Laboratory and the Department of Energy, Office of Magnetic Fusion Energy.

INTRODUCTION

Cast stainless steels are being considered for structural applications in high-energy superconducting devices operating at 4 K [1]. Castings offer economic advantages over wrought products where large, complex shapes are required. Owing to microstructure, however, the mechanical properties of castings are often inferior compared with those of wrought products. There are few published studies of the mechanical properties of cast stainless steels at cryogenic temperatures. In particular, there are no fracture toughness data for stainless steel castings at 4 K. Since fracture toughness is a critical design parameter for any large cryogenic structure, a brief study was conducted to provide such data for CF8 castings.

CF8 stainless steel is the cast counterpart of wrought AISI 304. The base composition for both AISI 304 and CF8 is: Fe, 18 to 20% Cr, and 8 to 12% Ni. But AISI 304 is virtually 100% austenite (γ) at room temperature, whereas CF8 typically contains a body-centered-cubic second phase, delta (δ)-ferrite, within an austenitic matrix. The amount of δ-ferrite is controlled by manufacturing variables; from zero to 40% δ-ferrite may be present in CF8, although typically there is not more than 20% [1]. Delta-ferrite in the austenite matrix generally increases the strength and lowers the fracture toughness of welds and castings [2], especially at cryogenic temperatures [3]. At room temperature the δ-ferrite is considered advantageous, serving as a strengthener and grain refiner while improving weldability. At cryogenic temperatures the δ-ferrite is relatively hard and brittle, and, as demonstrated quantitatively

in this paper, even small amounts of δ-ferrite (3.2 to 14.5%) can have a detrimental effect on fracture toughness. The present work is a continuation of mechanical property sutdies initiated at Brookhaven National Laboratory, and Brookhaven provided the fracture specimens from the steels previously tested [1].

MATERIALS

Samples from six CF8 stainless steel tubes, centrifugally cast by three separate manufacturers, were tested. One casting had a single-phase, fully-austenitic structure (0% δ-ferrite), whereas all others had a duplex (austenite plus δ-ferrite) structure. The tubes had a 0.495-m outside diameter and a 19-mm wall thickness. After casting, five of the tubes were solution-treated at 1040°C for 2 h. However, one heat containing 12% δ-ferrite was not solution treated, but was tested in the as-cast condition. The heat designations, chemical compositions, and volume percentage δ-ferrite of the castings are listed in Table 1.

PROCEDURES

Specimens and Apparatus: Tensile tests at 4 K were performed using smooth bar tensile specimens [1]. Fracture toughness tests were conducted at NBS using compact specimens. The compact specimens were 12.7-mm thick (B) and 50.8-mm wide (W), having planar dimensions that were previously diagrammed [4]. For all tests in this study, the notches were machined parallel to the tube axes in a CL orientation [5], which is shown in Figure 1. The notch was modified to enable clip-gage placement at the loadline, and the starting notch-to-width ratio was 0.3. Tests at 4 K were achieved by immersion in liquid helium, using the cryogenic test facility previously described [6].

Precracking: Using a sinusoidal load cycle, a frequency of 25 Hz, a maximum load of 12 kN, and a minimum-to-maximum load ratio of 0.1, the compact specimens were precracked at 76 K to a crack-length-to-width ratio (a/W) of 0.5. Final precracking was then performed at 4 K, extending the a/W ratio to 0.57. The final maximum fatigue stress intensity factor was 51 $MPa \cdot m^{1/2}$, and the maximum fatigue load was between 40 and 55% of the observed maximum loads in subsequent J tests.

J-integral testing: Although δ-ferrite undergoes a ductile-to-brittle transition as temperature is lowered to 4 K, the 12.7-mm-thick CF8 castings at 4 K retain sufficient levels of plasticity to invalidate direct measurements of K_{Ic} (the plane-strain fracture toughness) via the linear-elastic ANSI/ASTM Method E-399-78a [5]. Therefore, single-specimen J-integral tests were used to measure J_{Ic}, which is a material parameter for nonlinear elastic fracture conditions enabling quantitative toughness comparisons of ductile materials to be made [7].

The computer-aided unloading-compliance technique [4] was used. The precracked specimens were incrementally loaded in displacement control, and periodic unloadings were performed during the course of the test. The load reduction during unloading was typically ten percent of the maximum load. Using a crack-length-vs.-compliance correlation, the crack extension increment (Δa) at each unloading was inferred. The J value at each unloading point was calculated from the expression: $J = \frac{\lambda A}{Bb}$, where λ is the Merkle-Corten factor, A is the area under the load-vs.-deflection curve at the unloading point, and specimen dimensions B and b are defined in Figure 1 [7].

J-resistance curves consisting of many sets of J and Δa data points were generated, and J_{Ic} was taken as the point of intersection of the resistance curve and the nearly vertical blunting line. The blunting line is given by $J = 2\ \Delta a\ \sigma_f$, where σ_f is the average of the yield and ultimate strengths. The J_{Ic} data were used to obtain estimates of K_{Ic}, denoted $K_{Ic}(J)$:

$$K_{Ic}^2(J) = \frac{J_{Ic} \cdot E}{1 - \nu^2} \qquad (1)$$

Young's modulus E, was taken to be 206.8 GPa at 4 K and Poisson's ratio, ν, was taken as 0.3.

In these tests, the Δa values inferred from compliance measurements and the actual Δa values measured on heat-tinted fracture specimen surfaces were not in exact agreement. The inferred values were less than the actual values, by up to 50%. One reason for the disagreement is that the crack extension in specimens containing δ-ferrite was non-uniform, as noted by example in the text (see section entitled Fracture surface topography under RESULTS). This phenomenon causes a sizable error in the slope of the J-Δa curve, but has less effect on the measured J_{Ic} values. The estimated uncertainty of the experimental J_{Ic} values is ±30%, which translates to an uncertainty in the calculated $K_{Ic}(J)$ of ±15%.

Microscopy: Specimens of the centrifugally cast CF8 stainless steel were subjected to scanning electron microscopy after fracture testing, as well as optical microscopy before and after testing.

Specimens from heat numbers 429517 (0% δ-ferrite), 82118 (8% δ-ferrite) and 526631 (14.5% δ-ferrite) were prepared for optical examination by standard metallograhpic polishing procedures. The 0% δ-ferrite microstructure was revealed by electroetching with aqueous oxalic acid solution (10 g/100 ml H_2O; 2 V, 295 K). The 8 and 14.5% δ-ferrite microstructures were revealed by electroetching in a 10N KOH solution (∿2 V, 295K). The latter procedure tinted the δ-ferrite light brown to light blue in color.

Observations were made on specimens obtained by sectioning the tested compact specimens. Specimens for general assessment of the microstructure in an untested state were obtained from regions remote from the crack front. The compact specimens were also sectioned perpendicular to the crack front and macroscopic crack plane in order to make observations of the crack profile in the region of plane-strain loading. Specimens for general microstructure assessment were viewed on two surfaces: perpendicular to the casting radius, R, and perpendicular to the casting axis, L. This was done to determine anisotropy in the microstructure introduced during solidification and cooling of the casting.

RESULTS

General microstructural assessment: The microstructures of untested material are depicted in Figures 2 and 3. The single-phase austenitic casting structure is characterized by a coarse grain structure and a uniformly distributed porosity. Note the surface "rumpling" produced by electroetching. This is due to local variations in chemical

composition produced by solidification. Although the general distribution of the porosity is uniform, on a finer scale the porosity is mainly confined to "troughs" in the surface relief, which correspond to interdentritic regions in the as-solidified microstructure. Figures 3(a) and (b) depict two other interesting aspects of cast grain structure associated with the grain boundaries:

(1) There is an obvious traversing of dendrite arms (delineated by surface rumpling) by grain boundaries. This indicates the occurrence of grain growth in the solid state after solidification is complete. A good example of this is located at A in Figure 2(b).

(2) There is a marked difference in grain morphology between grains viewed in the two sections. The grains in Figure 2(a) are elongated whereas the grains in Figure 2(b) are equiaxed. Similar anisotropies are to be expected for the other ferrite contents.

The as-cast 8 and 14.5% δ-ferrite microstructures are characterized by filamentary particles of δ-ferrite that sometimes appear to form diffuse cell-like networks [Figure 3(a) and (b)]. An interesting feature of the δ-ferrite that is especially obvious in the 14.5% microstructure is the faceting of many δ/γ interfaces.

Mechanical properties: The yield strength, ultimate strength, and elongation measurements for the materials of this study (as measured by Lee[1]) are listed in Table 2. At 4 K, the fully-austenitic, (zero-ferrite) casting exhibited a 413 MPa yield strength and a 46% elongation. These tensile properties are comparable to handbook values for AISI 304 stainless steel. Castings containing δ-ferrite show higher strength and

lower elongation compared with the fully austenitic casting. The yield strengths range from 413 to 689 MPa, and elongations range from 47 to 10.7% for δ-ferrite contents from 0 to 14.5%. But there is not a perfect correlation between the tensile properties at 4 K and the δ-ferrite content, because the lowest elongation at 4 K (10.7%) is reported for the 12% δ-ferrite casting that was not solution-treated.

Figures 4 and 5 show selected load-versus-deflection records and J-resistance curves obtained during fracture tests of compact specimens. The single-phase (γ) and duplex (γ+ δ) castings differ markedly in their fracture behavior. The presence of δ-ferrite lowers the critical J value as well as the deflection at maximum load. In every case, fracture progresses by a series of instabilities that give the load-versus-deflection curves a serrated appearance. The load drops corresponding to the serrations are relatively small in magnitude, especially for the zero-ferrite casting. It is possible that these serrations represent unstable plastic deformation, unstable crack extension, or both.

The critical J values and K_{Ic} estimates for each CF8 specimen are listed in Table 2, and the yield strength-versus-fracture toughness data are plotted in Figure 6. Also shown in Figure 6 is a band of data for wrought plates obtained from tests on a series of AISI 304 type stainless steels in which property variations were achieved by altering the interstitial carbon and nitrogen contents [4]. The fracture toughness data for the wrought plates were derived from 24.5-mm-thick compact specimens of the TL orientation [5], tested with the same J_{Ic} technique used in testing

CF8. This provides a good comparison of the 4-K properties of Fe-18/20Cr-8/12Ni stainless steels in both the wrought and cast forms.

The data for AISI 304 wrought plate clearly show an inverse linear relationship, the toughness decreasing with increasing strength. Similarly, for CF8 castings, higher strength is generally associated with lower toughness. But the detrimental effect of the δ-ferrite on the fracture toughness of castings at 4 K is quite severe and clearly outweighs any strengthening benefits. As shown in Figure 6, the single-phase austenitic casting is nearly equivalent in toughness to wrought plate having a similar yield strength, whereas duplex castings containing 3.2 to 14.5% δ-ferrite exhibit toughness values well below half the values for wrought steels at similar yield strengths.

Crack profiles: Microstructural observations of the crack profile in J-tested specimens demonstrated that the fracture of the 0% δ-ferrite specimen was accompanied by extensive plastic deformation and martensitic transformation. Figure 7 depicts the nature of martensitic transformation within slip bands of the plastic deformation. It is evident that the pre-existing voids in the microstructure influence the fracture behavior, as discussed below.

Figure 8 depicts the crack profile for the 14.5% δ-ferrite material. Fracture of this casting is associated with less extensive plastic deformation and martensitic transformation than in the 0% δ-ferrite casting. The fracture path in the 14.5% δ-ferrite specimen is tortuous and the failure mechanism differs markedly from that of the 0% δ-ferrite specimen. The 14.5% δ specimen shows numerous regions of apparent void formation at δ/γ interfaces, as well as the presence of

cracked δ particles in advance of the crack tip. There is also ample evidence of crack branching.

Fracture surface topography: At low magnifications the casting fracture surfaces appear rough, and this roughness appears to increase with the δ-ferrite content (Figure 9). The 0% ferrite casting fracture surface is relatively smooth, regular, and close to the nominal plane of the machined notch. In contrast, the 12% δ-ferrite casting fracture surface is particularly rough, and deviates at an angle of 15° to the notch plane. The 12% δ-ferrite specimen is also unique in that the main crack front was irregular, running ahead of numerous small ligaments that remained behind the main crack front. After J-testing, heat-tinting, and final fracture, the 12% δ-ferrite fracture surface exhibited a unique speckled appearance caused by unoxidized areas at sites where ligaments of the ductile γ phase had remained intact.

Fracture in the 0% δ-ferrite casting at 4 K occurred exclusively by a ductile, dimpled failure mechanism involving void coalescence, despite the fact that body-centered-cubic martensitic phase transformations occurred in the plastic zone prior to crack extension. As shown by scanning electron microscopy in Figure 10, the dimple pattern is actually duplex: large isolated dimples, representing preexisting porosity or inclusion sites, are surrounded by a network of smaller dimples arising from nucleation and growth owing to slip. Figure 10(a) shows a strip-like zone transverse to the direction of crack extension, wherein the average dimple size is smaller than in areas outside this zone; this variation probably reflects the influence of cast macrostructure and

perhaps represents fracture along intercolumnar, as opposed to trans-columnar, grain paths.

As shown in Figures 11 through 13, the scanning electron micrographs of the castings containing 8, 12, or 14.5% δ-ferrite reveal a mixed failure mode at 4 K. This mixed mode consists of cleavage in the δ phase and dimpled failure in the partially transformed γ phase. For the 8% δ-ferrite casting, Figure 11(b) shows a δ-ferrite particle that has cleaved on three orthogonal planes, the fracture apparently originating at a large pore near the δ/γ interface. Higher magnifications of the 14.5%- and 12% δ-ferrite specimens are shown in Figures 12(b), and 13.

DISCUSSION

Microstructural observations: Considerable research has been conducted into the evolution of microstructure in austenitic stainless steel welds and castings [8-16]. These studies have centered about factors affecting the volume fraction, scale, and morphology of δ-ferrite. The present investigation illustrates the potency of relatively minor variations in steel chemistry in producing a significant variation of the volume-percent δ-ferrite (0 to 14.5%). With the exception of the 0% δ-ferrite casting, the castings employed in this work solidified with ferrite as the primary phase (first solid phase to form) so that the microstructure can contain an appreciable amount of ferrite upon completion of solidification. The greatly reduced volume fraction of δ-ferrite actually observed in the microstructure upon cooling to room temperature (Figures 2 and 3) is then due to a solid-state $\delta \rightarrow \gamma$ transformation subsequent to solidification.

Extensive solute-redistribution as well as microstructural change takes place during the $\delta \rightarrow \gamma$ transformation. Controversy exists as to whether the $\delta \rightarrow \gamma$ transformation occurs via a massive or diffusion-controlled nucleation and growth mechanism. Whatever the actual mechanism, the faceting and characteristic angles frequently observed between facet variants indicate the presence of low-energy interfaces with a high degree of lattice matching. Other studies at the authors' laboratory have indicated the facet morphology to be consistent with a Kurdjunov-Sachs type of orientation relationship between δ and γ; this orientation relationship has been observed previously [12].

A note of caution should be introduced with regard to general microstructural assessment of δ-ferrite in an austenitic stainless steel. On any given plane of polish, the δ-ferrite appears dispersed in the austenite matrix with only occasional indications of continuity. Investigations involving dissolution of the matrix have indicated the δ-ferrite is partly to completely continuous above approximately 10% [17]. This could have significant implications with respect to deformation and fracture behavior by limiting the mean free path through a region of the austenite matrix. Thus, the network distribution of δ-ferrite and its brittleness at 4 K may have contributed to the relative coarseness of the 12% δ-ferrite specimen fracture surface.

The difference in grain morphology observed on different specimen sections [Figures 2(a) and (b)] is consistent with the heat flow during

casting and the manner in which the compact specimens were cut from the centrifugal casting. Figure 1 is a schematic diagram of the centrifugal casting and the specimen position. Heat flow, as indicated on the diagram, is in a radial direction. Investigation of the microstructure produced by the $\delta \rightarrow \gamma$ transformation in primary-δ-solidifying steels has indicated that the resulting austenite grains are columnar and follow heat flow regardless of the prior solidification structure [18]. Thus, the longitudinal axes of the elongated austenite grains are parallel to the crack front in our CL-oriented specimens. One might not expect to find a significant difference in mechanical properties if compact specimens of the LC orientation (Figure 1) had been tested. However, if specimens of a third orthogonal orientation were available (cracks propagating radially, through the tube thickness), a property dependence on orientation might be expected since the longitudinal axes of the grains would then be perpendicular to the crack front. Limited testing on austenitic stainless steel welds [19] suggests that the grain size in the plane of the crack profile controls fracture behavior. The rationale tendered for this behavior is that in a plane-strain, ductile fracture mode the strain is confined to the above-mentioned plane, and the plastic zone size at the crack tip is then affected by the grain size in that plane. Even though the austenitic grain size in the δ-ferrite containing specimens is expected to behave in a similar manner, the δ-ferrite in these steels becomes the overiding factor in deformation and fracture behavior. This is especially so since the δ-ferrite structure is generally not strongly associated with the final austenite grain structure in castings.

Fracture toughness comparisons: The J-integral data of this study must be interpreted cautiously. The degree of specimen-to-specimen variability in J_{Ic} values is not known since there was no replicate testing. Of the six different specimens tested, three did not satisfy criteria for valid J_{Ic} data as formulated in the recommended method of testing (see notes to Table 2). Nevertheless, the J-integral technique used in this study appears to have yielded the first practical estimates of K_{Ic} for these materials at liquid helium temperature.

Although the present results are discussed primarily as a function of the δ-ferrite, the δ-ferrite content was not the only variable in these tests. The castings were produced by different suppliers using variable composition and cooling rates. In particular, the 12%-δ-ferrite casting was not solution heat-treated. Solution heat treatment offers benefits such as slightly reducing the δ-ferrite content, modifying the δ-ferrite morphology by rounding off angular corners of the as-cast δ phase, and dissolving carbides [1]. Therefore, lack of solution heat treatment may account for the lower tensile ductility and lower fracture toughness of the 12%-δ casting compared with the 14.5%-δ casting [1].

Fracture mechanisms: The fracture mode of the fully austenitic casting with its higher volume fraction of interdendritic voids differs significantly from that of the δ-ferrite containing castings. The pre-existing void distribution appears to play a major role in the fracture process of the 0%-δ-ferrite steel. The crack in Figure 7 appears to be extending and branching by the growth and subsequent linking of voids. The mechanism of void growth is presumably via their

intersection with slip bands and might be enhanced by the internal stresses and strain associated with the martensitic transformation. The ligaments between the preexisting voids eventually rupture in a ductile manner to complete the crack extension. Consequently, the fracture surface consists of a duplex size distribution of dimples, as observed in Figure 10. The striations visible on the inside of the large dimples are then slip lines owing to the intersection of slip bands, surface rumpling owing to martensitic transformation, or both. We noted earlier that the amount of strain and martensitic transformation product in the 0%-δ-ferrite specimen is relatively large, owing to the larger plastic zone developed during J-testing of this high toughness material. But the role of the martensitic transformation on fracture behavior is unknown at this time.

Based on the observations recorded in this study, the following picture of the fracture process for duplex CF8 castings containing up to 14.5% δ-ferrite has been formulated: the δ-ferrite phase or δ/γ interfaces fracture first, at localized areas within the plastic zone ahead of the crack front (Fig. 8). The austenite then fails by ductile void coalescence in those ligaments necessary to bridge gaps between the fractured δ phase (Fig. 11). The crack front advances by linking many fractured δ particles that are not necessarily coplanar. Consequently, the fracture surfaces of δ-ferrite containing specimens are more tortuous than those of the fully austenitic specimens (Figs. 8,9), and the fracture surfaces apparently display a higher percentage of cleavage than would be expected based on the proportion of δ phase encountered on a perfectly planar

section through the microstructure. That the δ-ferrite is brittle at 4 K is demonstrated by the cleavage fractures in SEM micrographs. But the specific roles played by void formation at δ/γ interfaces, martensitic transformation, and possible constraints imposed by the relatively hard δ phase on the softer γ phase are uncertain at this time.

Finally, it is interesting that in concurrent studies, CF8M (316) castings with similar δ-ferrite content possessed higher fracture toughness, less evidence of martensitic transformation, and practically no evidence of ferrite cracking in areas ahead of the main crack front. This suggests a variation in behavior due to alloying. The highly-alloyed CF8M matrix is more stable compared with CF8, and it is possible that the composition of the δ-ferrite is also different from that of the CF8 casting. Data for ferritic steels at 4 K show a strong beneficial effect of Ni on toughness [20]. If the Ni contents of the two δ ferrites (CF8 vs. CF8M) were significantly different, this might explain the observed differences in fracture behavior and also indicate an important variation in ductility of the ferrite at low temperature.

SUMMARY

The fracture behaviors of six CF8 stainless steel castings in liquid helium at 4K were studied and compared. On the basis of microstructure, there are two categories of materials. The results are summarized as follows:

1) Single-phase austenitic CF8 castings are capable of exhibiting cryogenic tensile and fracture properties nearly equivalent

to the properties of wrought steels having a similar composition. The Fe-18Cr-11Ni casting tested in this study at 4K exhibited a K_{Ic} estimate of 331MPa·$m^{1/2}$ and a yield strength of 413 MPa. Slight differences in properties between cast and wrought steels may be attributed to the presence of solidification shrinkage porosity and the greater chemical inhomogeniety associated with castings, as well as grain size effects. Interdendritic porosity in CF8 evidently combines with smaller voids formed during straining to produce a duplex dimpled failure mode.

2) In duplex CF8 castings, the presence of body-centered cubic δ-ferrite severely reduces tensile ductility and toughness. For CF8 specimens containing 3.2 to 14.5% δ-ferrite, the estimated K_{Ic} values at 4K ranged from 84 to 179 MPa·$m^{1/2}$, or about half the fracture toughness expected for wrought steels of similar compositions. Failure in the duplex castings occurs by cleavage of the δ-ferrite, followed by ductile void coalescence of the surrounding austenite at load levels significantly higher than required to fracture the δ-phase. The adverse effects of δ-ferrite are reflected in all aspects of fracture behavior.

ACKNOWLEDGMENT

The authors gratefully acknowledge the assistance of Drs. D. Dew-Hughes, J. Chow, and K. S. Lee of Brookhaven National Laboratory, in providing the test materials, tensile property data, and manuscript review.

REFERENCES

1. Dew-Hughes, D. and Lee, K. S., The Choice of Steel for the Isabelle Magnet Tubes, Adv. Cryo. Engr., Vol. 26, 1981, pp. 151-157.
2. Zemzin, V. N. and Petrov, G. L., Influence of Ferrite Content on the Properties of Austenitic Weld Metal, Svarka. Proizvod., No. 5, 1967, pp. 5-8.
3. Read, D. T., McHenry, H. I., Steinmeyer, P. A., and Thomas, R. D., Jr., Metallurgical Factors Affecting the Toughness of 316L Weldments at Cryogenic Temperatures, Weld. J. Res. Suppl., Vol. 59, 1980, p. 104-s.
4. Tobler, R. L., Read, D. T., and Reed, R. P., Strength/Toughness Relationship For Interstitially Strengthened AISI 304 Stainless Steels At Four Kelvin, presented at the Thirteenth National Symposium on Fracture Mechanics, Philadelphia, PA, June 1980.
5. Standard Method of Test for Plane Strain Fracture Toughness of Metallic Materials (Designation E 399-74), 1974 Annual Book of ASTM Standards, Part 10, American Society for Testing and Materials, Philadelphia, PA, 1974, pp. 432-451.
6. Fowlkes, C. W. and Tobler, R. L., Fracture Testing and Results for a Ti-6Al-4V Alloy at Liquid Helium Temperature, Engr. Fract. Mechs., Vol. 8, 1976, pp. 487-503.
7. Clarke, G. A., Andrews, W. R., Begley, J. A., Donald, J. K., Embley, G. T., Landes, J. D., McCabe, D. E., and Underwood, J. H., A Procedure for the Determination of Ductile Fracture Toughness Values Using J Integral Techniques, J. Test. Eval., Vol. 7, No. 1, 1979, pp. 49-56.

8. Lippold, J. C. and Savage, W. F., Solidification of Austenitic Stainless Steel Weldments: Part 1-A Proposed Mechanism, Weld. J. Res. Suppl., Vol. 58, No. 11, 1979, p. 330-s.

9. David, S. A., Goodwin, G. M., and Braski, D. N., Solidification Behavior of Austenitic Stainless Steel Filler Metals, Weld. J. Res. Suppl., Vol. 58, No. 11, 1979, p. 330.

10. Suutala, N., Takalo, T., and Moisio, T., The Relationship Between Solidification and Microstructure in Austenitic and Austenitic-Ferritic Stainless Steel Welds, Met. Trans. A, Vol. 10A, No. 4, 1979, p. 512.

11. Suutala, N., Takalo, T., and Moisio, T., Single-Phase Ferritic Solidification Mode in Austenitic Stainless Steel Welds, Met. Trans. A, Vol. 10A, No. 8, 1979, p. 1173.

12. Suutala, N., Takalo, T., and Moisio, T., Ferritic - Austenitic Solidification Mode in Austenitic Stainless Steel Welds, Met. Trans. A, Vol. 11A, No. 5, 1980, p. 717.

13. Lippold, J. C. and Savage, W. F., Solidification of Austenitic Stainless Steel Weldments: Part 2 - The Effect of Alloy Composition on Ferrite Morphology, Weld. J. Res. Suppl., Vol. 59, No. 2, 1980, p. 48-s.

14. McTighe, J. M. and Beech, J., The Structure of As-Cast Austenitic Stainless Steels, J. Res., SCRATA, No. 37, 1977, p. 43.

15. Raghunathan, V. S., Seetharaman, S., Venkadesan, S., and Rodriguez, P., The Influence of Post Weld Heat Treatments on the Structure, Composition and the Amount of Ferrite in Type 316 Stainless Steel Welds, Met. Trans. A, Vol. 10A, No. 11, 1979, p. 1683.

16. Hammar, O. and Svensson, U., Influence of Steel Composition on Segregation and Microstructure During Solidification of Austenitic Stainless Steels, in Solidification and Casting of Metals, Proceedings of an International Conference on Solidification, University of Sheffield, England, 1977, p. 401.

17. Gill, T. P. S., Dayal, R. K., and Gmadamoorthy, J. B., Estimation of Delta Ferrite in Austenitic Stainless Steel Weldments by an Electrochemical Technique, Weld. J. Res. Suppl., Vol. 58, No. 12, 1979, p. 375-s.

18. Fredriksson, H., The Solidification Sequence in an 18-8 Stainless Steel, Investigated by Directional Solidification, Met. Trans., Vol. 3, No. 11, 1972, p. 2989.

19. Whipple, T. A., McHenry, H. I., and Read, D. T., Fracture Behavior of Ferrite-Free Stainless Steel Welds in Liquid Helium, Weld. J. Res. Suppl. vol. 60, No. 4, 1981, p. 725.

20. Tobler, R. L., Mikesell, R. P., and Reed, R. P., Cryogenic Effects on the Fracture Mechanics Parameters of Ferritic Nickel Alloy Steels, in: Fracture Mechanics, ASTM STP 677, C. W. Smith, Ed., American Society for Testing and Materials, Philadelphia, PA, 1979, pp. 85-105.

Table 1. Chemical compositions of CF8 castings tested [11].

Material Designation Number	δ Ferrite[c] %	Fe	Cr	Ni	C	Mn	P	S	Si	Mo	N
429517[a]	0	balance	18.0	11.0	0.02	1.00	0.04	0.04	0.72	0.10	0.044
334951A	3.2	"	18.6	9.5	0.05	0.37	0.03	0.02	1.12	0.06	0.033
326541A	7.7	"	20.1	8.2	0.07	0.74	0.02	0.02	1.57	0.04	0.014
821128[a]	8	"	19.4	10.0	0.05	1.07	0.011	0.009	1.21	----	0.09
526631[a]	14.5	"	19.6	8.4	0.06	0.19	0.02	0.02	1.62	0.08	0.049
147922[b]	12	"	20.9	8.5	0.05	0.69	0.019	0.017	0.97	0.106	0.085

[a] solution treated, 1040°C, ∿2 h

[b] as-cast

[c] measured at BNL by using metallographic and magnetometer methods

Table 2. Tensile properties and fracture toughness results for CF8 castings at 4 K.

CF8 Material Designation	δ ferrite, %	Yield Strength, σ_y MPa	Ultimate Strength, σ_U MPa	Elongation, %	J-Integral, J_{Ic} kJ/m^2	Size Factor, $25(J_{Ic}/\sigma_f)$ mm	$K_{Ic}(J)$[a], MPa·m$^{1/2}$
429517	0	413	1251	46.1	481	14[b]	331
334951A	3.2	455	1542	36.2	141	3.5	179
326541A	7.7	498	1206	30.6	132	3.9	174
821128	8	470	1512	47.6	175[c]	5.4	199[c]
526631	14.5	689	920	20.2	69	1.7	125
147922	12[d]	578	753	10.7	31	1.2	84.5

[a] converted from J_{Ic}.

[b] actual specimen thickness is 12.7 mm, whereas 14 mm is required [4].

[c] upperbound value (clip gage failure).

[d] fracture in this specimen was at a 15° angle to the notch plane.

LIST OF FIGURES

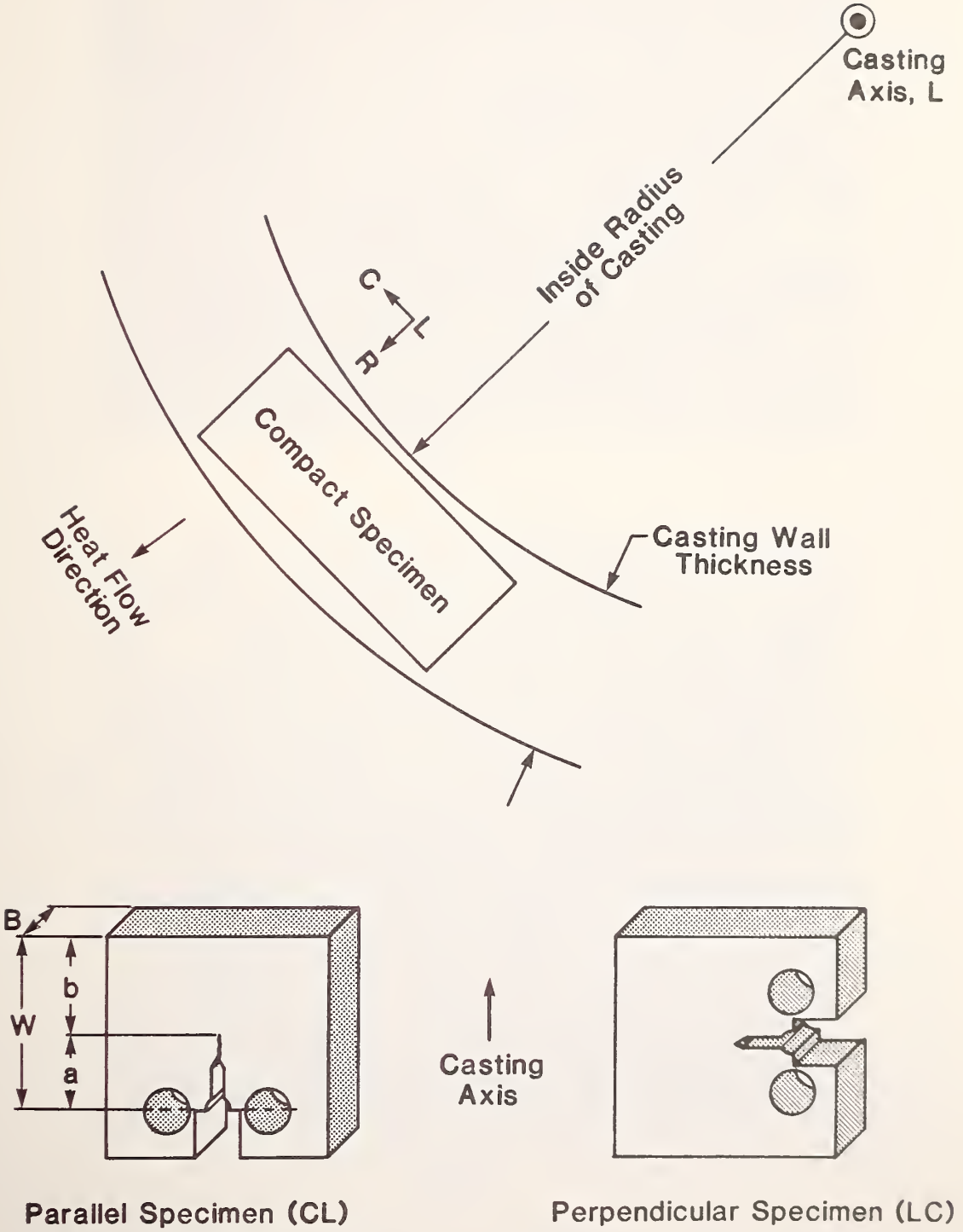

Figure 1. Compact specimen orientations with respect to tubular casting stock.

(a)

(b)

Figure 2. As-received microstructure of single-phase CF8 casting: (a) perpendicular to the tube circumference, (b) perpendicular to the tube radius.

(a)

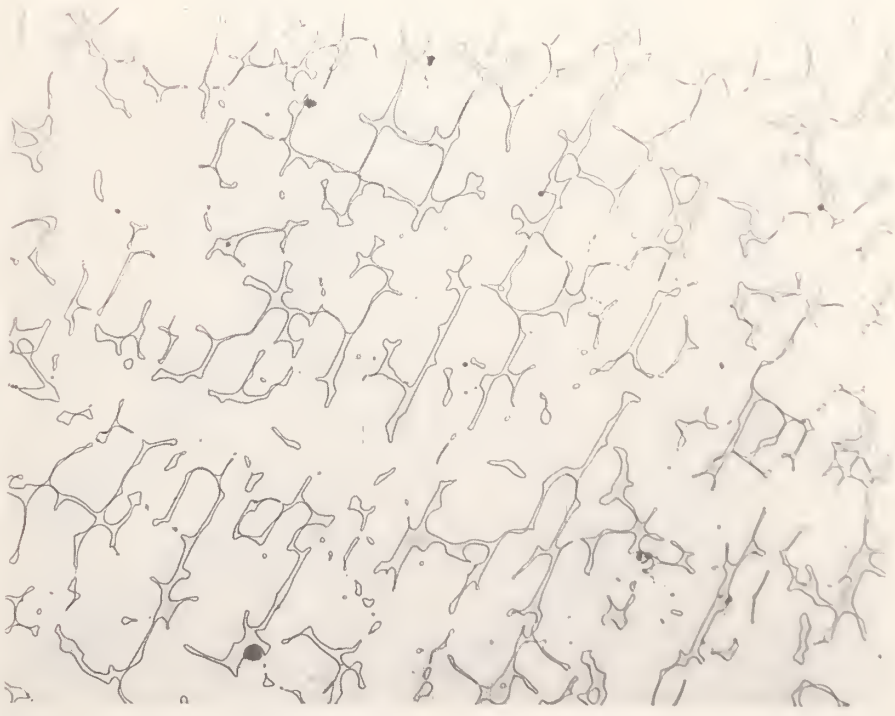

(b)

Figure 3. As-received microstructure of duplex CF8 castings containing (a) 8% δ-ferrite, (b) 14.5% δ-ferrite (sections perpendicular to the tube radius.

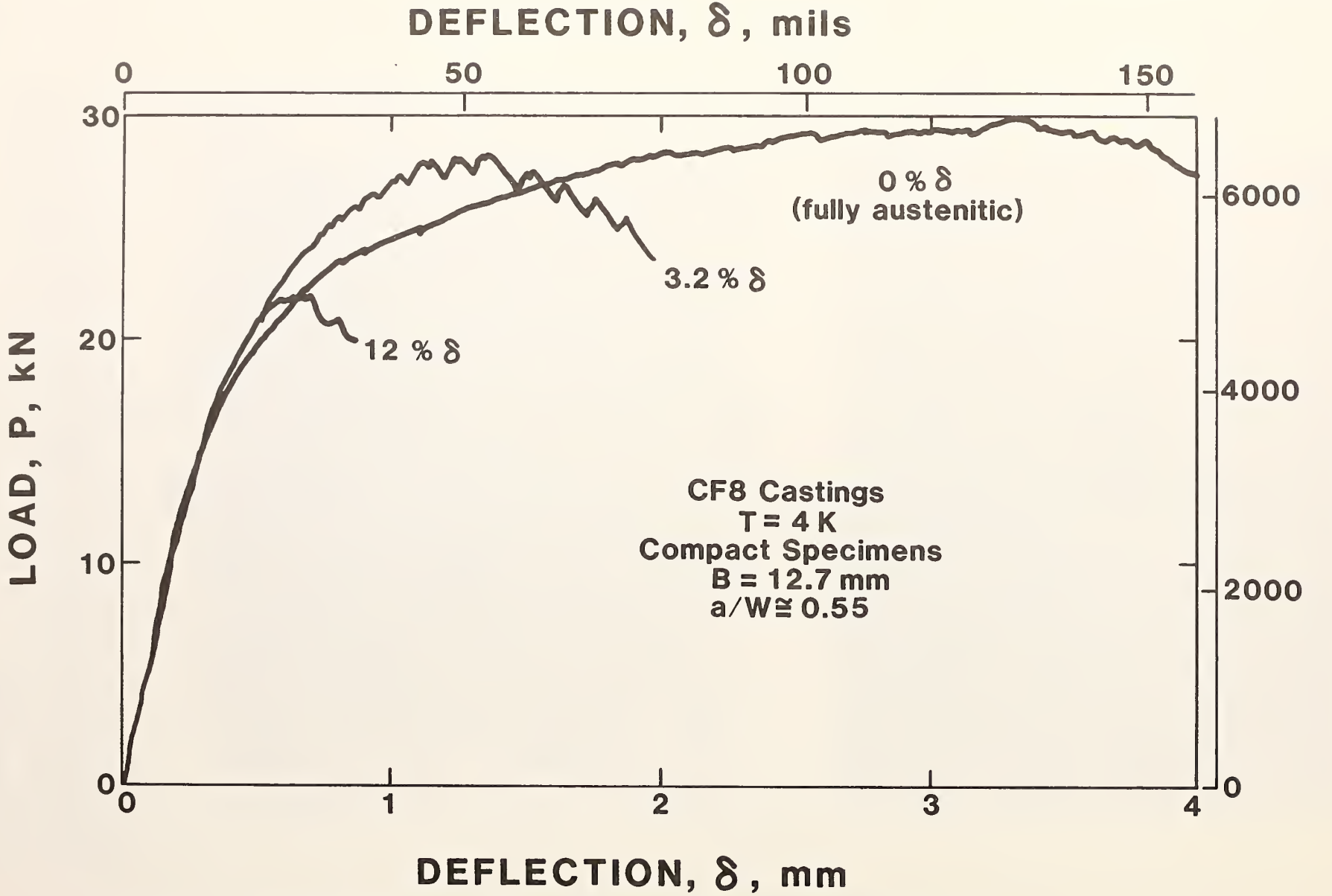

Figure 4. Fracture test records for selected CF8 compact specimens at 4K.

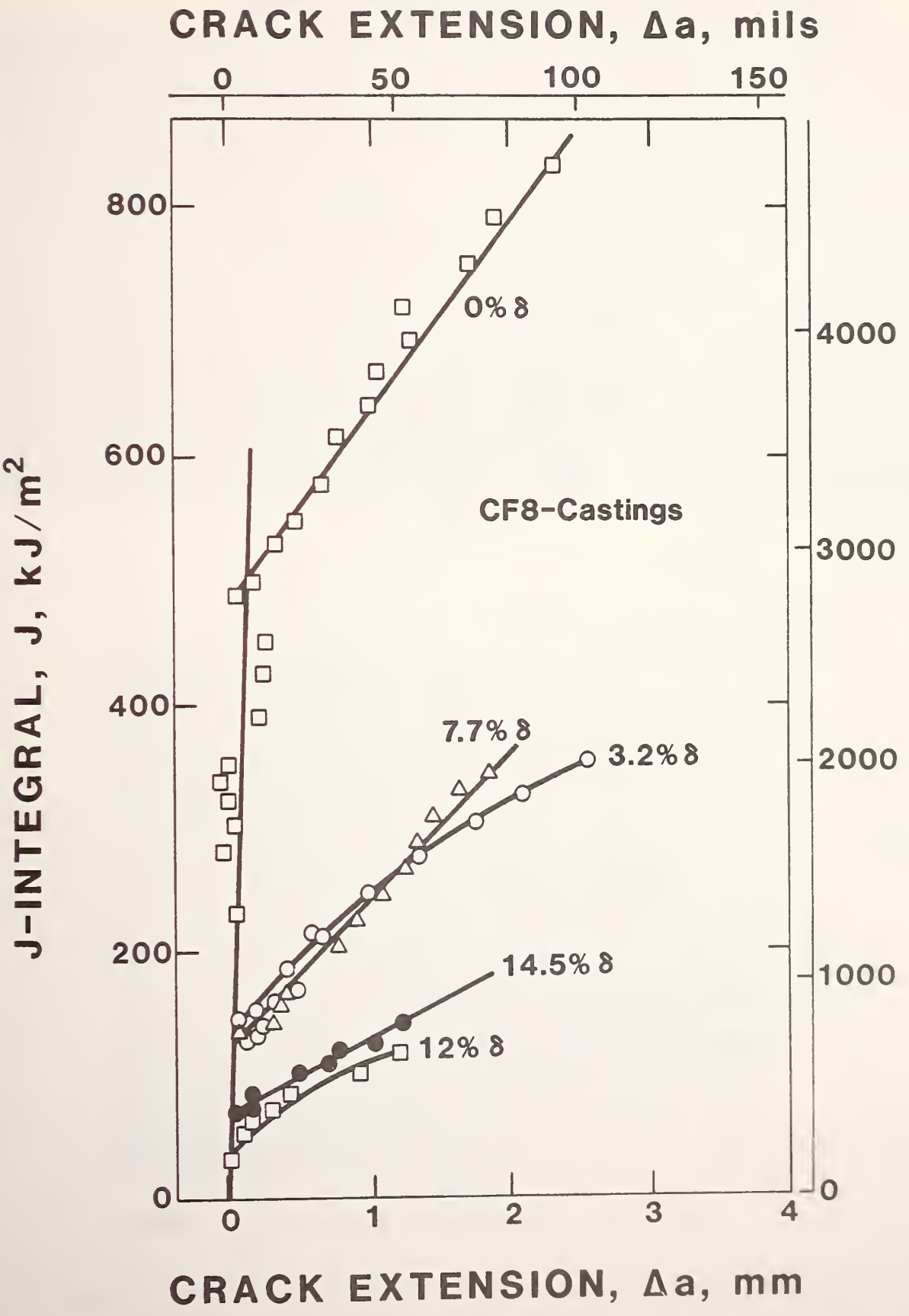

Figure 5. J-resistance curves for CF8 compact specimens at 4K.

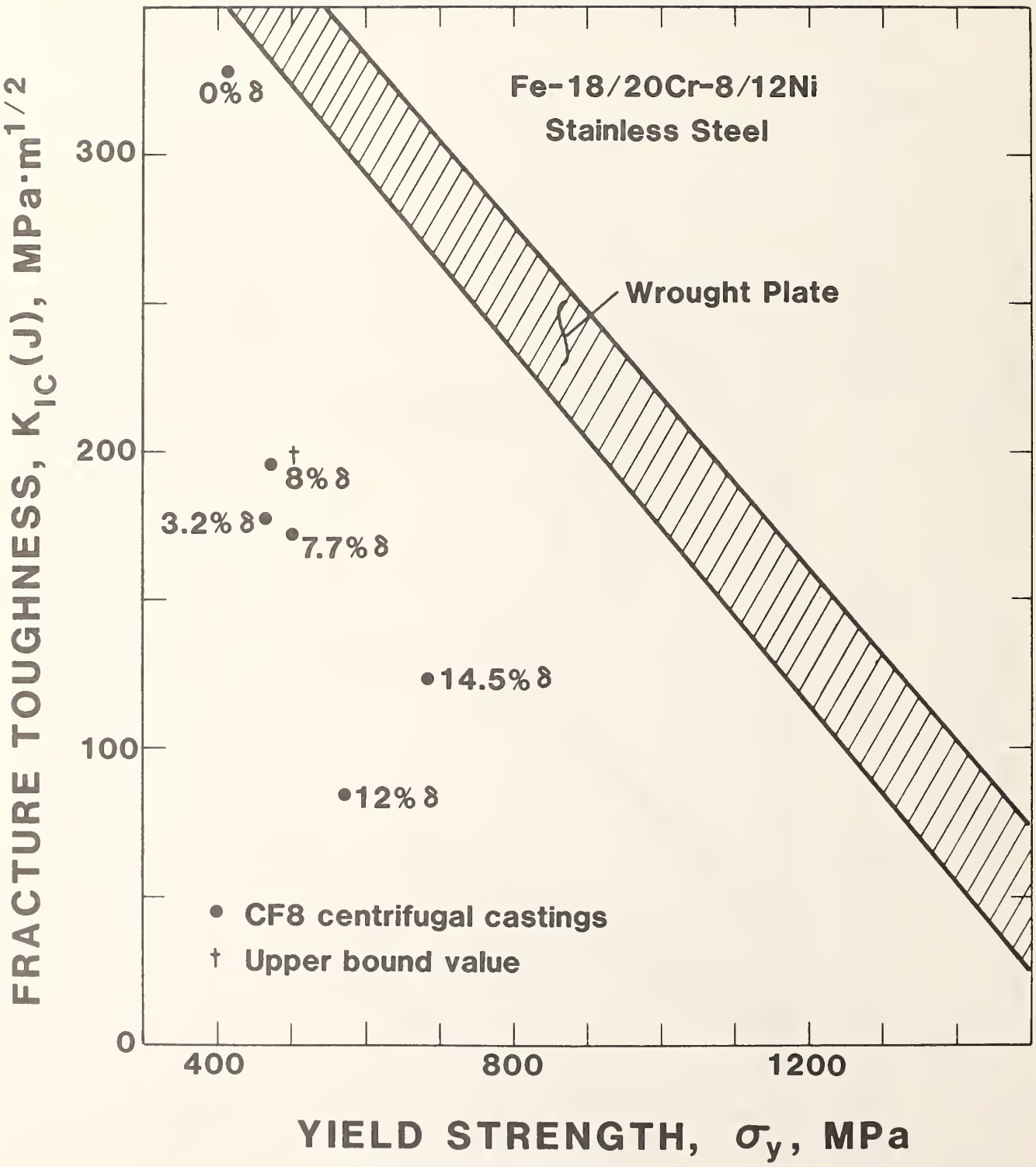

Figure 6. Toughness-versus-strength comparison for Fe-Cr-Ni stainless steels in wrought and cast forms at 4K.

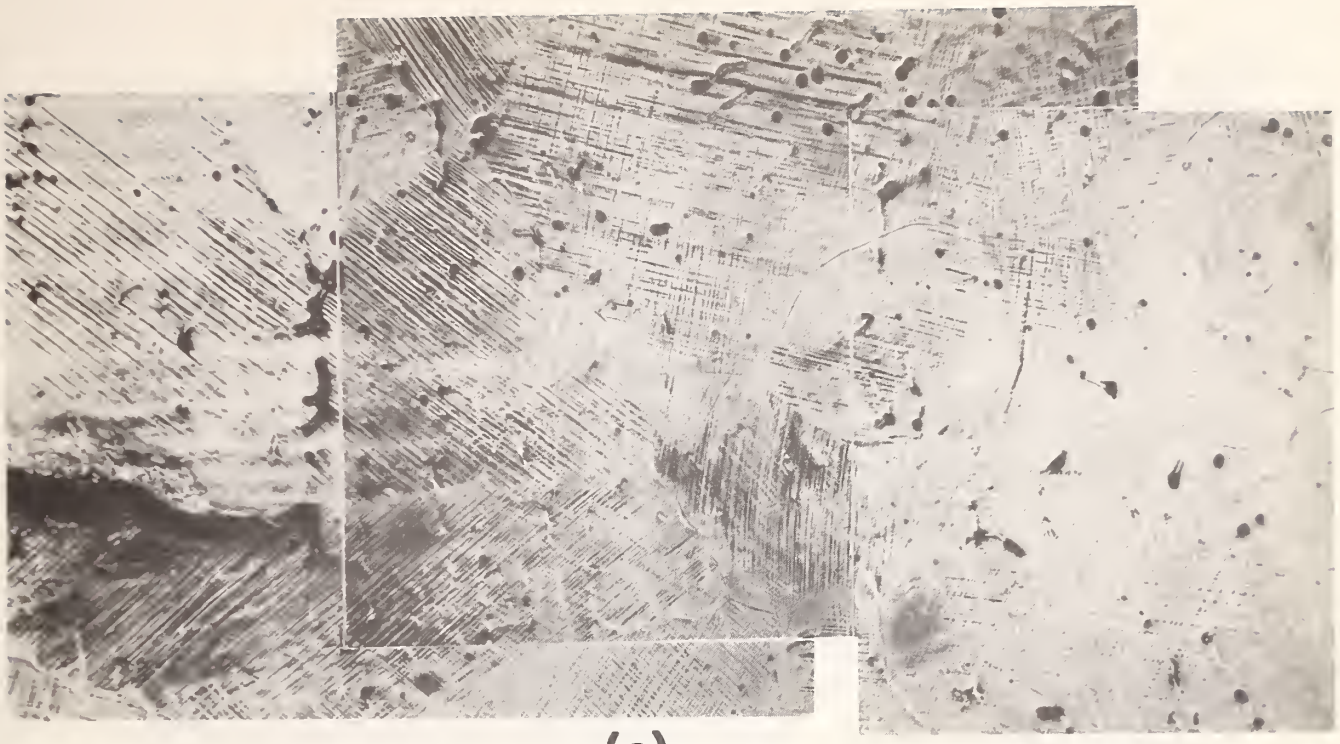

(a)

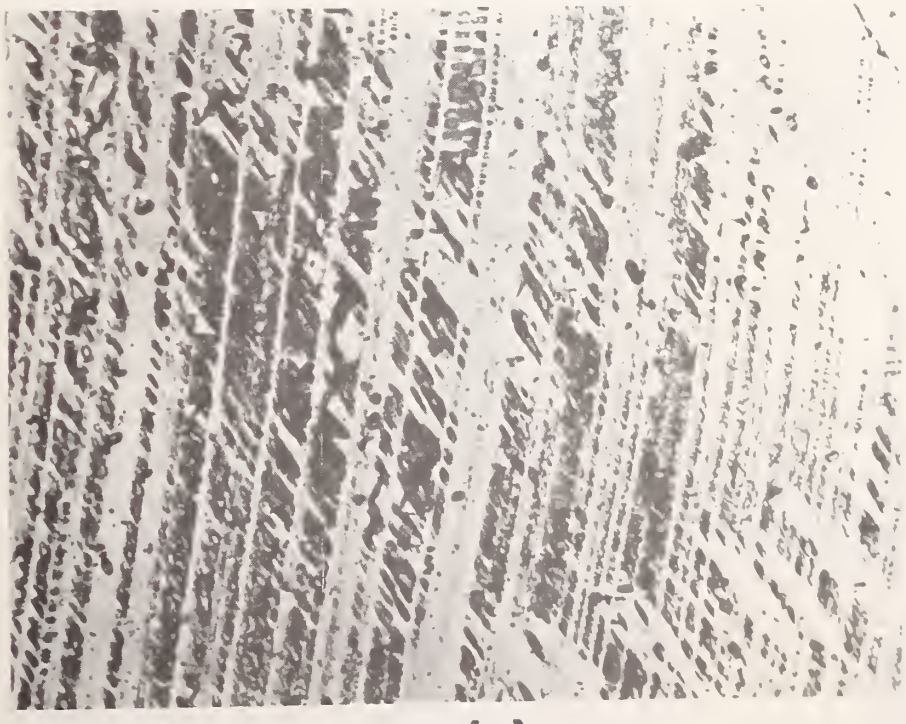

(b)

Figure 7. Fracture profile in 0% δ-ferrite CF8 compact specimen.

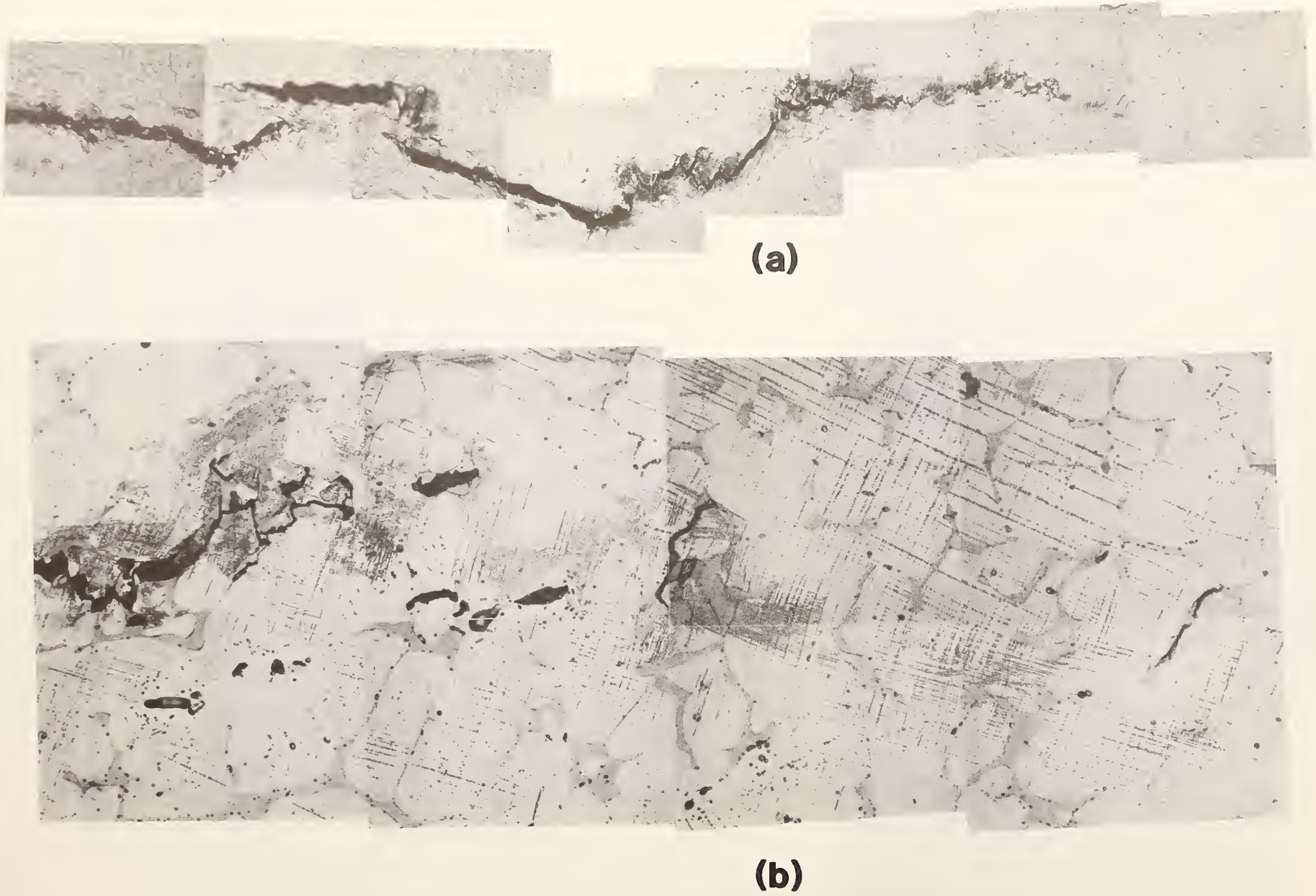

Figure 8. Fracture profile in 14.5% δ-ferrite CF8 compact specimen.

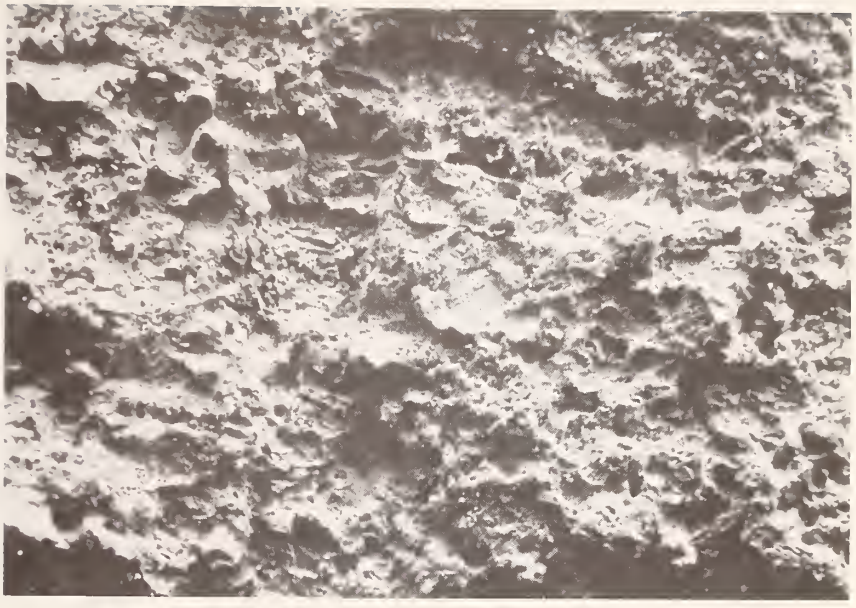

(a)

200μm

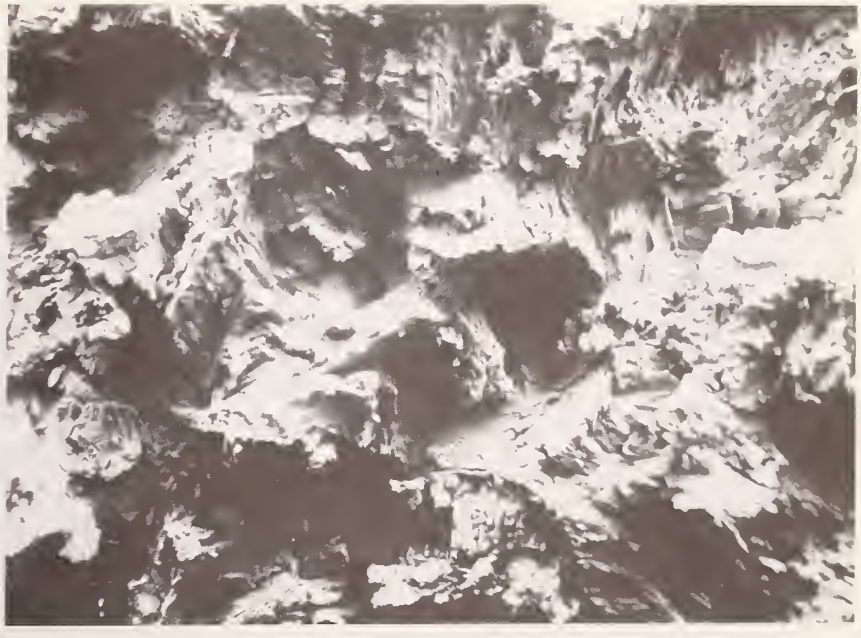

(b)

1mm

Figure 9. Macroscopic view of the 4K fracture surfaces of CF8 castings: (a) 0% δ-ferrite specimen, (b) 12% δ-ferrite specimen.

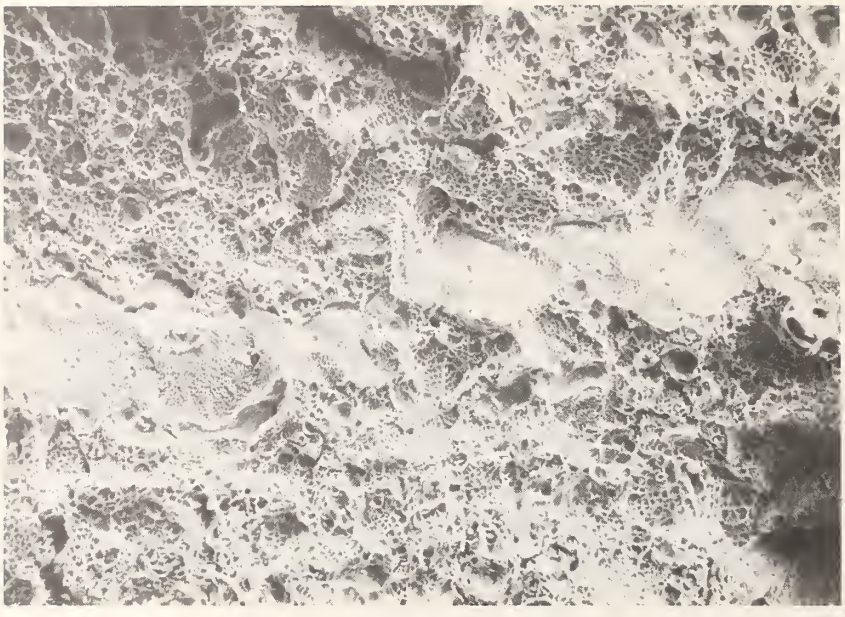

(a)

100 μm

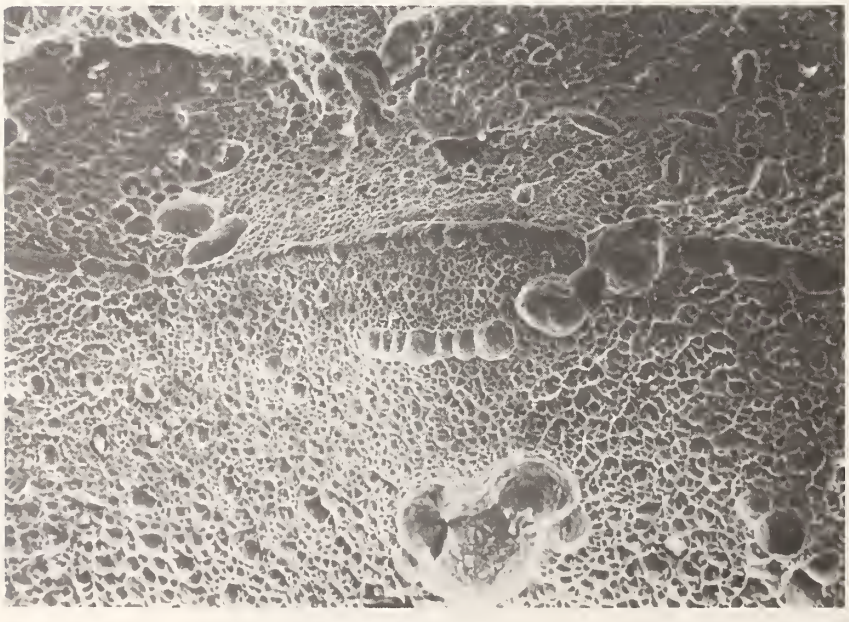

(b)

40μm

Figure 10. 4K fracture surface of a 0% δ-ferrite casting, showing dimpled failure.

(a)

100 μm

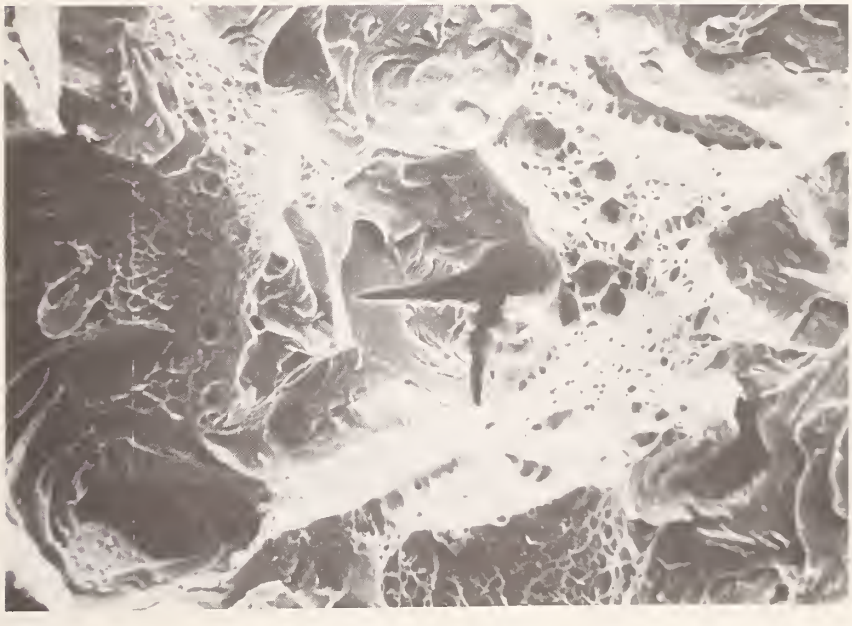

(b)

20μm

Figure 11. 4K fracture surface of an 8% δ-ferrite casting, showing both cleavage and dimpled failure modes.

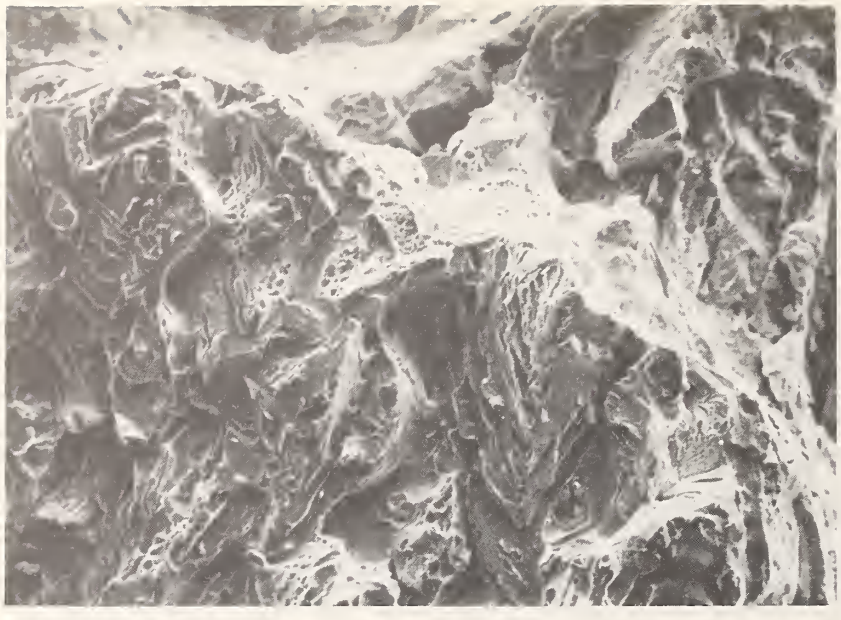

(a)

40μm

(b)

10μm

Figure 12. The 4K fracture surface of a 14.5%δ ferrite casting, showing:(a) duplex failure mode,(b) cleaved δ phase.

(a)

40μm

(b)

20μm

Figure 13. The 4K fracture surface of a 12% δ-ferrite casting, showing cleavage of a δ at high magnification.

DUCTILE FRACTURE WITH SERRATIONS IN AISI 310S STAINLESS STEEL AT LIQUID HELIUM TEMPERATURE *

R. L. Tobler and R. P. Reed
Fracture and Deformation Division
National Bureau of Standards
Boulder, Colorado 80303

ABSTRACT

Fracture toughness tests were performed on annealed austenitic stainless steel AISI 310S, immersed in liquid helium at 4 K, using 25-mm-thick compact specimens. The J_{Ic} results (360 to 380 kJ/m^2) from single- and multiple-specimen test techniques are compared and shown to be in close agreement. Attention is called to the remarkable failure process of this steel at 4 K: crack extension occurs by ductile tearing, while the test records exhibit serrations due to repeated bursts of unstable plastic flow and arrests. The nature of this behavior is discussed, and the performance of stable austenitic AISI 310S is compared with that of related steels, including those that transform from austenite to martensite during testing at 4 K.

Key Words: Austenitic stainless steel; cryogenic properties of materials; fracture of materials; J-integral tests; low-temperature properties; stainless steels.

*Work supported by the Department of Energy, Office of Magnetic Fusion Energy.

INTRODUCTION

AISI 310S is a low-carbon (C $\leq$ 0.08 wt.%) modification of Fe-25Cr-20Ni stainless steel. This steel has an austenitic (face-centered cubic) structure, and so remains highly ductile at extreme cryogenic temperatures. Owing to its high alloy content, the austenitic structure is completely stable and does not undergo martensitic phase transformations during deformation at low temperatures. Fracture toughness data for this material at 4 K were desired to serve three purposes:

1) to evaluate the NBS single-specimen J_{Ic} measurement procedure,

2) to illustrate the unique serrated plastic flow behavior that accompanies fracture of such materials at extreme cryogenic temperatures, and

3) to compare the toughness of a stable austenitic stainless steel with previously tested metastable stainless steels.

MATERIAL AND SPECIMENS

The tested material was a 25.4-mm-thick plate of AISI 310S in the as-received condition: annealed at 1950°F (1339 K), water quenched, and descaled. In weight percent, the chemistry is: Fe-24.6Cr-20.4Ni-1.65Mn-0.07C-0.70Si-0.18Mo-0.041P-0.027S. The hardness and tensile properties were measured by conventional methods [1,2] and are presented in Table 1.

Six compact fracture specimens of the TL orientation were machined from the as-received stock. These were not side grooved. The specimen thicknesses (B) and widths (W) were 25 and 50.8 mm, respectively. A diagram is given elsewhere [3].

In addition, one side-grooved specimen was prepared from a special portion of stock that had been reannealed in the laboratory: 1950°F (1339 K), 1 h, water quench. Symmetrical side grooves were machined on

both faces, reducing the section thickness by 10% (B_{net} = 22.8 mm). The notch root radii were 0.100 mm.

PROCEDURES

Precracking was accomplished in liquid nitrogen (76 K) or liquid helium (4 K), but the temperature of precracking had no apparent affect on results. The maximum and minimum fatigue loads were 22 and 2.2 kN, well below 40% of the maximum load reached in J tests. The final a/W ratio was nominally 0.62.

Both the single-specimen and multiple-specimen test techniques were applied. In the absence of accepted standards, the measurement techniques followed those reported elsewhere [3-5]. In the single-specimen technique, crack extension (Δa) was inferred periodically by unloading compliance measurements made with computer-aided data analysis. One specimen was loaded extensively to obtain a well-defined J-resistance curve. Five similar specimens were also tested with periodic 10% unloadings, but these tests were terminated at successively lower Δa values according to the multiple-specimen technique [5]. Displacement control was used. Each specimen was completely unloaded at the end of J testing and heat-tinted or refatigued to mark the final Δa, which was measured with a microscope at nine loctions, and averaged.

RESULTS

Loading Behavior

Figure 1 shows a typical load-versus-deflection curve for AISI 310S steel at 4 K. The behavior is fully plastic in that a limit load is reached. However, the curves are marked by serrations, which become more pronounced as the test proceeds. Superimposing test records for

similarly sized specimens showed that the behavior was reproducible, with major serrations occurring at nearly equivalent loads and deflections. Test records for this type of steel at 295 and 76 K (not reported here) do not show these serrations.

Fracture Mode

In appearance, the serrations of Fig. 1 resemble a type of "pop-in" phenomenon, which is frequently observed in other materials at room temperature. Such behavior is usually caused by spurts of brittle cracking and arrest. However, annealed AISI 310S steel is not at all brittle. A fractured specimen is shown in Fig. 2, and a scanning electron micrograph of the 4-K fracture surface is shown in Fig. 3. The microscopy reveals a heavily dimpled fracture surface evidently produced by void formation, growth, and coalescence. There is no visual evidence of a change in fracture mechanism or surface markings that might be associated with the serrations of Fig. 1. Apparently, then, we have here an example of a material in which a single mechanism of crack extension (ductile tearing) is associated with first stable, then unstable loading conditions in the same test specimen. Rarely has this been observed.

J-Resistance Curves and J_{Ic}

A J-versus-Δa curve for the AISI 310S steel from the single specimen technique is shown in Fig. 4. The curves follow a linear regression line, as assumed in the recommended procedure [5]. The recommended procedure also assumes that crack-tip-blunting behavior will conform to the equation:

$$\Delta a = 2J\sigma_f \qquad (1)$$

where σ_f is the average of the yield and ultimate strengths. Although the data for one specimen did follow this equation, the data for all other specimens deviated, owing to a slight zero shift during the early stage of blunting line development just after the first unloading (see Fig. 4). For the single-specimen technique used in this study at 4 K, the initial crack length, a_0, inferred from compliance was 3% lower than the value measured from broken specimens. This could be attributed to errors in the compliance function used and in the assumed value of Young's modulus (206.4 GPa) at 4 K.

Table 2 and Fig. 5 present the relevant J-integral data from the multiple-specimen technique for AISI 310S at 4 K. These data for specimens with no side grooves show little scatter, except for one relatively low toughness specimen, which was excluded from the analysis. In comparison, the result from extrapolation for the multiple-specimen technique gives J_{Ic} = 360 kJ/m^2, whereas the single-specimen technique indicates 380 kJ/m^2.

The J_{Ic} measurement point was traced to its location on the load-versus-deflection curve; it does not coincide with the first sizable load drop or with the attainment of maximum load, but falls intermediate between these points, as shown in Fig. 1. Since the J value at the first significant load drop ($\sim$327 kJ/m^2) is lower than J_{Ic}, the first load drop must be due only to unstable plastic flow, not true crack extension. This was confirmed by compliance measurements made before and after the first load drop: only a small increase of Δa was indicated, not greater than the amount predicted from Eq. (1) for crack tip blunting.

Comparisons of the measured and inferred crack extensions for the five specimens without side grooves reveal an error that increases significantly as the J test proceeds, with disagreements as high as 55%. Since this error is less at low Δa values, the J_{Ic} measurement from the single-specimen technique is reasonably accurate (within 5%) of the value given by the multiple-specimen technique. However, the slope of the J-Δa curve for the single-specimen technique is inaccurate, being 65% greater than the slope given by the multiple-specimen technique. Therefore, our unloading compliance technique could not be used to determine the tearing modulus of the material at 4 K which, based on the multiple-specimen technique, is 60.

K_{Ic} Estimates

The J_{Ic} data are often used to estimate the linear-elastic plane strain fracture toughness, K_{Ic}. From the single- and multiple-specimen techniques, the K_{Ic} estimates for AISI 310S steel at 4 K are 290 and 285 $MPa \cdot m^{1/2}$, respectively. The uncertainty in J_{Ic} is ±15%, which translates to an uncertainty in K_{Ic} of ±8% [1]. We note, however, that the existence of K_{Ic} for annealed austenitic stainless steels has never been proved, since linear-elastic fracture behavior for these materials has never been observed. To determine experimentally whether linear-elastic fracture behavior could be achieved in AISI 310S at 4 K, it would be necessary to test a specimen of impractical size, having a thickness of about 0.5 m:

$$B \geq 2.5 \left(\frac{K_{Ic}}{\sigma_y}\right)^2 = 2.5 \left(\frac{285 \text{ MPa} \cdot m^{1/2}}{645 \text{ MPa}}\right)^2 = 0.49 \text{ m} \qquad (2)$$

Fracture Toughness Comparisons

Although it would be interesting to compare the J_{Ic} values for AISI 310S at 4 K and at room temperature, this is impossible because J_{Ic} data for 25-mm-thick specimens are invalid at 295 K. Comparisons are, therefore, limited to results for other heats and stainless steels that have also been tested at 4 K.

Logsdon, Wells, and Kossowsky [6] also tested a heat of AISI 310S steel at 4 K, reporting a K_{Ic} estimate of 262 MPa·$m^{1/2}$ and an 819-MPa yield strength. The K_{Ic} result is quite consistent with ours, because K_{Ic} scales as an inverse function of the yield strength, as shown in Fig. 6. The somewhat higher strength and lower fracture toughness of the heat tested by Logsdon et al. is easily explained by compositional differences, notably higher carbon content.

Considerable low temperature fracture toughness data are now available for the two categories of austenitic stainless steels: 1) stable with respect to phase transformation at 4 K (e.g., AISI 310S and Fe-20Cr-16Ni-6Mn-0.2N steels [7]) and 2) metastable with respect to phase transformation at 4 K (e.g., AISI 304 type steels [3,4]). Figure 6 summarizes data pertaining to the effect of structural stability on fracture toughness in the Fe-Cr-Ni-Mn system. The results shown in this figure are for equivalent specimen orientation, specimen size, and test technique; all of the steels represented in this figure exhibited the dimpled fracture mode, as verified by scanning electron microscopy. We see that the data for three stable steels fall within the scatterband for unstable steels, so that a single inverse-linear dependence on yield strength appears to govern fracture toughness, regardless of whether

martensitic phase transformation takes place or not. Additional data will be needed to support this conclusion.

Side Grooves

One specimen having side grooves was J-tested, and the inferred Δa was 24% lower than the measured value. From Fig. 5, the error for an ungrooved specimen at the same value of measured crack extension would be 33%. This indicates that side grooves may improve the final Δa prediction for ductile austenitic stainless steels tested by the unloading compliance technique. Confirmation is needed using deeply side-grooved specimens.

DISCUSSION

AISI 310S at 4 K furnishes a remarkable example of a material that fails by repeated bursts of instability and arrests, the same mechanism of failure (ductile tearing) associated with alternating stable and unstable conditions in a single test specimen. The first few serrations in the load displacement record result from unstable plastic deformation that causes crack-tip blunting, but no true crack extension.

Subsequent serrations at J values exceeding J_{Ic} are presumed to be associated with both plastic flow and crack extension by ductile tearing. As discussed later, this type of ductile fracture with serrations can be expected in many ductile alloys, but only at temperatures near absolute zero.

Mechanism of Serrated Flow

The serrations observed in tests of compact specimens at 4 K are analogous to the serrations observed in stress-strain curves during conventional unnotched tensile tests. The phenomenon as it occurs in

tensile tests is documented in studies of a wide variety of materials at temperatures below 20 K, including stable and transforming stainless steels, aluminum, and copper alloys [8-12]. In tensile tests of austenitic stainless steels at 4 K, the serrations begin after small initial plastic strains of about 2%, and the deformation propagates as a Lüders band [8].

Observations from our tests of AISI 310S show that the serrations at 4 K cannot be attributed to brittle cracking or to phase transformation. The most widely accepted explanation is based on adiabatic heating, as described by Basinski [9,10] and later confirmed [11], although not everyone is in agreement [12].

The adiabatic heating model is plausible at 4 K because of the very strong changes of specific heat (large decrease) and flow strength (large increase) as temperature is lowered from room temperature to 4 K. Many materials exhibit these trends, and serrated flow behavior is also widespread [13]. For AISI 310S, the specific heat shows a 200-fold reduction between 295 and 4 K [14]. Thus, the amount of thermal energy necessary to produce an appreciable temperature rise is relatively low at 4 K.

The adiabatic heating mechanism might be pictured as follows: Heating during dislocation movement causes appreciable softening, and deformation becomes unstable. Low thermal conductivity at 4 K (compared with that at 295 K) contributes to a localization of the heat to produce load instability. During instability the load drops suddenly and the plastic flow becomes localized when thermal softening due to heat generated by plastic straining is greater than the strain-rate hardening.

The instability is eventually arrested at some strain and temperature where the flow process becomes stable, owing to local specimen strain hardening that distributes the load over an ever-increasing area at a time when the rise of specific heat precludes continued temperature increases. Once the flow has become stable again, the specimen cools to 4 K, and with further deformation, the process repeats.

As noted in the text, the tensile and fracture test records at 295 and 76 K (not shown) do not exhibit serrations. In fact, serrations of the type occurring at 4 K are seldom observed at temperatures above 40 K. The instability criterion is satisfied only at the lowest temperatures because 1) the volume specific heat is reduced so that relatively large temperature increases are possible in straining and 2) the flow stress is more strongly temperature dependent.

Test Methodology

According to the proposed convention [5], two offset lines for data qualification are drawn parallel to the blunting line at Δa = 0.15 and 1.5 mm, and data falling outside the specified interval are discounted. Although two data points in Fig. 5 do fall outside the specified interval, both lie on the linear regression line and so were used in the analysis of results. The near agreement of our single- and multiple-specimen results is taken as evidence that the deviations from the recommended guidelines are not sufficient to invalidate the conclusions of this study.

The experimental evidence for AISI 310S shows that the initiation of crack extension at 4 K occurs at a point after the first serration and before the maximum load. Therefore, taking the first load drop or

the maximum load point as the J_{Ic} measurement point is an inaccurate procedure for austenitic stainless steels at 4 K. The unloading compliance technique used here enables J_{Ic} to be measured at 4 K with good accuracy (uncertainty = ±15%), but gives an inaccurate resistance curve slope (dJ/da). The multiple-specimen technique gives both parameters accurately, but is more costly in materials and time. Normally, as many points as desired can be obtained in the single-specimen technique. But owing to the serrated loading behavior at 4 K, fewer data points are obtained than usual, since unloadings cannot be performed at points of instability on the load-versus-deflection curve.

Martensitic Phase Transformations

The role of martensitic phase transformations on fracture toughness is a subject of fundamental interest, with potential practical applications in the development of austenitic stainless steels. Apparently, the effects are different for different steel families. Two opposite trends have been observed:

1) Since martensitic phases forming in metastable austenitic steels have hcp or bcc structures which are typically brittle at 4 K, it might be expected that transformations at cryogenic temperatures could reduce the fracture toughness, as in AISI 200 series stainless steels [15].

2) Since the martensitic phases forming in metastable steels can absorb energy that otherwise might be converted to crack extension, it might be expected that these transformations could improve fracture toughness, as in TRIP steels at 295 K [16].

Neither of these trends was observable in our study. From a simple comparison of stable and transforming steels having similar yield strengths (as in Fig. 5), we observed that the effects of phase transformation on toughness were negligible for the compositions studied. Unfortunately, it is not possible to vary the alloy stability while holding the composition constant. The relative stability of the Fe-Cr-Ni-Mn steels in Fig. 5 is a function of composition and is strongly dependent on nickel content. The unstable Fe-18Cr-8 to 10Ni steels featured in this comparison transformed locally to as much as 90% bcc martensite, as measured from x-ray examination of the 4 K fracture surfaces. Such large amounts of martensite were formed gradually with increasing plastic strain. The initial transformation began locally at slip plane intersections, and high percentages of bcc phase were detectable only after extensive plastic deformation. Significantly, fracture surface appearance remained dimpled, as is the case for stable steels. The martensite phase transformation did affect the strain-hardening behavior of tensile specimens, but how this relates to the J_{Ic} results is not clear.

CONCLUSIONS

J-integral tests were performed on 25-mm-thick compact specimens of AISI 310S stainless steel immersed in liquid helium at 4 K. The major conclusions are:

1) The unloading compliance technique used here at 4 K gave a reasonably accurate J_{Ic} value but an inaccurate J-Δa slope. Improvements to reduce the error in inferred Δa values and blunting line deviations are needed. Side gooves may help.

2) Serrations resembling "pop-ins" occurred in the 4 K test records of compact fracture specimens, analogous to the serrations observed in conventional tensile tests of unnotched specimens. These serrations are thought to be caused by plastic flow instability and are not necessarily associated with true crack extension. Therefore, J_{Ic} should not be measured at the first "pop-in," unless it is demonstrated that crack extension is the true cause of the instability.

3) The failure mode for this AISI 310S steel at 4 K was ductile tearing. This same tearing mechanism was associated with both stable and unstable regions of the load-deflection fracture test record.

4) Comparison of existing data for steels in the Fe-Cr-Ni-Mn family shows a universal rate of decrease of fracture toughness with increasing yield strength at 4 K, regardless of whether martensitic phase transformations occur, suggesting that structural stability does not necessarily influence toughness.

REFERENCES

1. Reed, R. P. and Tobler, R. L., in Advances in Cryogenic Engineering-Materials, Vol. 28, Plenum Press, New York, 1982, to be published.
2. Ledbetter, H. M., Weston, W. F., and Naimon, E. R., Journal of Applied Physics, Vol. 46, 1975, pp. 185-194.
3. Tobler, R. L., Read, D. T., and Reed, R. P., in Proceedings of the Thirteenth National Symposium on Fracture Mechanics, American Society for Testing and Materials, Philadelphia, to be published.
4. Tobler, R. L. and Reed, R. P., in Advances in Cryogenic Engineering-Materials, Vol. 28, Plenum Press, New York, 1982, to be published.
5. Clarke, G. A., Andrews, W. R., Begley, J. A., Donald, J. K., Embley, G. T., Landes, J. D., McCabe, D. E., and Underwood, J. H., Journal of Testing and Evaluation, Vol. 7, No. 1, 1979, pp. 49-56.
6. Logsdon, W. A., Wells, J. M., and Kossowsky, R., in Proceedings of the Second International Conference on Mechanical Behavior of Materials, American Society for Metals, Metals Park, Ohio, 1976, pp. 1283-1289.
7. Reed, R. P., Tobler, R. L., Elmer, J. W., McHenry, H. I., and Yushchenko, K. A., in: Proceedings of the International Cryogenic Engineering Conference, ICEC 8, Rizzuto, C., Ed., IPC Science and Technology Press, Guildford, Surrey, England, 1980.
8. Powell, G. W., Marshall, E. R., and Backofen, W. A., Transactions of the ASM, Vol. 50, 1958, pp. 478-497.
9. Basinski, Z. S., Proceedings of the Royal Society, Vol. A240, 1957, pp. 229-242.

10. Basinski, Z. S., Australian Journal of Physics, Vol. 13, 1960, pp. 354-358.

11. Read, D. T., in Advances in Cryogenic Engineering-Materials, Vol. 28, Plenum Press, New York, 1982, pp. 91-101.

12. Obst, B. and Pattanayak, D. in Advances in Cryogenic Engineering-Materials, Vol. 28, Plenum Press, New York, 1982, to be published.

13. Wessel, E. T., Transactions of the ASM, Vol. 49, 1957, pp. 149-172.

14. Corsan, J. M. and Mitchem, N. I., in Proceedings of the Sixth International Cryogenic Engineering Conference, IPC Science and Technology Press, Guildford, Surrey, England, 1976, pp. 342-344.

15. Brickner, K. G. and Defillippi, J. D., in Handbook of Stainless Steels, D. Peckner and I. M. Bernstein, Eds., McGraw-Hill, New York, 1977, Chapter 20.

16. Gerberich, W. W., Henings, P. L., Zackay, V. F., and Parker, E. R., in Fracture 1969, P. L. Pratt, Ed., Chapman and Hall, London, 1969, pp. 288-296.

Table 1. Mechanical Properties of AISI 310S Stainless Steel[a]

Temperature, K	Yield Strength, MPa	Ultimate Strength, MPa	Elongation in 4D, %	Reduction in Area, %	Rockwell Hardness
295	251	600	43	50	R_B80
4	645	1259	36	31	NA

[a]It is assumed that at 4 K Young's modulus is 206.4 GPa and Poisson's ratio is 0.293 [2].

Table 2. J-Integral Fracture Results* for AISI 310S at 4 K

Specimen No.	a_o, mm	B, mm	W, mm	J, kJ/m^2	Δa, mm
1	31.267	25.489	50.8	475	0.673
4	31.953	25.400	50.8	900	2.304
6[a]	31.318	25.456	50.8	413	1.019
7	30.328	25.400	50.8	654	1.290
8	30.378	25.400	50.8	387	0.313
10	30.683	25.476	50.8	621	1.173
x[b]	29.718	25.253	50.8	482	0.432

J_{Ic} = 360 kJ/m^2; $K_{Ic}(J)$ = 285 $MPa \cdot m^{1/2}$ where $K_{Ic}(J)$ is estimated using $K_{Ic}(J) = (J_{Ic} \cdot E^1)^{1/2}$ where $E = E/(1-\nu^2)$ = 226 GPa.

[a]abnormally low toughness (excluded from analysis).

[b]reannealed and side grooved (B_{net} = 22.860 mm).

List of Figures

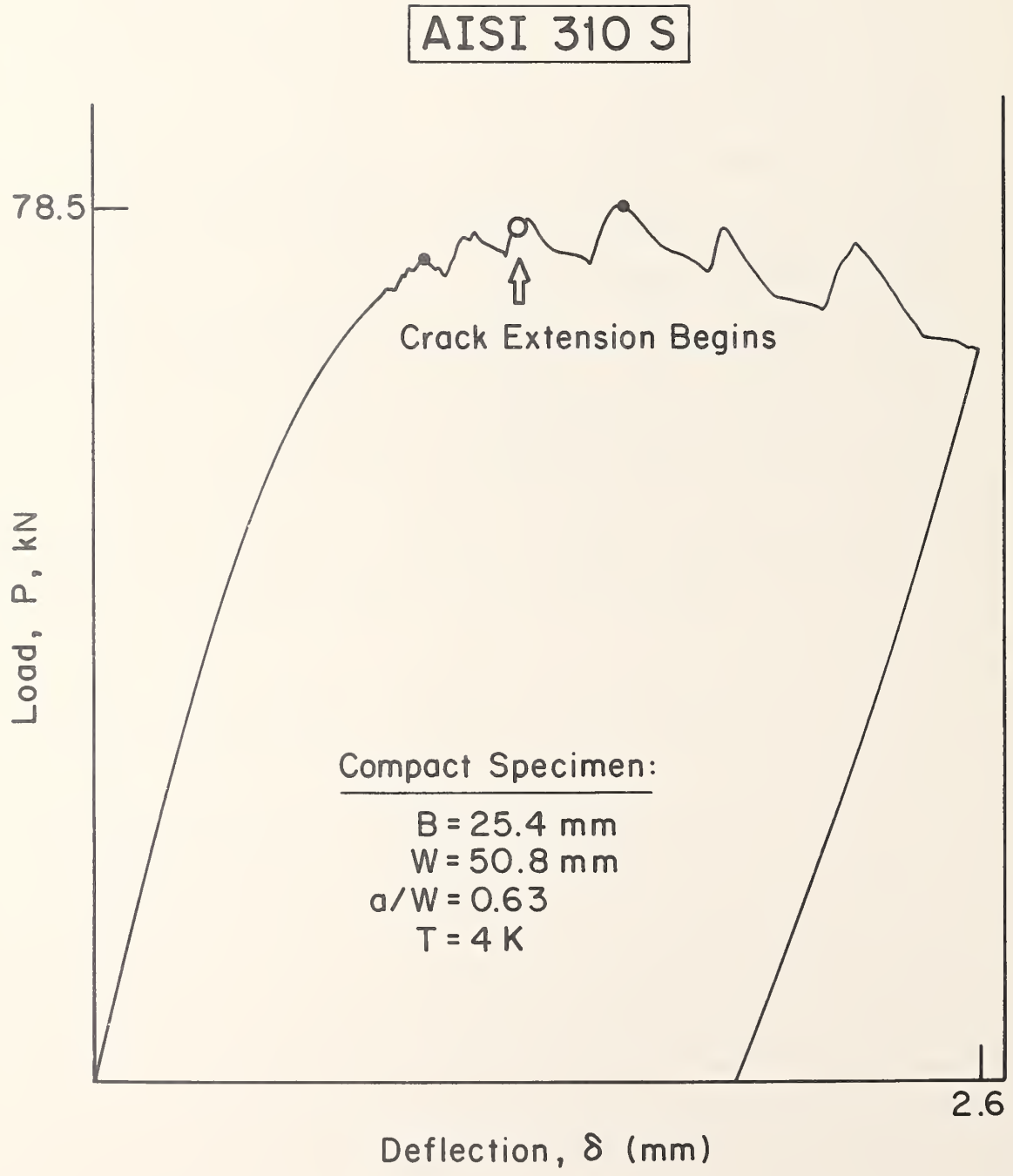

Figure 1. Typical load-versus-diffraction curve for AISI 310S steel at 4 K.

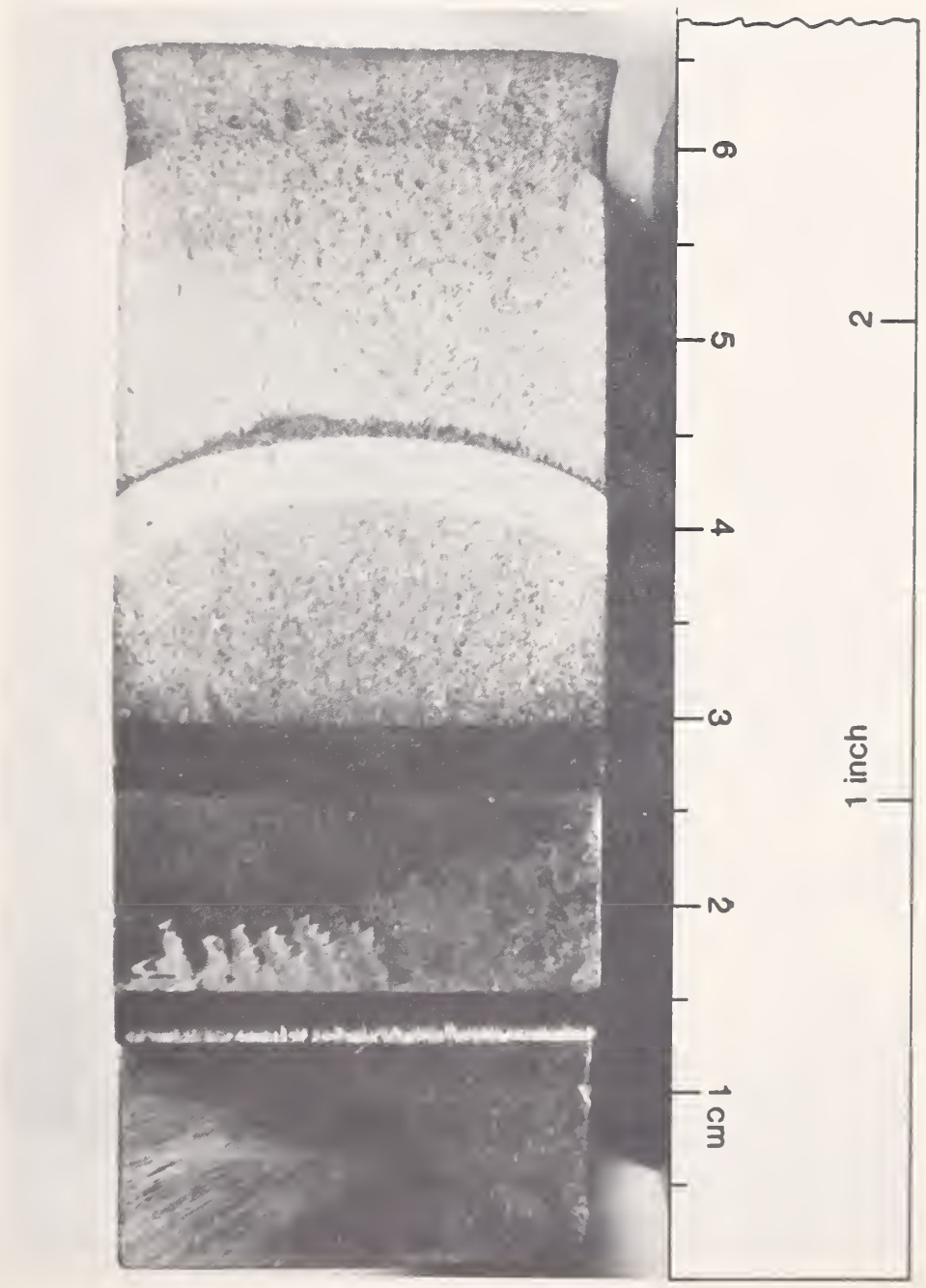

Figure 2. Fractural compact speciman of AISI 310S steel, tested at 4 K.

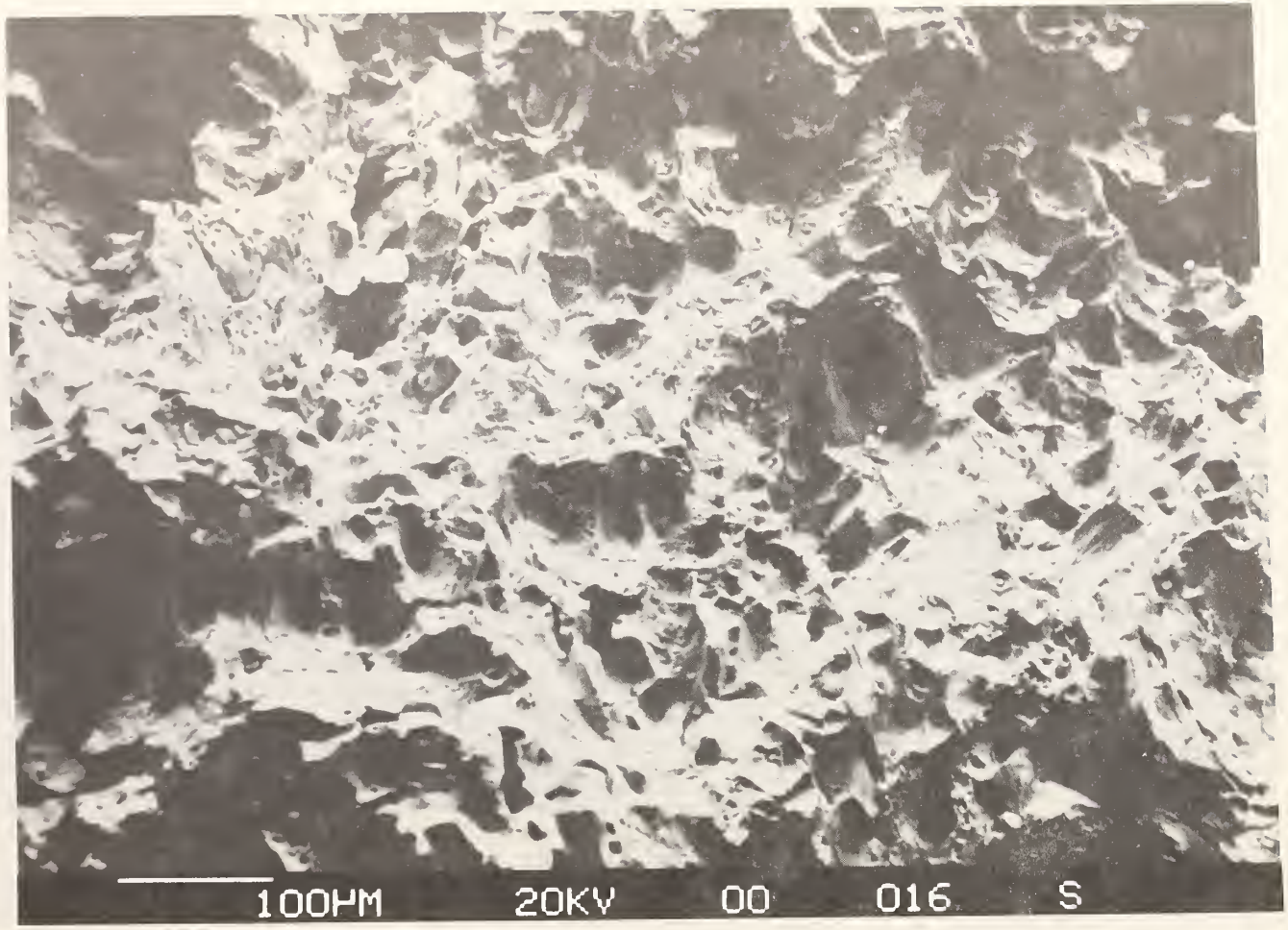

Figure 3. Scanning electron microscope picture of AISI 310S compact tensile specimen fracture surface.

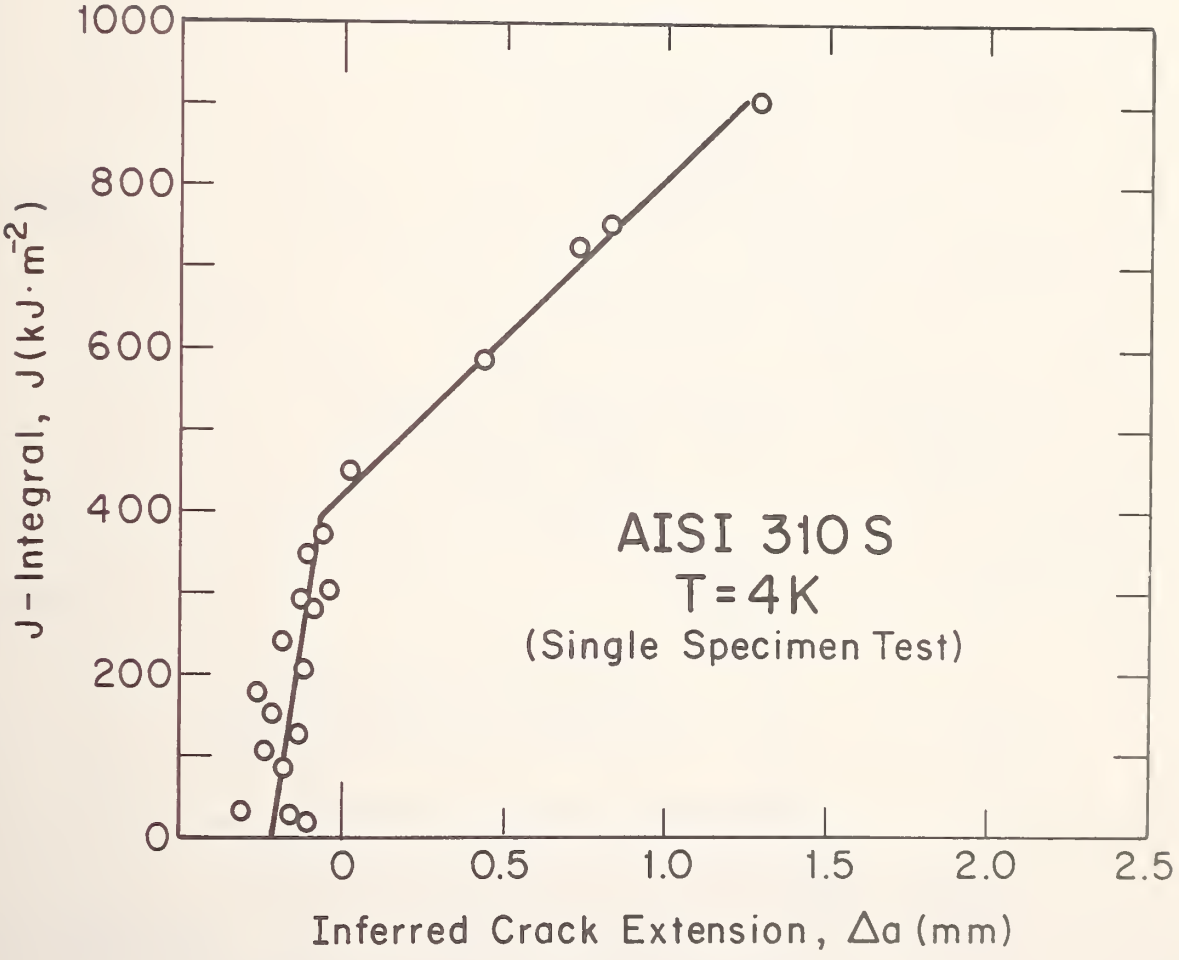

Figure 4. J-versus-Δa curve for AISI 310S using single-specimen technique.

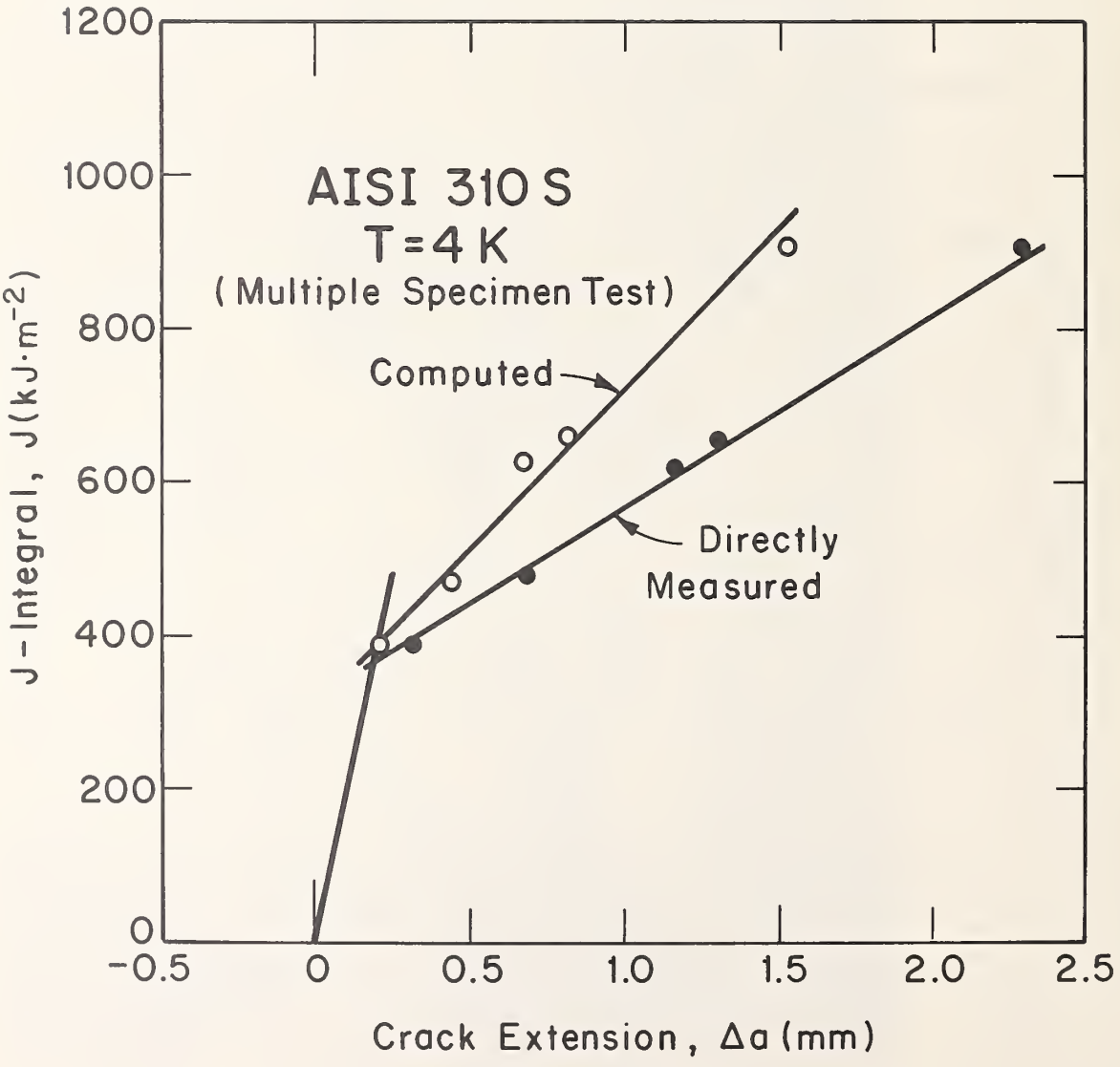

Figure 5. Computed directly measured J-versus-Δa curves for AISI 310S using multiple-specimen technique.

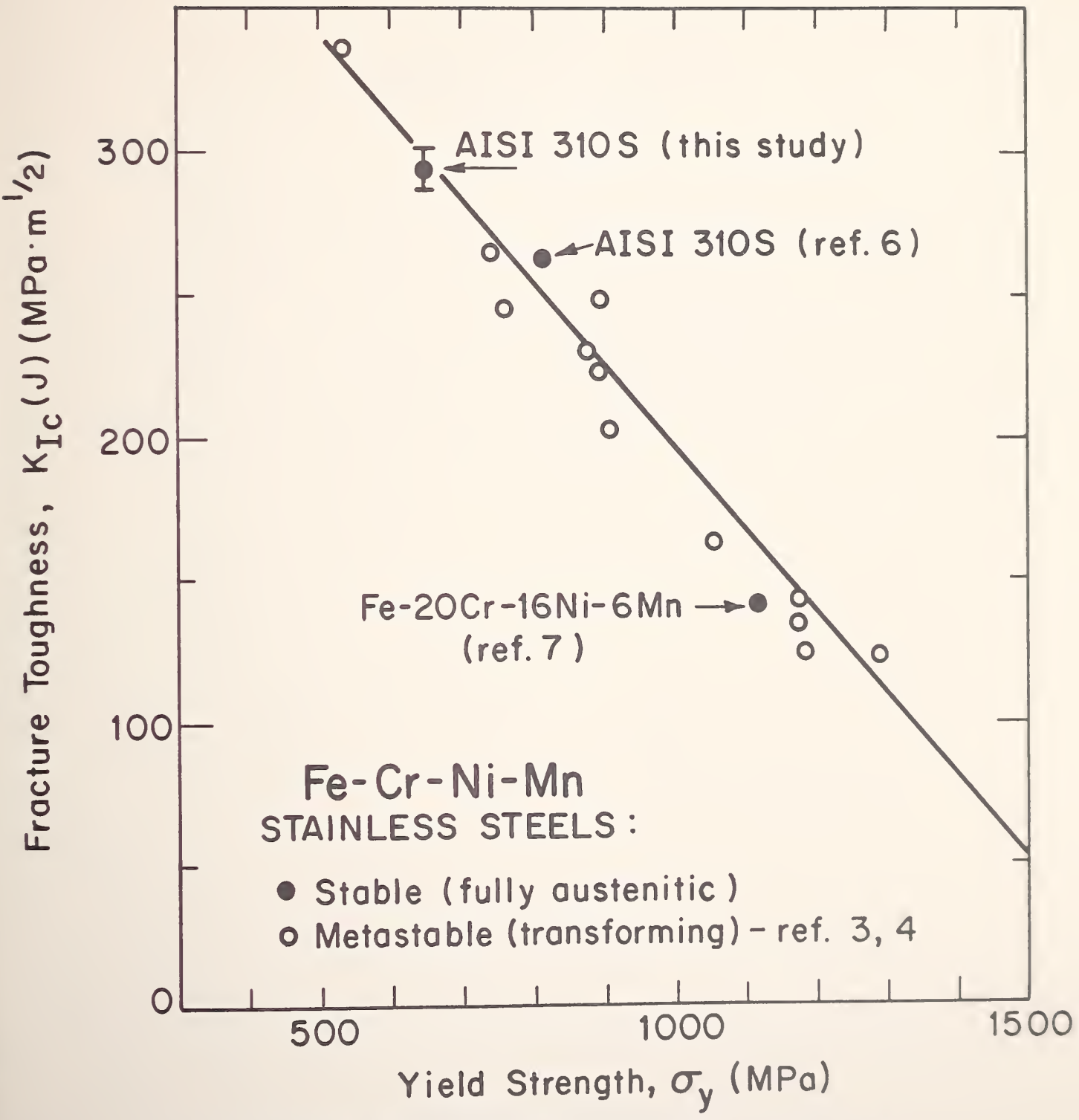

Figure 6. Fracture toughness versus tensile yield strength for many austenitic stainless steels, all measured at 4 K.

MECHANICAL PROPERTY MEASUREMENTS AT LOW TEMPERATURES*

D. T. Read and R. L. Tobler
Fracture and Deformation Division
National Bureau of Standards
Boulder, Colorado

ABSTRACT

The status of mechanical test methods for the liquid-helium temperature range is reviewed. Fracture toughness testing and the use of toughness data are emphasized. Facilities and test methods for fracture toughness, fatigue crack growth rate, tensile, and elastic properties at NBS in Boulder are described. Apparatus and techniques for temperature measurement and control during mechanical tests are briefly discussed.

*To be published in Advances in Cryogenic Engineering-Materials, Vol. 28, A . F. Clark and R. P. Reed, Eds., Plenum Press, New York (1982).

INTRODUCTION

Accurate material mechanical properties data at low temperatures are essential for design of economical, efficient, and safe structures for low temperature operation. Fracture toughness, tensile properties, and fatigue crack growth resistance characterize the mechanical performance of structural materials. Because construction of a sizeable welded structure free from geometrical defects is a practical impossibility, adequate material toughness is needed to prevent crack growth and eventual fracture at such defects. Strength and stiffness enable a material to support its applied loads without stretching or buckling. Adequate fatigue crack growth resistance allows a part to continue to perform its function for a lifetime of load cycles. Compromises among toughness, strength, and fatigue resistance are required because no one material is best in all properties and because economy in material costs is necessary.

Previous papers[1-3] have described our earlier apparatus and techniques for obtaining mechanical property data at low temperatures. In this paper improved measurement techniques for toughness, strength, and fatigue resistance are described. Some brief remarks on the use of the data are also included.

MEASUREMENT TECHNIQUES

Fracture Toughness

Fracture toughness is the measure of a cracked material's resistance to tearing and fracture. The most direct measurements

of this property are considered to be the fracture mechanics toughness tests in which K_{Ic}, the critical stress intensity factor for mode I fracture, or J_{Ic}, the critical J-contour integral for mode I fracture, are measured. The stress intensity factor is better-established theoretically and in practice, but it is only applicable to very large specimens or low-toughness material. The J-integral is additionally applicable to relatively small specimens of high-toughness material. The J-R (resistance) curve concept allows characterization of a material by its crack propagation resistance over a range of crack extensions instead of only at the initiation of tearing.

All of these techniques employ a specimen with a fatigue-sharpened crack; the specimen is extended to failure in the low-temperature environment of interest while load and displacement values are continuously measured. Quasistatic loading is used routinely. The loading may be monotonic and continuous or it may be interrupted by periodic partial unloadings. The load and displacement values are analyzed according to various standard procedures to obtain K_{Ic}, J_{Ic}, or a J-R curve.

To date, compact specimens 25 x 61 x 64 mm have been routinely used, primarily because they offer a high toughness measurement capability for their size. But 3-pt bend specimens (25 x 25 x 114 mm) are now being developed for J-integral tests at 4 K. The bend specimen is less expensive to machine.

Apparatus to cool the fracture toughness specimen to 4 K, extend it to failure in a controlled fashion, and sense and record load and displacement throughout the test are required. The apparatus at NBS/Boulder is based on a commercially-supplied servohydraulic testing device capable of extending a specimen under load or displacement control with loads up to 100 kN and displacements of up to 10 cm. The hydraulic actuator which supplies the load is mounted vertically at the top of the device. Tensile loads are transmitted through a load cell at room temperature, along a pull rod to the upper clevis grip (Fig. 1). The specimen is pinned to the upper and lower clevis grips (Fig. 2). The lower clevis grip is attached to a compressive load frame which transmits the reactive load back up to the actuator mount. This re-entrant scheme allows the use of conventional dewars without low temperature force feedthroughs.

Load is sensed by a conventional commercially-supplied load cell in the room-temperature environment. Displacement is sensed by a clip gage which is mounted on knife-edges spot-welded onto the specimen at the load line and retained by the spring action of the gage beams. These gages are either fabricated in-house or custom-built by a local supplier. The electrical signals from

Fig. 1 Low temperature fracture toughness testing apparatus in use at NBS/Boulder.

the load and displacement gages are conditioned using the conventional circuitry built into the commercially supplied mechanical testing system.

An earlier paper[1] described an elaborate 2 h cool down procedure, involving installation of copper baffles around the load frame members, sealing the cryostat lid, and vacuum pumping of the liquid nitrogen precoolant to reduce its temperature below 76 K. However we usually prefer the following alternative procedure, which eliminates the baffles and the time consuming steps involving mechanical pumping. After precooling the cryostat to 76 K, the dewar of liquid nitrogen is removed, emptied, and replaced in 30 s. Helium transfer then begins. The use of an outer dewar of liquid nitrogen (double-dewar arrangement) is also dispensable, especially when the test will be of short duration. This procedure reduces the time to accomplish cool-down to about 40 minutes, at the cost of several additional liters of liquid helium.

Several improvements have been made to the instrumentation. Instead of the carbon resistor liquid level indicator previously used[1], we now have a 30 cm continuous liquid level monitor which attaches to one of the cryostat load frame columns. This meter

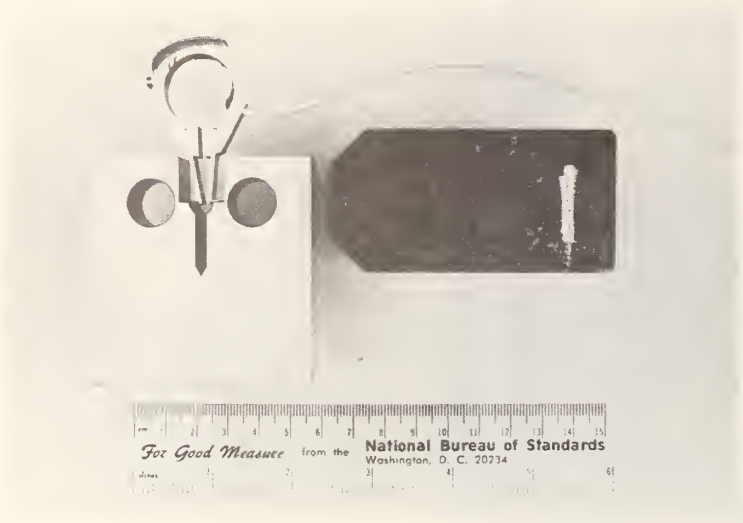

Fig. 2 Fracture toughness test specimen, clevis grip, and clip gage.

gives a continuous read out of the helium level in the cryostat and its relation to the specimen, rather than a simple on/off indication. Flexible transfer lines with vacuum jackets have replaced the former rigid transfer lines.

We have also replaced the previous fiberglass-reinforced plastic dewars with stainless steel dewars. The fiberglass dewars are more thermally efficient[1], but leaks that were very difficult to repair developed after 1 or 2 years of service. The stainless steel dewars offer fewer maintenance problems. Glass dewars were used briefly, but these are fragile and eventually get broken.

We have found that most of our apparatus problems in toughness testing occur because of a malfunctioning clip gage. The gage must be able to survive many thermal cycles between room and liquid helium temperature, with attendant moisture and freeze-up problems, while maintaining its linearity and accuracy. The ring design clip gage (Fig. 2) is a departure from the double-cantilever beam style displacement gages recommended in the ASTM E 399-74 Method. The new design consists of an aluminum alloy (7075-T651) ring which is slotted to accept short beams fabricated from 17-7 PH stainless steel. The rear of the ring is reduced in thickness and provides the bending member onto which four electrical resistance strain gages chosen for good low temperature performance are mounted. The linear operating range is from 2.5 to 7 mm of opening displacement (higher operating ranges are possible). Sensitivity is greater and linearity is improved, as

compared to double-cantilever designs of the ASTM E 399-74 type. Conventional laboratory-quality signal conditioning circuitry is adequate to read out the displacement signal if it contains no excessive electrical noise. Noise can come from inadequate solder joints, a conductive film of debris on the gage surface, or other sources. Well constructed gages can survive millions of fatigue cycles and tens of tests at 4 K. The mechanical apparatus shown in Figs. 1 and 2 has endured hundreds of fracture toughness tests.

A recent addition to the NBS/Boulder test apparatus is a minicomputer system for data acquisition, storage, and real-time analysis. The details of this system are described elsewhere[3]. The signals are applied to the input of a high-resolution analog-to-digital converter, from which their values are transmitted to a minicomputer. In the computer, load-displacement data are stored on floppy disk. To conduct a single-specimen J-integral test, periodic unloadings are performed under manual control to obtain the instantaneous crack length by the compliance technique. This involves execution of a sub-program for extracting the specimen compliance from load and displacement data. The J-integral is also calculated from load and displacement data. The computer plots each crack length J-integral data point as soon as it is acquired. This provides the operator with guidance for taking the next data point. The loading is under control of the operator through the machine console; only the data acquisition is done by computer. This apparatus and cooldown procedure allow up to four low-temperature toughness tests to be conducted in an 8 h day by the undergraduate and graduate students who conduct our tests.

The single-specimen unloading compliance technique enables J_{Ic} to be measured with good accuracy, but gives an erroneous measurement of tearing modulus, that is, dJ/da, because of errors in the crack extension, Δa. The discrepancy between actual and compliance-measured Δa increases progressively with Δa. Since this error is less at low Δa values, the J_{Ic} measurement from the single-specimen technique is reasonably accurate (within 5% of the value measured when the multiple specimen method) but the slope of the resistance curve is inaccurate. Comparison of results from both methods for AISI 310S at 4 K are shown in Fig. 3.

Measurement uncertainties in individual J values are considered to be 5% or less, while the bias due to systematic error in the inferred Δa values contributes an uncertainty of 10% or less to the J_{Ic} measurement. The cumulative uncertainty in J_{Ic} values is estimated to be ±15% or less, so the measurement uncertainty in K_{Ic} values inferred is 8% or less, since K_{Ic} is

proportional to $\sqrt{J_{Ic}}$. If errors in fracture toughness associated with material variability are large, the accuracy of J_{Ic} results will be further limited.

Strength

In this era of computerized fracture toughness testing the most familiar mechanical property, strength, must not be neglected. Tensile testing provides the material yield strength, ultimate strength, elongation to failure, and reduction of area. Elastic constants are measured to within ±2% at NBS/Boulder by sound-propagation techniques using separate specimens and apparatus[4].

Again, apparatus to cool tensile specimens to 4 K, extend the specimen to failure in a controlled fashion, and sense and record load and displacement is used. Screw-driven, mechanically controlled devices are in use at NBS/Boulder for tensile testing (Fig. 4). These machines are more economical in initial cost and laboratory space than the hydraulic testing machines, and tensile testing does not require rapid testing machine response. Load is

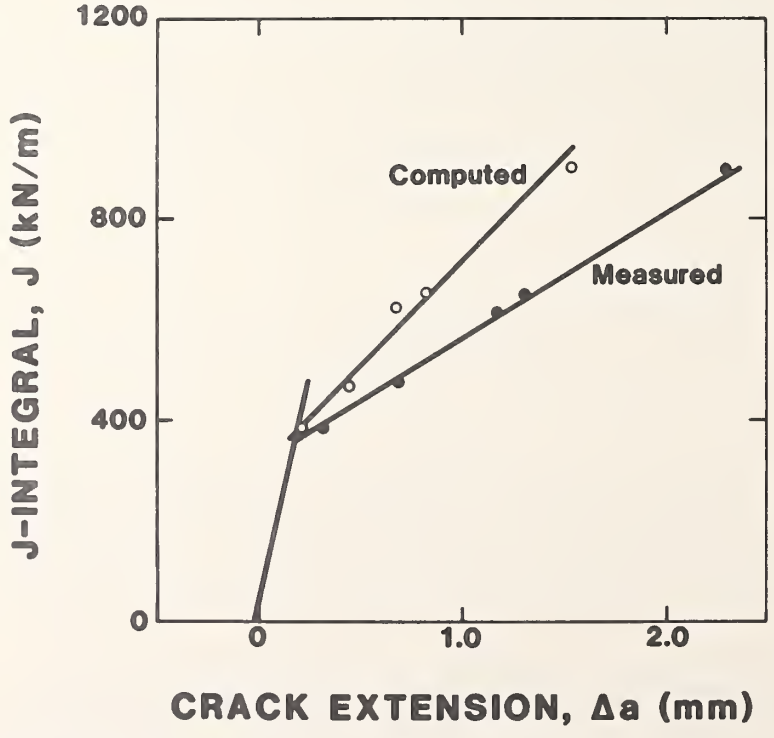

Fig. 3 Graph of J-integral versus crack extension for AISI 310S at 4 K. Crack extension values obtained from the compliance technique using one specimen (open circles) are compared with optically measured values from five specimens.

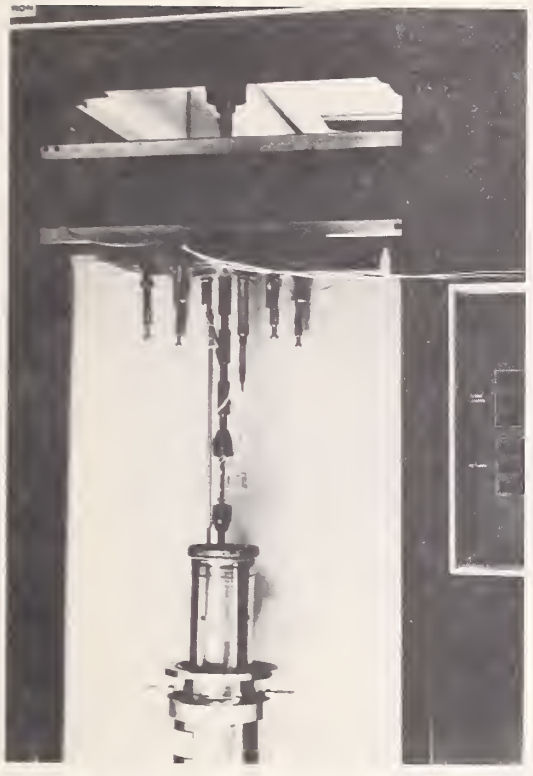

Fig. 4 Low temperature tensile testing apparatus in use at NBS/Boulder.

transmitted from the fixed upper crosshead with built-in load cell down a pull rod to the upper specimen grip. The reactive load is transmitted from the lower grip through a compression tube to the moving crosshead of the machine. Conventional glass or stainless steel dewars without force feed-throughs are used for immersion of the specimen in cryogen during the test. The extension of the specimen within its gage length is sensed by a cantilever beam gage whose two arms are attached to the specimen at the ends of the gage section (Fig. 5). The gage is clipped in between retaining pins which are fixed to the specimen. When the specimen has been extended to about 10% strain, the gage simply falls away. The gages are fabricated in-house or custom made by a local supplier. Calibrations are conducted at each test temperature using a vertically mounted dial micrometer.

The yield and ultimate strengths are calculated in the usual way from the measured load and strains. Uncertainties in tensile flow strength measurements are estimated at ±2% or less, owing to uncertainties in specimen dimensions, load values as read from recorder traces, and (for yield strength) specimen strains from the extensometer. The elongation and reduction of area are obtained conventionally from specimen dimensional differences before and after testing.

Flow stress data at temperatures intermediate between the boiling points of the common cryogens are obtained by controlled

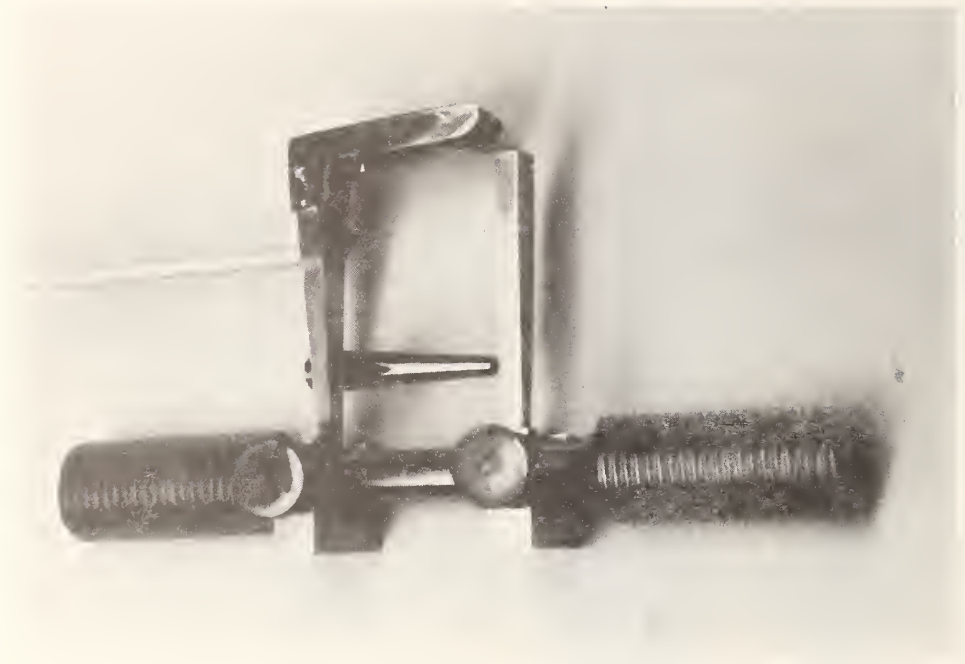

Fig. 5 Cantilever beam extension gage attached to tensile specimen.

thermal conduction using liquid helium or nitrogen reservoirs and heaters. The experimental arrangement shown in Fig. 6 has been used in several studies. The specimen is cooled by two cryogen reservoirs, one at the bottom of the push tube and the other mounted on the pull rod. The specimen is heated by electrical resistance heaters wound on each grip. The specimen temperature is sensed by two diode thermometers, one mounted at each end of the gage section. The current to the heaters is controlled so that the thermometers, and so the specimen, remain at the desired temperature (±1 K). With this apparatus temperatures from 4 to 300 K can be obtained in metal specimens. Nonmetal specimens must be surrounded by a thermal shield controlled at the desired test temperature.

In a recent series of experiments, capacitive sensing of specimen extension was used. Concentric aluminum cylinders, one mounted to each grip, form the two capacitor elements (Fig. 7). A capacitance bridge and a lock-in amplifier were used to detect specimen extension. This apparatus was needed because attachment of conventional extensometers to soft viscoelastic foams could have influenced the measured material properties. The noise level of the displacement signal was about 0.3 microns. This could be reduced by at least one order of magnitude for measurement on metals by reducing the separation between the capacitance cylinders. In this apparatus the inner capacitor

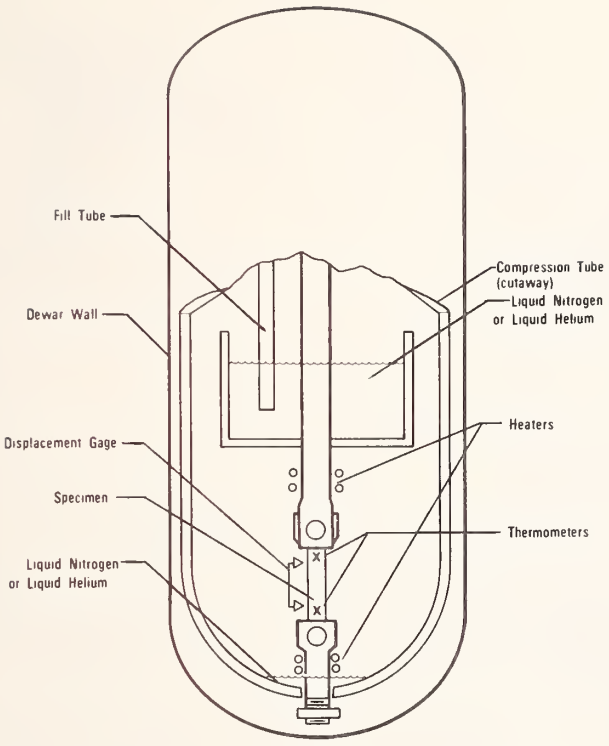

Fig. 6 Experimental arrangement for tensile testing at temperatures above cryogen boiling points.

tube also served as a thermal shield, allowing the temperature of the thermally non-conductive foam to be accurately controlled[5].

Fatigue

The fatigue lifetime of a structural component is characterized by its fatigue crack growth rate (FCGR). In our laboratory the servohydraulic apparatus described earlier is also used for fatigue tests. The specimens used are the same for K_{Ic} or J_{Ic} testing, but shorter initial crack sizes are specified.

The compliance method of FCGR measurement is the most suitable method for cryogenic testing. The technique is applicable at all temperatures, even if the specimen is enclosed in a cryostat and inaccessible. It is based on the correlation between compliance (specimen deflection per unit load) and crack length: compliance increases as crack length increases. This method offers advantages for testing thick specimens, because crack-front curvature is accounted for in the average crack length derived from the compliance value.

The procedure previously described is illustrated in Fig. 8. The specimen is loaded cyclically at a selected load range and at

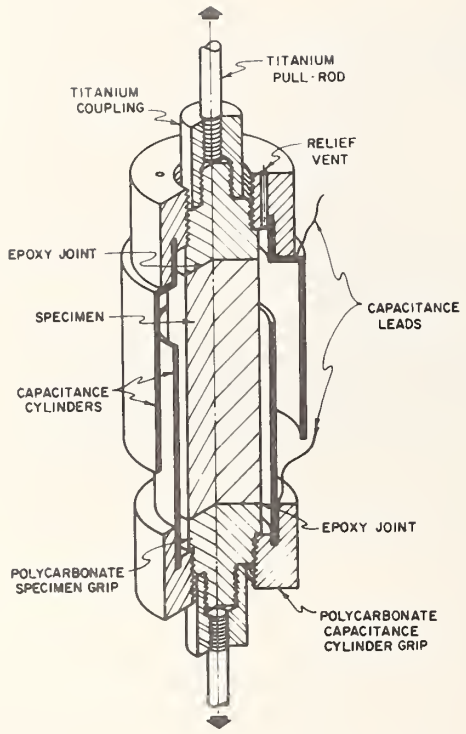

Fig. 7 Capacitance extensometer assembly for foam specimen testing.

a frequency of 20 Hz. At intervals ranging from 100 to 20,000 load cycles (N), the specimen compliance is recorded and used to obtain the instantaneous crack length. The FCGR is simply the change in crack length per cycle, which is calculated as the slope of the a-versus-N curve at a given value of a. The cycle number is easily monitored by electronic or mechanical counters.

To calibrate this method, crack front striations on specimen fracture surfaces are created by changes in the minimum fatigue load. After breaking open the calibration specimen, the values of a are measured, averaged, and plotted against their compliance values. The resultant curve is fit using the appropriate polynomial expression, which in turn is used to infer crack lengths from compliance data recorded during FCGR tests.

The FCGR data are commonly plotted against the cyclic applied stress intensity factor range (ΔK), which is calculated from load, crack length, and specimen dimensions. Uncertainties of measurement and material variability may be significant, and standard deviations of 20 to 40% from the average value of FCGR at a given ΔK value are typical for our results. The accuracy of FCGR data can be degraded if highly variable materials such as welds are tested.

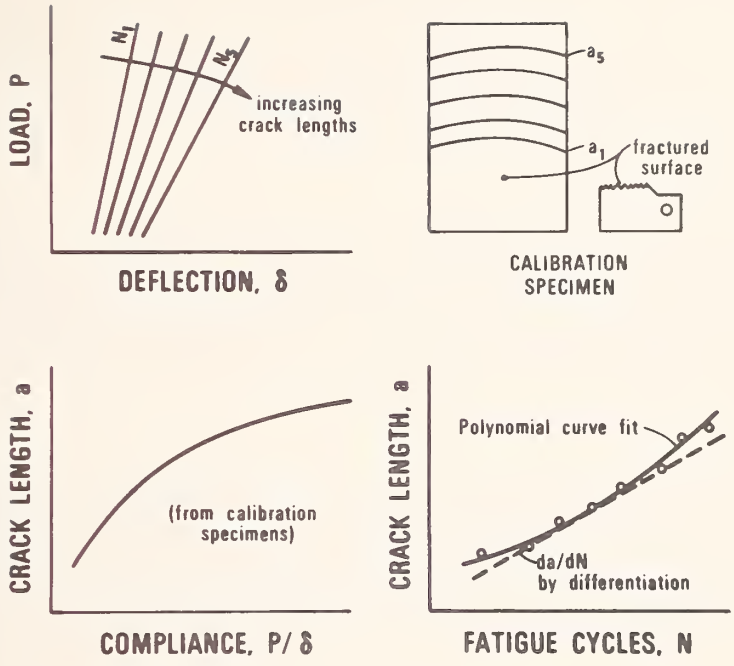

Fig. 8 Compliance method for measurement of fatigue crack growth rate da/dN using the specimen compliance.

USE OF TOUGHNESS AND STRENGTH DATA

A structure can tear and fracture because of inadequate toughness or inadequate strength. Toughness is required in large sections with cracks of large absolute size. Strength is a problem in smaller sections with cracks which may be small on an absolute scale but are large relative to the section size. An estimate of the size scale of interest for cracks can be made from a fracture mechanics formula for stress intensity. In a material whose yield strength is 850 MPa and whose toughness is 150 MPa$\sqrt{m}$, a crack of large absolute size would be one over about 1 cm in length (through crack). A large section dimension would be one greater than 10 cm. In large sections, the critical stress intensity factor can be reached before the section yields, producing failure at loads "lower than expected." The greater the material toughness, the larger the crack that can be tolerated at a given load. If the material toughness is improved and permitted cracks get larger, or if the size of the section is scaled down with crack size held constant, the section containing a crack can yield before crack extension. Once a section has reached yield, it will extend at a nearly constant load until the load is relieved or the section fails. The critical factor in such a case is the material strength. Higher strength holds off section yielding to a higher load. Higher toughness will allow

slightly more yield-load extension before fracture, but the amount is small, of the order of millimeters or less. From these considerations it is clear that inspection for large defects is necessary to insure fracture prevention in severely loaded structural members.

CONCLUSION

Techniques are described for the measurement of fracture toughness, tensile properties (including yield and ultimate strengths, elongation to failure, and reduction of area) and fatigue crack growth rates at temperatures down to 4 K. Accuracy is generally limited by specimen-to-specimen variation.

ACKNOWLEDGMENTS

J. Shepic contributed by designing and building the cryogenic clip gages. This work was supported by the U.S. Department of Energy, Office of Fusion Energy.

REFERENCES

1. R. P. Reed, "A Cryostat for Tensile Tests in the Temperature Range 300 to 4 K," in: Adv. Cryo. Eng., 7 (1961) 448-454.
2. C. W. Fowlkes and R. L. Tobler, "Fracture Testing and Results for a Ti-6Al-4V Alloy at Liquid Helium Temperature," Eng. Fract. Mechs., 8 (1976) 487-500.
3. R. L. Tobler, D. T. Read, and R. P. Reed, "Strength and Toughness Relationship for Interstitially Strengthened AISI 304 Stainless Steels at 4 K," in: Fracture Mechanics: Thirteenth Conference, ASTM STP 743, to be published.
4. H. M. Ledbetter, N. V. Frederick, and M. W. Austin, "Elastic Constant Variability in Stainless Steel 304," J. Appl. Phys., 51 (1980) 305-309.
5. J. M. Arvidson, "Capacitive Technique for High-Sensitivity Low Temperature Extension Measurement," to be published.

PREDICTED SINGLE-CRYSTAL ELASTIC CONSTANTS OF STAINLESS-STEEL 316*

H. M. Ledbetter
Fracture and Deformation Division
National Bureau of Standards
Boulder, Colorado

*Published in British Journal of Non-destructive Testing, Vol. 23, 286-7 (1981)

Predicted Single-Crystal Elastic Constants of Stainless-Steel 316—

H. M. Ledbetter, B.Sc., M.Sc., Ph.D.

For stainless-steel 316, the author gives an improved prediction of the three C_{ij} elastic-stiffness constants, which determine the optimum direction for acoustic beams used to locate and size flaws. The predictive method applies generally to all cubic-crystal-structure anisotropic materials.

1. Introduction

Since the late 1800's, single-crystal elastic-stiffness constants have provided considerable understanding of the mechanics, chemistry, and physics of crystals. These constants, the C_{ij}'s in Voigt's notation, relate to many fundamental solid-state phenomena. For example: interatomic potentials, lattice-defect energies, theoretical strength, diffusion, and Debye characteristic temperatures.

Technologists, that is, those concerned with technological materials such as steels, have largely ignored these constants. Most technological materials show macroscopic isotropy. They are completely characterised elastically by two independent elastic constants: for example, the Young modulus, E, and the Poisson ratio, ν, the two constants that arise naturally in describing a uniaxially loaded rod. Elastic constants appropriate to other loading configurations—shear, torsion, hydrostatic stress, etc.—can be computed simply from E and ν.

More recently, technologists are increasingly recognizing the value of single-crystal elastic constants for revealing anisotropy-related behaviour of engineering materials. Effects of anisotropy on ultrasonic propagation in solids were reviewed by Smith and Stephens[1].

Several authors[2–4] have emphasized the importance of the C_{ij}'s for studying welds, where elastic anisotropy enters two ways. First, as the anisotropy of individual crystallites, which can be indexed for cubic crystallites by Zener's anisotropy ratio

$$A=2C_{44}/(C_{11}-C_{12})=C_{44}/C' \tag{1}$$

Second, as a nonrandom (preferred) distribution of crystallite orientations. Called 'texture', this anisotropy arises from the welding process where heat flow and solidification do not proceed randomly.

Quite recently, Silk, Lidington, and Hammond[4] investigated theoretically the propagation of ultrasound in a model stainless-steel-316 weld, and found it necessary to estimate this alloy's C_{ij}'s, which remain unmeasured. For cubic symmetry there are three independent C_{ij}'s, usually C_{11}, C_{12}, and C_{44}. In this application the C_{ij}'s are useful in several ways: (1) as an overall anisotropy indicator—as A approaches unity, anisotropy effects disappear; (2) for determining the deviation of the directions of wave propagation and energy flux; (3) to determine the optimum acoustic-beam angle for studying a weld; (4) to allow computation of velocity, slowness, and wave surfaces, which are useful for interpreting nuances of acoustic waves in anisotropic media. Kupperman and Reimann[3] give many further references that show the importance of the C_{ij}'s for ultrasonic weld studies.

The present paper gives an improved method for predicting the three stainless-steel-316 single-crystal elastic stiffnesses. Compared with the results of Silk et al., they differ by −9, 0, and +7 per cent for C_{11}, C_{12}, and C_{44}, respectively. These differences are significant for the applications described above.

The prediction method uses existing isotropic polycrystalline elastic constants and a theory due to Kröner[5] for relating the single-crystal and polycrystal elastic-stiffness tensor. The method is quite general, being applicable to other austenitic steels, to ferritic steels, and indeed to any material.

The author is with the Fracture and Deformation Division, National Bureau of Standards, Boulder, Colorado 80303, USA.

2. Theory

Especially for cubic crystal symmetry, the problem of relating the single-crystal elastic constants (C_{11}, C_{12}, C_{44}) to the quasi-isotropic polycrystalline elastic constants (B, G) has been studied extensively, both theoretically[6] and experimentally[7]. The bulk modulus, B, because it is a rotational invariant of the elastic-stiffness tensor, is always given by

$$B=(C_{11}+2C_{12})/3, \tag{2}$$

even for a highly textured material. The expression for the shear modulus, G, depends on the assumptions of the model. Considering the self-consistent problem of an anisotropic single-crystal inclusion embedded in a corresponding isotropic matrix, and assuming stress equilibrium at the interface, Kröner[5] showed that

$$G^3+\alpha G^2+\beta G+\gamma=0 \tag{3}$$

where

$$\alpha=(5C_{11}+4C_{12})/8 \tag{4}$$

$$\beta=-C_{44}(7C_{11}-4C_{12})/8 \tag{5}$$

and

$$\gamma=-C_{44}(C_{11}-C_{12})(C_{11}+2C_{12})/8. \tag{6}$$

In the forward case, these relationships permit the calculation of B and G from the C_{ij}'s, the isotropic from the anisotropic, two elastic constants from three.

With one additional piece of information, from either theory or observation, from some single relationship among the C_{ij}'s, the reverse-case can be computed also. The C_{ij}'s can be computed from B and G.

3. The Present Case: Stainless Steel 316

For a relationship among the C_{ij}'s of stainless steel 316, we consider the existing C_{ij} measurements on f.c.c. Fe-Cr-Ni alloys summarized in Table 1. At least two approximate relationships emerge. First, the elastic anisotropy is relatively constant, being 3.51 ± 0.19. Second, the $y=C_{12}/C_{11}$ ratio is relatively constant, being 0.642 ± 0.037. Ledbetter[11] showed that a slightly better y value results if values for f.c.c. Fe and Ni are also included with these four alloys, the value being $y=0.635\pm0.031$. Table 1 probably contains other C_{ij} relationships. But these two are simple and sufficient.

For B and G values, we use those reported by Ledbetter:[12] $B=1.575\pm0.014$ and $G=0.752\pm0.015.10^{11}$ N/m^2.

4. Results

Table I contains the results of two calculations of the C_{ij}'s of stainless steel 316. Both calculations involve eqs. (2) and (3). The first assumes $y=0.635$; the second assumes $A=3.51$. The bottom line of Table I averages the two calculations.

5. Discussion

The present theoretical C_{ij} results in Table I seem quite satisfactory on several counts: both cases agree exactly with observed B and G values; both give reasonable A values; both C_{11} and C_{12} agree within one per cent; C_{44} agrees within five per cent.

Why A remains relatively constant among these alloys remains unexplained. For f.c.c. crystals, in a central-force model, nearest-neighbour-only interactions require that $A=2$. Deviations from this indicate significant noncentral forces between (or among) atoms. Excluding as somehow anomalous those f.c.c. elements where $A<2$ (Al=1.22, Ir=1.56, Pt=1.59), we find that the average A for f.c.c. elements is 3.17 ± 0.52 (Ni=2.66, Pd=2.81, Au=2.85, Ag=2.88, Cu=3.27, Th=3.62, Pb=4.07). Thus, Fe-Cr-Ni alloys have typical A values. High A values indicate a high vibrational entropy and a tendency toward mechanical instability[13].

Similarly, the relative constancy of $y=C_{12}/C_{11}$ remains unexplained. For an f.c.c. nearest-neighbour-only central-force model, $y=0.50$. Ledbetter[11] showed that volume-dependent energy terms tend to increase y above this value.

In summary, this study focuses on a theoretical method for predicting the single-crystal elastic constants, the C_{ij}'s, of cubic materials. The method requires two polycrystalline elastic constants and a C_{ij} interrelationship determined either from observation or from theory. We believe the stainless-steel-316 C_{ij}'s predicted in this study are the best values now available. These elastic constants are useful for many purposes, including the ultrasonic nondestructive evaluation of welds. Future studies by the author will use these results to predict the effects of texture on elastic-wave propagation through welds.

References

1. Smith, R. T. and Stephens, R. W. B. Effects of anisotropy on ultrasonic propagation in solids. Progress in Applied Materials Science, Volume 4. National Trade Press, London, 1964, pp. 4–64.
2. Dewey, B. R., Adler, L., King, R. T. and Cook, K. V. 1977. Measurements of anisotropic elastic constants of type 308 stainless-steel electroslag welds. Exper. Mech. *17*, 420–426.
3. Kupperman, D. S. and Reimann, K. J. 1980. Ultrasonic wave propagation and anisotropy in austenitic stainless steel weld metal. IEEE Trans. Sonics Ultrason. *SU-27*, 7–15.
4. Silk, M. G., Lidington, B. H. and Hammond, G. F. 1980. A time domain approach to crack location and sizing in austenitic welds. Brit. J. NDT *22*, 55–61.
5. Kröner, E. 1958. Berechnung der elastischen Konstanten des Vielkristalls aus den Konstanten des Einkristalls. Z. Phys. *151*, 504–518.
6. Ledbetter, H. M. and Naimon, E. R. 1974. Relationship between single-crystal and polycrystal elastic constants. J. Appl. Phys. *45*, 66–69.
7. Ledbetter, H. M. 1980. Sound velocities and elastic-constant averaging for polycrystalline copper. J. Phys. D: Appl. Phys. *13*, 1879–1884.
8. Salmutter, K. and Stangler, F. 1960. Elastizität u. Plastizität eines austenitischen Chrom-Nickel-Stahls. Z. Metallkde. *51*, 1–4.
9. Kikuchi, M. 1971. Elastic anisotropy and its temperature dependence of single crystals and polycrystal of 18–12 type stainless steel. Japan. Inst. Met. *12*, 417–421.
10. Mangalick, M. C. and Fiore, N. F. 1968. Orientation dependence of dislocation damping and elastic constants in Fe-18Cr-Ni single crystals. Trans. Met. Soc. AIME *242*, 2363–2364.
11. Ledbetter, H. M. 1981. Predicted single-crystal elastic constants of stainless steel 304. To be published.
12. Ledbetter, H. M. 1980. Sound velocities and elastic constants of steels 304, 310, and 316. Metal Sci. J., forthcoming.
13. Zener, C. Elasticity and Anelasticity of Metals. Univ. Chicago Press, Chicago, 1948, p. 37.

Acknowledgement

Major support for this study came from the DoE Office of Fusion Energy and the NBS Office of Nondestructive Evaluation. Dr. C. M. Fortunko of NBS pointed out this application of the C_{ij}'s together with several valuable references.

TABLE I

Single-crystal elastic constants of several face-centred-cubic Fe-Cr-Ni alloys in units of 10^{11} N/m^2, except A and y, which are dimensionless

Alloy	C_{11}	C_{12}	C_{44}	B	C'	A	y	*Ref.*
Experiment								
Fe-12Cr-18Ni	2.332	1.626	1.225	1.862	0.353	3.45	0.697	8
Fe-18Cr-12Ni	1.912	1.179	1.386	1.423	0.367	3.78	0.617	9
Fe-18Cr-14Ni	1.98	1.25	1.22	1.49	0.365	3.34	0.631	10
Fe-18Cr-19Ni	1.91	1.19	1.24	1.43	0.360	3.44	0.623	10
Theory								
Stainless 316	2.261	1.336	1.114	1.644	0.463	2.41	0.591	4*
Stainless 316	2.08	1.32	1.16	1.575	0.380	3.06	0.635	Present-1
Stainless 316	2.04	1.34	1.22	1.575	0.348	3.51	0.659	Present-2
Stainless 316	2.06	1.33	1.19	1.575	0.365	3.27	0.647	Present-average

*Corrected to a mass density of 7.958 g/cm^3.

Manganese contributions to the elastic constants of face-centered-cubic Fe-Cr-Ni stainless steels

H. M. Ledbetter
Fracture and Deformation Division
National Bureau of standards
Boulder, Colorado 80303
USA

Abstract

We determined experimentally the effect of manganese on the elastic constants of Fe-Cr-Ni alloys. By a pulse-echo-overlap method, longitudinal and transverse sound-wave velocities were determined in ten alloys containing up to six percent Mn. All the elastic stiffnesses decrease linearly with increasing Mn. The bulk modulus decreases most strongly. Poisson's ratio changes least. We consider what the elastic constants reveal concerning changes in chemical bonding.

Key Words: Bulk modulus; chromium alloys; elastic constants; iron alloys; mechanical properties; nickel alloys; physical properties; Poisson ratio; shear modulus; sound velocities; stainless steel; Young modulus.

Introduction

Manganese decreases the elastic stiffness of bcc Fe.[1] Studies of alloys containing up to ten atomic percent Mn show a linear decrease in both Young's modulus, E, and the shear modulus, G. The decrease amounts to approximately 0.3 percent per atomic percent Mn. Vegard's law predicts a 0.06 percent decrease for G and a 0.65 percent decrease for the bulk modulus, B.

Effects of Mn on the elastic stiffness of fcc Fe remain unknown. Manganese's peculiar elemental properties--a 58-atom unit cell, a bulk modulus 0.35 that of Fe's, antiferromagnetic electronic interactions, negative low-temperature thermal expansivity--preclude any reliable predictions of such effects. Despite the proximity of Mn and Fe in the first long row of the periodic table of elements, their properties differ dramatically; Mn dissolved in Fe may behave very differently from Mn dissolved in Mn. From available elastic constants of fcc Ni and Mn, Vegard's law predicts that Mn lowers all the elastic stiffnesses and Poisson's ratio, ν: B by 0.33 percent, E by 0.18 percent, G by 0.18 percent, and ν by 0.16 percent. Here, we assume that the unknown elastic constants of fcc Fe do not differ significantly from those of fcc Ni; because Fe's atomic volume exceeds Ni's by eight percent, fcc Fe may be slightly softer elastically.

Face-centered-cubic Fe-Cr-Ni alloys provide the basis for commercial stainless steels. Manganese also occurs in such steels, mainly to improve fabricability and weldability.

Effects of Mn on the elastic properties of Fe-Cr-Ni alloys remain undetermined. Such knowledge of basic mechanical-physical properties underlies any modeling of macroscopic mechanical properties such as strength and toughness.

The present study sought to determine how Mn affects the polycrystalline elastic constants of Fe-Cr-Ni alloys containing up to six percent Mn. Such results would test the conjecture[2] that these alloys should "show large changes in their elastic moduli as functions of composition." Complete sets of polycrystalline elastic constants were determined: Young's modulus, shear modulus, bulk modulus, and Poisson's ratio. The experimental approach consisted of measuring longitudinal and transverse sound velocities using a pulse-echo-overlap method.

One may ask also whether Mn affects chemical bonding in Fe-Cr-Ni alloys. As described above, Mn is truly a maverick metallic element. In considering chemical bonding in both nonmetals and metals, Pauling[3] referred to "the anomalous Mn radius" and to Mn's "striking abnormality in behavior." We know that elastic stiffness depends relatively sensitively on atomic radius, r, varying as r^{-4}. Thus, Mn's larger atomic volume arising from magnetic repulsions explains in part its lower elastic stiffness.

Experiment

Materials

All alloys are Mn-modified type-304LN face-centered-cubic stainless steels. Custom-composition alloys were obtained from a commercial steel company in the form of plates approximately 2.5 cm by 14 cm by 41 cm.

Each plate was hot rolled at approximately 1175°C (2150°F), annealed for 0.5 h at 1065°C (1950°F), water quenched, and acid pickled. Table 1 shows chemical composition, hardness, mass density, and grain size. Grain size was measured in the plane perpendicular to the transverse-plate direction.

Methods

Sound velocities were determined by a method described in detail previously.[4] Briefly, 1.5-cm cubes were prepared by grinding so that opposite faces were flat and parallel within 5 μm. Quartz piezoelectric crystals with fundamental resonances between 4 and 7 MHz were cemented with phenyl salicylate to the specimens. An x-cut transducer was used for longitudinal waves and an ac-cut for transverse waves. Ultrasonic pulses 1 to 2 cycles long were launched into the specimen by electrically exciting the transducer. The pulses propagated through the specimen, reflected from the opposite face, and propagated back and forth. The pulse echoes were detected by the transducer and displayed on an oscilloscope equipped with a time delay and a microprocessor for time-interval measurements. The sound velocity was computed by

$$v = 2\ell/t \qquad (1)$$

where ℓ denotes specimen length, and t the round-trip transit time. On the oscilloscope, t was the time between adjacent echoes, the first and second echoes usually being measured, and within these the time between leading cycles. Elastic constants were computed from the general relationship

$$C = \rho v^2 \qquad (2)$$

where ρ denotes mass density. The usual engineering elastic constants are related to the longitudinal and transverse sound velocities, v_ℓ and v_t, by

$$\text{longitudinal modulus} = C_\ell = \rho v_\ell^2 \tag{3}$$

$$\text{shear modulus} = G = \rho v_t^2 \tag{4}$$

$$\text{bulk modulus} = B = C_\ell - (4/3)G \tag{5}$$

$$\text{Young's modulus} = E = 3GB/(C_\ell - G) \tag{6}$$

$$\text{Poisson's ratio} = \nu = (E/2G) - 1 \tag{7}$$

$$= (1/2)(C_\ell - 2G)/(C_\ell - G)$$

Results

Table 2 gives for two alloys the variation of sound velocites and elastic constants with direction. In this table, n denotes propagation direction and p denotes polarization direction. Table 3 contains the principal results of the study: for ten alloys the longitudinal and transverse sound velocities, v_ℓ and v_t, and the various elastic constants C_ℓ, G, B, E, ν defined in Eqs. (3)-(7). Figure 1 shows these constants versus Mn concentration. Table 4 contains the results of linear least-squares fits to these compositional changes. In this table, a and b have units of the elastic constants. The dimensionless ratio a/b gives the quantity $(1/y)(dy/dx)$ at $x = o$, the fractional change in the elastic constant due to alloying. Also included in Table 4 are predicted values of b/a based on Vegard's law and handbook elastic constants for Ni and Mn. (Elastic constants of fcc Fe are not available.)

Discussion

First, we consider the possibility of texture. Results in Table 2 indicate the absence of texture in these alloys. For alloy 10, for example, in three orthogonal directions (corresponding to the rolling direction, transverse direction, and through-thickness direction) the longitudinal modulus varies less than 0.1 percent and the shear modulus less than 0.4 percent. These results agree with those reported previously for 304 stainless steel. In these alloys the Zener anisotropy ratio $A = 2C_{44}/(C_{11} - C_{12})$ is approximately 3.5[5], that is, moderately high. Thus, significant texture would evidence itself in the elastic constants. Recent calculations by Ledbetter[6] concerning the elastic constants of textured aggregates show that for 304 stainless steel along principal axes, fiber textures such as <100>, <110>, and <111> change C_ℓ an average of 11 percent and G an average of 19 percent. These elastic constants can be measured readily within a fraction of a percent. We ascribe the lack of texture to the thermomechanical treatment: annealing after hot deformation.

We consider now what the elastic constants reveal concerning changes in the chemical bond when Mn is alloyed substitutionally into the fcc Fe-Cr-Ni matrix. Essentially, we look for changes in the degree of covalent bonding, which manifests itself as a resistance to bond bending, a manifestation of many-body forces. Köster and Franz[7] concluded that "Poisson's ratio depends to a much greater extent on the conditions of bonding than do the other elastic coefficients." This assertion remains without theoretical basis, probably because theory does not predict directly the Poisson ratio, which is the negative ratio of two fourth-rank elastic compliances, $-S'_{iijj}/S'_{iiii}$, where primes denote rotation of the coordinate system.

For quasi-isotropic solids, Poisson's ratio is a scalar that relates simply to the bulk and shear moduli:

$$\nu = (1/2)(3B-2G)/(3B+G) = (1/2)(3y-2)/(3y+1) \qquad (8)$$

where y is defined to be B/G. Thus, the dependence of ν can be studied parametrically as the dependence of y. For cubic elements, Leibfried and Breuer[8] give a graph of B/C_{44} versus elastic anisotropy, C_{44} being one of the usual two cubic-crystal elastic shear moduli. They point out that purely longitudinal first-neighbor spring interactions require that $B/C_{44} = 4/3$. For Voigt averaging, the equivalent ratio for polycrystals is B/G = 5/3; for Reuss averaging it is 28/15; thus, the Hill arithmetic average is B/G = 280/159 = 1.76. Departure from this ratio indicates that many-body forces occur in the solid. In terms of a force-constant model, this means that bond-bending forces must occur along with more familiar bond-stretching (bond-compressing) forces. One should note that from Eq.(8) it follows that B/G is a more sensitive parameter than ν because for typical ν values $d\nu/\nu \cong (1/2)\, dy/y$.

Examination of Table 3 shows that B/G = 2.005 ± 0.014 for all ten alloys. Thus, the marked departure from a value of 1.76 shows that many-body forces occur in these alloys. That many-body forces exist in transition-metal alloys is already well known.[9] The surprising result is that the ratio is nearly constant for all alloys, indicating no significant change in the character of the chemical bonding. Table 3 shows that the Poisson's ratio is also nearly invariant with Mn content: ν = 0.286 ± 0.001, but also different from the ν = 0.261 predicted for longitudinal-force-constant-only bonding. As described above, B/G and ν must behave similarly.

In terms of the single-crystal cubic-symmetry elastic constants C_{11}, C_{12}, and C_{44}, this means that C_{12}/C_{11} must be nearly constant. This follows because the usual crystal-axis Poisson's ratio is

$$\nu = -\frac{S_{12}}{S_{11}} = \frac{C_{12}}{C_{11}+C_{12}} = \frac{y}{1+y} \qquad (9)$$

where $y = C_{12}/C_{11}$.

Conclusions

1. Alloying Mn into a stainless-steel-304-type Fe-Cr-Ni alloy decreases all the elastic stiffness constants and also decreases Poisson's ratio.

2. The bulk modulus decreases most, reflecting the high compressibility of Mn atoms.

3. Poisson's ratio and the B/G ratio both vary slowly with Mn concentration. This indicates that Mn does not change the nature of the chemical bonding. Manganese's unusual bonding characteristics lead one to expect possible changes.

4. By factoring into force constants, the relationship of many-body forces to elastic constants and bonding becomes more clear.

Acknowledgment

This study was supported in part by the DoE Office of Fusion Energy.

Appendix: Force-constant approach

One always profits from considering elastic constants in terms of force constants, which relate more directly to forces between pairs of atoms in solids. Many force-constant models exist[10]. For fcc lattices, Leibfried and Breuer[11] consider a three-force-constant model summarized in Fig. A1. The three parameters consist of a longitudinal spring, f_1, and two different transverse springs, f_2 and f_3, corresponding to bending along [001] and [110], respectively. The coupling matrix for this model is

$$-\phi_{ij}^{[110]} = \begin{matrix} \alpha & \beta & 0 \\ \beta & \alpha & 0 \\ 0 & 0 & \gamma \end{matrix} \qquad \text{(A1)}$$

Physically, $\phi_{i\ell}^{[\underset{\sim}{d}]}$ denotes the force in the i direction on the atom at the origin when the atom at $\underset{\sim}{d}$ is displaced a unit length in direction ℓ. If the displacement vector corresponds to an eigenvector, then $-\phi_{i\ell}^{[\underset{\sim}{d}]}$ corresponds to a spring constant. By symmetry $\phi_{11}^{[110]} = \phi_{22}^{[110]}$ and $\phi_{12}^{[110]} = \phi_{21}^{[110]} = \phi_{23}^{[110]} = \phi_{32}^{[110]}$. Components such as $\phi_{13}^{[110]}$ vanish because force and displacement are perpendicular, thus no coupling. Diagonalization of ϕ_{ij} gives three eigenvalues:

$$f_1 = \alpha + \beta \qquad \text{(A2)}$$

$$f_2 = \gamma \qquad \text{(A3)}$$

$$f_3 = \alpha - \beta \qquad \text{(A4)}$$

Leibfried and Breuer relate the f's to the six eigenvalues of the 6x6 Voigt C_{ij} matrix:

$$f_1 = \frac{a}{24}\left(4\overset{1}{C} + 2\overset{2}{C} + 3\overset{4}{C}\right) \qquad \text{(A5)}$$

$$f_2 = \frac{a}{12}\left(-\overset{1}{C} - 2\overset{2}{C} + 3\overset{4}{C}\right) \qquad \text{(A6)}$$

$$f_3 = \frac{a}{8}\left(2\overset{2}{C} - \overset{4}{C}\right) \qquad \text{(A7)}$$

where a denotes cubic unit-cell size.

From the cubic-symmetry invariants,

$$\overset{1}{C} = C_{11} + 2C_{12} \tag{A8}$$

$$\overset{2}{C} = \overset{3}{C} = C_{11}-C_{12} \tag{A9}$$

$$\overset{4}{C} = \overset{5}{C} = \overset{6}{C} = 2C_{44} \tag{A10}$$

the f's relate to the Voigt C_{ij}'s:

$$f_1 = \frac{a}{4}(C_{11} + C_{12} + C_{44}) \tag{A11}$$

$$f_2 = \frac{a}{4}(-C_{11} + 2C_{44}) \tag{A12}$$

$$f_3 = \frac{a}{4}(C_{11} - C_{12} - C_{44}) \tag{A13}$$

and vice versa:

$$C_{11} = \frac{1}{a}(2f_1 + 2f_3) \tag{A14}$$

$$C_{12} = \frac{1}{a}(f_1 - 2f_2 - 3f_3) \tag{A15}$$

$$C_{44} = \frac{1}{a}(f_1 + 2f_2 + f_3) \tag{A16}$$

More-interesting physical C_{ij} combinations are:

$$(C_{11}-C_{12}) = \frac{1}{a}(f_1 + 2f_2 + 5f_3) \tag{A17}$$

$$(C_{11}+C_{12}) = \frac{1}{a}(4f_1 - 4f_2 - 4f_3) \tag{A18}$$

$$(C_{12}-C_{44}) = \frac{1}{a}(-4f_2 - 4f_3) \tag{A19}$$

$$A=2C_{44}/(C_{11}-C_{12}) = (2f_1+4f_2+2f_3)/(f_1+2f_2+5f_3) \tag{A20}$$

$$(C_{11}-C_{12}-2C_{44})=\frac{1}{a}(-f_1-2f_2+3f_3) \tag{A21}$$

$C_{11}-C_{12}$ is the resistance to shear on a [110]-type plane in a [$\bar{1}$10]-type direction. Since this deformation involves both bond stretching (and shortening) and bond bending, not surprisingly it includes f_1, f_2, and f_3. $C_{11}+2C_{12}$ is three times the bulk modulus (reciprocal compressibility). Since uniform dilatation changes bond lengths but not bond angles, it may seem surprising that B depends on f_2 and f_3 in addition to f_1. This occurs because the spring constants f_2 and f_3 relate also to many-body forces. (Recall that the third-order perturbation-theory calculation of Axilrod and Teller[12] for interactions

between triplets of atoms contained three interatomic distances--r_{12}, r_{23}, r_{13}--and three included angles--γ_1, γ_2, γ_3--with γ being the angle between r_{12} and r_{13}). C_{12}-C_{44} is the Cauchy (noncentral-force) discrepancy for cubic crystals. Thus, if accidently f_2=-f_3, then the material will appear to have central forces by the familiar Cauchy criterion $C_{12} = C_{44}$. Thus, this criterion is necessary but not sufficient. The Zener anisotropy ratio, A, depends on all three force constants. For vanishing many-body forces, A = 2. Thus, departures of A from this value also indicate the contribution of many-body forces. In summary, vanishing many-body forces imply that $C_{11} = 2C_{12} = 2C_{44} = 4C'$, where $C' = \frac{1}{2}(C_{11}-C_{12})$. Finally, elastic isotropy demands that $C' = C_{44}$ or that $C_{11} - C_{12} - 2C_{44} = 0$. In terms of force constants, isotropy demands that $f_1 = 3f_3 - 2f_2$, a condition that arises only accidently.

We now consider the polycrystalline case, which has two independent elastic constants. Following Stokes[13], we choose to consider B and G, the elastic constants that represent the two extreme types of deformation--pure dilatation (volume change without shape change) and pure shear (shape change without volume change). For aggregates of cubic crystallites, because the bulk modulus is a rotational invariant, it is

$$B = (C_{11}+2C_{12})/3 \qquad \text{(A22)}$$

For the shear modulus, no unique averaging method exists. Many methods using different physical principles have been proposed[14]. A method due to Hershey,[15] Kroner,[16] and Eshelby[17] is used increasingly. For copper, Ledbetter[18] verified that this method agrees best with observation.

For simplicity, we use Voigt's averaging method here. Voigt[19] showed that when the aggregate has uniform elastic strain the shear modulus of cubic aggregates is

$$G_V = (C_{11}-C_{12}+3C_{44})/5 \qquad \text{(A23)}$$

In terms of force constants:

$$G_V = \frac{4}{5a}(f_1+2f_2+2f_3) \qquad \text{(A24)}$$

The Reuss[20] shear modulus, based on constant stress in the aggregate, is

$$G_R = \frac{5}{2} C_{44}(C_{11}-C_{12})/[\tfrac{3}{2}(C_{11}-C_{12})+2C_{44}] \qquad \text{(A25)}$$

and must also depend on all three force constants.

Consider now a typical metal--copper, where C_{11}=1.696, C_{12}=1.224, and C_{44}=0.754·10^{11}N/m^2. Thus, f_1/a=0.9185, f_2/a=-0.0470, and f_3/a=-0.0705 in the same units. Table A1 shows how the three force constants contribute to various elastic constants and to the elastic anisotropy, A. For both A and C_{12}/C_{11}, we made the very rough approximation that both f_2 and f_3 are small compared with f_1. Except for the Cauchy discrepancy, C_{12}-C_{44}, f_1 dominates every elastic constant. As expected, many-body effects show most strongly in C_{12}-C_{44}, but also strongly in C', A, and C_{12}/C_{11}. The bulk modulus is least sensitive to many-body terms. In all cases except C_{44} the f_2 force constant contributes less than the f_3 force constant; bending out of the (100) plane contributes less than bending in the plane. Negative f_2 and f_3 values apparently imply instabilities with respect to bending. But one must remember that the bending springs represent many-body, not two-body, interactions. Thus, they do not represent simple local effects but, rather, complicated "environmental", long-range effects. Even if all springs are longitudinal and positive, a negative transverse spring can arise quite naturally.

Table A1 contains results also for stainless steel. Principal differences are that f_2 and f_3 are approximately double those of copper with the sign on f_2 being reversed. This means that the stainless steel elastic anisotropy is higher (higher negative f_3). Except for Th, and Du, all fcc elements exhibit a negative f_2. Implications of a positive f_2 remain unclear. Because both Th and Pu are relatively unstable in the fcc structure, a positive f_2 may indicate a tendency toward chemical instability.

References

1. W. C. Leslie, Iron and its dilute substitutional solid solutions, Metall. Trans. 3, 5-25 (1972).

2. J. F. Janak and A. R. Williams, Giant internal magnetic pressure and compressibility anomalies, Phys. Rev. B 14, 4199-4204 (1976).

3. L. Pauling, The Nature of the Chemical Bond (Cornell U.P., Ithaca, 1960), pp. 254, 419.

4. H. M. Ledbetter, N. F. Frederick, and M. W. Austin, Elastic-constant variability in stainless-steel 304, J. Appl. Phys. 51, 305-309 (1980).

5. H. M. Ledbetter, Predicted single-crystal elastic constants of stainless-steel 304, in NBSIR 81-1645 (1981), pp. 227-236.

6. H. M. Ledbetter, Sound velocity as a texture probe: application to stainless-steel welds, intended for J. Appl. Phys.

7. W. Koster and H. Franz, Poisson's ratio for metals and alloys, Metall. Rev. 6, 1-55 (1961).

8. G. Leibfried and N. Breuer, Point Defects in Metals I (Springer-Verlag, Berlin, 1978), p. 127.

9. C. C. Matthai, P. J. Grout, and N. H. March, Force fields in d-band metals, Int. J. Quant. Chem. Symp. 12, 443-459 (1978).

10. R. A. Moore and J. C. Upadhyaya, Comparison of the major force constant models for cubic systems using a self-consistency condition, Can. J. Phys. 57, 2053-2065 (1979).

11. Reference 8, p. 42.

12. B. M. Axilrod and E. Teller, Interaction of the van der Waals type between three atoms, J. Chem. Phys. 11, 299-300 (1943).

13. G. G. Stokes (1845); reported in I. Todhunter and K. Pearson, A History of the Theory of Elasticity and of the Strength of Materials (Cambridge U. P., Cambridge, 1886).

14. H. M. Ledbetter, Estimation of Debye temperatures by averaging elastic coefficients, J. Appl. Phys. 44, 1451-1454 (1973).

15. A. V. Hershey, The elasticity of an isotropic aggregate of anisotropic cubic crystals, J. Appl. Mech. 21, 236-240 (1954).

16. E. Krŏner, Berechnung der elastischen Konstanten des Vielkristalls aus den Konstanten des Einkristalls, Z. Phys. 151, 504-518 (1958).

17. J. D. Eshelby, Elastic inclusion and inhomogeneities, in Progress in Solid Mechanics, Volume II (North-Holland, New York, 1961), pp. 87-140.

18. H. M. Ledbetter, Sound velocities and elastic-constant averaging for polycrystalline copper, J. Phys. D: Appl. Phys. 13, 1879-1884 (1980).

19. W. Voigt, Ueber die Beziehung zwischen den beiden Elasticitätsconstanten isotroper Korper, Ann. Phys. 38, 573-587 (1889).

20. A. Reuss, Berechnung der Fliessgrenze von Mischkristallen auf Grund der Plastizitätshedingung fur Einkristalle, Z. Angew. Math. Mech. 9, 49-58 (1929).

Figure Captions

Fig. 1. Compositional variation of elastic constants of Fe-Cr-Ni alloys containing Mn. Units on E, B, and G are 10^{11} N/m^2. ν is dimensionless.

Fig. 2. Face-centered-cubic unit cell showing eigenvectors and eigenvalues of the coupling matrices to the nearest-neighbor atoms at $[\frac{1}{2}\ \frac{1}{2}\ 0]$-type positions.

Table 1. Chemical composition (weight percent), hardness, grain size, and mass density.

	Mn	Cr	Ni	C	N	P	S	Si	Mo	Cu	Hardness (Rockwell B)	Grain Size (ASTM No.)	Mass density (g/cm^3)
1	1.02	18.19	8.68	0.025	0.11	0.022	0.013	0.53	0.32	0.30	82	5.4	7.925
2	1.19	19.36	7.81	0.025	0.19	0.023	0.015	0.60	0.32	0.28	88	5.5	7.873
3	2.00	18.10	8.66	0.028	0.11	0.021	0.013	0.63	0.31	0.28	88	5.5	7.884
4	2.01	19.35	7.89	0.022	0.19	0.023	0.013	0.64	0.32	0.30	94	5.5	7.862
5	3.85	18.22	8.70	0.025	0.11	0.023	0.013	0.59	0.31	0.29	84	5.8	7.878
6	3.85	19.25	7.84	0.024	0.19	0.022	0.014	0.65	0.31	0.29	90	5.6	7.850
7	4.03	18.71	8.22	0.023	0.15	0.023	0.014	0.62	0.31	0.30	89	5.6	7.862
8	5.79	19.48	7.83	0.024	0.21	0.024	0.014	0.61	0.31	0.30	90	5.6	7.827
9	5.80	18.42	8.29	0.031	0.15	0.024	0.014	0.62	0.31	0.30	90	5.6	7.855
10	5.81	18.06	8.62	0.021	0.11	0.023	0.014	0.64	0.33	0.30	84	5.4	7.881

Table 2. Directional variation of sound velocities and elastic constants

Alloy	n	p	Velocity (cm/μs)	C_ℓ (10^{11}N/m^2)	G (10^{11}N/m^2)
1	100	100	0.576	2.631	
		010	0.314		0.780
		001	0.315		0.784
	010	010	0.576	2.628	
		100	0.314		0.780
		001	0.315		0.785
	001	001	0.576	2.622	
		100	0.314		0.783
		010	0.314		0.784
10	100	100	0.572	2.579	
		010	0.314		0.778
		001	0.314		0.773
	010	010	0.572	2.580	
		100	0.313		0.771
		001	0.313		0.772
	010	001	0.572	2.576	
		100	0.314		0.778
		010	0.313		0.773

Table 3. Sound velocities and elastic constants for ten manganese-alloyed stainless-steel-304-type alloys

Alloy	Mn Pct.	v_ℓ (cm/μs)	v_t (cm/μs)	C_ℓ (10^{11}N/m^2)	G (10^{11}N/m^2)	B (10^{11}N/m^2)	E (10^{11}N/m^2)	ν	B/G
1	1.02	0.575	0.315	2.622	0.784	1.577	2.017	0.287	2.011
2	1.19	0.577	0.315	2.621	0.779	1.583	2.007	0.289	2.032
3	2.00	0.574	0.315	2.601	0.783	1.558	2.011	0.285	1.990
4	2.01	0.576	0.315	2.609	0.778	1.573	2.003	0.288	2.022
5	3.85	0.574	0.314	2.594	0.778	1.556	2.001	0.286	2.000
6	3.85	0.575	0.314	2.592	0.775	1.559	1.993	0.287	2.012
7	4.03	0.574	0.314	2.586	0.775	1.552	1.994	0.286	2.003
8	5.79	0.573	0.314	2.571	0.772	1.541	1.985	0.285	1.996
9	5.80	0.572	0.314	2.573	0.775	1.539	1.992	0.284	1.986
10	5.81	0.572	0.313	2.576	0.772	1.546	1.987	0.286	2.003

Table 4. Compositional variation of elastic constants based on $y = a + bx$ type relationship.

y	a	b	b/a	b/a (Vegard)
G	0.783	$-1.77 \cdot 10^{-3}$	$-2.26 \cdot 10^{-3}$	$-1.79 \cdot 10^{-3}$
B	1.585	$-7.43 \cdot 10^{-3}$	$-4.69 \cdot 10^{-3}$	$-3.31 \cdot 10^{-3}$
E	2.017	$-5.20 \cdot 10^{-3}$	$-2.58 \cdot 10^{-3}$	$-1.75 \cdot 10^{-3}$
ν	0.288	$-0.47 \cdot 10^{-3}$	$-1.62 \cdot 10^{-3}$	$-1.59 \cdot 10^{-3}$

Table A1. For a typical metal, copper, and for stainless steel, relative contributions of three force constants to various elastic constants.

		Copper		Stainless Steel	
	f_1	f_2	f_3	f_2	f_3
C_{11}	1.00	0.00	-0.08	0.00	-0.12
C_{12}	1.00	0.10	0.23	-0.17	0.36
C_{44}	1.00	-0.10	-0.08	0.17	-0.12
C'	1.00	-0.10	-0.38	0.17	-0.59
B	1.00	0.05	0.08	-0.09	0.12
$C_{12} - C_{44}$	0.00	-1.00	-1.00	-1.00	-1.00
$C_{11} - C_{12} - 2C_{44}$	-1.00	-0.10	0.23	0.17	0.36
A	1.00	(0.0)[a]	(0.31)	(0.00)	(0.47)
C_{12}/C_{11}	1.00	(0.10)	(0.31)	(-0.17)	(0.47)

[a]Parentheses indicate the approximation that both f_2/f_1 and f_3/f_1 are small relative to unity.

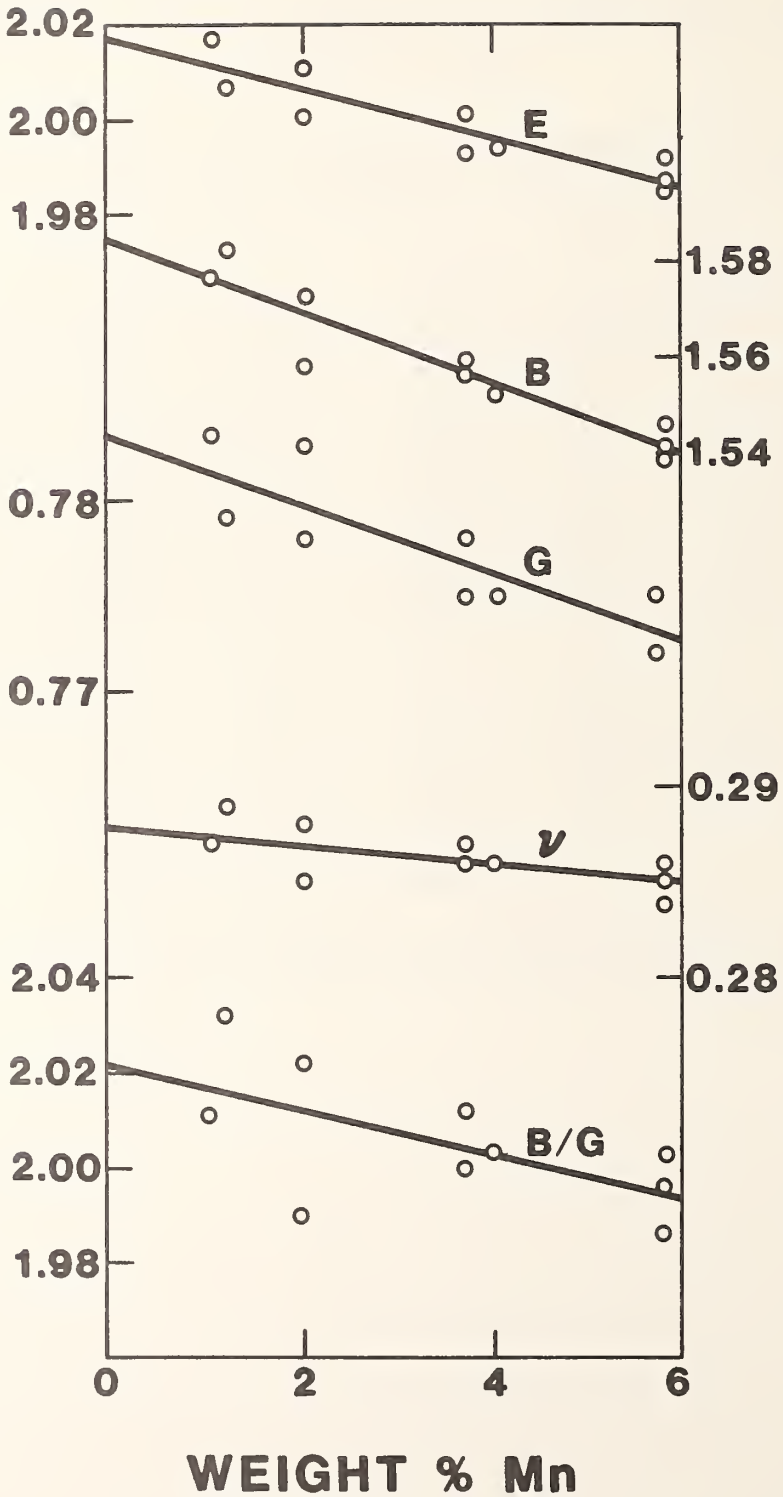

Fig. 1. Compositional variation of elastic constants of Fe-Cr-Ni alloys containing Mn. Units on E, B, and G are 10^{11} N/m^2. ν is dimensionless.

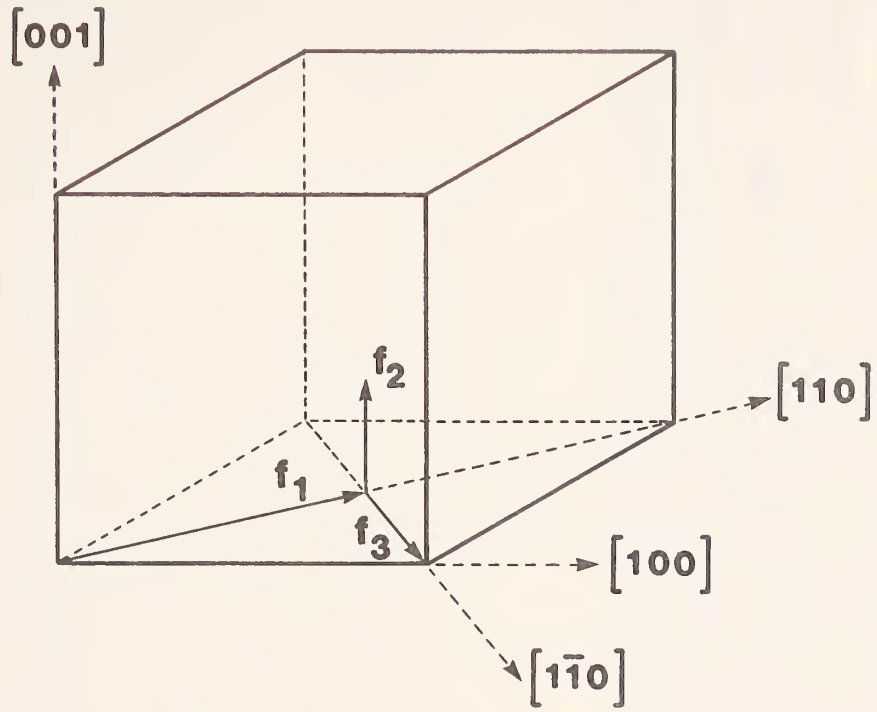

Fig. 2. Face-centered-cubic unit cell showing eigenvectors and eigenvalues of the coupling matrices to the nearest-neighbor atoms at $\lceil \frac{1}{2}\ \frac{1}{2}\ 0 \rceil$-type positions.

Anomalous low-temperature elastic-constant behavior of Fe-20Cr-16Ni-6Mn

H. M. Ledbetter and M. W. Austin

Fracture and Deformation Division
National Bureau of Standards
Boulder, Colorado 80303

Abstract

For this high-nickel-content austenitic stainless steel we determined ultrasonically the complete set of polycrystalline elastic constants between 295 and 4 K. A reversible magnetic transition occurs near 54 K. During cooling, the bulk modulus begins to soften at a much higher temperature, near 150 K. Local moments above the transition temperature may explain this peculiarity.

Key Words: Bulk modulus; elastic constants; iron alloy; low temperatures; magnetic phase transition; Néel transition, Poisson ratio; shear modulus; stainless steel; ultrasonic waves; Young modulus.

Several recent studies[1-7] show that austenitic stainless steels undergo magnetic phase transitions at low temperatures. These studies[2] show the effect of Mn, which raises the transition temperature.

The present study shows the effect of Ni. In selecting a high-Ni stainless steel for study we chose Fe-20Cr-16Ni-6Mn, a Soviet steel intended for low-temperature weldments. Mechanical properties of this alloy were reported recently.[8]

The actual chemical composition by weight percent is 20.31 Cr, 16.42 Ni, 6.12 Mn, 0.26 Si, 0.21 Mo, 0.19 N, 0.09 Cu, 0.026 S, and 0.025 P. Hardness was Rockwell B 88, grain size was 39 μm (ASTM No. 6.4), mass density was 7.879 g/cm^3, and the 1.9-cm plate was ferrite free as determined by a magnetic balance.

Elastic constants were determined by measuring ultrasonic velocities between 300 and 4 K using equipment and procedures described elsewhere.[5] The key experimental parameters include: orthogonal-prism specimen, 1.3 by 1.3 by 1.6 cm; opposite faces flat and parallel within 5 μm; quartz transducers 1 cm diam, x-cut and ac-cut, rough polished; gold electroplated two sides, 4-MHz fundamental frequencies; bonding agents phenyl salicylate at room temperature and a cyanoacrylate adhesive at lower temperatures.

Table 1 gives for selected temperatures the longitudinal and transverse sound velocities, v_ℓ and v_t, which Fig. 1 shows as longitudinal and shear moduli:

$$C_\ell = \rho v_\ell^2 \tag{1}$$

and,

$$C_t = \rho v_t^2 \tag{2}$$

where ρ denotes mass density. Table 1 and Fig. 2 give derived elastic constants:

$$\text{Shear modulus} = G = C_t \tag{3}$$

$$\text{Bulk modulus} = B = C_\ell - \frac{4}{3} G \tag{4}$$

$$\text{Young modulus} = E = 9GB/(G + 3B) \tag{5}$$

and

$$\text{Poisson ratio} = \nu = (E/2G) - 1. \tag{6}$$

Maximum experimental uncertainties are believed to be 1.0 percent for G and E and 1.5 percent for B and ν.

All this steel's elastic constants show anomalies near 54 K, corresponding presumably to its magnetic-transition temperature, T_c, for critical temperature.

The bulk-modulus behavior shows that a second and broader transition, probably also magnetic, occurs at a higher temperature, near 150 K. This transition does not affect noticeably the shear-dominated elastic constants such as G, E, and ν. The exact nature of this high-temperature transition remains unknown. Unlike the low-temperature transition, it does not exhibit a magnetic-susceptibility maximum.[1]

Bulk-modulus softening implies a possible magnetic transition where the onset of magnetization causes repulsive atom-atom interactions. This repulsive interaction expands the lattice and softens B because, as discussed by Gilman,[9] B varies with atomic radius as r^{-4}.

The question arises: what bulk-modulus change does a simple model predict? To answer this, we consider a Stoner,[10] collective-electron, itinerant-electron, or band, model. In this model, d or f electrons belong to a degenerate band where electrons of + and - spins possess different energies. Transfer of an electron from the top (antibonding) band to the bottom (bonding) band increases its kinetic energy (lower wavelength). But the potential energy decrease, the exchange energy, may offset this. If so, then

magnetic ordering occurs. By assuming that the exchange energy depends only weakly on atomic volume, the bulk modulus will depend only on the kinetic energy

$$E = M^2/2N \tag{7}$$

where M is magnetic moment in Bohr magnetons per atom and N is the electronic density of states at the fermi level in Ry^{-1}. There arises a magnetic "pressure"

$$P_m = -(\partial E/\partial V)_{V = V_o} \tag{8}$$

$$= \frac{M^2}{2} \frac{\partial N}{\partial V} \tag{9}$$

$$2N$$

Heine[11] showed that d-electron bandwidth, W, varies with atomic radius, r, as r^{-5}. Assuming the product NW is constant, then N varies as r^5 and

$$\frac{dN}{N} = \frac{5}{3} \frac{dV}{V} \tag{10}$$

and

$$P_m = (5/3)\ E/V_o \tag{11}$$

where V_o denotes atomic volume.

The bulk modulus is

$$B_m = V(\partial^2 E/\partial V^2) = -V(\partial P_m/\partial V) \tag{12}$$

which becomes after differentiation

$$B_m = (65/18)\ M^2/NV_o = (65/9)\ E/V_o \tag{13}$$

For iron, M = 2.12 μ_B, N = 27.4 states/atom·Ry, V_o = 7.094 cm^3/g·atom. Thus,

$$B_m = 0.303 \cdot 10^{11} N/m^2$$

For Fe, this amounts to 18 percent of the zero-temperature bulk modulus. Thus, magnetic effects can be quite large.

The exchange energy, the companion to the kinetic energy, must contribute more, but negatively, to the bulk modulus since the net result is elastic

softening. However, present theory[12] does not permit the calculation of the exchange contribution. For this one needs a relationship between the exchange energy and atomic volume. Figure 2 shows that the bulk modulus softens about 1.5 percent. Thus, the negative exchange term must offset the positive kinetic-energy term by this amount.

That B, but not G, softens at higher temperatures suggests a magneto-volume effect akin to spontaneous volume magnetostriction. This effect is designated ΔE_ω, where $\omega = (V - V_P)/V_P$ is the spontaneous volume magnetostriction, V is the total volume, and V_P is the volume in the paramagnetic state. The effect was first reported by Engler[13] for an Fe-42Ni alloy. It was explained first by Döring[14] using a thermodynamic analysis. Herein, this phenomenon will be called the Döring effect. Döring reasoned that in the paramagnetic region the elastic constant is measured at constant magnetization, M, while in the ferromagnetic or antiferromagnetic region the elastic constant is measured at constant magnetic field, H. Döring showed that the magnitude of the anomaly in the Young's modulus is given by

$$\frac{\Delta E_\omega}{E^2} = \frac{1}{E_M} - \frac{1}{E_H} = -\frac{1}{9}\left(\frac{\partial \omega}{\partial H}_{\sigma,T}\right)^2 \left(\frac{\partial M}{\partial H}_{\sigma,T}\right)^{-1} \qquad (14)$$

where $\partial\omega/\partial H$ is the forced volume magnetostriction due to the magnetization, $\partial M/\partial H$ is the high-field susceptibility χ, E^2 is $E_M E_H$, and σ is the tensile stress. An alternative derivation of Eq. (8) was given by Hausch[12]. Wohlfarth[15] stated, without proof, that the factor of 1/9 in Eq. (8) should be replaced by $(1 - 2\nu)^2$ where ν is Poisson's ratio. For the present materials this introduces a factor of approximately 1.6, which is insignificant for present purposes. It should be noted that the Döring effect always lowers the moduli ($E_M > E_H$), whether the volume magnetostriction is positive or negative. This is related to the fact that a relaxation mechanism is involved in going

to a magnetic state, and such mechanisms always soften the elastic stiffness. The Döring effect in iron-nickel alloys was discussed by Köster,[16] who denoted it as ΔE_γ rather than as ΔE_ω. The effect was invoked by several authors to explain elastic anomalies in magnetic materials, usually of the invar type. Hausch[12] criticized the relevance of the Döring effect in most of these cases. Schlosser[17] discussed the magnetovolume contribution to the compressibility of invar, but Hausch[12] showed that an exchange-energy contribution is also required in this case. The present results for an Fe-Cr-Ni-Mn (stainless-steel) alloy seem to constitute a clear case of a Döring-type effect.

Shiga[18] discussed recently that magnetovolume effects in transition-metal alloys originate in the onset of local moments. His argument is the following: Energy-band polarization increases the kinetic-energy (as described above). This kinetic energy is offset by volume expansion because kinetic energy is proportional to 3d bandwidth that varies as r^{-5}. Shiga concludes that the volume increase varies as M^2. Shiga concludes further that the large volume changes predicted theoretically by Janak and Williams[19] do not occur because 3d-band polarization persists above T_c because of local moments.

We conjecture that local moments above T_c explain the bulk-modulus anomaly beginning during cooling near 150 K. Since local moments lead to a magnetovolume effect, this explains why dilatational modes are altered while shear modes remain unaffected. Volume expansion would explain the softening of B, which varies as r^{-4}. Other physical properties, such as thermal expansivity and specific heat, probably also change less abruptly than expected because M does not vanish immediately above the apparent T_c (near 54 K for the present alloy).

Finally, we consider the effect of Ni on the elastic properties by comparing present results with those obtained previously for 304 stainless-steel, nominally Fe-18Cr-8Ni. Table 2 shows these results together with the present results corrected for Mn content. One concludes from Table 2 that Ni increases slightly all the elastic stiffnesses; Poisson's ratio remains essentially unchanged. One expects this because Ni's elastic stiffnesses exceed those of Fe-18Cr-8Ni (see Table 2). And, Ni, with lower atomic volume than Fe, would also lower the elastic stiffness, which varies as r^{-4}, where r denotes atomic radius. However, several previous experimental studies imply an opposite effect. Table 3 contains elastic constants of five stainless-steel single crystals[21-24] averaged using Kröner's[25] method. However, these averaged results remain unconvincing because they disagree significantly with the observed bulk and shear moduli for 304 stainless-steel.[26] Thus, the effect of Ni on stainless-steel elastic constants remains uncertain.

Acknowledgment

The DoE Office of Fusion Energy and the National Science Foundation partially supported this study.

References

1. H. M. Ledbetter and E. W. Collings, Low-Temperature magnetic and elastic-constant anomalies in three manganese stainless steels, in Metal Science of Stainless Steels (AIME, New York, 1979), 22-40.

2. E. W. Collings and H. M. Ledbetter, Sound velocity anomalies near the spin-glass transition in an austenitic stainless steel alloy, Phys. Lett. 72A, 53-56 (1979).

3. H. M. Ledbetter, Anomalous low-temperature elastic-constant behavior in Fe-13Cr-19Mn, Metall. Trans. 11A, 543-544 (1980).

4. H. M. Ledbetter, Room-temperature elastic constants and low-temperature sound velocities for six nitrogen-strengthened stainless steels, Metall. Trans. 11A, 1067-1069 (1980).

5. H. M. Ledbetter, Stainless steel elastic constants at low temperatures, J. Appl. Phys. 52, 1987-1589 (1981).

6. H. M. Ledbetter, Low-temperature variability of stainless-steel-304 elastic constants, intended for Cryogenics.

7. H. M. Ledbetter and E. W. Collings, Elastic-constant anomalies at the Neel transition in Fe-18Cr-3Ni-12Mn, to be published.

8. R. P. Reed, R. L. Tobler, J. W. Elmer, H. I. McHenry, and K. A. Yushchenko, Strength and toughness of USSR Fe-20Cr-16Ni-6Mn-0.2N weldments at cryogenic temperatures, NBS Boulder Fracture and Deformation Division (1981), to be published.

9. J. J. Gilman, Micromechanics of Flow in Solids (McGraw-Hill, New York, 1969), p. 29-41.

10. E. P. Wohlfarth, Iron, cobalt, and nickel, in Ferromagnetic Materials, Volume 1 (North-Holland, Amsterdam, 1980), p. 1-70.

11. V. Heine, 5-d interaction in transition metals, Phys. Rev. 153, 673-682 (1967).

12. G. Hausch, Magnetic exchange energy contribution to the elastic constants and its relation to the anomalous elastic behavior of invar alloys, Phys. Stat. Solidi (a) 15, 501-510 (1973).

13. O. Engler, Der Elastizitätsmodul ferromagnetischer Stoffe in Abhängigkeit von der Temperatur und vom Magnetfeld, Ann. Phys. (Leipz.) 31, 145 (1938).

14. W. Döring, Über die Temperaturabhangigkeit des Elastizitätsmoduls ferromagnetischer Substanzen, Ann. Phys. (Leipz.) 32, 465 (1938).

15. E. P. Wohlfarth, Contributions to the invar problem, v. the ΔE effect, Phys. Stat. Solidi (a) 10, K39-K42 (1972).

16. W. Köster, Elastizitätsmodul und ΔE-Effekt der Eisen-Nickel Legierungen, Z. Metallke. 35, 194 (1943).

17. F. Schlosser, Magnetic contributions to the compressibility of invar, Phys. Stat. Solidi (a) 18, 235-239 (1973).

18. M. Shiga, Magnetovolume effects in ferromagnetic transition metals and alloys, in Physics of Transition Metals, 1980 (Inst. Phys., Bristol, 1981), p. 241-250.

19. J. F. Janak and A. R. Williams, Giant internal magnetic pressure and compressibility anomalies, Phys. Rev. B 14, 4199-4204 (1976).

20. H. M. Ledbetter, Manganese contributions to the elastic constants of face-centered-cubic Fe-Cr-Ni alloys, to be published.

21. K. Salmutter and F. Stangler, Elastizität und Plastizität eines austenitischen Chrom-Nickel-Stahles, Z. Metallke. 51, 544-548 (1960).

22. H.-U. Richter, Zur Ultraschallprüng austenitischer Schweissverbindungen (Teil I), die Technik 23, 610-619 (1968).

23. M. Kikuchi, Elastic anisotropy and its temperature dependence of single crystals of 18-12 type stainless steel, Trans. Jap. Inst. Met. 12, 417-421 (1971).

24. M. C. Mangalick and N. F. Fiore, Orientation dependence of dislocation damping and elastic constants in Fe-18Cr-Ni single crystals, Trans. Met. Soc. AIME 242, 2363-2364 (1968).

25. E. Kröner, Berechnung der elastischen Konstanten des Vielkristalls aus den Konstanten des Einkristalls, Z. Phys. 151, 504-518 (1958).

26. H. M. Ledbetter, N. V. Frederick, and M. W. Austin, Elastic-constant variability in stainless-steel 304, J. Appl. Phys. 51, 305-309 (1980).

Table 1. Elastic constants of Fe-20Cr-16Ni-6Mn at selected temperatures.

T (K)	v_ℓ (cm/μs)	v_t (cm/μs)	E (10^{11}N/m^2)	G (10^{11}N/m^2)	B (10^{11}N/m^2)	ν
295	0.5735	0.3134	1.992	0.774	1.560	0.287
285	0.5742	0.3140	1.999	0.777	1.562	0.287
275	0.5751	0.3144	2.004	0.779	1.567	0.287
264	0.5758	0.3152	2.013	0.783	1.568	0.286
255	0.5765	0.3157	2.020	0.785	1.571	0.286
245	0.5771	0.3163	2.027	0.788	1.573	0.285
235	0.5779	0.3169	2.033	0.791	1.576	0.285
225	0.5787	0.3177	2.043	0.795	1.579	0.284
215	0.5793	0.3183	2.049	0.798	1.580	0.284
204	0.5800	0.3188	2.056	0.801	1.583	0.284
194	0.5807	0.3195	2.064	0.805	1.584	0.283
184	0.5810	0.3201	2.070	0.807	1.584	0.282
175	0.5817	0.3206	2.076	0.810	1.586	0.282
165	0.5824	0.3212	2.083	0.813	1.589	0.282
155	0.5830	0.3218	2.090	0.816	1.590	0.281
143	0.5833	0.3222	2.095	0.818	1.590	0.280
133	0.5841	0.3227	2.101	0.821	1.593	0.280
123	0.5844	0.3233	2.107	0.823	1.593	0.280
112	0.5849	0.3239	2.114	0.827	1.594	0.279
103	0.5852	0.3243	2.118	0.828	1.594	0.278
91	0.5853	0.3247	2.122	0.830	1.592	0.278
82	0.5857	0.3250	2.127	0.832	1.593	0.277
71	0.5857	0.3253	2.129	0.834	1.591	0.277
61	0.5855	0.3255	2.131	0.835	1.588	0.276
51	0.5851	0.3253	2.128	0.834	1.586	0.276
39	0.5844	0.3253	2.127	0.834	1.579	0.276
26	0.5844	0.3253	2.127	0.834	1.580	0.276
13	0.5846	0.3252	2.126	0.833	1.582	0.276
4	0.5848	0.3253	2.127	0.834	1.583	0.276

Table 2. Room-temperature elastic constants of two stainless steels and nickel.

	Fe-20Cr-16Ni-Mn		Fe-18Cr-8Ni	Ni
	observed	corrected[a]		
E (10^{11} N(m^2))	1.992	2.014	1.996	2.217
G (10^{11} N/m^2)	0.774	0.782	0.774	0.851
B (10^{11} N/m^2)	1.560	1.592	1.582	1.868
ν	0.287	0.289	0.290	0.302

[a]For Mn content using results of ref. 20.

Table 3. Monocrystal and averaged polycrystal elastic constants of five Fe-Cr-Ni alloys. All units are 10^{11} N/m^2, except ν, which is dimensionless.

	C_{11}	C_{12}	C_{44}	B	E	G	ν	Ref.
Fe-12Cr-18Ni	2.332	1.626	1.225	1.861	2.006	0.759	0.320	2
Fe-18Cr-12Ni	2.16	1.45	1.29	1.687	2.037	0.784	0.299	22
Fe-18Cr-12Ni	1.912	1.179	1.386	1.423	2.077	0.826	0.257	23
Fe-18Cr-14Ni	1.98	1.25	1.22	1.493	1.997	0.763	0.282	24
Fe-18Cr-19Ni	1.91	1.19	1.24	1.430	1.951	0.777	0.273	24

Figure Captions

Fig. 1. Temperature dependence of longitudinal and shear moduli of Fe-20Cr-16Ni-6Mn.

Fig. 2. Temperature dependence of three elastic constants of Fe-20Cr-16Ni-6Mn: Young modulus, bulk modulus, and Poisson ratio.

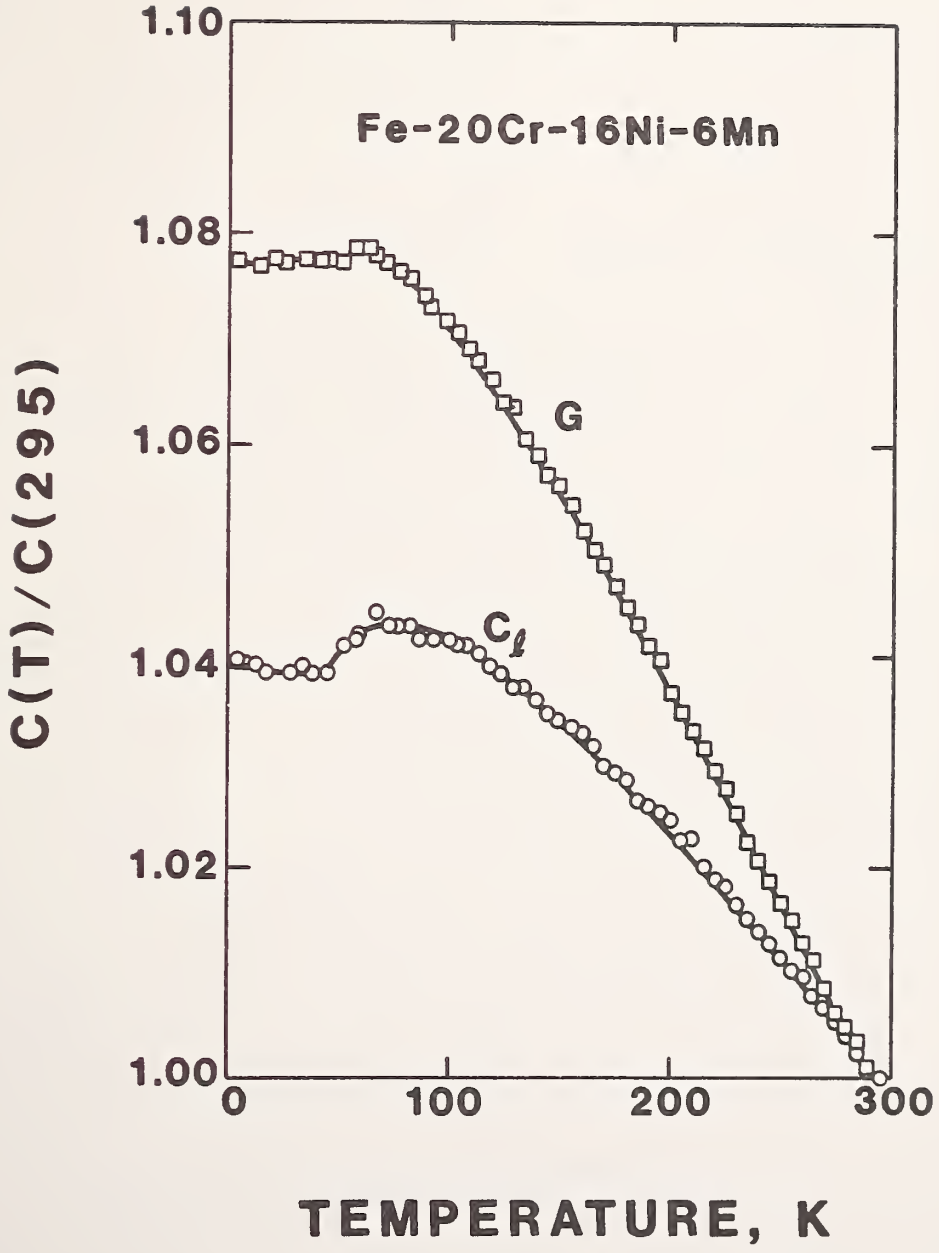

Fig. 1. Temperature dependence of longitudinal and shear moduli of Fe-20Cr-16Ni-6Mn.

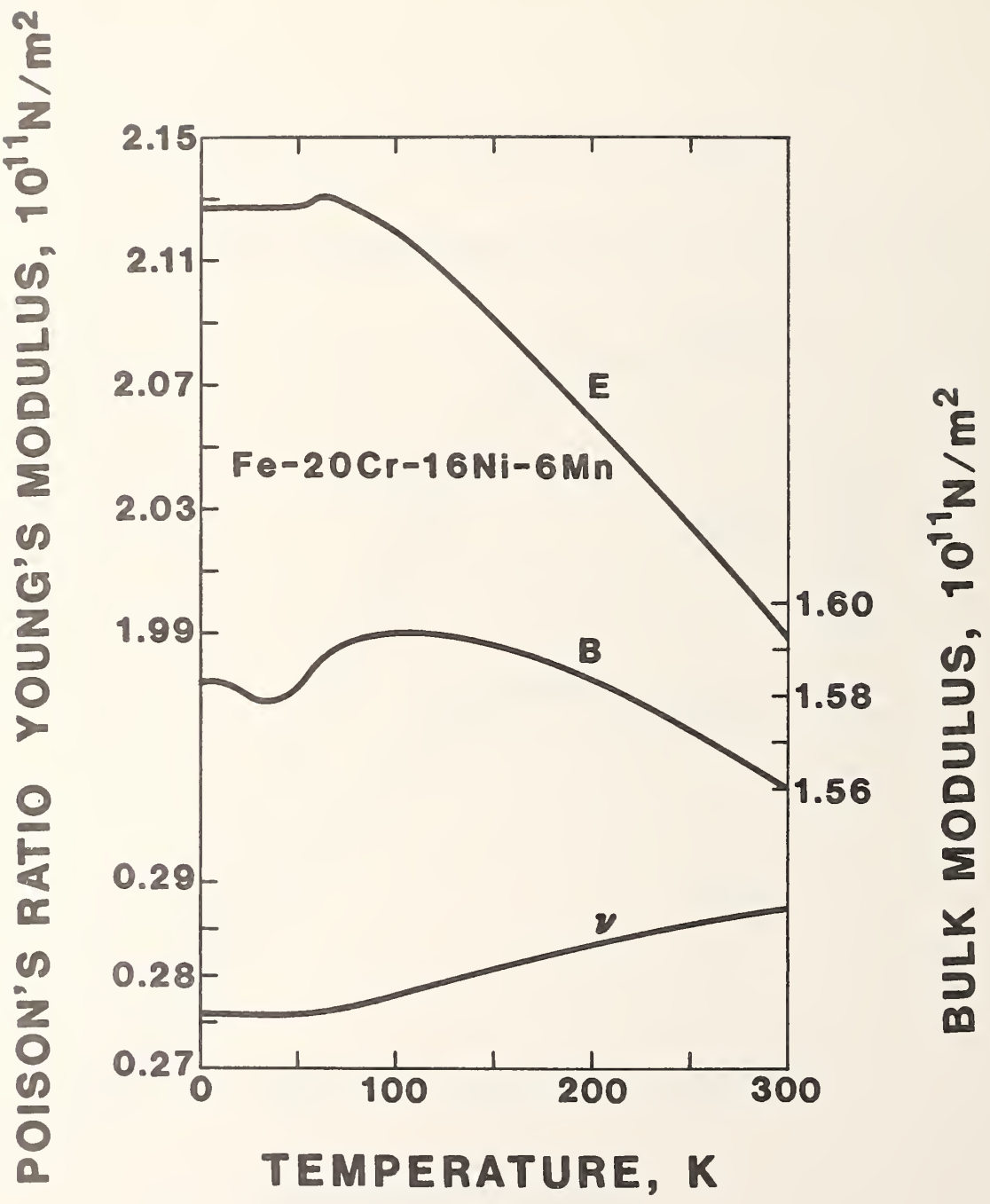

Fig. 2. Temperature dependence of three elastic constants of Fe-20Cr-16Ni-6Mn: Young modulus, bulk modulus, and Poisson ratio.

WELDING AND CASTING

WELDMENTS AND CASTINGS PROGRAM

LEADER: H. I. McHenry, NBS
STAFF: T. A. Whipple, J. W. Elmer, C. M. Fortunko, H. M. Ledbetter, NBS
CONTRACTS: None

OBJECTIVES:

(1) To investigate the metallurgical factors that affect the mechanical properties of stainless steel weldments and castings at cryogenic temperatures.
(2) To contribute to the development of improved filler metals for welding stainless steels for liquid helium service.
(3) To evaluate the mechanical properties of weldments and castings at 4 K.
(4) To develop methods of detecting defects and evaluating their significance in stainless steel weldments.

RESEARCH PAST YEAR (1981):

(1) The tensile properties and fracture toughness of a series of five CF8M castings with delta-ferrite contents ranging from 0 to 28 percent were measured at 4 K.
(2) Work has continued on a study to relate metallographic observations of duplex austenite delta-ferrite microstructures to the deformation and fracture of stainless steel welds and castings.
(3) The fracture toughness and fatigue crack growth rates of a 25Mn-5Cr-1Ni alloy, plate and welds, were measured at 4 K.
(4) Two 316L stainless steel weldments were tested at 4 K in support of the LCP program.
(5) An improved method of ultrasonic testing of stainless steel weldments was conceived and demonstrated.
(6) The elastic constants of stainless steel weldments have been related to texture in the weldment.

RESEARCH THIS YEAR (1982):

(1) The five CF8M stainless steel castings with varying nitrogen content and constant delta-ferrite content will be tested at 4 K.
(2) The metallographic study on deformed and fractured stainless steels with duplex structures will continue.
(3) A set of stainless steel weldments will be produced with varying delta-ferrite morphologies. These weldments will be used to verify and extend the deformation model for duplex structures to the finer structures found in weldments.
(4) A set of submerged-arc weldments will be produced with variations in the delta-ferrite and oxygen contents.
(5) A series of stainless steel weldments with varying austenite stability will be produced and tested with the weld reinforcement left on.
(6) The elastic properties of the CF8M stainless steel castings will be measured ultrasonically.
(7) Mechanical property testing at 4 K, in support of superconducting magnet design and construction, will continue.

WELDMENTS AND CASTINGS FOR LIQUID HELIUM SERVICE

T. A. Whipple and H. I. McHenry
Fracture and Deformation Division
National Bureau of Standards
Boulder, Colorado

ABSTRACT

The FY 81 results of the NBS program to evaluate weldments and castings for liquid helium service are reviewed. The tensile properties and fracture toughness of a series of five CF8M castings with delta-ferrite contents ranging from 0 to 28 percent were measured at 4 K. Work is continuing on a study to relate metallographic observations of duplex austenite delta-ferrite microstructures to the deformation and fracture of stainless steel welds and castings. The fracture toughness and fatigue crack growth rates of a 25Mn-5Cr-1Ni alloy, plate and welds, were measured at 4 K. Two 316L stainless steel weldments were tested at 4 K in support of the LCP program. The elastic properties of 316L stainless steel welds have been related to the texture in the weldment. An improved method of ultrasonic testing of stainless steel weldments was conceived and demonstrated; the method uses electromagnetic acoustic transducers (EMATs) to inspect the weldments with horizontal shear (SH) waves that are inherently less sensitive to the anisotropy of stainless steel welds. The research planned for FY 82 is also described.

INTRODUCTION

The evaluation of weldments and castings for structural applications at 4 K [1-4] was continued in FY 81. This program has four objectives:

1. To investigate the metallurgical factors that affect the mechanical properties of stainless steel weldments and castings at cryogenic temperatures.
2. To contribute to the development of improved filler metals for welding stainless steels for liquid helium service.
3. To evaluate the mechanical properties of weldments and castings at 4 K.
4. To develop methods of detecting defects and of evaluating their significance in stainless steel weldments.

Work continued on the first three objectives with evaluations of CF8M stainless steel castings, 316L stainless steel weldments, and 25Mn-5Cr-1Ni austenitic steel weldments. Research was started on the fourth objective with the development of a new technique for ultrasonic inspection of stainless steel weldments. This paper briefly summarizes the research completed in FY 81 and the plans for FY 82. Detailed summaries of the research completed in FY 81 are given in the other papers of this section.

STAINLESS STEEL WELDMENTS

Austenitic Cr-Ni stainless steels, particularly the nitrogen-strengthened grades, are the most commonly used alloys for structural applications in superconducting magnets for fusion energy devices. These steels have the best combination of strength, stiffness, and toughness at 4 K. However, the development of a matching-strength filler metal with sufficient toughness and resistance to microfissuring for welding the nitrogen-strengthened alloys does

remain a problem. A new approach to the development of a base metal/weld metal system with a satisfactory match in properties has been taken by Japanese investigators [5]. The new alloys are high-manganese austenitic steels that are not stainless steels owing to their low chromium content. One such alloy, 25Mn-5Cr-1Ni, was evaluated. The results, reported here by McHenry, Elmer, and Inoue, indicate the base plate and welds have a favorable combination of strength, toughness, and fatigue crack growth resistance at 4 K. The weld metal properties are particularly encouraging; specifically, the yield strength (961 MPa) is sufficiently high to match the base metal, the toughness (157 MPa$\sqrt{m}$) is satisfactory, and the microfissuring tendencies appear to be minimal.

Support of the LCP magnet design and construction program has continued with the testing of a 316L submerged-arc weld (SAW) and a modified 316L shielded metal-arc weld (SMAW). The results of the tensile, fracture toughness, and fatigue crack growth rate tests at 4 K are presented in Tables 1, 2, and 3, respectively. The modified 316L weldment has a high nitrogen content (0.147%), which results in the relatively high strength and moderate fracture toughness. A good combination of strength and toughness was achieved in the 316L submerged arc weld. It is anticipated that the testing of qualification and test weldments will be reduced in the future, since the LCP magnets are now in the final stages of manufacture and there are now additional facilities for cryogenic fracture toughness testing [6,7].

The inspectability of stainless steel weldments by ultrasonic methods is fundamentally limited by the textured columnar grain structure of the weld metal. The velocity of vertical shear (SV) and longitudinal (L) waves is strongly anisotropic, resulting in reflections and mode conversions that may

clutter the ultrasonic signals received and mask the defect indication. A new approach to ultrasonic inspection has been developed and demonstrated; it is reported herein by Fortunko and Moulder. The principal idea is to use horizontally polarized shear (SH) waves whose wave velocities are not as strongly anisotropic as SV and L waves. In addition, the wave impedances of the weld and base metal can be matched more readily with SH waves, and therefore, there is significantly lower scatter and higher sensitivity. The SH waves are transmitted and received by electromagnetic acoustic transducers (EMATs). Unlike piezoelectric crystals, EMATs can readily transmit and receive SH waves.

Ultrasonic techniques are also being used to study the elastic properties of a series of 316L stainless steel weldments with ferrite contents ranging from 0 to 10 percent. Ultrasonic wave velocities, both longitudinal and transverse, were measured along the weld axis. Preliminary results indicate that the elastic properties depend only weakly on ferrite content and that strong elastic anisotropy occurs in the welds. Theoretical calculations by Ledbetter show that ultrasonic velocity provides a very sensitive probe for both detecting and measuring the amount of texture in the stainless steel welds.

STAINLESS STEEL CASTINGS

Research on the mechanical behavior of stainless steel castings is being conducted to evaluate CF8M castings for liquid helium service and to improve understanding of the deformation and fracture of duplex austenite/delta-ferrite microstructures at 4 K. The improved understanding should be applicable to welds as well as castings because both are duplex structures of austenite and delta ferrite. Castings were selected for the study because their coarser microstructure facilitates metallographic observation of the

response of the two phases to deformation. The research was started in FY 80 [8] and continued this year. The results, reported herein by Whipple and Brown, include the observation of deformation twinning in delta-ferrite at 4 K and the fractographic examination of the CF8M stainless steel castings with varying ferrite contents. The fractographic study has revealed that a relatively low delta-ferrite content causes a high proportion of the fracture surface to be brittle in nature. The fracture path is completely through the ferrite phase at about 15 percent delta-ferrite.

The tensile and fracture toughness properties of a series of CF8M stainless steel castings with ferrite contents ranging from 0 to 28 percent were measured at 4 K. The results, reported herein by Whipple and Brown, are consistent with two-phase deformation models, which assume that the delta-ferrite is a nonplastically deforming phase at 4 K. The tensile tests showed that the effect of delta-ferrite is to increase the strain-hardening rate in the low plastic strain region (less than $\sim$2.5 percent). The fracture toughness tests showed a decrease in fracture toughness with increasing delta-ferrite content, up to approximately 15 percent; at higher delta-ferrite contents, the fracture toughness was essentially constant. This has been attributed to the establishment of a continuous delta-ferrite crack path.

TEST METHOD DEVELOPMENT

In FY 81, the capability for doing single-specimen J_{Ic} tests at 4 K on three-point-bend specimens has been developed. This specimen design has several advantages over the previously used compact-tension (CT) specimen. These advantages include lower specimen machining costs and greater flexibility in choosing specimen orientation. The test procedures are very similar to those used for CT specimens, and only minor modifications to the computer-aided J-integral test facility were necessary.

FUTURE WORK

In FY 82, the study on the deformation and fracture of duplex austenite/delta-ferrite structures will continue with the objectives outlined below. Also, new programs designed to evaluate the effects of weld reinforcement and oxygen content will be initiated. These factors have not been comprehensively studied to date. Specifically, the FY 82 research will have the following objectives:

1. The tensile and fracture toughness properties of five CF8M stainless steel castings with varying nitrogen content and constant delta-ferrite content will be measured at 4 K. This work is an extension of the study on the fracture and deformation of duplex structures. It is designed to test the effects of changing the austenite matrix properties.
2. The metallographic study on deformed and fractured stainless steels with duplex structures will continue and will concentrate mainly on TEM studies of dislocation structures and deformation twinning.
3. A set of stainless steel weldments will be produced with varying delta-ferrite morphologies. These weldments will be used to verify and extend the deformation model for duplex structures to the finer structures found in weldments.
4. A set of submerged-arc weldments will be produced with variations in the delta-ferrite and oxygen contents. Increasing the oxygen content will cause an increase in the number of nonmetallic inclusions in the weld, which has previously been shown to have an effect on the properties at 4 K [9]. This study is intended to quantify the effect.

5. A series of stainless steel weldments with varying austenite stability will be produced and tested with the weld reinforcement left on. There has been some indication that the combination of weld reinforcement and austenite stability has an effect on weldment strength [10].
6. The elastic properties and internal friction of the CF8M stainless steel castings will be measured ultrasonically.
7. Mechanical property testing at 4 K, in support of superconducting magnet design and construction, will continue.
8. Elastic-constant studies of stainless-steel weldments will be completed.

REFERENCES

1. H. I. McHenry, "Evaluation of Stainless Steel Weld Metals at Cryogenic Temperatures," in Materials Studies for Magnetic Fusion Energy Applications at Low Temperatures-I, National Bureau of Standards, Boulder, CO, NBSIR 78-884 (1978), pp. 159-166.
2. H. I. McHenry, D. T. Read, and P. A. Steinmeyer, "Evaluation of Stainless Steel Weld Metals at Cryogenic Temperatures," in Materials Studies for Magnetic Fusion Energy Applications at Low Temperatures-II, National Bureau of Standards, Boulder, CO, NBSIR 79-1609 (1979), pp. 299-308.
3. H. I. McHenry and T. A. Whipple, "Weldments for Liquid Helium Service," in Materials Studies for Magnetic Fusion Energy Applications at Low Temperatures-III, National Bureau of Standards, Boulder, CO, NBSIR 80-1627 (1980), pp. 155-165.
4. T. A. Whipple and H. I. McHenry, "Evaluation of Weldments and Castings for Liquid Helium Service," in Materials Studies for Magnetic Fusion Energy Applications at Low Temperatures-IV, National Bureau of Standards, Boulder, CO, NBSIR 81-1645 (1981), pp. 273-287.
5. H. Yoshimura, H. Masumoto, and T. Inoue, "Properties of Low Carbon 25Mn-5Cr-1Ni Austenitic Steel for Cryogenic Use," in Advances in Cryogenic Engineering-Materials, Vol. 28, Plenum Press, New York (1982), pp. 115-125.
6. W. G. Dobson and C. H. Kano, "Mechanical Testing at 4.2 K," Technical Report Tr-A771-1, Teledyne Engineering Services, Waltham, MA, July 11, 1981.

7. D. Duncan, M. C. Juhas, and R. Streit, "Development of a Facility for Fatigue and Fracture Testing of Stainless Steel Weldments and Base Metal at Liquid Helium Temperature," Lawrence Livermore National Laboratory, Livermore, CA, unpublished, 1981.

8. T. A. Whipple and E. L. Brown, "Deformation and Fracture of Stainless Steel Castings and Weldments at 4 K," in Materials Studies for Magnetic Fusion Energy Applications at Low Temperatures-IV, National Bureau of Standards, Boulder, CO, NBSIR 81-1645 (1981), pp. 415-452.

9. T. A. Whipple and D. J. Kotecki, "Weld Process Study for 316L Stainless Steel Weld Metal for Liquid Helium Service," in Materials Studies for Magnetic Fusion Energy Applications at Low Temperatures-IV, National Bureau of Standards, Boulder, CO, NBSIR 81-1645 (1981), pp. 303-322.

10. K. A. Yushchenko and S. A. Voronin, "The Use of Low-Temperature Strengthening of Steels in Welded Cryogenic Structural Codes," in Advances in Cryogenic Engineering Materials, Vol. 28, Plenum Press, New York (1982), pp. 137-145.

Table 1. Tensile Properties of Test Weldments at 4 K

Weld	σ_y, MPa	σ_y, (ksi)	σ_u, MPa	σ_u, (ksi)	Elongation, %	Reduction in Area, %
316L (SAW)	655	(95.0)	1485	(215)	40.0	29.3
	646	(93.7)	1489	(216)	39.6	32.2
	662	(96.0)	1485	(215)	41.6	34.9
	654	(94.9)	1486	(215)	40.4	32.1

Table 2. Fracture Toughness Properties of Test Weldments at 4 K

Weld	J_{Ic}, $\frac{J}{m^2}$	J_{Ic}, $(\frac{in\text{-}lb}{in^2})$	$K_{Ic}(J)$, MPa$\sqrt{m}$	$K_{Ic}(J)$, (ksi$\sqrt{in}$)
316L (SAW)	120	(685)	165	(150)
	103	(590)	153	(139)
	135	(770)	175	(159)
	119	(682)	164	(149)
Modified 316L (SMAW)	46.9	(325)	114	(104)
	80.5	(460)	135	(123)
	68.7	(393)	125	(114)

Table 3. Fatigue Crack Growth Rate Properties of Test Weldments at 4 K.

Weld	n*	c*
316L (SAW)	4.08	6.47×10^{-11}
Modified 316L (SMAW)	3.99	6.19×10^{-11}

*Constants fit the equation: $da/dN = C\Delta K^n$, with da/dN in mm/cycle and ΔK in MPa$\sqrt{m}$.

FRACTURE PROPERTIES OF A 25 MN AUSTENITIC STEEL AND ITS WELDS AT 4 K*

H. I. McHenry, J. W. Elmer
National Bureau of Standards
Fracture and Deformation Divisions
Boulder, Colorado 80303 USA

and

T. Inoue
Nippon Steel Corporation
Fundamental Research Laboratory
Kawasaki, Japan

ABSTRACT

Tensile properties, fracture toughness, and fatigue crack growth rates of 40-mm and 80-mm-thick plates of a 25Mn-5Cr-1Ni steel were measured in liquid helium at 4 K. Similar tests were conducted on 40-mm-thick shielded-metal-arc welds with a composition of 25Mn-2.8Ni-6.5Cr-1.4Mo. The tensile yield strengths at 4 K were 895 MPa for the base metal and 961 MPa for the weld metal; these values are much higher than the yield strength at room temperature (282 MPa for the base metal). Fracture mechanics tests were conducted using 25.4-mm-thick compact tension specimens. The fracture toughness values measured by the J-integral method were 249 MPa$\sqrt{m}$ for the base metal and 158 MPa$\sqrt{m}$ for the weld. The fatigue crack growth rates of both the base metal and the weld were similar to the fatigue crack growth rates of 316 stainless steel plate over the stress intensity range evaluated, 29-80 MPa$\sqrt{m}$. The results indicate that the 25Mn-5Cr-1Ni alloy has a favorable combination of strength, toughness, and fatigue crack growth resistance at 4 K. The fracture surface of representative fracture toughness specimens of the plate and the weld were examined by scanning electron microscopy, transmission electron microscopy, and magnetic measurements; they were ductile and contained no evidence of α' martensite.

*Accepted for presentation at the International Cryogenic Materials Conference Kobe, Japan 11-14 May, 1982.

INTRODUCTION

A low-carbon, 25Mn-5Cr-1Ni, austenitic steel has been developed for cryogenic applications [1,2,3]. Previous work indicates that the 25Mn steel has excellent strength and ductility to 4 K [1], high Charpy impact toughness to 23 K (the minimum temperature tested) [1,2], a stable austenite microstructure [1,2], and a low (relative to austenitic stainless steels) thermal expansion coefficient [3]. A weld metal with nearly matching composition, 25Cr-2.8Ni-6.5Cr-1.4Mo, has comparable properties (1).

The objective of the present study is to measure the tensile properties, fracture toughness, and fatigue crack propagation characteristics of 25Mn steel plates and welds in liquid helium at 4 K. The test results are compared with the corresponding properties of nitrogen-strengthened, austenitic, stainless steels.

TEST MATERIALS

The test plates of 25Mn steel were produced on a trial commercial scale from a 45-Mg electric furnace heat, heat M2 from Ref. 1. Bottom-poured 14-Mg ingots were reheated to 1200°C and rolled into 230 mm slabs. The slabs were reheated to 1200°C and rolled into 40 and 80 mm thick plates. The plates were solution treated at 1050°C for 90 min., then water quenched. The chemical composition (ladle analysis) is shown in Table 1. The steel is microalloyed with niobium (0.04%) to achieve a fine grain size due to precipitation of niobium carbonitrides. Note that the steel contains only 0.04 percent nitrogen and thus, nitrogen, a potent solution strengthener, does not contribute appreciably to the base metal strength.

The test weldments were 40-mm-thick plates welded by the shielded metal arc (SMA) process using dc reversed polarity. Welding was done in the flat position at 140 A, 25 v and 2.2 to 3 mm/s. The joint preparation was a 35 mm

deep U-groove with a 30° included angle and a 3-mm root radius. This groove was filled with 39 weld passes. The weld was back-gouged to a depth of 15 mm and finished with 15 weld passes. The weld was x-ray inspected and no defects were detected. The chemical composition of the weld metal is given in Table 1.

TEST PROCEDURES

Tensile

Tensile properties were determined for the base metal and the welds using 3.5-mm-diameter, 20-mm-gage-length specimens. Tests were conducted in liquid helium at 4 K using a cylindrical support cryostat similar to the type described by Reed [4]. Strain rates ranged from 4.2×10^{-4} to $4.2 \times 10^{-3} s^{-1}$. Base plate tensile specimens were aligned transverse to the rolling direction and were taken from the midthickness of the plates. Weld metal tensile specimens were aligned both transverse to and along the centerline of the weld; specimens were taken from the quarter- and midthickness of the weldment. The complete test sections of the weld tensile specimens from each location were located within the weld, as shown in Figure 1. The tensile properties measured were the 0.2 percent offset yield strength, the ultimate tensile strength, and the percent elongation in 20 mm.

Fracture Toughness

Fracture toughness was measured by the J-integral method [5] for the base metal and welds using 25-mm-thick and 51-mm-wide compact tension specimens. Tests were conducted in liquid helium at 4 K using a cryostat described by Fowlkes and Tobler [6]. The single-specimen unloading-compliance technique was used to measure J-Δa resistance curves for the base metal and the weld. Additional J-integral tests were conducted on the base plate using multiple-specimen procedures, i.e, the specimen was unloaded after an increment of crack extension, Δa. The Δa value was delineated after unloading by fatigue

crack growth, then the specimen was fractured and Δa was measured on the fracture surface. The base metal specimens were taken from the midthickness of the plates tested in the LT orientation (loaded transverse to the rolling direction). The weld metal specimens were oriented as shown in Figure 1.

The J-Δa resistance curves were used to determine the J_{Ic} values for the base metal and weld, i.e., J_{Ic} is defined as the intersection of the blunting line ($J = \bar{\sigma}\Delta a$, where $\bar{\sigma}$ is the flow strength) and the tearing line. The plane strain fracture toughness $K_{Ic}(J)$ was calculated from J_{Ic} using the relation [5]:

$$K_{Ic}^2 = J_{Ic}E/1-\nu^2 \qquad (1)$$

where E is Young's modulus and ν is Poisson's ratio.

Fatigue Crack Growth Rate

Fatigue crack growth rate tests of the base metal and welds used the same specimen configuration and orientations and the same cryostat as the fracture toughness tests. The specimens were initially precracked in liquid nitrogen at 76 K. Final precracking (approximately 2 mm) and testing were conducted in liquid helium at 4 K. Crack lengths were measured by the compliance technique. A sinusoidal load cycle with frequencies of 10 to 20 Hz was used.

TEST RESULTS AND DISCUSSION

Tensile

The tensile test results for the base metal and welds are summarized in Table 2. The base metal tensile properties were essentially the same for the 40-mm- and 80-mm-thick plates. Similarly, the weld metal tensile properties were similar for the longitudinal and transverse orientations and for the quarter- and midthickness positions. The yield strength of the weld metal was about 10 percent greater than that of the base metal, and the tensile strength of the weld metal was about 10 percent less than that of the base metal. The

overmatching yield strength of the weld metal is particularly important because it avoids strain concentration in the weld.

Fracture Toughness

The results of the fracture toughness tests at 4 K are summarized in Table 3: $K_{Ic}(J)$ for the base metal is 242 MPa$\sqrt{m}$ and $K_{Ic}(J)$ for the weld metal is 158 MPa$\sqrt{m}$. Equation (1) was evaluated using elastic constants of the base metal at 4 K measured by Ledbetter and Austin [7]: $E = 190$ GPa and $\nu = 0.274$. The yield strength and toughness data for 25Mn steel are compared with Read and Reed's [8] trend line for austenitic stainless steels in Figure 2. Note that the combination of yield strength and toughness for the 25Mn base metal slightly exceeds the trend line. The weld metal properties fall below the trend line, but the 25Mn welds have a favorable combination of strength and toughness when compared with austenitic stainless steel [9, 10, 11] weld metals.

Determination of the fracture toughness of the base metal was complicated by the steep slope of the J-Δa curve. Originally, $K_{Ic}(J)$ was to be measured by the single-specimen J-integral technique. Single-specimen tests were conducted on specimens from the 40-mm- and 80-mm-thick plates. In both cases, J_{Ic} could not be determined because there was not a significant change in slope of the J-Δa curve upon tearing. Eight additional tests (four specimens from each plate thickness) were conducted using the multiple-specimen technique. The results are plotted in Figure 3. In each of these tests, the specimen was unloaded and Δa was marked after one of the major load drops that characterized the load-displacement records, as shown in Figure 4. The specimens with small Δa values were unloaded after one major load drop, the specimens with larger Δa values were unloaded after two major load drops, etc. Close examination of the data in Figure 3 indicates that the data occur in four groups separated by gaps of crack extension. The crack appears to propagate in steps, accompanied by load drops, rather than in a continuous manner. Each successive drop and

increment of crack extension is larger, giving rise to a tearing line with a lower slope at large crack extensions.

The fracture toughness of the weld metal was determined by the single-specimen J-integral method. The J-Δa curves for the two specimens, are shown in Figure 5, did not clearly define tearing lines for determination of J_{Ic} owing to scatter of about $\pm$ 0.1 mm in Δa values. The tearing line for specimen MW-2 was determined by the ASTM method [5], i.e., linear least squares fit of valid data points The tearing line for specimen MW-4 could not be determined by the ASTM procedure because the valid data were clustered within a Δa range of .25 mm. The position of the tearing line for specimen MW-4 was the best fit through the valid data plus the data within 0.15 mm of the blunting line. The measurement problem is due, in part, to the large increments of cracks extension that occur after the initial 0.5 mm of crack extension. The load-displacement curves for the weld specimens had numerous small load drops prior to maximum load, and then one (specimen MW-4) or three (specimen MW-2) large load drops prior to fracture.

Fatigue Crack Propagation

The results of the fatigue crack growth rate tests at 4 K are summarized in Figure 6 and Table 4. The base metal data for both plate thicknesses fall in the same scatter band. Similarly, the data for two weld metal specimens fall in the same scatter band. The crack growth rates in the base metal are slightly higher than the rates in the weld metal, particularly at the lower ΔK levels; however, the difference is not considered to be statistically significant because of the overlapping scatter bands.

The fatigue crack growth rates measured in the 25Mn austenitic steel plates at 4 K are essentially the same as those observed in AISI grades 310S and 304L, as reported by Tobler and Reed [12]. The rates measured in the 25Mn steel

weldments are significantly lower at low ΔK values than those observed in 316L weldments, as reported by Whipple, McHenry, and Read [10].

Fracture Surface Observations

The fracture surfaces of representative fracture toughness and fatigue crack growth rate specimens of the plate and the weld metal were examined by scanning electron microscopy (SEM), transmission electron microscopy (TEM), and magnetic measurements.

Examination of the fracture surface using the SEM revealed that both the base metal and the weld failed in a tough ductile manner. The fracture surface of the base metal (Figure 1) has a coarse texture, which is indicative of high toughness; however, the dimples characteristic of ductile fracture by microvoid coalescence were not observed. Apparently, the inclusion content of the base metal was sufficiently low to reduce the formation of dimples, which are initiated at inclusions. In contrast, the fracture surface of the weld metal, shown in Figure 7, had many dimples that initiated at fine nonmetallic inclusions. This suggests that the weld metal toughness could be improved by reducing the inclusion content, e.g. by welding with the gas metal arc or the gas-tungsten-arc processes.

A thin foil was taken near the fracture surface and examined by TEM. No transformation was observed. In addition, magnetic measurements on the fracture surfaces did not indicate any ferromagnetism. Consequently, it is concluded that the austenitic stability of the 25 mn steel is sufficient to prevent α' martensite from forming at 4 K even in regions of high deformation, such as the fracture surfaces.

Visual examination of the fracture surfaces led to two interesting observations. First, in the base metal, secondary fractures occurred in a plane at a slight inclination to the fracture plane. These appeared as slivers

and may have contributed to the high toughness of the base metal. Second, no evidence of microfissuring was found on the fracture surfaces of the weld metal specimens. If microfissures were present in the weld, they would have been apparent on the fracture surface as small cracks perpendicular to the fracture surface.

CONCLUSIONS

The tensile properties, fracture toughness, and fatigue crack growth rates of a 25Mn austenitic steel plates and welds have been determined in liquid helium at 4 K. The results indicate that

1. The yield strength of the weld metal (961 MPa) overmatches the yield strength of the base metal 894 MPa.

2. The combination of yield strength and toughness of the base metal and welds compares favorably with the corresponding properties in the austenitic stainless steels.

3. The fatigue crack growth rates are similar in the base metal and welds and fall in the range of behavior observed in the 300-series austenitic stainless steel.

REFERENCES

1. Yoshimura, H., Masumoto, H., and Inoue, T., in Advances in Cryogenic Engineering, Vol. 28, Plenum Press, New York, (1982).

2. Yoshimura, H., Shimizu, T., Yada, H., and Kitajima, K., Transactions of the Iron and Steel Institute of Japan, 20, 187 (1980).

3. Yoshimura, H., Yamada, N., Honma, H., and Ito, T., Transactions of the Iron and Steel Institute of Japan, 16, 98 (1976).

4. Reed, R. P., in Advances in Cryogenic Engineering, Vol. 7, Plenum Press, New York, 448 (1962).

5. "ASTM Designation: E813-81, Standard Test for J_{Ic}, a Measuare of Fracture Toughness," in Annual Book of ASTM Standards, Part 10, American Society for Testing and Materials, Philadelphia, PA (1981).

6. Fowlkes, C. W., and Tobler, R. L., Engineering Fracture Mechanics, 8, 487 (1976).

7. Ledbetter, H. M. and Austin, M. W., Private Communication, National Bureau of Standards, Boulder, CO (1982).

8. Read, D. T., Reed, R. P., Cryogenics, 21, 415 (1981).

9. Elmer, J. W., McHenry, H. I., and Whipple, T. A., Strength and Toughness of Fully Austenitic Stainless Steel Filler Metals at 4 K, National Bureau of Standards, Boulder, CO, NBSIR 81-1645, 289 (1976).

10. Read, D. T., McHenry, H. I., Steinmeyer, P. A., and Thomas, R. D., Jr., Welding Journal Research Supplement 59, 104s (1980).

11. Whipple, T. A., McHenry, H. I., and Read, D. T., Welding Journal Research Supplement, 60, 72s (1981).

12. Tobler R. L., and Reed, R. P., in Advances in Cryogenic Engineering, Vol. 24, Plenum Press, New York, 82 (1978).

LIST OF TABLES

Table 1. Compositions of the 25Mn Austenitic Steel Base Plate and Welds (Ladle Analysis).

	C	Si	Mn	P	S	Ni	Cr	Mo	Al	Nb	N
Base Plate, %	0.22	0.86	25.6	0.024	0.001	0.97	4.67	-	0.009	0.043	0.040
Weld, %	0.185	0.63	25.0	0.010	0.003	2.79	6.50	1.41	-	-	-

Table 2. Tensile Properties of 25Mn Austenitic Steel at 4 K

Type	Plate Thickness, mm	Position/ Orientation	Yield Strength, MPa	Tensile Strength, MPa	Elongation, %
Base Metal	40	½T Transverse	876	1494	50
	40	½T "	882	1516	48
	80	½T "	907	1553	50
	80	½T "	911	1537	50
			894 Avg	1525 Avg	49
Weld metal	40	¼T Longitudinal	989	1278	36
	40	½T "	962	1351	39
	40	¼T "	958	1360	39
	40	¼T Transverse	968	1329	38
	40	½T "	983	1351	30
	40	¼T "	907	1360	29
			962 Avg	1338 Avg	35

Table 3. Fracture Toughness of 25Mn Austenitic Steel at 4 K.

Type	Test Method	J_{Ic}, kJ/m^2	$K_{Ic}(J)$, $MPa\sqrt{m}$
Base Metal	Multiple specimen	280	242
Weld Metal	Single specimen, MW-2	122	160
Weld Metal	Single specimen, MW-4	116	156

Table 4. Fatigue Crack Growth Rates of 25Mn Austenitic Steel at 4 K.

Specimen	Type	C*	n*	R**	ΔK range, MPa√m
M40-1	40-mm-thick plate	2.5×10^{-10}	5.0	0.996	29.9-51.7
M80-1	80-mm-thick plate	4.5×10^{-9}	4.2	0.998	34.4-69.7
M40-1, M80-1	Plate	2.6×10^{-9}	4.3	0.994	29.9-69.7
MW-1	Weld	1.6×10^{-10}	5.5	0.999	36.2-66.1
MW-3	Weld	1.9×10^{-10}	4.9	0.995	36.2-66.1
MW-1, MW-3	Weld	6.0×10^{-11}	5.2	0.995	33.0-71.5

* Empirical constants defined by:

$$\frac{da}{dN} = C(\Delta K)^n$$ where: da/dN is in mm/cycle
ΔK is in MPa√m

**R = linear correlation coefficient

List of Figures

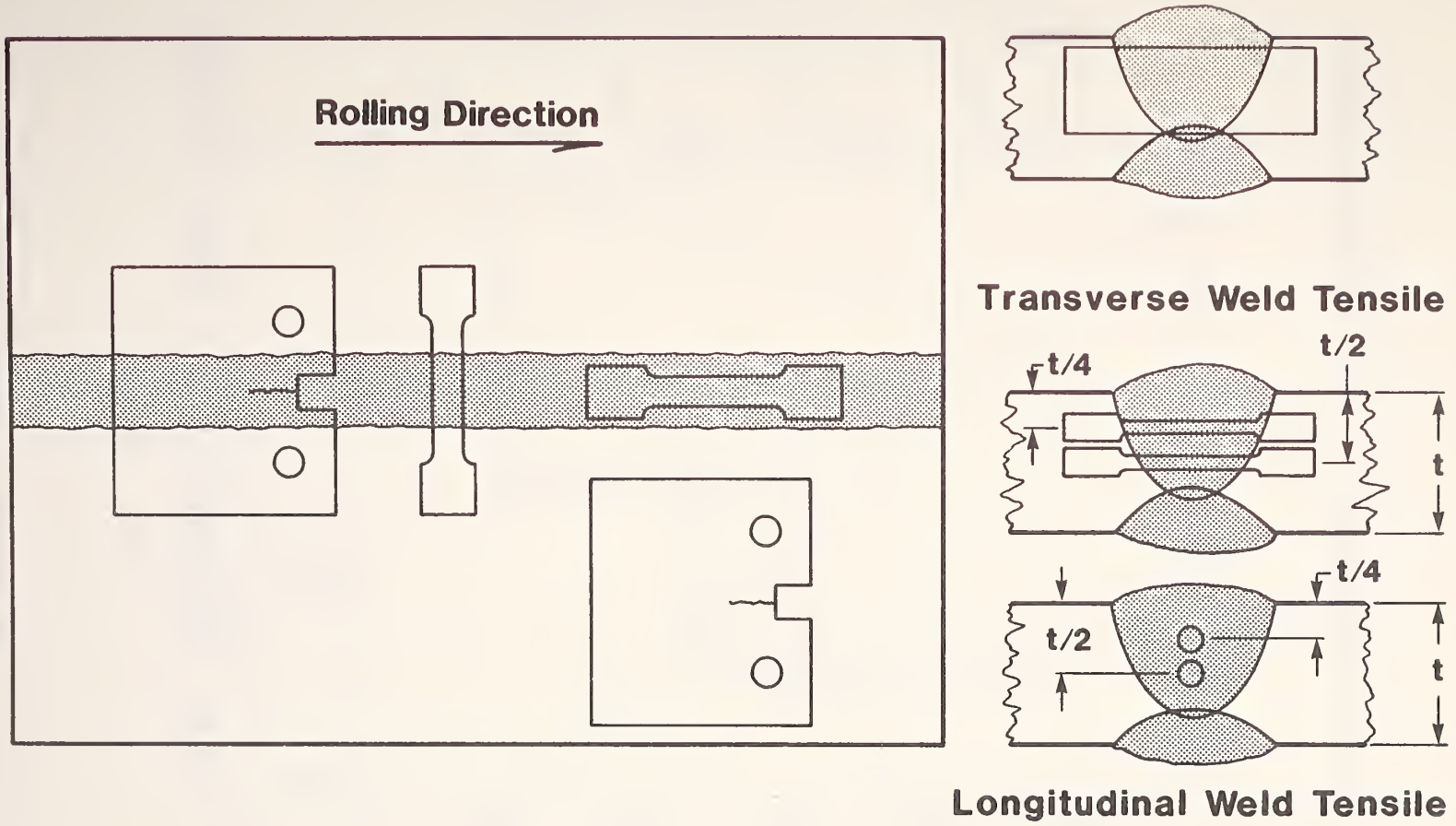

1. Test specimen locations and orientations.

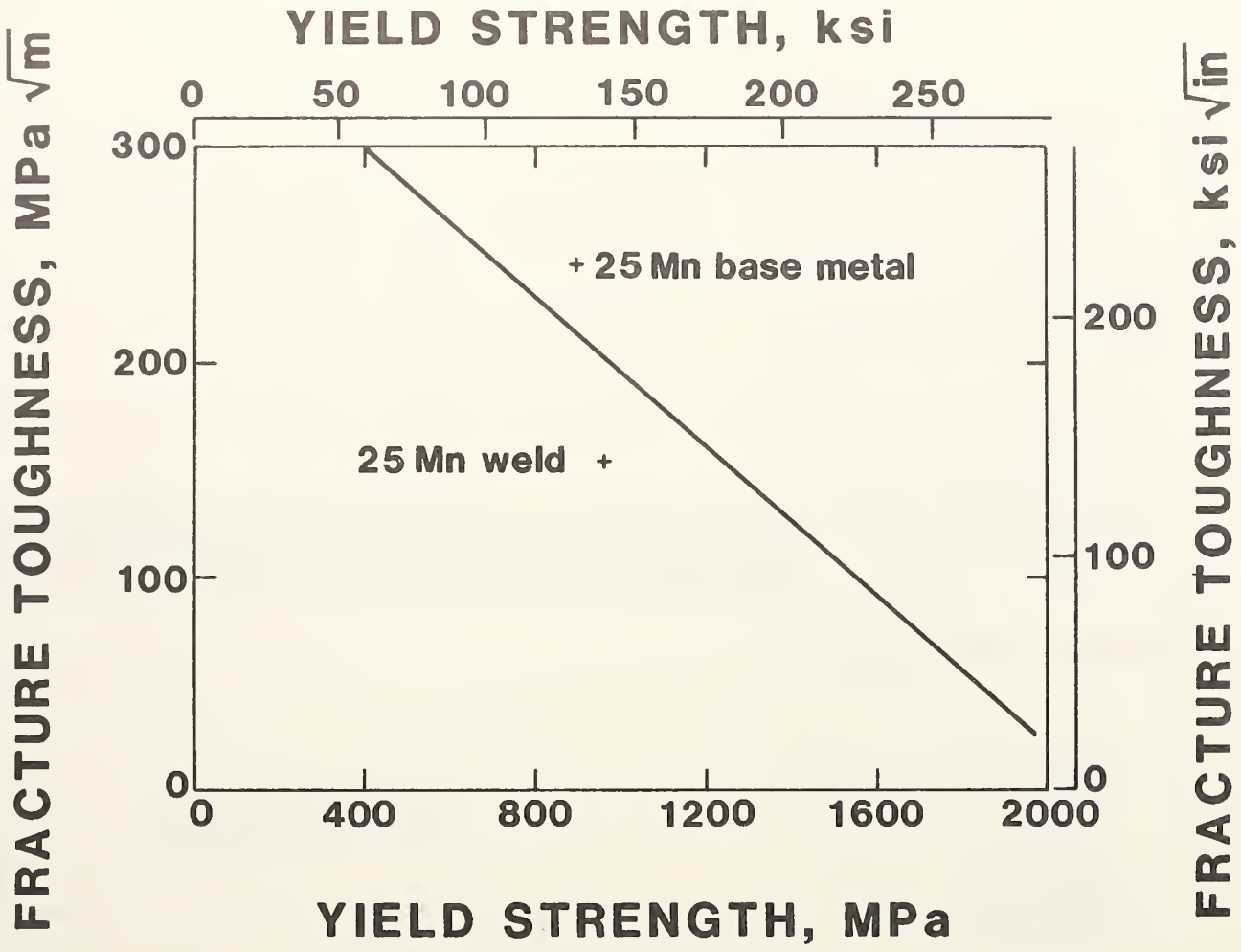

2. Fracture toughness vs. yield strength for 25Mn austenitic steel at 4 K. The trend line is for austenitic stainless steels at 4 K [8].

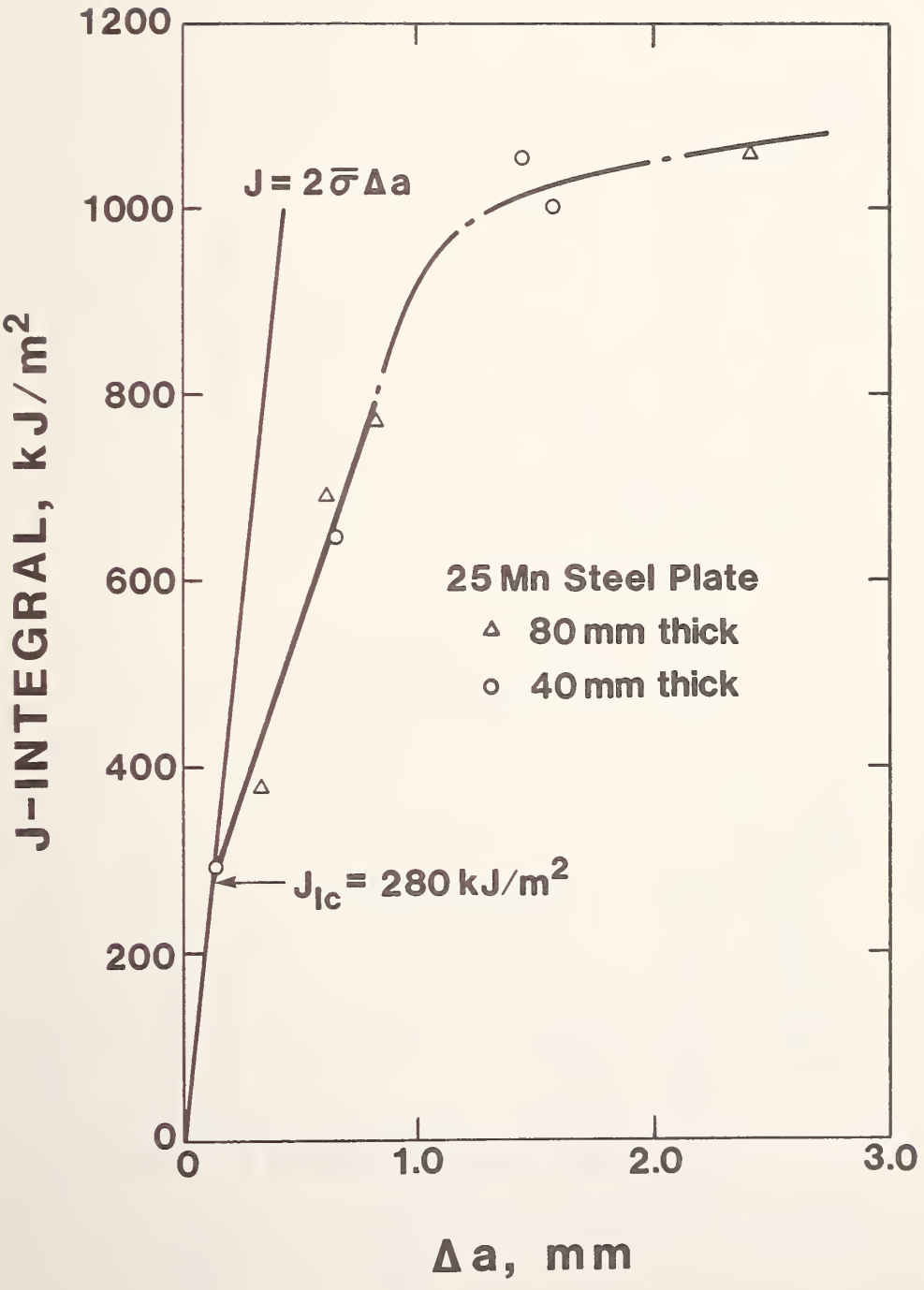

3. J-Δa resistance curve for 25Mn austenitic steel at 4 K.

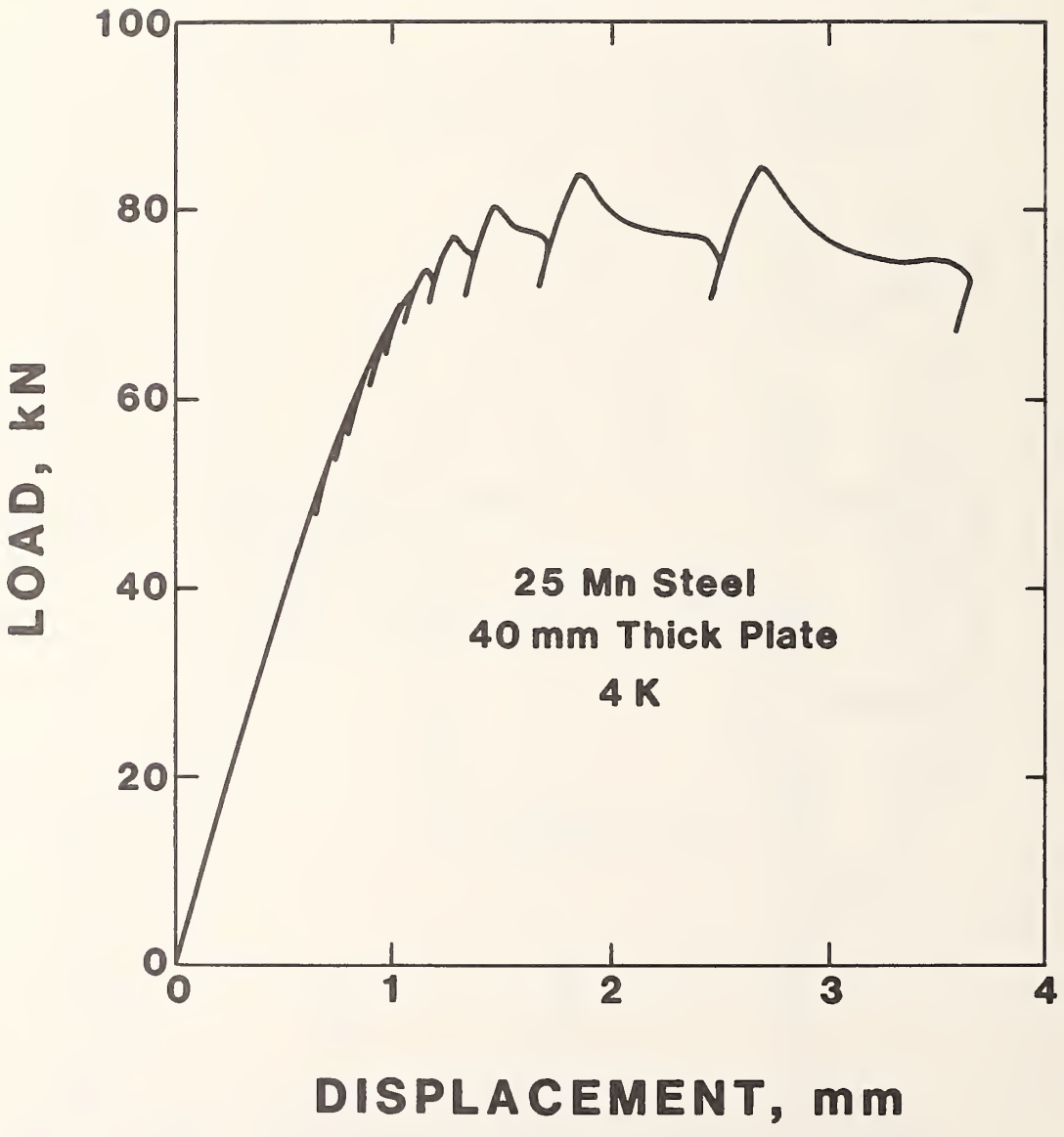

4. A load-displacement record for a fracture toughness test on 25Mn austenitic steel at 4 K.

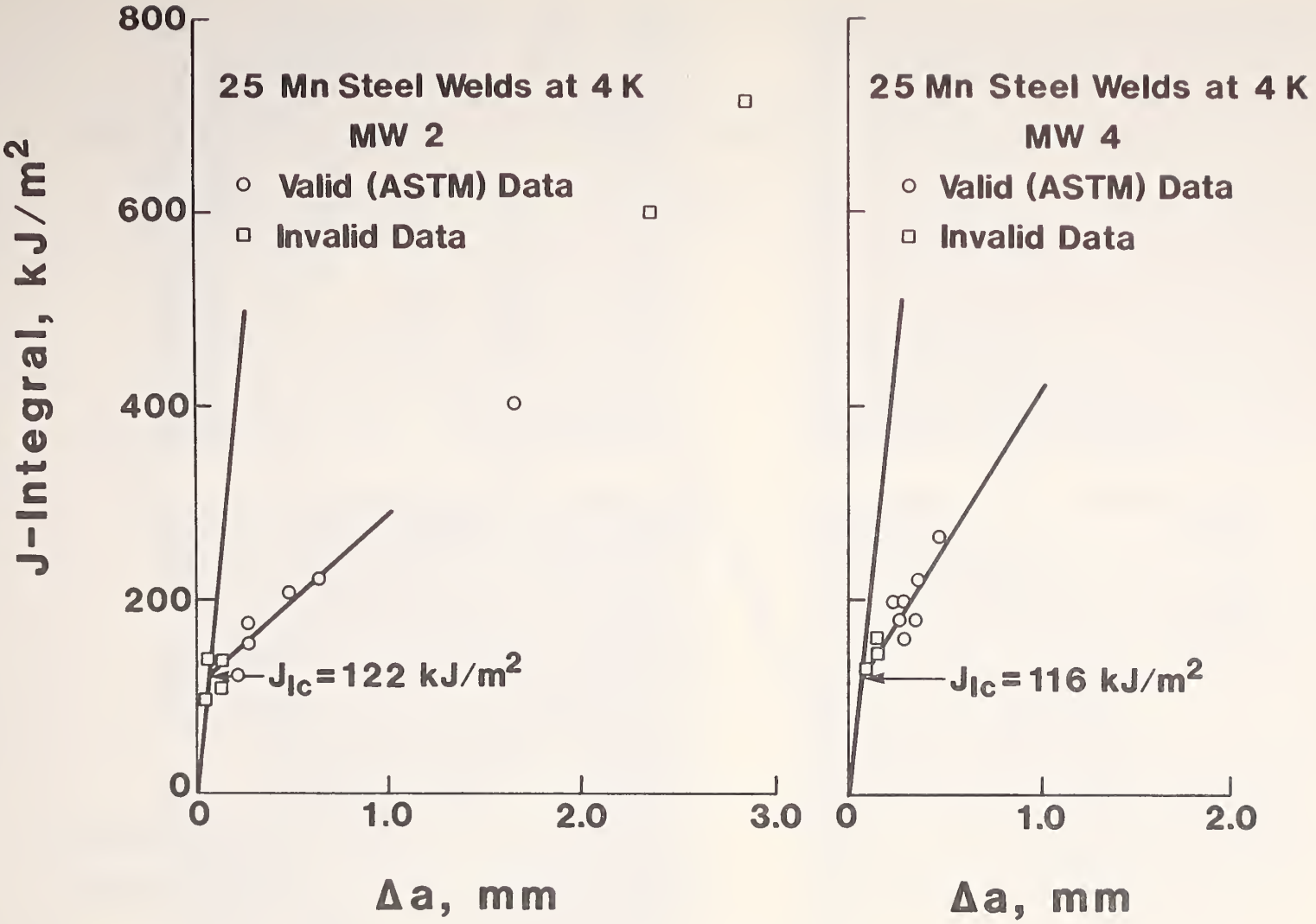

5. J-Δa resistance curve for 25Mn austenitic steel welds at 4 K.

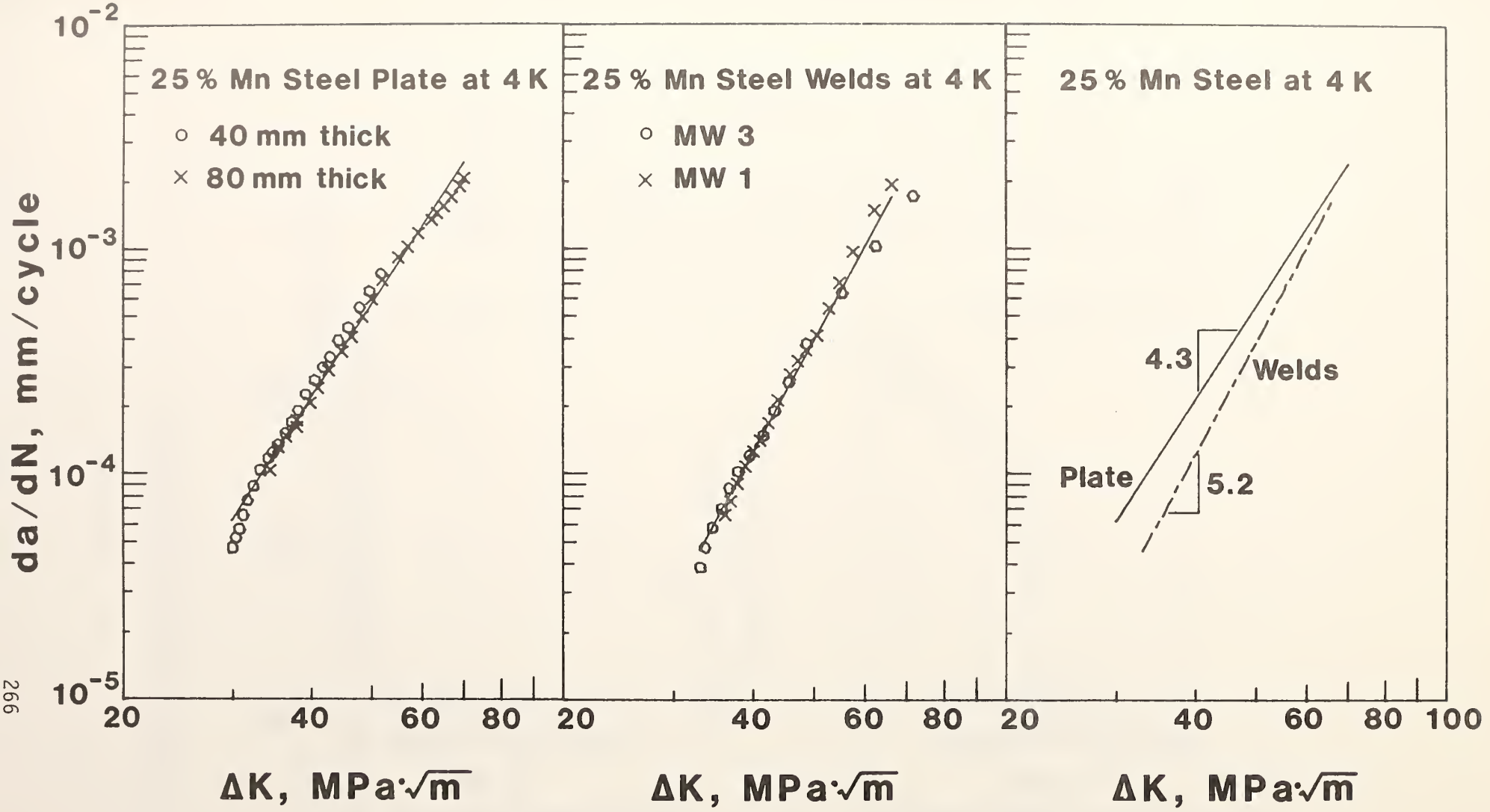

6. Fatigue crack growth rates for 25Mn austenitic steel at 4 K.

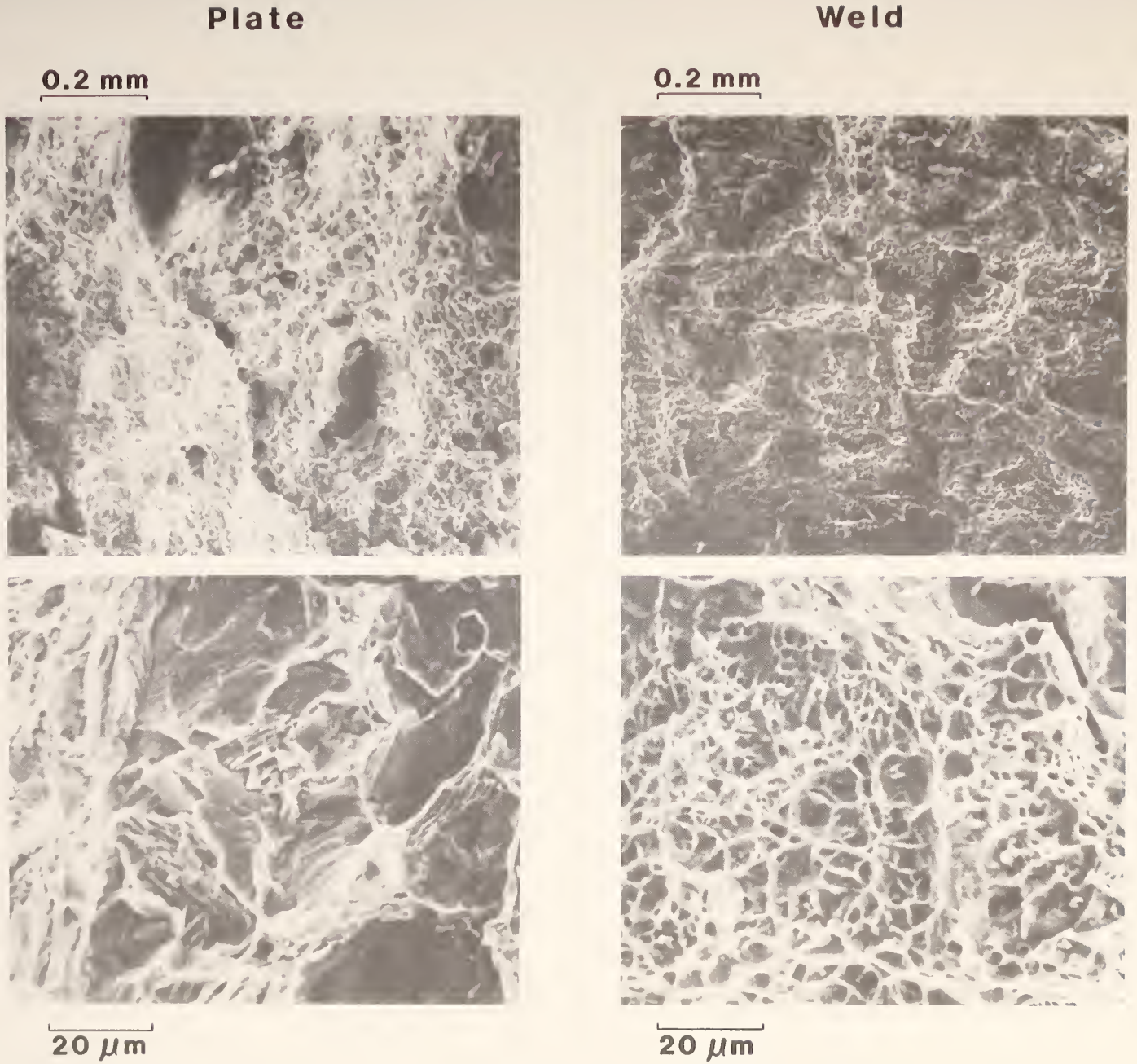

7. Scanning electron microscope photographs of fracture surfaces of 25Mn austenitic steel fracture toughness specimens tested at 4 K.

DEFORMATION AND FRACTURE BEHAVIOR OF DUPLEX AUSTENITE/DELTA-FERRITE MATERIALS AT 4 K.

T. A. Whipple
Fracture & Deformation Division
National Bureau of Standards
Boulder, Colorado

E. L. Brown
Department of Metallurgical Engineering
Colorado School of Mines
Golden, Colorado

ABSTRACT

A series of CF8M stainless steel castings, with varying ferrite contents, that were deformed at 4 K have been examined with optical and electron microscopy. The purpose of this study is to investigate the deformation and fracture modes in duplex austenite/delta-ferrite materials at 4 K.

It is shown that the typical fracture mechanism in duplex stainless steels is a brittle fracture in the delta-ferrite, followed by a ductile failure of the remaining ligaments of austenite. A completely brittle failure can occur if there is enough delta-ferrite to form a continuous crack path. It has also been found that the delta-ferrite, which was previously thought to be nondeforming at 4 K, does deform by a twinning mechanism. The importance of this deformation twinning in determining the macroscopic mechanical properties will be the subject of further investigation.

INTRODUCTION

To establish specific criteria for the selection of stainless steel weld filler alloys or casting alloys for cryogenic structural applications, it is first necessary to establish the effects that alloy variables have on the cryogenic mechanical properties of these materials. To date, a number of factors have been established that have an effect on the cryogenic properties of stainless steel weldments: the delta-ferrite content of the weldment, the nitrogen concentration in the weld, and the fusion zone grain size of fully austenitic weldments (1,2,3,4). Nevertheless, it still is not possible to predict the properties of a stainless steel weldment on the basis of these factors. Apparently there are factors beyond those stated above that cause the observed wide variations in fracture toughness (2,5,6). This paper is a continuation of a previous report (7), which presented metallographic observations on the fracture and deformation of duplex austenite/delta-ferrite structures at 4 K. This investigation is on a series of CF8M stainless steel castings that have been tested at 4 K.

There are currently very few 4-K mechanical property data on castings, but a few initial tests have shown a wide variation in fracture toughness similar to weldments (5). This is not surprising because weldments are actually rapidly solidified castings. Stainless steel castings also generally contain a certain percentage of delta-ferrite, although on a much coarser scale than that of weldments, owing to the slower solidification of castings. Because of the coarser structure and less directional nature of the delta-ferrite in castings, they provide an excellent model material for the study of basic deformation and fracture mechanisms in duplex austenite/delta-ferrite materials. It is anticipated that this study will aid in understanding the causes of the property variations in weldments and castings.

MATERIALS

The materials used in this investigation are a series of five CF8M stainless steel castings. The chemical compositions of these castings are given in Table 1. The nickel and chromium contents of the castings were varied to obtain five residual delta-ferrite contents, ranging from 1.1 to 28.5 volume percent. The castings were produced by a commercial vendor; the procedures used and room temperature mechanical properties have been reported previously (8). The castings were received in the form of 30.5 cm (12 in) x 61.0 cm (24 in) x 10.2 cm (4 in) blocks. All specimens were removed from areas at least 15.2 cm (6 in) from either end and 3.8 cm (1.5 in) from either surface. This was done to avoid any effects of the columnar grain structure near the casting surfaces.

Figures 1 and 2 show typical undeformed microstructures of the 1.1 and 28.5 percent delta ferrite castings, respectively.

PROCEDURES

For this investigation a number of sectioning, metallographic and fractographic techniques were employed. Each technique allows the observation of different phenomena. Macroscopic examination, optical microscopy, and scanning electron microscopy (SEM) were used for making observations.

For the most part, metallographic specimens were prepared by using standard mechanical grinding and polishing techniques, but in a few cases electrolytic polishing was used. A 10 percent oxalic acid electrolytic etch was used as a general purpose etch to reveal ferrite morphology and grain boundaries. A 10 N KOH electrolytic etch was used to reveal ferrite structure only. This is a deposition etch that colors the ferrite light blue to brown. The main attribute of this etchant is that it does not remove any material; therefore, it will not round the edges of cracks or produce pitting and other

etching artifacts. A boiling solution of 1 part H_2O_2 and 2 parts H_3PO_4 was used to reveal strain induced martensite.

RESULTS AND DISCUSSION

Low Temperature Deformation

It is generally true that bcc materials, such as delta-ferrite, go through a ductile-to-brittle transition at low temperatures, whereas fcc materials, such as austenite, do not. This is due to the difficulty of operating non-close-packed slip systems at low temperatures. The temperature at which this transition occurs in steels is influenced mainly by alloy content and microstructure; a higher nickel content and a smaller grain size lead to a lower transition temperature. Another factor to consider is the increase in strength with a reduction in temperature; bcc materials have a much more dramatic increase in yield strength than fcc materials at low temperatures.

These general observations lead to some expectations for the behavior of duplex stainless steels. At higher temperatures, both austenite and ferrite are ductile and have similar strengths; in this case the amount and morphology of delta-ferrite is expected to have a much smaller effect on strength and ductility than at low temperatures where the delta-ferrite is strong and brittle. The effect of the property transition in the delta-ferrite should be to increase the strain-hardening rate of the duplex alloy. Data that demonstrate the greater strengthening effect of delta-ferrite at cryogenic temperatures have been presented by Read, McHenry, Steinmeyer, and Thomas (1).

Evidence to date had indicated that delta-ferrite does not deform at 4 K. However, work on the series of CF8M castings has shown that this is not strictly true. As can be seen in Figure 3, the delta-ferrite does deform by a

twinning mechanism. The jogs in the delta-ferrite/austenite interface and the fact that twins are not observed in undeformed structures (Figures 1 and 2) demonstrate that they are, in fact, deformation twins. Further evidence of this conclusion is given in Figure 4 in which three twin variants are shown. A stereographic projection of the angles between the three variants shows that they are consistent with (112) twin planes, which is typical for deformation twinning in ferritic materials.

In a macroscopic sense, the deformation associated with twinning in the delta-ferrite is small; however, it may have some significant secondary effects. One of these effects can be seen in Figures 5 and 6. These figures show bands of intense martensite formation in the austenite at the ends of deformation twins in the delta-ferrite. This intense deformation could create preferred sites for void nucleation in the austenite.

Low Temperature Fracture

As discussed in the previous report (7), it appears appropriate to classify duplex austenitic stainless steel at low temperatures as a ductile matrix composite with hard, brittle discontinuous fibers. This is not an exact classification, since the delta-ferrite does show some evidence of deformation and can be either continuous or discontinuous, depending on solidification and cooling conditions, but this classification does provide a good starting point for the discussion of fracture mechanisms. There are three possible mechanisms for the fracture of ductile matrix/hard-discontinuous fiber composites (8).

1. Brittle fracture of the fibers.
2. Matrix/fiber interface separation.
3. Fiber pull-out.

Brittle fracture of the fibers occurs when the local stress in the fiber exceeds its fracture strength. The local stress in the fiber is not neces-

sarily the same as the macroscopic stress on the sample, it can be considerably higher owing to inhomogeneous plastic deformation in the matrix. Interface separation is an important consideration with artificial composites and with metal-matrix/particulate composites; however, the interface between austenite and delta-ferrite appears to be very strong and no evidence of interfacial separation has been observed. Fiber pull-out is sometimes associated with interface separation, but for the purpose of this discussion it means a ductile failure of the matrix near the matrix/fiber interface. This occurs when the fiber does not fracture, but the highly inhomogeneous deformation of the matrix near the fiber results in void nucleation at this location. The occurrence of one of these mechanisms over the others depends on fiber strength, content, and morphology.

In the previous study (7), evidence was found for both fiber fracture and fiber pull-out. Until that investigation there had been no direct observation of the brittle fracture of ferrite in weldments and castings at 4 K. Although this had long been assumed to be the cause of the reduction in toughness of stainless steel weldments with increasing ferrite content, direct observation was difficult because of the extremely small size of the ferrite in weldments.

From the observations made to date, fiber pull-out appears to be the less prevalent of the two fracture mechanisms observed. The most commonly observed mechanism is brittle fracture of the delta-ferrite. If the delta-ferrite is continuous, the brittle fracture will result in specimen failure. However, in the case of discontinuous delta-ferrite, the brittle fracture of discrete particles will cause stress concentrations that will result in ductile failure of the austenite matrix. An example of this mechanism is shown in Figure 7, where, brittle fractures in a delta-ferrite particle are shown with ductile fracture in the austenite between two cracks. This mechanism will result in a

fracture surface displaying a mixed mode fracture (shown in Figure 8), which is commonly observed in these materials.

The deformation twinning in the delta-ferrite does have an effect on the fracture process. The different orientation of the cleavage planes in the twins causes the crack to change direction. This can be seen in the micrograph in Figure 9. The deformation twinning and the change in crack path can result in additional energy being absorbed in the fracture process, which could result in a higher fracture toughness. It is not possible, at this time, to determine the quantitative effect that this has on the fracture toughness of these materials.

SUMMARY

Samples of stainless steel castings and weldments that had been deformed and fractured at 4 K were examined. The thrust of the investigation was to determine the mechanisms by which residual delta-ferrite affects the deformation and fracture of duplex austenite/delta-ferrite structures at cryogenic temperatures. Evidence was presented indicating that at low temperatures the delta-ferrite acts as a hard, brittle second phase particle. The manner in which these particles affect the mechanical properties of the material depends on the amount, properties and morphology of the second-phase particles. It was observed that the delta-ferrite reinforces the austenite matrix and causes the deformation to be inhomogeneous. Evidence was found for two fracture mechanisms: (1) brittle fracture of the delta-ferrite mixed with ductile failure of the matrix between delta-ferrite fractures and (2) ductile failure in the matrix near the austenite/ferrite interface, which was caused by the highly inhomogeneous deformation in this region. The occurrence of one of these mechanisms over the other depends on the morphology and properties of delta-ferrite. It was also observed that delta-ferrite deforms by a twinning mechanism at 4K. These deformation twins have an effect on the fracture process.

REFERENCES

1. D. T. Read, H. I. McHenry, P. A. Steinmeyer, and R. D. Thomas, "Metallurgical Factors Affecting the Toughness of 316L SMA Weldments at Cryogenic Temperatures," Weld. J. Res. Suppl., 59, 1980, p. 104s.

2. T. A. Whipple, H. I. McHenry, and D. T. Read, "Fracture Behavior of Ferrite-Free Stainless Steel Welds in Liquid Helium," Weld. J. Res. Suppl., 60, (4), 1981, p. 72s.

3. E. R. Szumachowski and H. F. Reid, "Cryogenic Toughness of SMA Austenitic Stainless Steel Weld Metals: Part I - Role of Ferrite," Weld. J. Res. Suppl., 57, 1978, p. 325s.

4. E. R. Szumachowski and H. F. Reid, "Cryogenic Toughness of SMA Austenitic Stainless Steel Weld Metals: Part II - Role of Nitrogen," Weld. J. Res. Suppl, 58, 1979, p. 34s.

5. T. A. Whipple and H. I. McHenry, "Evaluation of Weldments and Castings for Liquid Helium Service," in Materials Studies for Magnetic Fusion Energy Applications at Low Temperatures-IV, National Bureau of Standards, Boulder, CO, NBSIR 81-1645, 1981, p. 273.

6. T. A. Whipple and D. J. Kotecki, "Weld Process Study for 316L Stainless Steel Weld Metal for Liquid Helium Service," in Materials Studies for Magnetic Fusion Energy Application at Low TemperaturesIV, National Bureau of Standards, Boulder, CO, NBSIR 81-1645, 1981, p. 303.

7. T. A. Whipple and E. L. Brown, "Deformation and Fracture of Stainless Steel Castings and Weldments at 4 K," in Materials Studies for Magnetic Fusion Energy Applications at Low Temperatures-IV, National Bureau of Standards, Boulder, CO, NBSIR 81-1645, 1981, p. 415.

8. A. Kelly, "Particle and Fibre Reinforcement," in Strengthening Methods in Crystals, Halsted Press Division, John Wiley & Sons, New York, 1971, pp. 433-484.

Table 1. Chemical analysis of five heats of CF8M with variable ferrite content.

Heat	C	Mn	Si	Cr	Ni	Mo	N	% Delta-Ferrite* (volume)
1	0.06	1.10	0.59	18.04	13.24	2.12	0.05	1.1
2	0.06	0.38	1.16	19.62	10.61	2.12	0.05	8.2
3	0.06	0.36	1.13	19.23	8.25	2.16	0.05	17.2
4	0.06	0.35	0.95	20.40	8.22	2.13	0.05	23.1
5	0.05	0.39	1.11	22.54	9.84	2.26	0.05	28.5

*Measured by a metallographic point count.

LIST OF FIGURES

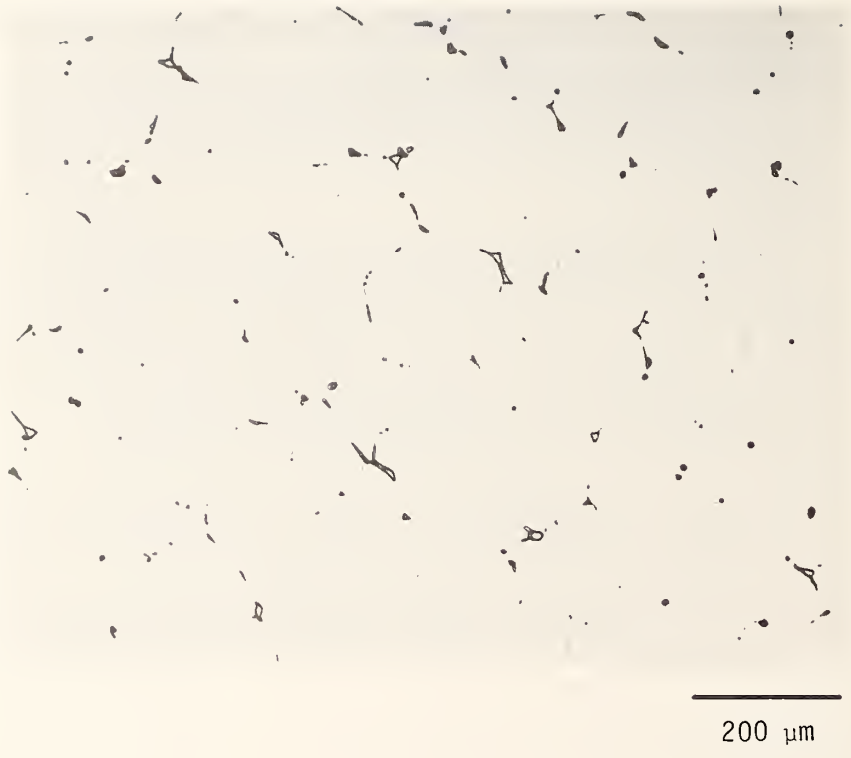

Figure 1. A micrograph of the undeformed initial structure of the 1.1 percent delta-ferrite casting.

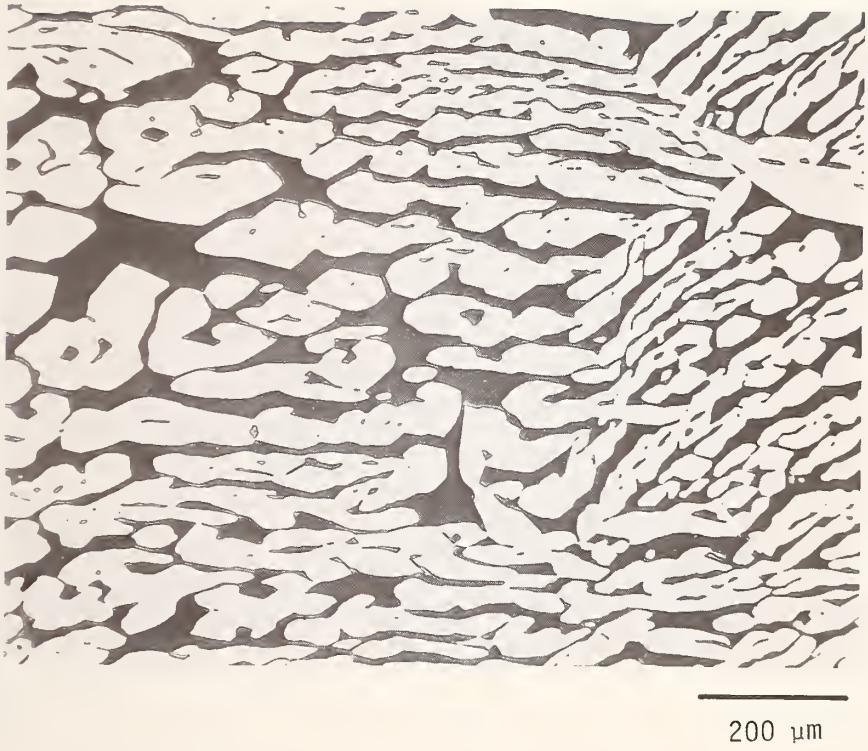

Figure 2. A micrograph of the undeformed initial structure of the 28.5 percent delta-ferrite casting.

Figure 3. A micrograph of a tensile specimen from the 28.5 percent delta-ferrite casting, showing deformation twinning.

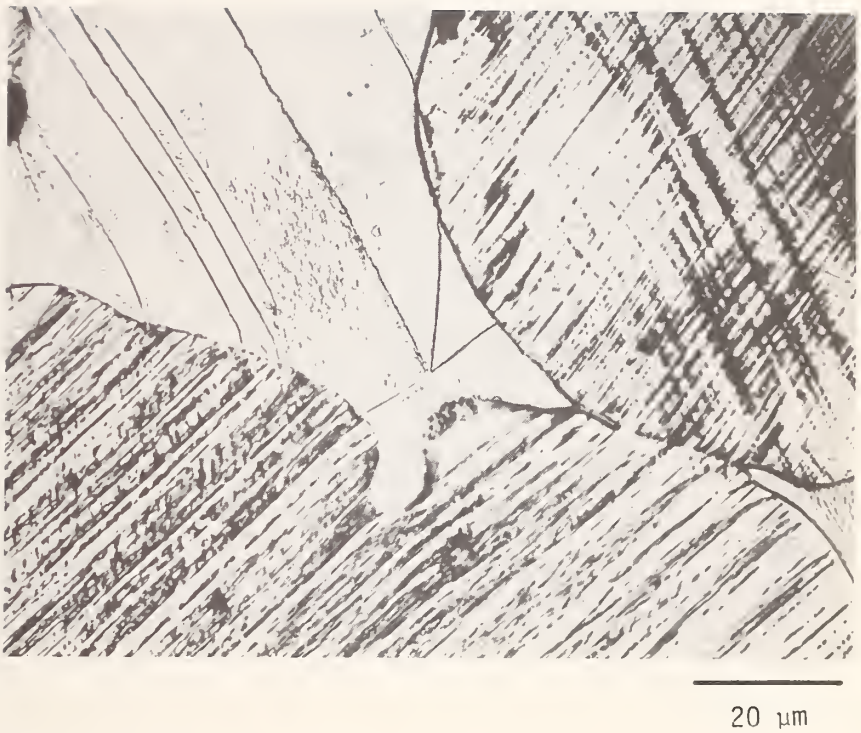

Figure 4. A micrograph of a tensile specimen from the 8.2 percent delta-ferrite casting, showing three deformation twin variants.

Figure 5. A high magnification micrograph of a tensile specimen from the 8.2 percent delta-ferrite casting, showing the intense deformation in the austenite associated with twinning in the delta ferrite.

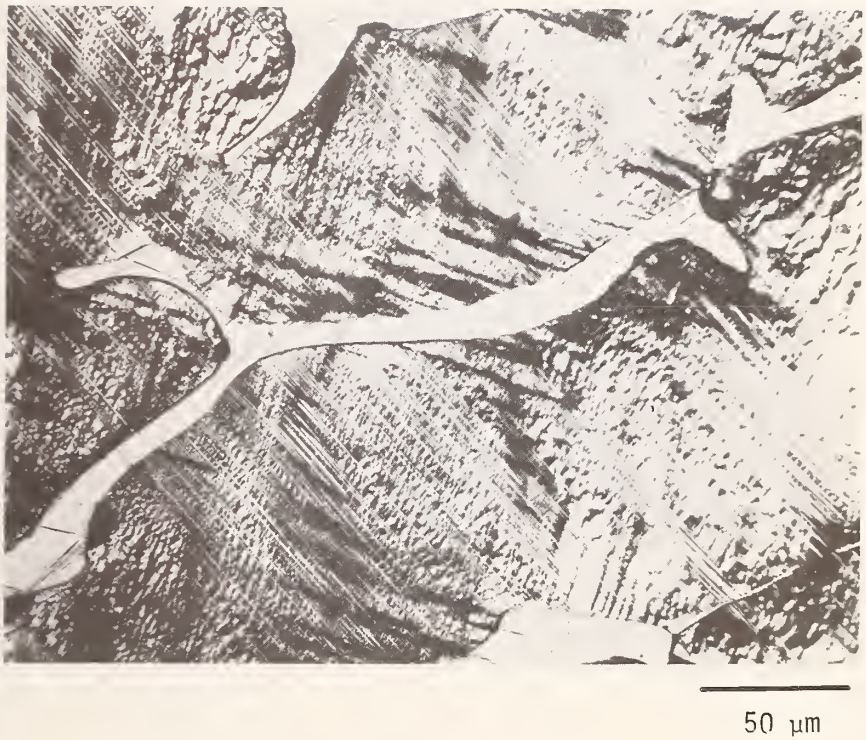

Figure 6. A micrograph of a tensile specimen from the 8.2 percent delta-ferrite casting, showing bands of deformation in the austenite caused by the deformation twinning of the delta ferrite.

Figure 7. A micrograph of a tensile specimen from the 28.5 percent delta-ferrite casting, showing ductile failure of austenite between brittle fracture of delta-ferrite particles.

Figure 8. A SEM fractograph of a fracture toughness specimen of the 8.2 percent delta-ferrite casting, showing the mixed mode fracture.

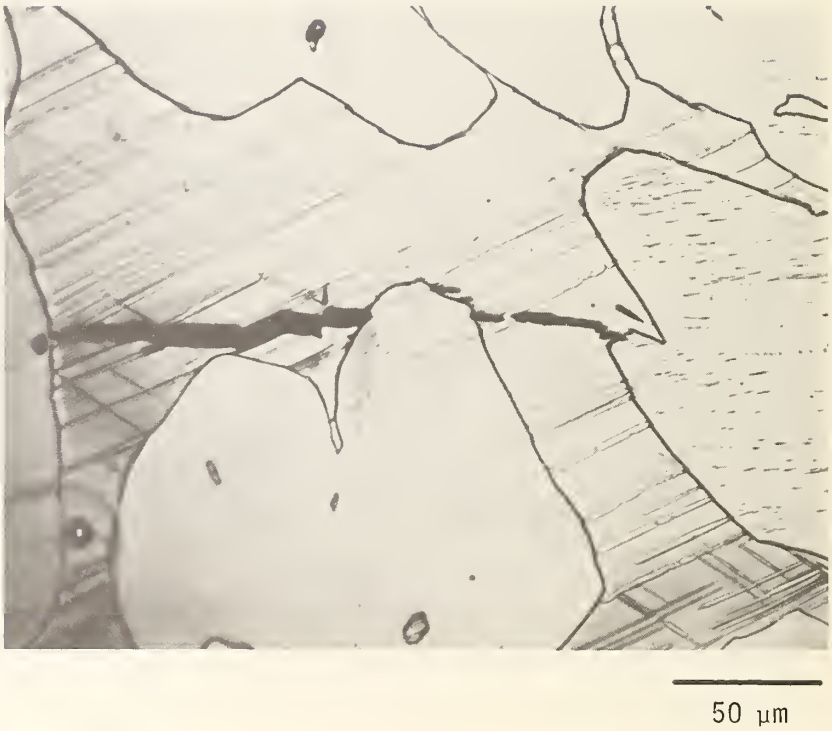

Figure 9. A micrograph of a tensile specimen from the 28.5 percent delta-ferrite casting, showing the effect of deformation twins on the crack path.

THE EFFECT OF DELTA-FERRITE ON THE MECHANICAL PROPERTIES OF CF8M STAINLESS STEEL CASTINGS AT 4 K

T. A. Whipple
Fracture and Deformation Division
National Bureau of Standards
Boulder, Colorado

ABSTRACT

A series of five CF8M stainless steel castings, with varying delta-ferrite contents, has been tensile and fracture toughness tested at 4 K. Tensile tests were conducted in the low strain region to establish the initial strain hardening behavior for comparison with two phase deformation theory. It was found that the tensile behavior of the duplex austenite/delta-ferrite structure fits very well with the two phase deformation theory proposed by Ashby. The initial strain hardening rate is determined by the mean-free-path between delta-ferrite particles. Fracture toughness results at 4 K show a decrease in fracture toughness with increasing delta-ferrite content up to approximately 15 percent; at this point a continuous delta-ferrite crack path is established, and the fracture toughness remains constant with increasing delta-ferrite.

INTRODUCTION

In some cryogenic structural applications it would be advantageous to use stainless steel castings, rather than wrought and welded construction. Castings have the advantage of a much lower cost of manufacture when complicated shapes are involved. To date, the use of stainless steel castings for 4-K service has been very limited; this may be partially due to the limited data available on the mechanical properties at 4 K (1).

The most significant data available on the tensile and fracture toughness properties of stainless steel castings at 4 K came from a series of CF8 centrifugal castings with varying delta-ferrite contents (1,2). There were six heats from three different vendors with delta-ferrite contents ranging from 0 to 14.5 percent. The results generally showed an increase in strength and a decrease in fracture toughness with increasing ferrite content. The purpose of this testing on CF8 castings was to select a material for use as the bore tube for a MHD superconducting magnet.

In the present study a series of five CF8M stainless steel castings was tensile and fracture toughness tested at 4 K. The purpose of this study is twofold: First, it is intended to develop a data base on the tensile and fracture toughness properties of CF8M at 4 K. Second, it is intended to aid in the understanding of the effects of delta-ferrite on the mechanical properties of duplex austenite/delta-ferrite structures at 4 K. It is anticipated that the description of the fundamental aspects of the deformation behavior of castings will also be applicable to stainless steel weldments, since they also generally contain delta-ferrite.

MATERIALS

The materials used in this investigation are a series of five CF8M stainless steel castings. The nickel and chromium contents of the castings were varied to obtain five residual delta-ferrite contents, ranging from 1.1 to 28.5 percent. The castings were produced by a commercial vendor; the procedures used and room temperature mechanical properties have been reported previously (4). The castings were received in the form of 30.5-cm (12-in) x 61.0-cm (24-in) x 10.2-cm (4-in) blocks. All specimens were removed from areas at least 15.2 cm (6 in) from either end and 3.8 cm (1.5 in) from either surface. This was done to avoid any effects near the casting surfaces.

PROCEDURES

Tensile Tests

The tensile tests at 4 K were conducted with the test apparatus and cryostat described by Reed (5). The test specimens were 0.635-cm (0.25-in) smooth bar tensile specimens, with a 2.54-cm (1.0-in) gage length. The high-sensitivity strain measurements were made using two resistance type strain gages mounted on the specimens 180° apart. The strain limit for these gages is usually about 2 percent. A strain gage extensometer was also mounted on the specimen; this measured up to 10 percent strain with lower sensitivity. The remainder of the stress-strain curve was obtained from a load-time record at a known crosshead displacement rate.

Plastic strain measurements in the low strain region (less than 0.5% plastic strain) were made using the resistance strain gages and signal conditioning equipment capable of resolving 10^{-6} strain. A load/unload technique was used in which the specimen is loaded to a given stress and then unloaded to zero stress. The residual plastic strain is recorded and the

specimen is reloaded to a higher stress and the process is repeated until a total plastic strain of about 0.5 percent is reached. At this point the specimen is loaded monotonically to failure and the strain is recorded using the extensometer and load/time record.

Fracture Toughness Tests

For these tests, a new fracture toughness test procedure using three-point-bend-specimens, rather than the previously used compact-tension (CT) specimens, has been developed. The single edge notched three point bend specimens are 2.54-cm (1.0-in) wide, 2.54-cm (1.0-in) thick, and have a span of 10.2 cm (4.0 in). The main difference in the single-specimen J-integral test procedure is that with three-point-bend specimens it is necessary to measure two displacements: the load-line displacement and the crack-mouth-opening displacement. With CT specimens, the two displacements are coincident. A direct measurement of the load-line displacement is made using the comparison bar method developed by Dawes (6). The load-line displacement is used to calculate the J-integral and the crack-mouth-opening displacement is used to calculate the crack length using a standard compliance function (7).

A three-point-bend fracture-toughness specimen, with the comparison bar and clip gages attached, is shown in figure 1. The three-point-bend test fixture used for cryogenic testing is shown in figure 2. The test data are acquired and reduced by a laboratory minicomputer, as described by Read (8).

Metallography

The volume percent delta-ferrite and the mean free path between delta-ferrite particles were measured metallographically, using a computerized image analyzer. The specimens were electrolitically etched using a 10 N KOH solution, which gives good phase contrast. The values reported for volume percent and mean free path represent the average for 400 fields at 100 times magnification.

RESULTS

The results of tensile tests at 4 K are given in table 2 and shown graphically in figures 3, 4, and 5. All results are the average of two tests. Figure 3 shows the stress versus plastic strain curves at less than 0.2-percent plastic strain (yield strain). Note that the proportional limit (the onset of plastic deformation) occurs at very close to the same stress for all five delta-ferrite contents. The differences in 0.2-percent offset yield strength arises from differences in the strain-hardening rate. In this plastic strain region, the curve for the 17.3-percent delta-ferrite casting lies below that of the 8.2 percent delta-ferrite casting, however, the higher delta-ferrite casting has a higher strain hardening rate, and the two curves intersect at 0.2 percent plastic strain.

Figure 4 shows the complete stress versus plastic strain curves for the five CF8M castings. As do most materials tested at 4 K, the castings did display serrated stress/strain curves. For clarity, the serrations are not shown and the curves are smooth lines drawn through the peak stresses. Also not shown is the remainder of the curve for the 1.1 percent delta-ferrite casting, which actually had a total elongation of 49 percent. The important features to note in figure 4 are that in the low plastic strain region (less than 5 percent) there is a very large increase in strain hardening rate with increasing delta-ferrite content and that above this strain level the curves are approximately parallel.

These observations are shown more clearly in figure 5, which gives the flow stress as a function of delta-ferrite content at various levels of plastic strain. At low strains, 10^{-5} and 10^{-4}, the stress shows no definite correlation with the delta-ferrite content; however, as the strain increases, the flow stress becomes linear with delta-ferrite content. Also note that at

0.025 strain and above the lines are parallel, indicating that the strain hardening rate is independent of delta-ferrite content.

The results of fracture toughness testing at 4 K as a function of delta-ferrite content are given in table 3 and shown graphically in figure 6. The fracture toughness result on the 1.1 percent delta-ferrite casting is invalid by specimen size requirements and is used here only as an approximate value. However, it can be said that the fracture toughness of this alloy is much higher than the other four heats and is comparable to that of wrought materials of similar compositions. The interesting feature of the fracture toughness data is that the three high delta-ferrite heats (17.3, 23.1, and 28.5 percent) have approximately the same fracture toughness. Also shown on figure 6 are the fracture toughness results from Reference 9 on a series of 316L weldments that are similar in composition to CF8M castings. These data indicate that at a given delta-ferrite content castings have a higher fracture toughness than weldments.

DISCUSSION

Extensive metallographic observations on stainless steel weldments and castings containing delta-ferrite, which have been deformed and fractured at 4 K, has qualitatively shown that these duplex materials can be treated as a ductile matrix/hard-brittle discontinuous fiber composite (10). The materials previously examined did not constitute a controlled series on which quantitative analysis could be performed. The present study on the controlled series of CF8M stainless steel castings with the chromium and nickel contents varied to change the delta-ferrite content does make this analysis possible. There are two basic approaches to modeling the deformation and fracture of two phase materials.

The composite modeling approach attempts to predict the properties based on the volume fraction of fibers and the properties of the two constituents.

This approach is best developed and most applicable to unidirectional continuous fiber composites (11). The composite model in its simplest form is called the "rule of mixtures," which predicts the total stress to be divided between the fiber and matrix in proportion to the volume fractions.

$$\sigma_c = \sigma_f V_f + \sigma_m V_m \quad , \tag{1}$$

where V_f and V_m are the volume fractions of the fiber and matrix, respectively. The assumption implicit in the use of this equation is that the strain in the fiber and matrix are equal. This assumption is good for unidirectional continuous fiber composites stressed axially with respect to the fiber orientation. Deviations from this assumption make the rule of mixtures less valid. Considerable effort has been made to modify this model for other cases (12,13); these efforts have resulted in varied success and are generally only applicable to very limited cases.

The results of this study do follow the form predicted by the rule of mixtures, that is, the stress is linearly related to the volume fraction of delta ferrite (see figure 5). However, beyond this point the composite modeling approach cannot do much towards describing the deformation mechanisms. For these reasons the following model is preferred.

The other approach to modeling the deformation of two phase materials is the micro-mechanical model. In this model the microscopic deformation mechanisms are used to predict the effect of second phase particles on the macroscopic properties. The model is described in detail by Ashby (14), and only the major points are discussed here. The case described by this model is that of a ductile matrix with a nonplastically deforming second phase. To describe the plastic deformation of this type of material the concept of two different types of dislocations is introduced: geometrically necessary and statistically stored dislocations. Geometrically necessary dislocations are those that are needed to accommodate the nonuniformity of strain in the matrix

when it contains a particle that does not deform. The density of these dislocations can be calculated as a function of the particle size, shape and arrangement and the plastic strain in the matrix. The other type of dislocations, statistically stored, are those dislocations that are produced in the matrix as a result of plastic strain, independent of the presence of a second-phase particle.

Ashby has shown that densities of geometrically necessary and statistically stored dislocations can be related to strain in a general way by

$$\rho^G = \frac{4\gamma}{\lambda^G b} \tag{2}$$

and

$$\rho^S = \frac{4\gamma}{\lambda^S b} \tag{3}$$

where λ^G is the geometric slip distance, λ^S is the slip distance for statistical storage, γ is the shear strain, and b is the Burgers vector. λ^G is a microstructural parameter related to the arrangement of second phase particles and does not vary with strain. λ^S, however, does vary with strain, becoming smaller as the strain increases.

How these dislocation densities affect the macroscopic stress-strain properties will now be considered. The general expression relating the flow stress to the dislocation density is (15).

$$\tau = \tau_0 + CGb\sqrt{\rho} \tag{4}$$

where τ is the applied shear stress, τ_0 is the frictional stress, G is the shear modulus and C is a constant. The dislocation density in this equation is the sum of the two densities discussed above; therefore the flow stress will be controlled by the larger of the two dislocation densities. At the onset of plastic deformation, λ^S (equation 3) can be taken as the grain size of the matrix. If the microstructural parameter, λ^G, is smaller than the grain size of the matrix, the geometrically necessary dislocation density will be

larger and will dominate the early stages of deformation. Since λ^S decreases with strain, the statistically stored dislocation density will increase more rapidly and eventually overtake the geometrically necessary dislocation density and dominate the flow stress at higher strains.

To discuss this model with respect to the duplex austenite/delta-ferrite stainless steel castings of this study the microstructure of the castings was considered to be the ideal case shown in figure 7. In this ideal microstructure the delta-ferrite occurs as a cubic array of square plates. Ashby (14) has shown the geometrically necessary dislocation density for this arrangement to be

$$\rho^G = \frac{4\gamma}{b\ell} \tag{5}$$

where ℓ is the mean free path between plates. This parameter has been measured for the five CF8M castings and is given in table 4. The effect of increasing the delta-ferrite content is to reduce this value.

Based on the Ashby model it is possible to predict, in a qualitative manner, the differences in stress-strain behavior between the five CF8M castings. Referring to equation 4, the onset of plastic deformation is only dependent on the frictional stress, τ_0, in the matrix and should be independent of delta-ferrite content. At low strain levels the flow stress will be controlled by the geometrically necessary dislocation density, since the mean free path between delta-ferrite particles is much smaller than the austenite grain size. If the geometrically necessary dislocation density is controlling, equation 5 can be substituted into equation 4

$$\tau = \tau_0 + CG\left(\frac{b\gamma}{\ell}\right)^{\frac{1}{2}} \tag{6}$$

and at a constant strain, the flow stress should be proportional to the inverse square root of the mean free path. At some higher strain the

statistically stored dislocation density will become controlling and the increase in flow stress with increasing strain (strain hardening rate) should be independent of delta-ferrite content. Since the strain at which the statistically stored dislocation density becomes controlling is dependent on the difference between the austenite grain size and the delta-ferrite spacing, it should also increase with increasing delta-ferrite content.

The tensile results, at 4 K, from the CF8M castings, (figures 3, 4, and 5), fit very well with the above predicted behavior. The only exception was that the onset of plastic strain, taken to be 10^{-5} plastic strain, did not occur at the same stress for all the castings. This means that τ_0 is not constant. The exact reason for this has yet to be determined, however, it could be due to differences in compositions of the austenite or a number of other factors. To eliminate this factor in the analysis τ_0 is taken to be the flow stress at 10^{-5} plastic strain and equation 6 is rearranged.

$$\tau - \tau_{10^{-5}} = CG\left(\frac{b\gamma}{\ell}\right)^{\frac{1}{2}} \qquad (7)$$

This predicts that the difference between the flow stress at a given strain and the flow stress at 10^{-5} strain is proportional to the inverse square root of the mean free path between delta-ferrite particles. The data for two strains are plotted on figure 8 and show a good fit with the theoretical slope.

The foregoing discussion demonstrates that the duplex structure of CF8M castings at 4 K behaves as predicted by two-phase deformation theory. This results in a better understanding of the deformation of duplex structures at 4 K and may lead to the determination of methods of improving the performance of these materials.

An analytical treatment of the fracture toughness properties of two phase materials is much more difficult than that of tensile properties. This analysis will be undertaken in future work. However, a few points can be made with respect to the fracture toughness results of this study. It is evident from numerous studies that an increase in the delta-ferrite content of stainless steel weldments and castings decreases the fracture toughness. This study has shown that at higher delta-ferrite contents the fracture toughness reaches a constant level. Metallographic and fractographic evidence has shown that this is related to the establishment of a continuous delta-ferrite path through which the crack can propagate, without the necessity of ductile failure in the austenite. The fracture toughness value at high delta-ferrite contents is consistent with what would be expected of a ferritic stainless steel of similar composition.

CONCLUSIONS

1. The tensile behavior of CF8M stainless steel castings at 4 K is consistent with a two-phase deformation model, which predicts the relative strain hardening rates as a function of the mean free path between delta-ferrite particles.

2. Increasing the delta-ferrite content of CF8M castings decreases the fracture toughness at 4 K, up to a delta-ferrite content of 17 percent. Above this point the fracture toughness is constant.

ACKNOWLEDGMENT

This study was supported by the Department of Energy Office of Magnetic Fusion Energy. The author would like to thank R. J. Fields of NBS for the quantitative metallography work he performed.

REFERENCES

1. D. Dew-Hughes and K. S. Lee, "The Choice of Steel for the Isabelle Magnet Tubes," Advances in Cryogenic Engineering, Vol. 26, Plenum Press, New York, (1981), pp. 151-157.

2. E. L. Brown, T. A. Whipple and R. L. Tobler, "Fracture Toughness of CF8 Castings in Liquid Helium," Met. Trans. To be published. Also in Materials Studies for Magnetic Fusion Energy Applications at Low Temperatures-V, National Bureau of Standards, Boulder, CO, NBSIR 82- (1982) pp. 107-143.

3. T. A. Whipple and H. I. McHenry, "Evaluation of Weldments and Castings for Liquid Helium Service," in Materials Studies for Magnetic Fusion Energy Applications at Low Temperatures-IV, National Bureau of Standards, Boulder, CO, NBSIR 81-1645, (1981), pp. 273-287.

4. L. Finch, "The Influence of Ferrite and Nitrogen on the Mechanical Properties of CF8M Cast Stainless Steel," in Materials Studies for Magnetic Fusion Energy Applications at Low Temperatures-IV, National Bureau of Standards, Boulder, CO, NBSIR 81-1645, (1981) pp. 337-355.

5. R. P. Reed, "A Cryostat for Tensile Tests in the Temperature Range 300 to 4 K," in Advances in Cryogenic Engineering, Vol. 7, K. D. Timmerhaus ed., Plenum Press, New York (1961), pp. 448-454.

6. M. G. Dawes, Welding Institute Research Bulletin, 7, (1976), p. 185.

7. A. Saxena and S. J. Hudak, Jr., "Review and Extension of Compliance Information for Common Crack Growth Specimens," Int. J. of Fracture, 14, 5, (1978), pp. 453-468.

8. D. T. Read, "The Computer-Aided J-Integral Test Facility at NBS," in Materials Studies for Magnetic Fusion Energy Applications at Low Temperatures-III, National Bureau of Standards, Boulder, CO, NBSIR 80-1127, (1980), p. 205.

9. D. T. Read, H. I. McHenry, P. A. Steinmeyer, and R. D. Thomas, "Metallurgical Factors Affecting the Toughness of 316L SMA Weldments at Cryogenic Temperatures," Weld. J. Res. Suppl., 59, (1980), pp. 104s-113s.

10 T. A. Whipple and E. L. Brown, "Deformation and Fracture of Stainless Steel Castings and Weldments at 4K," in Materials Studies for Magnetic Fusion Energy Applications at Low Temperatures-IV, National Bureau of Standards, Boulder, CO, NBSIR 81-1645, (1981), pp. 415-451.

11. A. Kelly, "Particle and Fibre Reinforcement," in Strengthening Methods in Crystals, Halsted Press Division, John Wiley & Sons, New York, (1971), pp. 433-484.

12. S. T. Mileiko, "The Tensile Strength and Ductility of Continuous Fibre Composites," J. of Mat. Sci., 4, (1969), pp. 974-977.

13. B. W. Rosen, "Mechanics of Composite Strengthening," in Fiber Composite Materials, ASM, Metals Park, Ohio, (1965), pp 37-75.

14. M. F. Ashby, "The Deformation of Plastically Non-Homogeneous Alloys," in Strengthening Methods in Crystals, Halsted Press Division, John Wiley & Sons, New York, (1971), pp. 137-192.

15. F. R. N. Nabarro, Z. S. Basinski and D. B. Holt, "The Plasticity of Pure Crystals" Adv. in Physics, 13, (1964), p. 193.

LIST OF TABLES

Table 1. Chemical analysis of five heats of CF8M with variable ferrite content.

Heat	C	Mn	Si	Cr	Ni	Mo	N	% Delta-Ferrite* (volume)
1	0.06	1.10	0.59	18.04	13.24	2.12	0.05	1.1
2	0.06	0.38	1.16	19.62	10.61	2.12	0.05	8.2
3	0.06	0.36	1.13	19.23	8.25	2.16	0.05	17.2
4	0.06	0.35	0.95	20.40	8.22	2.13	0.05	23.1
5	0.05	0.39	1.11	22.54	9.84	2.26	0.05	28.5

*Measured by a metallographic point count.

Table 2. Tensile properties of CF8M stainless steel castings at 4 K.

Heat	Flow Stress at Given Strain, MPa				Ultimate Strength	Elongation
	10^{-5}	10^{-3}	$2x10^{-3}$	10^{-2}	MPa	%
1	378	556	581	614	1215	49
2	448	613	653	700	986	21
3	308	574	641	779	1143	19
4	376	630	707	855	1221	19
5	410	783	851	962	1164	11

Table 3. Fracture toughness properties of CF8M castings at 4K.

Heat	J_{Ic} KJ/m^2	$K_{Ic}(J)$ $MPa\sqrt{m}$
1	562.0*	352*
2	99.4	148
3	62.1	117
	52.5	108
4	52.5	108
	48.1	103
5	49.0	104
	49.9	104

*Invalid by specimen size requirements.

Table 4. The mean free path between delta-ferrite particles in the CF8M castings.

Heat	Mean Free Path mm
1	1.55
2	0.185
3	0.074
4	0.064
5	0.044

LIST OF FIGURES

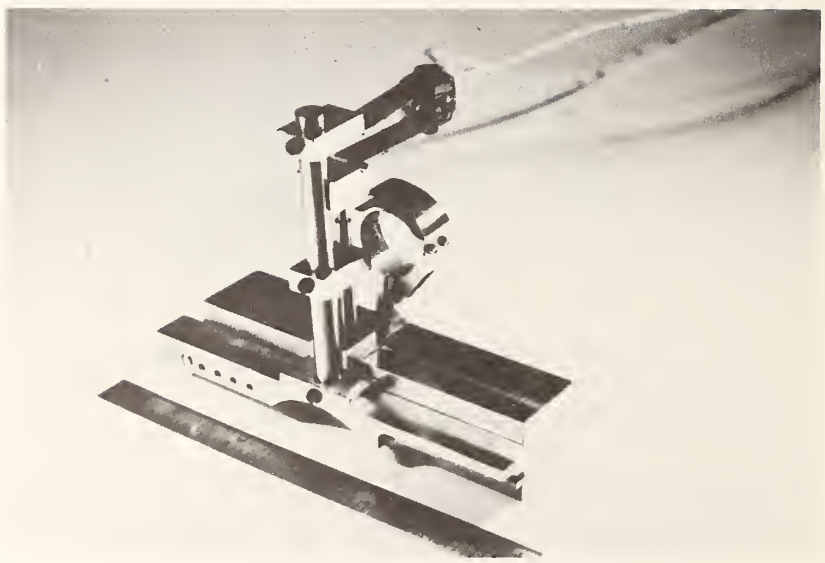

Figure 1. A three-point-bend fracture toughness specimen with the comparison bar and clip gages.

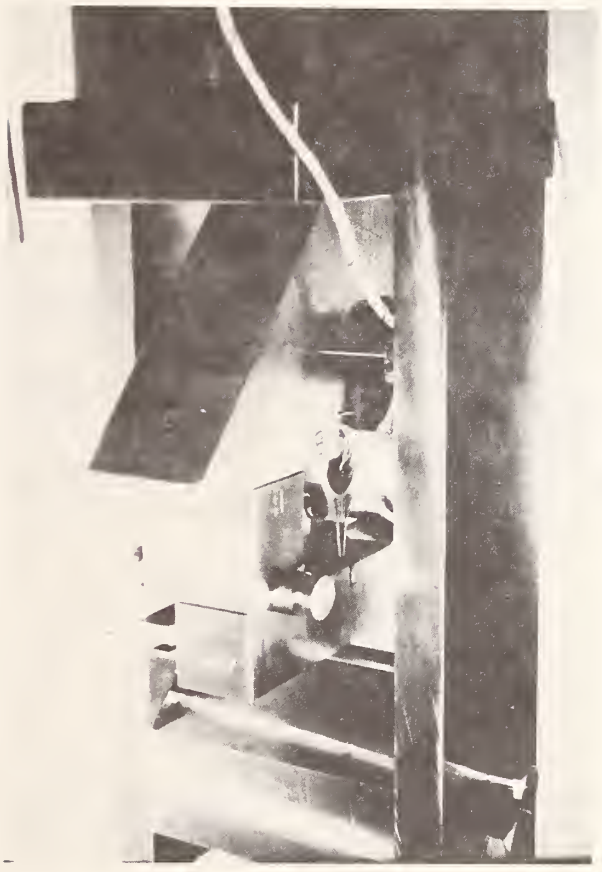

Figure 2. Test fixture for three-point-bend fracture toughness testing at cryogenic temperatures.

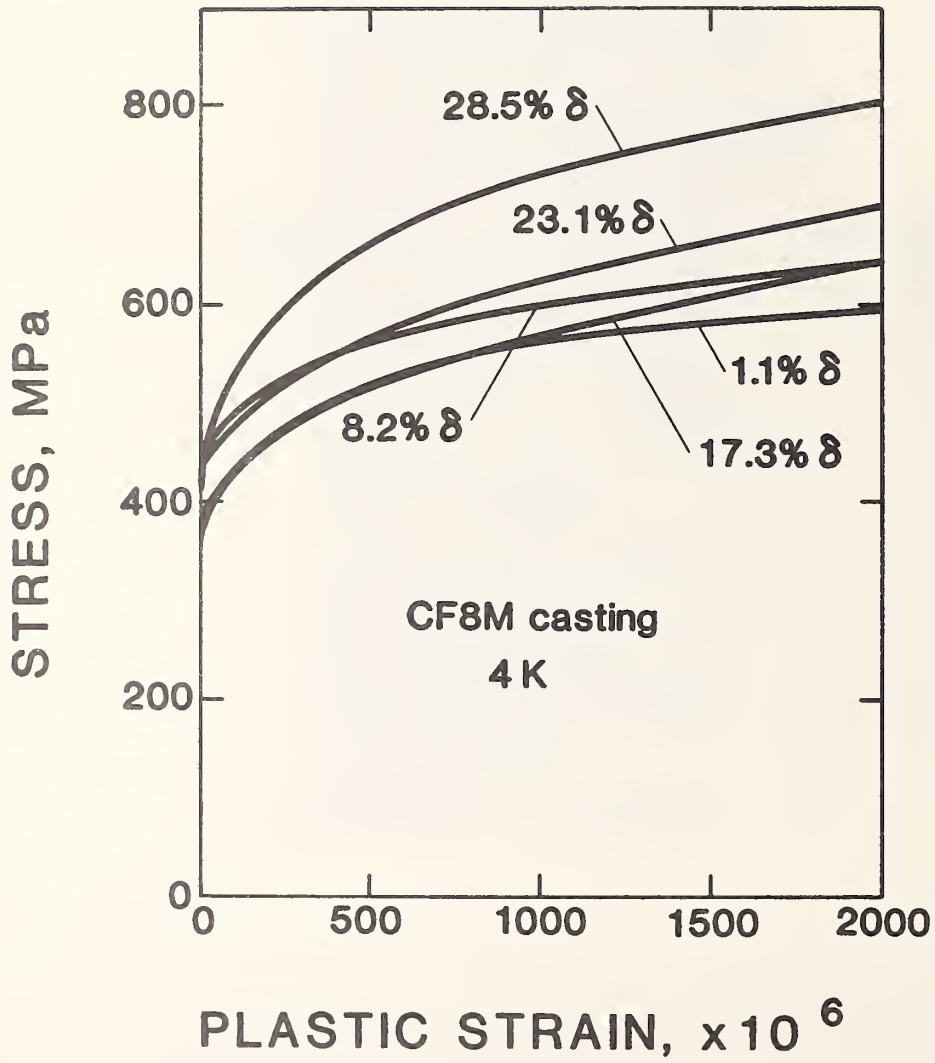

Figure 3. The stress versus microstrain results for the five CF8M stainless steel castings at 4 K.

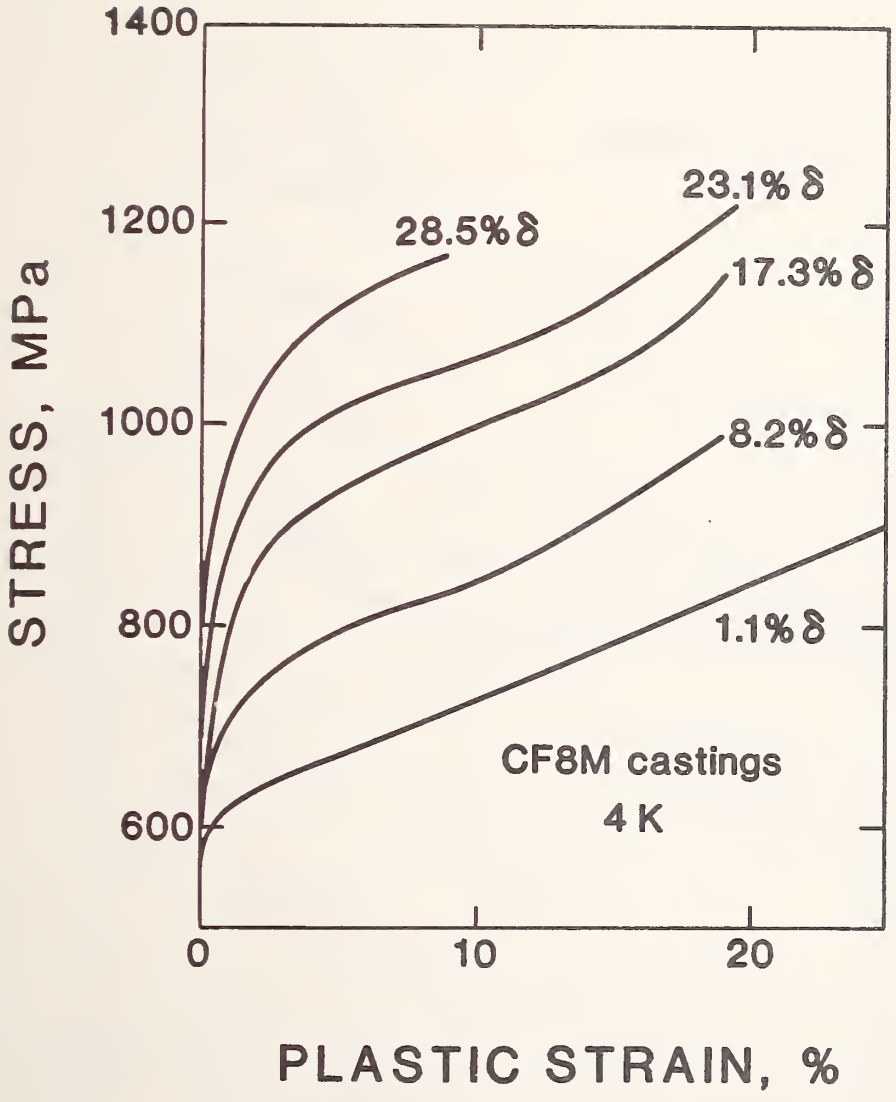

Figure 4. The total stress versus plastic strain curves for the CF8M castings at 4 K. The load drops and the remaining 24 percent strain for the 1.1 percent delta-ferrite casting are not shown.

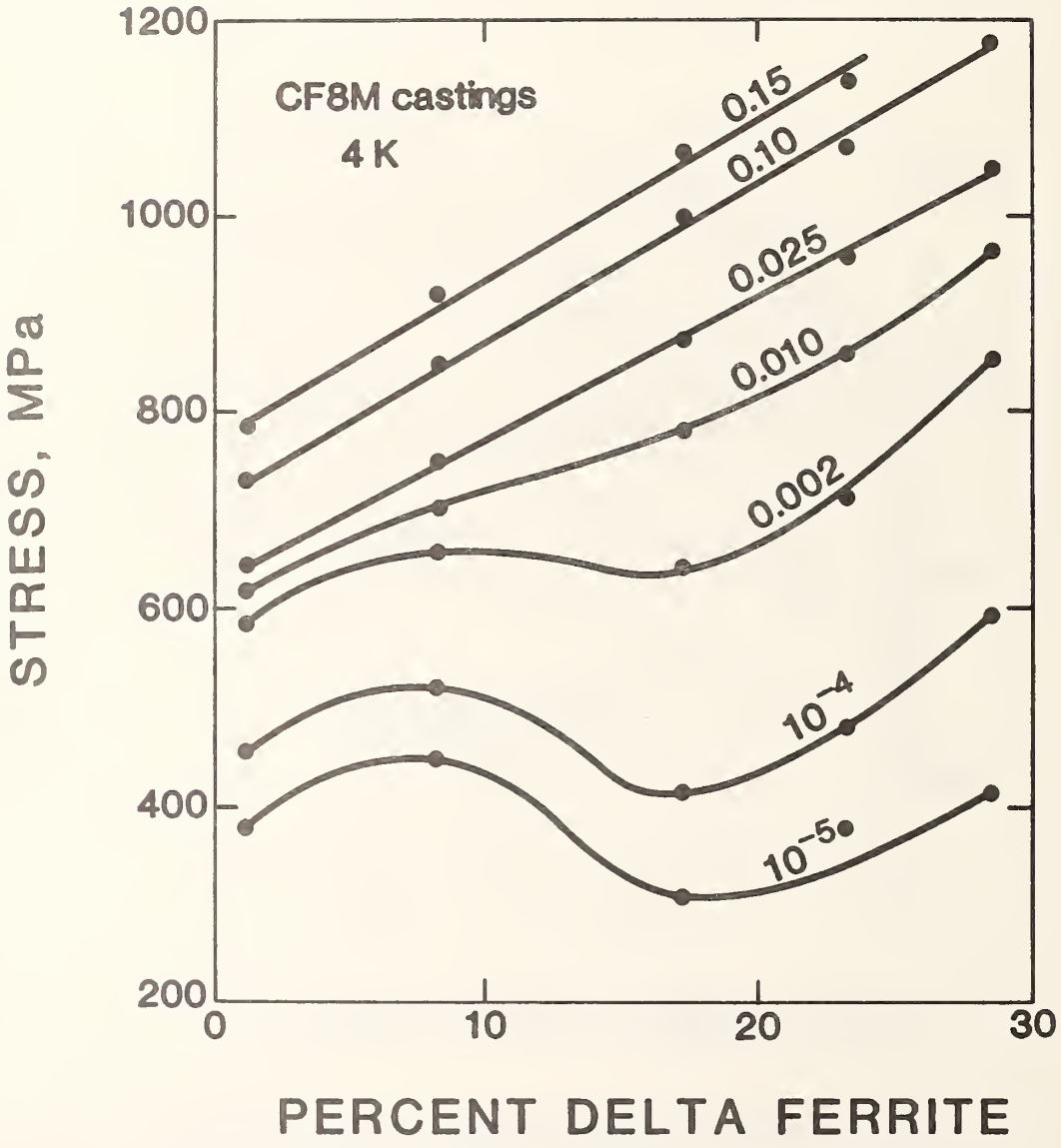

Figure 5. The flow stress as a function of delta-ferrite content at various strain levels for the CF8M castings at 4 K.

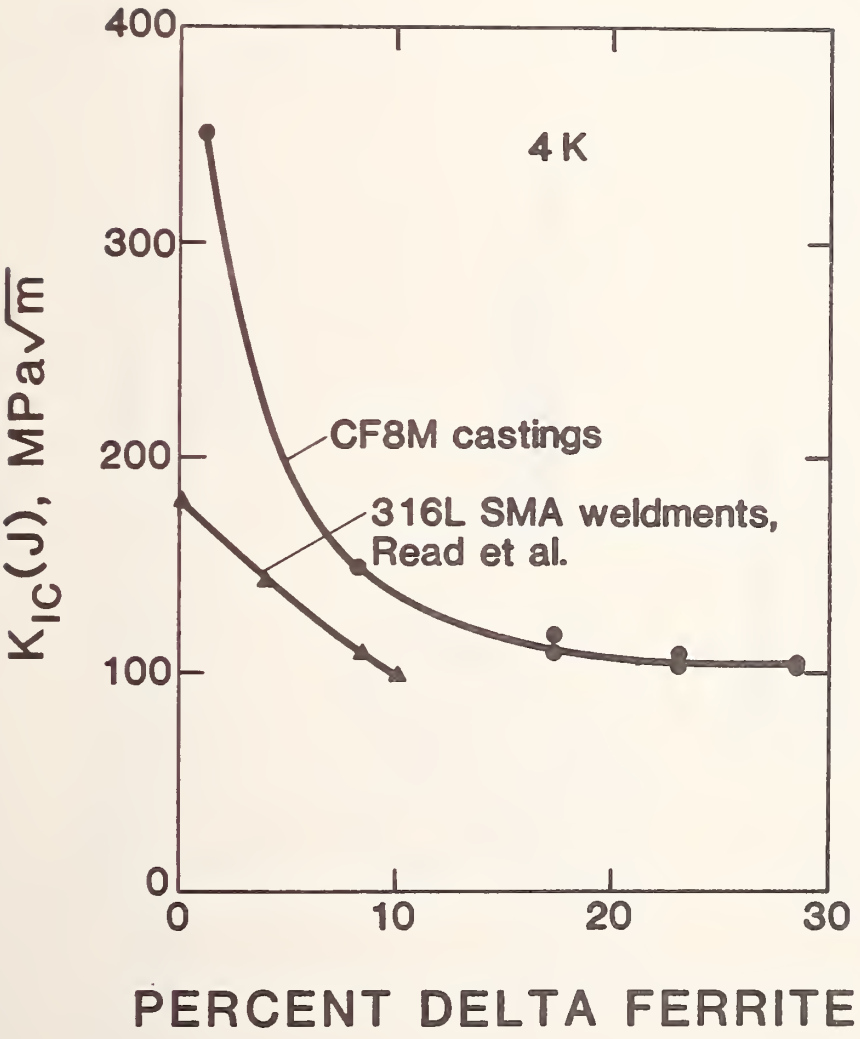

Figure 6. The plane strain fracture toughness, at 4 K, as a function of delta-ferrite content for CF8M castings and 316L weldments (8).

Plastically Nonhomogeneous Deformation Model - Ashby

Based on the concept of geometrically necessary and statistically stored dislocation densities.

Model Structure

3-dimensional square array of plates

This model predicts that the stress is proportional to $l^{-1/2}$ (similar to a Hall-Petch relationship).

Figure 7. An ideal representation of the microstructure of CF8M stainless steel castings used for modeling the deformation at 4 K. The delta-ferrite occurs as a cubic array of square plates.

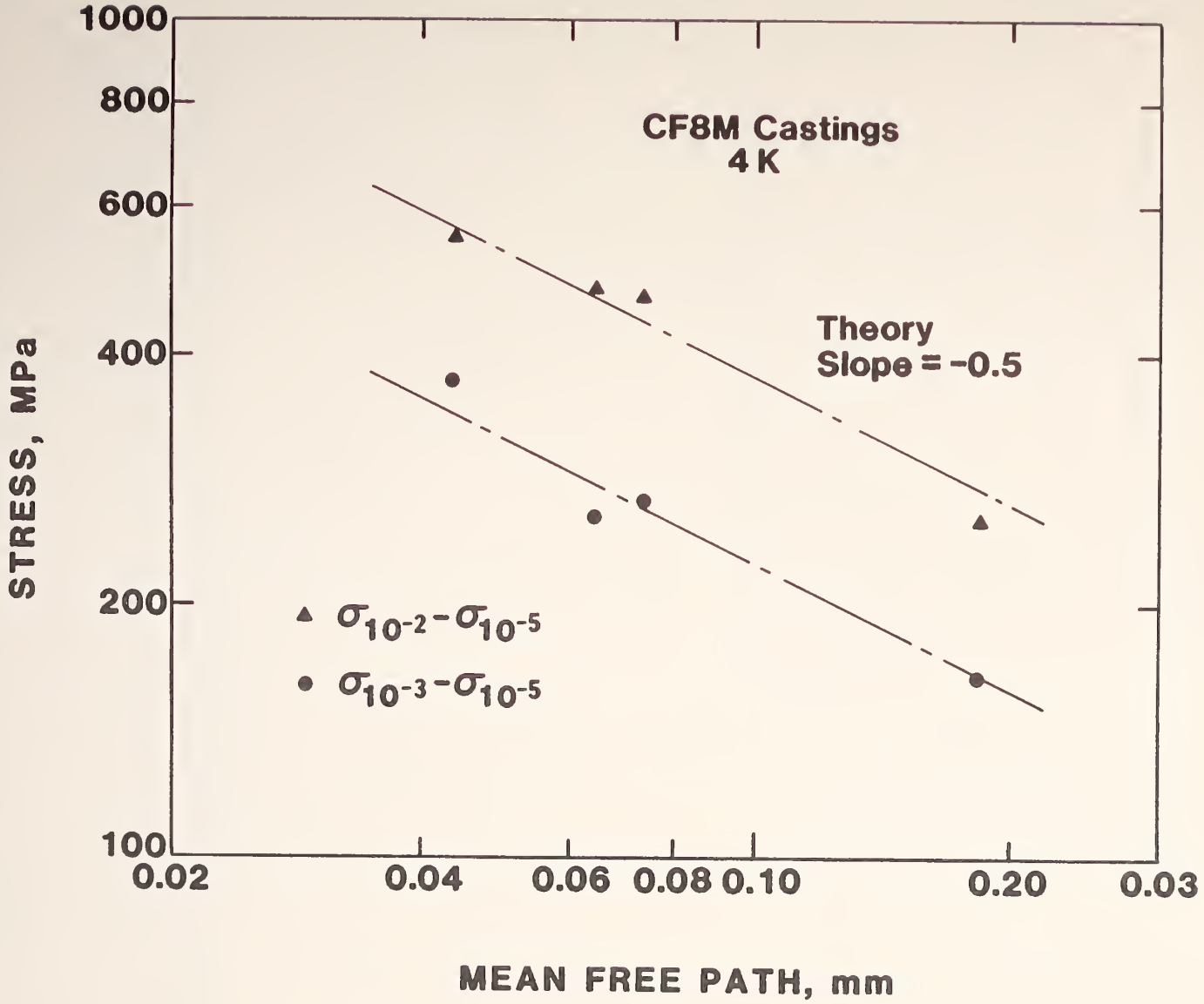

Figure 8. A log-log plot of the flow stress difference, at 4 K, as a function of the mean free path between delta-ferrite particles. The data are compared with the theoretical slope of -0.5.

ULTRASONIC INSPECTION OF STAINLESS STEEL BUTT WELDS USING HORIZONTALLY POLARIZED SHEAR WAVES*

C. M. Fortunko and J. C. Moulder
Fracture and Deformation Division
National Bureau of Standards
Boulder, Colorado

ABSTRACT

Inspection of austenitic stainless steel weldments by conventional ultrasonic means is fundamentally limited by the textured, columnar grain structure of the weld metal. It is shown that, for selected angles of incidence, shear waves normally polarized with respect to the columnar grains can pass through the weld metal-base metal interface without partial reflection. As a consequence, the inspectability of stainless steel weldments can be improved. The operation of a low frequency, ultrasonic system for stainless steel butt weldments is demonstrated.

Key Words: Acoustic waves; elastic anisotropy; nondestructive evaluation; nondestructive testing; stainless steel; ultrasonic scattering; ultrasonic waves.

*Submitted to Ultrasonics for publication.

Introduction

It is now recognized that the inspectability of stainless steel weldments by ultrasonic methods is fundamentally limited by the textured, columnar grain structure of the weld metal.[1] The grains within each weld pass grow with the [100] direction along the thermal gradient and continue to grow epitaxially from pass to pass.[2] The resultant grain structure causes large variations in the ultrasonic velocities as a function of the propagation and polarization directions.[3] Additional complications are introduced at the weld metal-base metal interface where the discontinuity in the elastic properties can result in trirefringent transmission and reflection of the probing ultrasonic signals. As a result, unless the angles of incidence and polarization of the incident ultrasonic signals are judiciously selected, many unwanted indications are produced that mask the defect indications.[3]

Conventional ultrasonic techniques for evaluating stainless steel weldments generally rely on the use of shear or longitudinal wave probing signals that are polarized in the plane normal to the weldment (i.e., the sagittal plane). The probing signals are generated by fluid-coupled piezoelectric transducers that can irradiate the material with only vertically polarized shear (SV) and longitudinal (L) wave vibrations. Upon incidence at the weld metal-base metal interface, these SV and L waves are split into reflected and refracted SV, L and horizontally polarized shear (SH) waves. Because stainless steel weld metals are elastically anisotropic, the tracing of the SV, L, and SH wave signals through the weld metal-base interface is generally very difficult, if not impossible.[4,5]

Recently, a different approach to the problem of ultrasonic detection and sizing of defects in stainless steel weldments has been investigated.[6,7] The new approach is different from conventional ultrasonic nondestructive evaluation (NDE) methods in three respects: 1) the wavelength of the ultrasonic signals is longer than the typical through-thickness defect dimension, 2) the ultrasonic probing signals are shear waves polarized in the plane of the weldment and perpendicular to the columnar grain direction, and 3) noncontacting, electromagnetic-acoustic transducers (EMATs) are used to generate and detect these special probing waves. The principles and operation of electromagnetic-acoustic transducers are described elsewhere.[8,9]

The new ultrasonic technique is particularly well suited for the detection and sizing of elongated incomplete fusion (IF), inadequate penetration (IP), and other crack-like defects in butt weldments. In

this application, shear waves polarized parallel to the welding direction exhibit important advantages over shear waves polarized in the sagittal plane and longitudinal waves. For example, they do not mode convert when polarized along the long defect dimension. Furthermore, they can be generated and detected with equal efficiency at any angle with respect to the surface normal.[9]

In this paper it is demonstrated that practical ultrasonic techniques, using shear waves polarized parallel to the welding direction, can be devised. In particular, it is shown that shear waves polarized parallel to the welding direction can be completely transmitted through the weld metal-base metal interface without significant reflection or mode conversion. As a consequence, the number of unwanted ultrasonic indications can be minimized. The conditions for complete transmission are determined theoretically and verified experimentally. In addition, the detection of real weld defects in a stainless steel weldment is demonstrated. The subject of sizing elongated defects in anisotropic stainless steel weld metals is addressed in Ref. 10.

Transmission of SH Waves through the Weld Metal-Base Metal Interface Region

The factors governing the propagation of ultrasonic signals in stainless steel weldments have been studied extensively. However, progress has been slow because of an incomplete understanding of the role of elastic anisotropy and the lack of efficient transducers for shear waves polarized parallel to the welding direction.

In many multipass stainless steel weld metals, the columnar grains are aligned uniformly.[11] In such cases, the weld metal exhibits a transverse-isotropic texture with the plane of transverse isotropy parallel

to the plane of the weldment and the propagation properties of ultrasonic waves within the weld metal exhibit circular symmetry about the normal to the plane of the weldment.[12]

The propagation properties of shear waves polarized in the plane of transverse isotropy are of particular interest here. It can be shown that such waves propagate as pure shear waves, unlike ultrasonic signals of other polarizations. In this paper, they are referred to as SH waves, in contrast to vertically polarized shear (SV) and longitudinal (L) waves.

The velocity of SH waves within the stainless steel weld metal, modeled as a transversely isotropic aggregate, is given by:

$$v^2(\theta) = \frac{c_{44}}{\rho}\left[1 + \sin^2\theta \, \frac{(c_{11} - c_{12} - 2c_{44})}{2c_{44}}\right] \qquad 1$$

where the angle θ is defined by the axis of the columnar grain growth and the wave normal. The constants C_{11}, C_{12}, and C_{44} are three of five elastic moduli needed to describe the ultrasonic wave propagation in transversely isotropic materials. Because the direction normal to the axis of grain growth usually coincides with the plane of a weldment, the pure shear wave is horizontally polarized (an SH wave). The weldment geometry is defined in Fig. 1.

To investigate the transmission of SH waves through the weld metal base metal interface in the geometry of Fig. 1, consider the case of normal incidence with respect to the welding direction. Since normally incident

SH waves are polarized parallel to the plane of the interface and propagate as pure shear waves in the weld metal, no mode conversion by polarization coupling to the L and SV waves can occur. The amplitudes and propagation directions of the transmitted and reflected SH waves can then be completely determined from a scalar relationship involving only the acoustic impedances of the SH waves and Snell's law considerations. In fact, since the densities of the weld and base metals are nearly equal, the transmission and reflection coefficients are determined only by the propagation directions and velocites of SH waves propagating in the sagittal plane.

The SH wave velocity surfaces for type 308 stainless steel weld metal and type 304 stainless steel base metal are shown in Fig. 2. The surfaces were calculated using experimental[13] and calculated[14] elastic moduli. It is observed that the surfaces intersect for two SH wave propagation directions. As a consequence, it should be possible to match the acoustic impedances of SH waves propagating in the sagittal plane for this particular combination of weld and base metals.

An experimental scattering configuration of considerable practical importance is illustrated in Fig. 3. In this case, the stainless steel weld metal is deposited in a "vee-groove" between two stainless steel plates that are assumed to be isotropic and homogeneous. The columnar grains are then aligned symmetrically along the normal to the plate. The direction of alignment is, therefore, tilted with respect to the weld metal-base metal interface that is illuminated by a beam of SH waves. The SH waves are excited by an EMAT that is placed on the top surface of the plate.

The transmission of SH waves through the weld metal-base metal interface can be investigated by using two coordinate systems: (x,z),

which is associated with the weld metal, and (x',z'), which is associated with the base metal. In the sagittal plane, (x x z or x' x z'), the (x,z) and (x', z') coordinate systems are rotated by an angle ϕ. The weld metal-base metal interface is then rotated by an angle $-\theta$ with respect to the z- axis. It is then of interest to identify the angle ϕ for which the SH wave is transmitted through the weld metal-base metal interface without reflection.

The transmission coefficient at the weld metal-base metal interface for SH waves propagating in the sagittal plane is given by:

$$T = \frac{2Z^{(B)} \cos(\theta+\phi)}{Z^{(B)} \cos(\theta+\phi) + Z^{(W)}(\psi-\theta+90°)\cos\psi} \qquad (2)$$

where $Z^{(B)}$ and $Z^{(W)}(\psi - \theta + 90°)$ are the acoustic impedances for SH waves in the base and weld metals, respectively, ψ is the angle of the transmitted SH wave normal with respect to the interface normal.

The angle ψ can be determined from Snell's law considerations, and a solution for ϕ, for complete transmission (T=1), can be found by inverting Eq. 2. However, it is instructive to obtain an approximate solution by noting that $\psi = \theta + \phi$ when the densities of the stainless steel weld and base metals are equal and T = 1. In this case ϕ can be determined from:

$$\cos^2\phi = \left[\frac{c_{44}^{(B)}}{c_{44}^{(W)}} - 1\right]\left[\frac{2c_{44}^{(W)}}{c_{11}^{(W)} - c_{12}^{(W)} - 2c_{44}^{(W)}}\right] \qquad (3)$$

A value of 27° is obtained for ϕ when the elastic constant values for 304 stainless steel base metal and 316 multipass stainless steel weld metal are substituted in Eq. 3. The values are:

$c_{44}^{(B)} = 0.744 \cdot 10^{11}$,[13] $c_{11}^{(W)} = 2.36 \cdot 10^{11}$, $c_{12}^{(W)} = 1.03 \cdot 10^{11}$, and

$c_{44}^{(W)} = 1.19 \cdot 10^{11} N/m^2$.[14]

It is interesting to compare the degree of skewing of SH wave beams, upon transit through the weld metal-base metal interface, with that of SV and L wave beams. For SH waves ϕ is independent of θ. The skewing for a 308/304 weld metal-base metal interface, calculated using the theory of Ref. 15, is shown in Fig. 4 for SH, SV, and L waves. The flux deviation angle, Δ, is plotted as a function of the angle of incidence, ϕ, with respect to the columnar grain direction. It is observed that for near-grazing incidence, $70° < \phi < 90°$, the flux deviation for SH waves is substantially smaller than for SV waves and is comparable to that for L waves. For $\phi = 70°$, the flux deviation angle, Δ, is $\sim -15°$. Thus, SH wave signals should be sensitive to in-plane and normal defects in stainless steel weld metals.[16] The above results confirm the experimental observations of Kupperman[3], which show that SH waves are more appropriate than SV and L waves for inspecting multipass stainless steel weldments.

Experimental Configurations

Two experimental configurations, which are useful for detecting defects in girth welds of stainless steel pipes, are illustrated in Fig. 5. Figure 5a shows a tandem EMAT ("pitch-catch") configuration that is useful for sampling SH wave signals backscattered from the weld. Figure 5b shows a different configuration of the two EMATs. The configuration

of Fig. 5b is useful for sampling SH wave signals transmitted through the weld. Both experimental configurations have been used to inspect ferritic butt weldments.[17]

Figure 6 shows a particular inspection configuration, including a block diagram of the signal processing system that has been used to detect crack-like defects in pipe girth welds. The operation of this system, in the "pitch-catch" configuration of Fig. 5a, is as follows. The EMATs are located on the outer surface of the pipe wall and are aimed colinearly along the normal to the weld. The transmitter EMAT is positioned between the weld and the receiver EMAT. The transmitter EMAT is bidirectional and, therefore, generates two SH wave signals of equal amplitude that travel in opposite directions along the normal to the weld. The ultrasonic signal 1, traveling to the left of the transmitter EMAT, illuminates the weld region. The ultrasonic signal 2, traveling to the right of the transmitter EMAT, passes directly beneath the receiver EMAT. The latter signal is used as a reference for calibrating the transduction efficiency of the transmitter EMAT. If a defect is present in the weld, a portion of the ultrasonic signal 1 is backscattered in the direction of the receiver EMAT.

The backscattered signal 3 arrives after the reference signal 2 because it travels a longer distance. This arrangement of the two EMATs ensures adequate temporal separation between the reference and defect signals. The ratio of signals 2 and 3 is used in defect detection and sizing.[17] As a result, the inspection system is less sensitive to variations in transducer coupling efficiency caused by lift-off.

Experimental Results

The experimental inspection system of Fig. 6 was used to examine the girth weld in a 304 stainless steel pipe specimen that had been prepared for NDE purposes. The specimen was a 0.9-m-long, 0.273-m-diameter pipe section with a 12.7-mm wall thickness. As shown in Fig. 5, a counterbore was ground on both sides of the weld. The weld contained a number of defects that were detected by conventional radiographic and ultrasonic techniques.

The ultrasonic inspection of the test specimen was carried out using the two experimental configurations illustrated in Fig. 5. The transmitter EMAT was driven with a 10-cycle RF tone burst with a 441-kHz center frequency. To measure the backscattered SH wave signals, the transmitter EMAT-to-receiver EMAT distance, ℓ, was approximately 0.15 m, center-to-center. The distance x, between the transmitter EMAT and the weld, was 0.1 m. In the transmission mode, the transmitter EMAT was separated by 0.15 m from the receiver EMAT, but the two transducers were positioned symmetrically on either side of the weld. Measurements were taken every 12.7 mm along the circumference to ensure complete coverage of the weld. The ultrasonic (3-dB) beam width at the weld was approximately 25 mm.

Figure 7 shows three sample waveforms that were obtained at different locations along the circumference of the pipe using the scattering configuration of Fig. 6. In Fig. 7, the first wave packet, extending from 0-40 μs, is associated with reference signal 1, which is propagated directly between the transmitter and receiver EMATs. The second wave packet,

centered near 75 μs, is associated with the SH wave signals that are backscattered from the weld region. The oscilloscope signals are displayed after signal averaging of 256 frames of the data. The averaging was necessary to improve the signal-to-noise ratio and to inhibit electromagnetic interferences. The first photo was obtained in a region of the weld that contained no defects. It is apparent that very little ultrasonic energy is backscattered from the weld. In this case most of the backscattering is attributed to the presence of the counterbore (∿1-mm deep) on the inside of the pipe. The second and third photos in Fig. 7 were obtained in regions containing a through-thickness crack and an inadequate penetration (IP) defect. In contrast to the first photo, the amplitudes of the backscattered signals in the second and third photos are comparable to the amplitude of the reference signal.

Figure 8 shows the complete ultrasonic inspection record that was obtained by scanning the stainless steel girth weld from both sides using the "pitch-catch" inspection configuration of Fig. 5a. In previous work, the defect detectability levels were determined by reflections from the weld reinforcement ("crown") and root, rather than by random electronic noise.[17] In the present case, the defect detectability limits are established by the presence of a sharp step (counterbore) on both sides of the weld root. Because of the poor spatial resolution at 441 kHz, the signals backscattered from the weld could not be distinguished from reflections from the counterbore. Therefore, a threshold level of 0.1, corresponding to peak counterbore indications, was adopted. This threshold setting is indicated in Fig. 8 by a horizontal line drawn across the inspection record.

Figure 9 shows the ultrasonic inspection record that was obtained by scanning the stainless steel girth weld using the transmission mode inspection configuration of Fig. 5b. In this case, the threshold was set at 0.71 on the basis of the average amplitude transmitted through the weld, relative to the average amplitude transmitted directly through the base material. It is observed that a significant fraction of the incident power is transmitted through the weld, as expected from the model.

A substantial degree of correlation is observed between the inspection results obtained using the 441-kHz SH wave system, and those obtained using conventional radiographic and ultrasonic techniques. The results obtained using conventional radiographic and ultrasonic techniques are indicated in Fig.s 8 and 9 with horizontal bars. It is observed that in the transmission mode three of the five defects are positively detected: inadequate penetration and the two cracks. On the other hand, in the reflection mode, only the inadequate penetration defect and the through-wall crack were positively detected. It is believed that the three undetected defects (slag, lack of fusion, and partial through-wall crack) were relatively shallow and had reflectivities comparable to or smaller than that of the counterbore. (The counterbore was separated by only 15 mm from the center of the weld. As a result, it could not be resolved using the relatively narrowband 441-kHz SH wave probing signal.)

Conclusions

The operation of a practical ultrasonic inspection system using low frequency, horizontally polarized shear (SH) waves has been demonstrated on an austenitic stainless steel weldment. It has been shown that SH waves can be completely transmitted through the weld metal-base metal

interface without mode conversion to longitudinal and vertically polarized shear waves. This results in a significant increase in sensitivty to defects in the weld metal.[3] In addition, the use of low frequency probing signals allows the use of long wavelength inversion algorithms for defect sizing.[10] As a consequence, automated ultrasonic inspection systems for stainless steel weldments may be possible.

Acknowledgment

The authors are indebted to the Electric Power Research Institute for making available the stainless steel weld specimens. Major support for this work was provided by the Department of Energy, Office of Fusion Energy.

REFERENCES

1. M. G. Silk, Propagation of Ultrasound in Anisotropic Weldments, Mater. Eval. 39 (1981) 462-467.

2. B. L. Baikie, A. R. Wagg, M. T. Whittle, and D. Yapp, Ultrasonic Inspection of Austenitic Welds, J. Br. Nucl. Energy Soc. 15 (1976) 257-261.

3. D. S. Kupperman and K. J. Reimann, Ultrasonic Wave Propagation and Anisotropy in Austenitic Stainless Steel Weld Metal, IEEE Trans. Sonics Ultrasonics 27 (1980) 7-15.

4. J. R. Tomlinson, A. R. Wagg, and M. J. Whittle, Ultrasonic Inspection of Austenitic Welds, Br. J. NDT 24 (1980) 119-127.

5. M. G. Silk, B. H. Lidington, and G. F. Hammond, A Time Domain Approach to Crack Location and Sizing in Austenitic Welds, Br. J. NDT 24 (1980) 55-61.

6. C. M. Fortunko, Ultrasonic Evaluation of Austenitic Stainless Steel Welds Using Shear Horizontal Waves, Appl. Phys. Lett. (in press).

7. C. M. Fortunko, R. B. King, and M. Tan, Nondestructive Evaluation of Planar Defects in Plates Using Low Frequency Shear Horizontal Waves (to be published).

8. R. B. Thompson, A Model for the Electromagnetic Generation and Detection of Rayleigh and Lamb Waves, IEEE Trans. Sonics Ultrasonics 20 (1973) 340-346.

9. C. F. Vasile and R. B. Thompson, Excitation of Horizontally Polarized Elastic Waves by Electromagnetic Transducers with Periodic Magnets, J. Appl. Phys. 50 (1979) 2583-2588.

10. S. K. Datta, A. H. Shah, and C. M. Fortunko, Diffraction of Medium and Long Wavelength SH-Waves by Edge Cracks (to be published).

11. L. Adler, K. V. Cook, and D. W. Fitting, Ultrasonic Characterization of Austenitic Welds, in Ultrasonic Materials Characterization, NBS Special Publication 596 (NBS, Gaithersburg, MD, 1980) 533-540.

12. M. J. P. Musgrave, Crystal Acoustics (Holden Day, San Francisco, 1970) 94-101.

13. H. M. Ledbetter, N. V. Frederick, M. W. Austin, Elastic Constant Variability in Stainless Steel 304, J. Appl. Phys. 51 (1980) 305-309.

14. H. M. Ledbetter, NBS, Boulder, Colorado, private communication.

15. M. J. P. Musgrave, On the Propagation of Elastic Waves in Aeolotropic Media, II. Media of Hexagonal Symmetry, Proc. R. Soc. 226 (1954) 356-366.

16. R. J. Hudgell and H. Seed, Ultrasonic Longitudinal Wave Examination of Austenitic Welds, Br. J. NDT 25 (1980) 78-85.

17. C. M. Fortunko and R. E. Schramm, Nondestructive Evaluation of Large Diameter Girth Welds Using Electromagnetic-Acoustic Transducers, in Fitness-for-Purpose Validation in Welded Constructions (The Welding Institute, Cambridge, England, 1981) (in press).

Figure Captions

1. The weldment geometry.
2. Velocity surfaces for SH waves propagating in the sagittal plane.
3. Configuration for analyzing the propagation of SH waves through the weld metal-base metal interface.
4. Skewing of SH, SV, and L wave signals as a function of the wave normal direction in a type 308 stainless steel weld metal.
5. Experimental configurations used in the nondestructive examination of stainless steel girth welds.
6. Block diagram of the experimental apparatus.
7. Ultrasonic reflections obtained with 441-kHz SH waves in different regions of the girth weld.
8. Ultrasonic inspection record obtained using the reflection configuration.
9. Ultrasonic inspection record obtained using the transmission configuration.

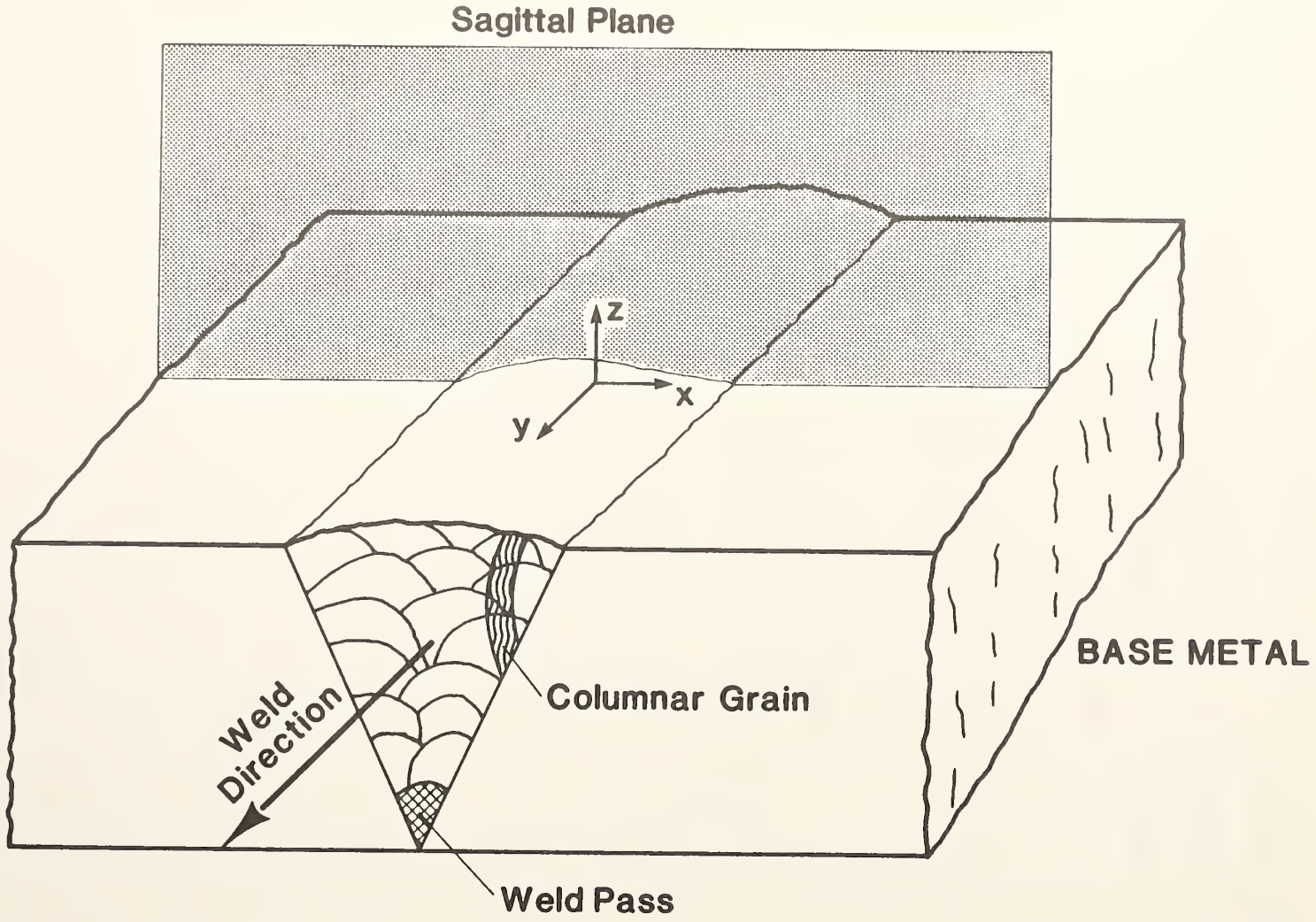

Figure 1. The weldment geometry.

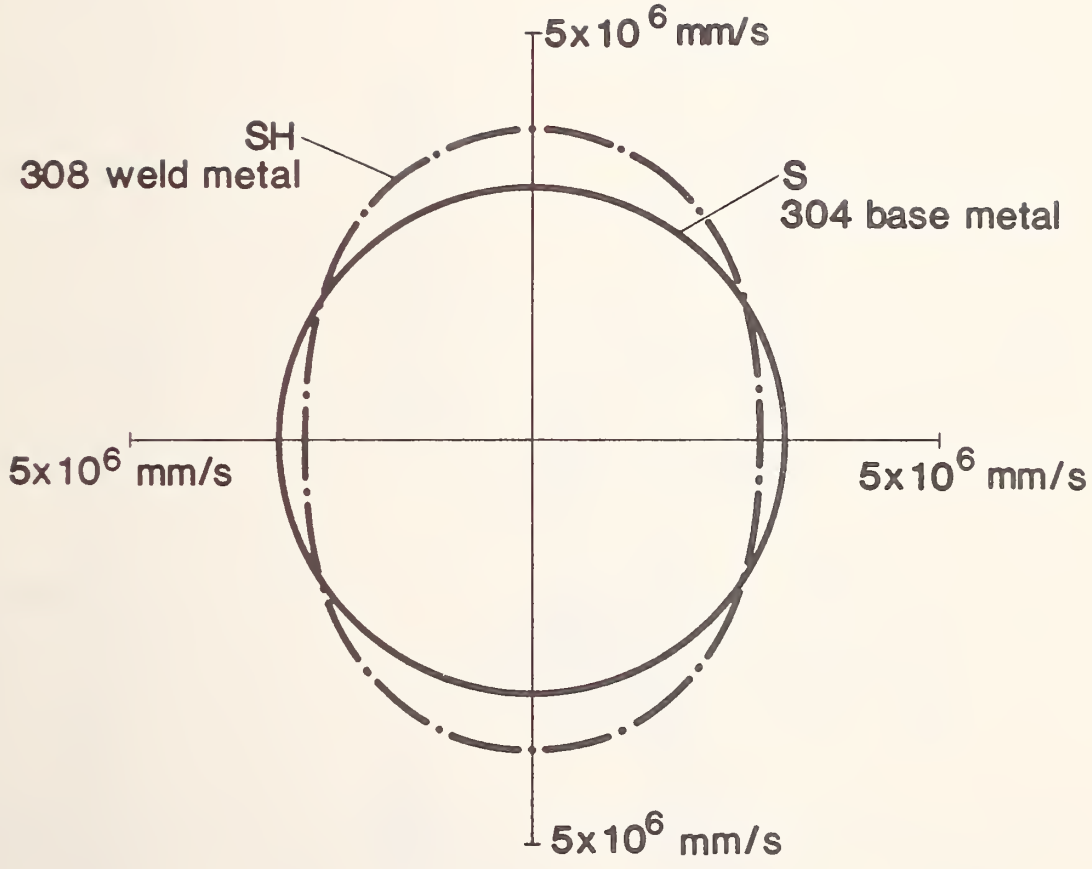

Figure 2. Velocity surfaces for SH waves propagating in the sagittal plane.

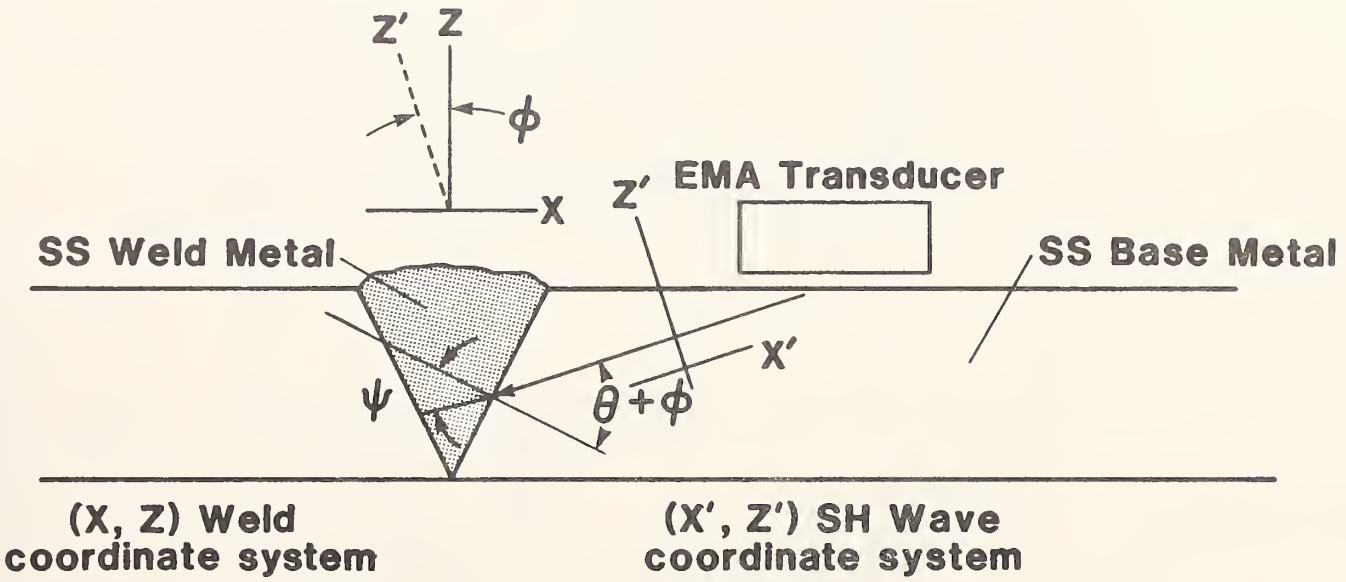

Figure 3. Configuration for analyzing the propagation of SH waves through the weld metal-base metal interface.

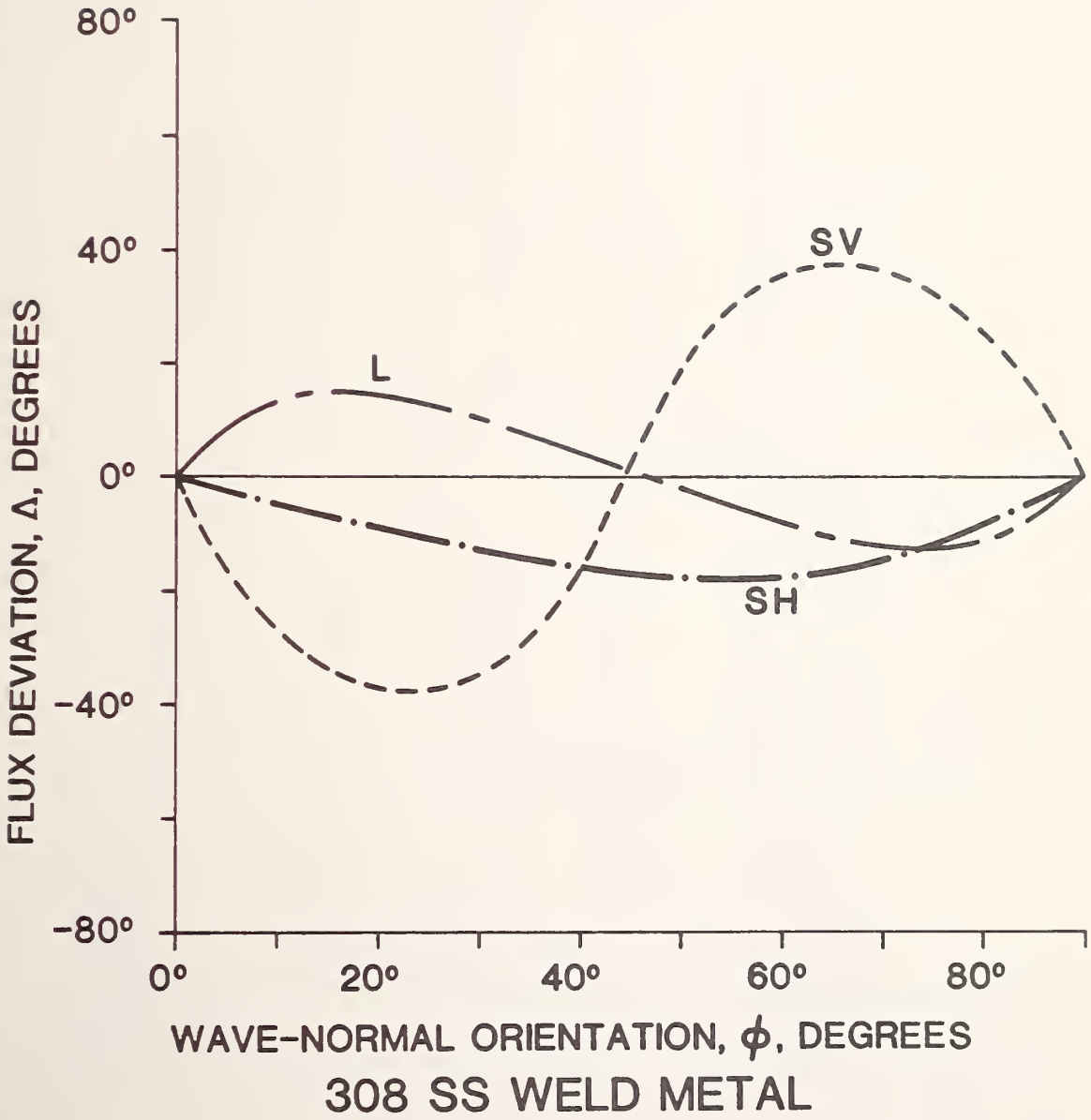

Figure 4. Skewing of SH, SV, and L wave signals as a function of the wave normal direction in a type 308 stainless steel weld metal.

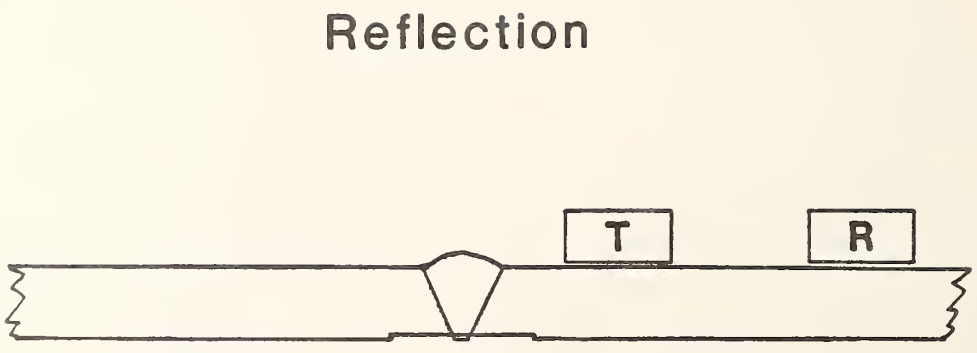

(a)

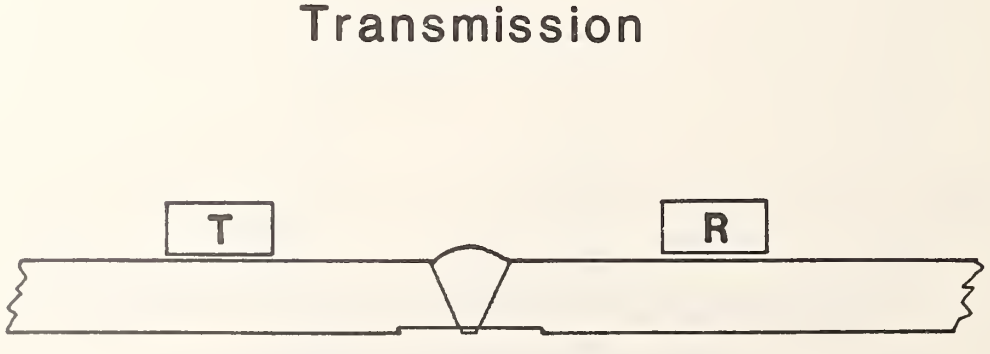

(b)

Figure 5. Experimental configurations used in the nondestructive examination of stainless steel girth welds.

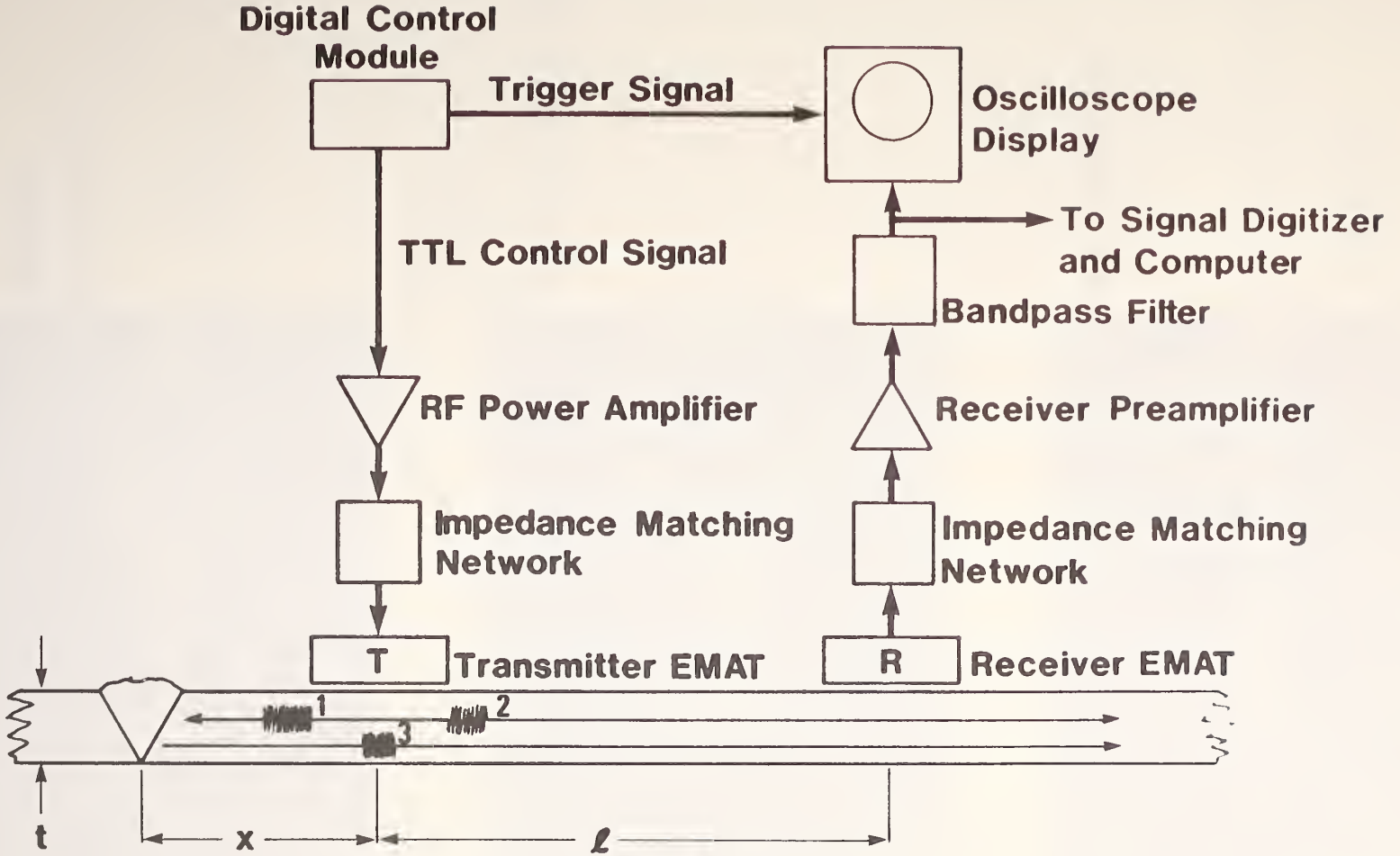

Figure 6. Block diagram of the experimental apparatus.

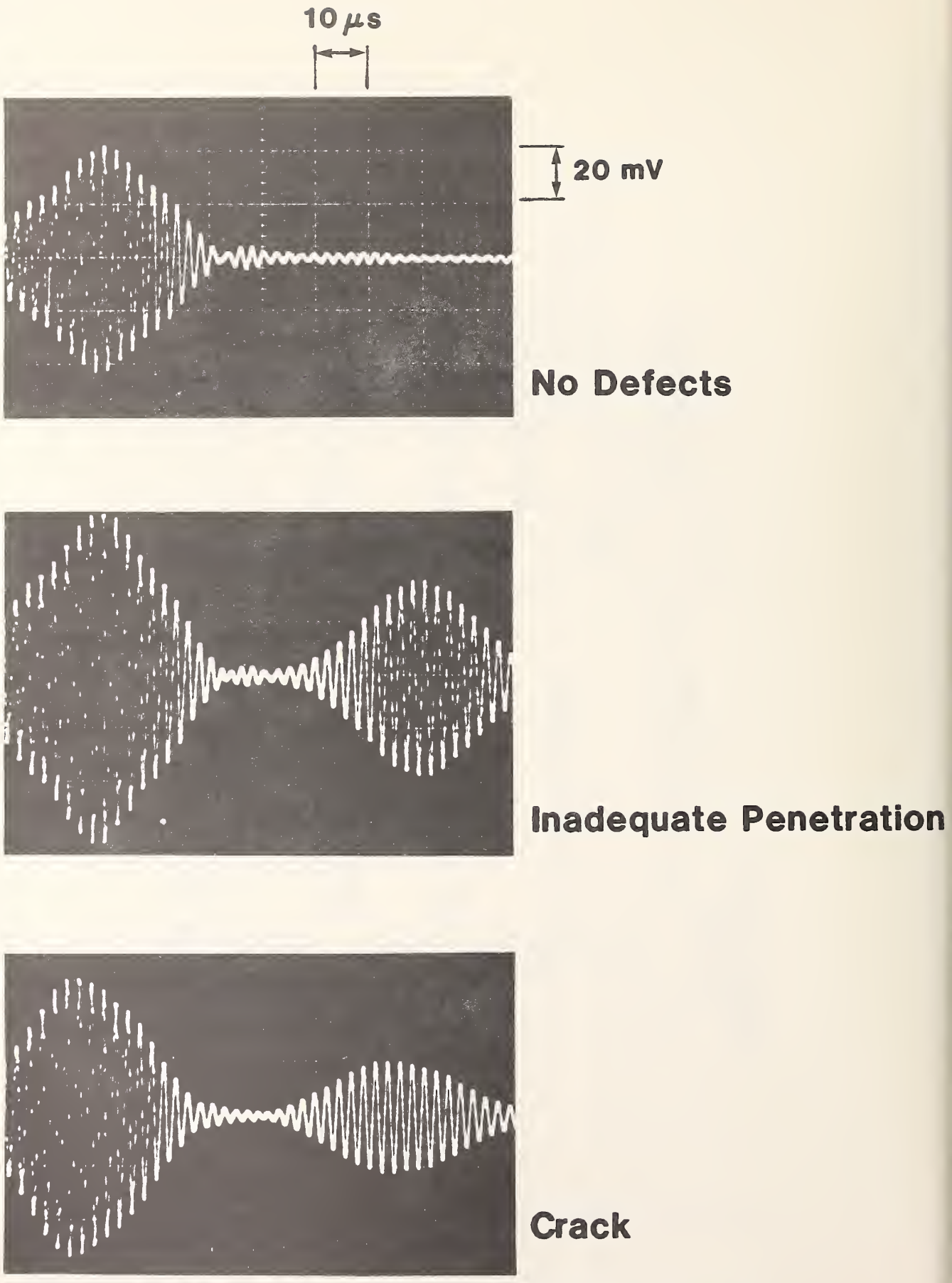

Figure 7. Ultrasonic reflections obtained with 441-kHz SH waves in different regions of the girth weld.

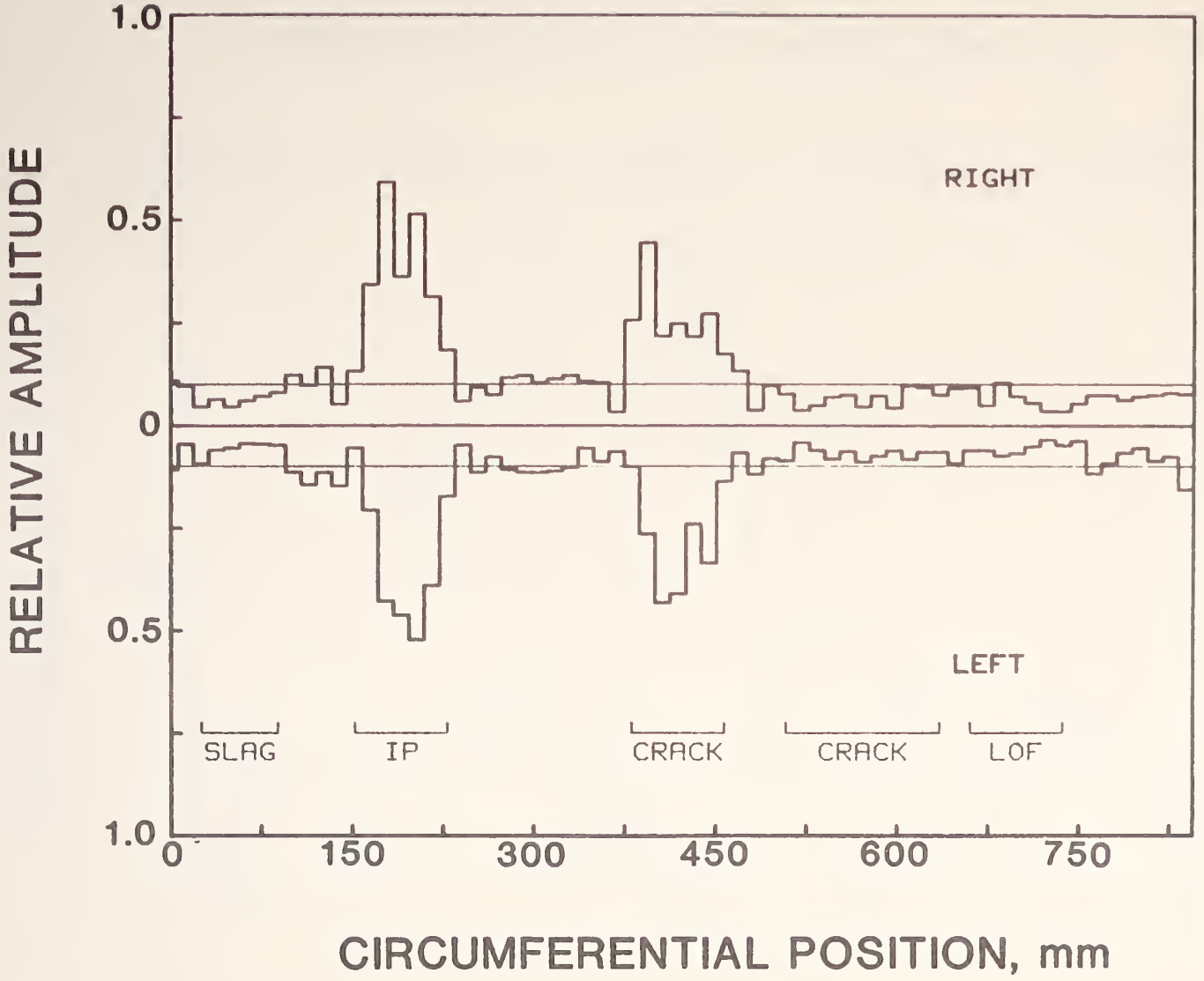

Figure 8. Ultrasonic inspection record obtained using the reflection configuration.

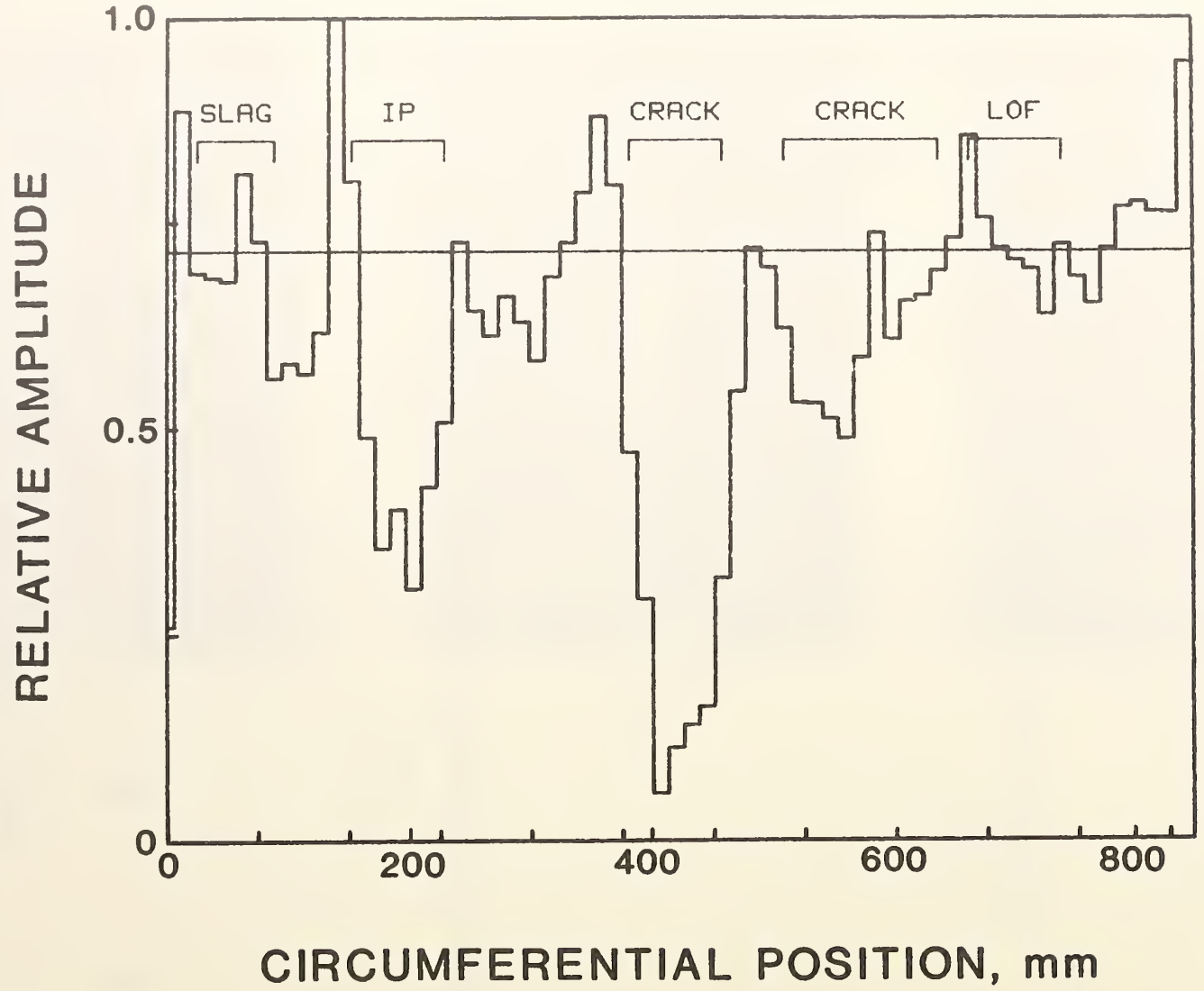

Figure 9. Ultrasonic inspection record obtained using the transmission configuration.

SINGLE-CRYSTAL ELASTIC CONSTANTS IN NONDESTRUCTIVE EVALUATION OF WELDS

H. M. Ledbetter
Fracture and Deformation Division
National Bureau of Standards
Boulder, Colorado

SINGLE-CRYSTAL ELASTIC CONSTANTS IN NONDESTRUCTIVE EVALUATION OF WELDS

H. M. Ledbetter
Fracture and Deformation Division
National Bureau of Standards
Boulder, Colorado 80303

ABSTRACT

For studying welds nondestructively using elastic waves, we describe the importance of knowing the material's single-crystal elastic constants, the C_{ij}'s. Where these are not known, we give some guidelines for estimating them from polycrystalline elastic constants such as Young's modulus and the shear modulus. We consider the important case of [100] texture. Being transversely isotropic, this case exhibits five macroscopic elastic constants, which we relate to the three cubic elastic constants: C_{11}, C_{12}, C_{44}. From these five constants we compute the angular variations of Young's modulus, the torsional modulus, and the sound velocities.

INTRODUCTION

Optimum ultrasonic inspection of welds requires knowing and understanding the weld's single-crystal elastic constants and how these constants relate to the macroscopic elastic constants of the textured aggregate. Several recent studies recognize these requirements [1-7].

The present study describes two basic relationships. First, how single-crystal elastic constants, the C_{ij}'s, can be obtained from polycrystalline elastic constants. Second, how the C_{ij}'s can be used to calculate the macroscopic elastic constants of textured aggregates, which occur often in welds.

As an example, we consider a stainless-steel-316 weld, which develops a <100> fiber texture. This Fe-Cr-Ni alloy exhibits a face-centered-cubic crystal structure and, therefore, three independent single-crystal elastic constants, usually taken to be C_{11}, C_{12}, and C_{44} in Voigt's contracted notation. A fiber texture being transversely isotropic has, macroscopically, hexagonal symmetry with five independent elastic constants: C_{13} and C_{33} in addition to those for cubic symmetry. An ideal <100> fiber texture means that [100]-type directions are parallel to the unique axis x_3 (the solidification direction in this case), and that the (100)-type planes perpendicular to x_3 are distributed randomly with respect to rotation about x_3. Figure 1 relates cubic and hexagonal coordinate systems to weld geometry.

THEORY FOR CUBIC-SINGLE-CRYSTAL C_{ij}'s

Especially for cubic crystal symmetry, the problem of relating the single-crystal elastic constants (C_{11}, C_{12}, C_{44}) to the quasi-isotropic polycrystalline elastic constants (B,G) has been studied extensively, both theoretically [8] and experimentally [9]. The bulk modulus, B, because it is a rotational invariant of the elastic-stiffness tensor, is always given by

$$B=(C_{11}+2C_{12})/3, \tag{1}$$

even for a highly textured material. The expression for the shear modulus, G, depends on the assumptions of the model. Considering the self-consistent problem of an anisotropic single-crystal inclusion embedded in a corresponding isotropic matrix, and assuming stress equilibrium at the interface, Kröner [10] showed that

$$G^3+\alpha G^2+\beta G+\gamma=0 \tag{2}$$

where

$$\alpha=(5C_{11}+4C_{12})/8 \tag{3}$$

$$\beta=-C_{44}(7C_{11}-4C_{12})/8 \tag{4}$$

and

$$\gamma=-C_{44}(C_{11}-C_{12})(C_{11}+2C_{12})/8 \tag{5}$$

In the forward case, these relationships permit the calculation of B and G from the C_{ij}'s, the isotropic from the anisotropic, two elastic constants from three.

With one additional piece of information, from either theory or observation, from some single relationship among the C_{ij}'s, the reverse-case can be computed also. The C_{ij}'s can be computed from B and G.

If B and G are unavailable, then any other pair of polycrystalline elastic constants will serve. For example, Young's modulus and Poisson's ratio. This is so because any isotropic elastic constant can be calculated from any other two isotropic elastic constants.

For a relationship among the C_{ij}'s of stainless steel 316, we consider the existing C_{ij} measurements on f.c.c. Fe-Cr-Ni alloys summarized in Table 1. At least two approximate relationships emerge. First, the elastic anisotropy is relatively constant, being 3.51 ± 0.19. Second, the $y=C_{12}/C_{11}$ ratio is relatively constant, being 0.642 ± 0.037. Ledbetter [11] showed that a slightly better y value results if values for f.c.c. Fe and Ni are also included with these four alloys, the value being y=0.640 ±

0.031. Table 1 probably contains other C_{ij} relationships. But these two are simple and sufficient.

For B and G values, we use those reported by Ledbetter [12]: B=1.575 ± 0.014 and G=0.752 ± 0.015 10^{11} N/m^2.

THEORY FOR TEXTURED-AGGREGATE C_{ij}'s

One expects that cubic-symmetry crystallites in welds occur either with random orientations or with a single preferred axis parallel to the principal heat-flow direction, denoted x_3 in Fig. 1. In the x_1-x_2 plane, crystallites are expected to orient themselves randomly because no preferred heat-flow direction occurs in that plane. Thus, an effective fiber texture occurs with x_3 being the fiber axis. Macroscopically, such a material exhibits transverse-isotropic symmetry, with five independent elastic constants. This is equivalent to hexagonal symmetry. In Voigt's contracted C_{ij} notation the symmetrical elastic-stiffness matrix is [13]:

$$C^H_{ij} = \begin{bmatrix} C^H_{11} & C^H_{12} & C^H_{13} & 0 & 0 & 0 \\ & C^H_{11} & C^H_{13} & 0 & 0 & 0 \\ & & C^H_{33} & 0 & 0 & 0 \\ & & & C^H_{44} & 0 & 0 \\ & & & & C^H_{44} & 0 \\ & & & & & C^H_{66} \end{bmatrix} \qquad (6)$$

where $C^H_{66} = \frac{1}{2}(C^H_{11} - C^H_{12})$. Thus, the theoretical problem is to express the five hexagonal-symmetry elastic constants, C^H_{ij}, in terms of the three cubic-symmetry elastic constants: C_{11}, C_{12}, and C_{44}.

Present theory does not permit calculation of the elastic constants of textured polycrystalline aggregates of cubic-symmetry crystallites. This is a special and more difficult case of determining the average elastic constants of a random polycrystalline aggregate. For this latter problem, Landau and Lifshitz [14] remind us that "there is...no general relationship between the moduli of elasticity of a polycrystal and those of a single crystal of the same substance." The fiber-texture case involves a two-dimensional, rather than a three-dimensional, average.

However, elastic-constant bounds can be calculated for textured aggregates. In this study we calculate the Voigt [15] (constant strain) and Reuss [16] (constant stress) bounds and use Hill's [17] suggestion of an arithmetic average to estimate the elastic constants. This approach turns out to be quite reasonable because the Voigt and Reuss bounds do not differ dramatically (a maximum of 37 percent). And for the important <100>-texture case, the bounds coincide for three elastic constants: C^H_{13}, C^H_{33}, and C^H_{44}. Thus, we know these three constants unambiguously. Kröner and Wawra [18] explain the systematics of this bounds coincidence.

Several studies [19-22] derive correctly the relationships for calculating the Voigt bounds of macroscopic elastic constants of fiber-textured cubic aggregates. We used the form given by Kröner and Wawra [18].

$$\begin{aligned} C^H_{11} &= C_1 + 3\beta C_3 \\ C^H_{12} &= C_2 + \beta C_3 \\ C^H_{13} &= C_2 - 4\beta C_3 \\ C^H_{33} &= C_1 + 8\beta C_3 \\ C^H_{44} &= \tfrac{1}{2}(C_1 - C_2) - 4\beta C_3 \\ C^H_{66} &= \tfrac{1}{2}(C^H_{11} - C^H_{12}) = \tfrac{1}{2}(C_{11} - C_{12}) + 2\beta C_3 \end{aligned} \qquad (7)$$

where

$$\begin{aligned} 5C_1 &= 3C_{11} + 2C_{12} + 4C_{44} \\ 5C_2 &= C_{11} + 4C_{12} - 2C_{44} \\ C_3 &= C_{11} - C_{12} - 2C_{44} \end{aligned} \qquad (8)$$

where $\beta = 1/20$ for the <100> fiber texture.

Apparently, relationships for the S_{ij}'s, which give the Reuss bounds by matrix inversion, do not occur in the literature. These are:

$$\begin{aligned} S^H_{11} &= \tfrac{1}{4}(3S_{11} + S_{12} + 8S_{44}) \\ S^H_{12} &= \tfrac{1}{4}(S_{11} - 3S_{12} - 8S_{44}) \\ S^H_{13} &= S_{12} \\ S^H_{33} &= S_{11} \\ S^H_{44} &= 4S_{44} \\ S^H_{66} &= 2(S^H_{11} - S^H_{12}) = S_{11} + 2S_{12} + 8S_{44} \end{aligned} \qquad (9)$$

In deriving these relationships, one must remember that the inverse C^{-1}_{ijkl} of a fourth-rank elasticity tensor relates to the inverse $C^{-1}_{\alpha\beta}$ of its associated 6x6 matrix by a factor multiplied times C_{ijkl}. This factor is 4 if both α and β exceed 3, is 2 if either α or β exceeds 3, and is 1 if neither α nor β exceeds 3.

RESULTS

Table 1 shows the predicted single-crystal elastic constants of stainless-steel 316. Other principal results of the study--elastic-stiffness, elastic compliance, and sound velocity--occur in Table 1, which shows Voigt and Reuss bounds together with their arithmetic average for the <100> ideal fiber texture. To obtain sound velocities, we used a mass density of 7.958 g/cm^3. From these results, the polar plots shown in Figs. 2-4 were determined using well-known relationships [23]. These figures give the angular variation of Young's modulus, E, torsional modulus, T, and sound velocities, both longitudinal, v_ℓ, and transverse, v_t. All curves in Figs. 2-4 represent arithmetic averages of Voigt and Reuss bounds.

DISCUSSION

The tables and figures show several interesting, potentially important, results:

1. Texture induces large elastic-constant changes (departures from isotropic values).

2. Shear elastic constants, C_{44}^H and C_{66}^H, change more than longitudinal constants, C_{11}^H and C_{33}^H, and more than the off-diagonal constants, C_{12}^H and C_{13}^H.

3. C_{44}^H offers the best opportunity for detecting texture and estimating its amount. C_{44} corresponds to a shear wave propagated along the fiber axis (x_3) and vibrating in the x_1-x_2 plane, which is elastically isotropic.

4. If high attenuation precludes accurate C_{44}^H measurement, C_{33}^H provides a good lower-attenuation alternative. C_{33}^H corresponds to a longitudinal wave propagating along the fiber axis.

5. For the principal crystallographic directions, with one exception, if texture increases v_ℓ it decreases v_t, and vice versa. Hardly surprising, this means simply that stiffening in a particular direction corresponds to softening in transverse directions.

6. Elastic constants affected least by texture are C_{66}^H and S_{66}^H. This result, at first surprising since C_{66}^H depends on the difference between C_{11}^H and C_{12}^H, arises presumably because C_{66}^H represents a shear wave both propagated and polarized in the x_1-x_2 plane, an elastically isotropic plane with properties determined, for all textures, by averaging over all directions perpendicular to the fiber axis.

7. Finally the remark concerning the bulk modulus of the fiber-textured aggregate. It equals identically the cubic-symmetry bulk modulus, $\frac{1}{3}(C_{11} + 2C_{12})$. It is a scalar. Hydrostatic stress would dilate uniformly the textured aggregate. This contrasts sharply with a microscopically hexagonal material that behaves anisotropically, altering its axial length ratio, in response to hydrostatic stress. This means that welds of cubic-symmetry alloys do not develop pressure-induced internal stresses due to texture. Such stresses would occur, of course, in lower-symmetry-alloy welds.

ACKNOWLEDGMENTS

Two agencies supported this study: The DoE Office of Fusion Energy and the NBS Office of Nondestructive Evaluation. J. Dahnke assisted with calculations.

REFERENCES

1. B. R. Dewey, L. Adler, R. T. King, and K. V. Cook, Measurements of anisotropic elastic constants of type 308 stainless-steel electroslag welds, Exper. Mech. 17, 420-426 (1977).

2. D. S. Kupperman and K. J. Reimann, Effect of shear-wave polarization on defect detection in stainless steel weld metal, Ultrasonics 16, 21-27 (1978).

3. D. S. Kupperman and K. J. Reimann, Ultrasonic wave propagation and anisotropy in austenitic stainless steel weld metal, IEEE Trans. Sonics Ultrason. SU-27, 7-15 (1980).

4. M. G. Silk, B. H. Lidington, and G. F. Hammond, A time domain approach to crack locations and sizing in austenitic welds, Brit. J. NDT 22, 55-61 (1980).

5. J. R. Tomlinson, A. R. Wagg, and M. J. Whittle, Ultrasonic inspection of austenitic welds, Brit. J. NDT 22 119-127 (1980).

6. M. G. Silk, The propagation of ultrasound in anisotropic weldments, Materials Evaluation 39 462-467 (1981).

7. C. M. Fortunko, Ultrasonic evalution of austenitic stainless steel welds using SH waves, submitted to J. Appl. Phys.

8. H. M. Ledbetter and E. R. Naimon, Relationship between single-crystal and polycrystal elastic constants, J. Appl. Phys. 45, 66-69 (1974).

9. H. M. Ledbetter, Sound velocities and elastic-constant averaging for polycrystalline copper, J. Phys. D; Appl. Phys. 13, 1879-1884 (1980).

10. E. Kröner, Berechnung der elastischen Konstanten des Vielkristalls aus den Konstanten des Einkristalls, Z. Phys. 151, 504-518 (1958).

11. H. M. Ledbetter, Predicted single-crystal elastic constants of stainless-steel 304, to be published.

12. H. M. Ledbetter, Sound velocities and elastic constants of steels 304, 310, and 316, Metal Sci. 14, 595-596 (1980).

13. J. F. Nye, Physical Properties of Crystals: Their Representation by Tensors and Matrices (Oxford, London, 1957), p. 141.

14. L. D. Landau and E. M. Lifshitz, Theory of Elasticity (Pergamon, Oxford, 1970), p. 42.

15. W. Voigt, Ueber die Beziehung zwischen den beiden Elastizitätsconstanten isotroper Körper, Ann. Phys. 38, 573-587 (1889).

16. A. Reuss, Berechnung der Fliessgrenze von Mischkristallen auf Grund der Plastizitätsbedingung für Einkristalle, Z. Angew. Math. Mech. 9, 49-58 (1929).

17. R. Hill, The elastic behavior of a crystalline aggregate, Proc. Phys. Soc. Lond. A65, 349-354 (1952).

18. E. Kröner and H. H. Wawra, Coincidence of bounds for some elastic moduli of polycrystals with fibre texture, Philos. Mag. 38, 433-437 (1978).

19. G. Bradfield and H. Pursey, The role of preferred orientation in elasticity investigations, Philos. Mag. 44, 437-443 (1953).

20. H. Pursey and H. L. Cox, The correction of elasticity measurements on slightly anisotropic materials, Philos. Mag. 45, 295-302 (1954).

21. I. P. Talashkevich and K. S. Aleksandrov, Effect of preferred grain orientation on the elastic properties of polycrystals, Fiz. Metal. Metalloved 14, 801-805 (1962).

22. G. Kneer, Über die Berechnung der Elastizitätsmoduln vielkristalliner Aggregate mit Textur, Phys. Stat. Solidi 9, 825-838 (1965).

23. E. Schmid and W. Boas, Plasticity of Crystals (Hughes, London, 1950), p. 21.

24. K. Salmutter and F. Stangler, Elastizität u. Plastizität eines austenitischen Chrom-Nickel-Stahls, Z. Metallkde. 51, 1-4 (1960).

25. M. Kikuchi, Elastic anisotropy and its temperature dependence of single crystals and polycrystal of 18-12 type stainless steel, Japan Inst. Met. 12, 417-421 (1971).

26. M. C. Mangalick and N. F. Fiore, Orientation dependence of dislocation damping and elastic constants in Fe-18Cr-Ni single crystals, Trans. Met. Soc. AIME 242, 2363-2364 (1968).

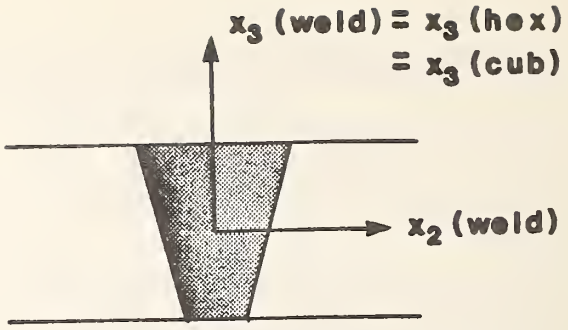

Fig. 1. Relationships between cubic and hexagonal co-ordinate systems and weld geometry. Cubic directions x_1 and x_2 are distributed randomly, perpendicular to x_3. Since hexagonal x_1-x_2 plane is elastically isotropic, x_2' (hex) can be any direction perpendicular to x_3 (hex).

Table 1. Single-crystal elastic constants of several face-centered-cubic Fe-Cr-Ni alloys in units of 10^{11} N/m^2, except A and y, which are dimensionless.

Alloy	C_{11}	C_{12}	C_{44}	B	C'	A	y	Ref.
Experiment								
Fe-12Cr-18Ni	2.332	1.626	1.225	1.862	0.353	3.45	0.697	24
Fe-18Cr-12Ni	1.912	1.179	1.386	1.423	0.367	3.78	0.617	24
Fe-18Cr-14Ni	1.98	1.25	1.22	1.49	0.365	3.34	0.631	26
Fe-18Cr-19Ni	1.91	1.19	1.24	1.43	0.360	3.44	0.623	26
Theory								
Stainless 316	2.07	1.33	1.17	1.57	0.373	3.15	0.640	present

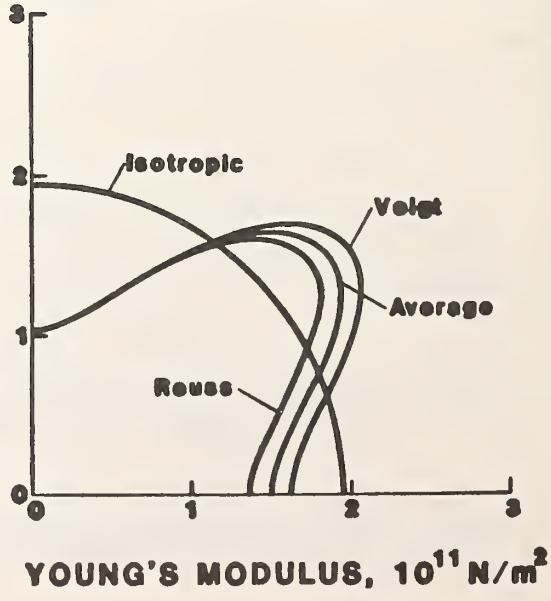

Fig. 2. Angular variation of Young's modulus for stainless-steel 316 for <001> texture. Vertical direction is x_3 (hex), about which figure has complete rotational symmetry. Average denotes simple arithmetic average of Voigt and Reuss bounds, which correspond to constant strain and constant stress, respectively.

Table 2. Elastic stiffnesses, elastic compliances, and sound velocities for stainless-steel 316 with <100> fiber texture.[a]

	Voigt	Reuss	Average	Isotropic
C_{11}^H	2.473	2.265	2.369	2.577
C_{12}^H	0.926	1.133	1.029	1.073
C_{13}^H	1.326	1.326	1.326	1.073
C_{33}^H	2.072	2.072	2.072	2.577
C_{44}^H	1.174	1.174	1.174	0.752
C_{66}^H	0.774	0.566	0.670	0.752
S_{11}^H	0.617	0.736	0.676	0.514
S_{12}^H	-0.029	-0.148	-0.088	-0.151
S_{13}^H	-0.376	-0.376	-0.376	-0.151
S_{33}^H	0.964	0.964	0.964	0.514
S_{44}^H	0.852	0.852	0.852	1.330
S_{66}^H	1.293	1.766	1.530	1.330
v_ℓ (x_1)	0.557	0.534	0.546	0.569
v_ℓ (x_3)	0.510	0.510	0.510	0.569
v_t (x_1)	0.312	0.267	0.289	0.307
v_t (x_3)	0.384	0.384	0.384	0.307

[a]Units on C_{ij}, S_{ij}, and v are 10^{11}N/m^2, 10^{-11}m^2/N, and cm/μs, respectively.

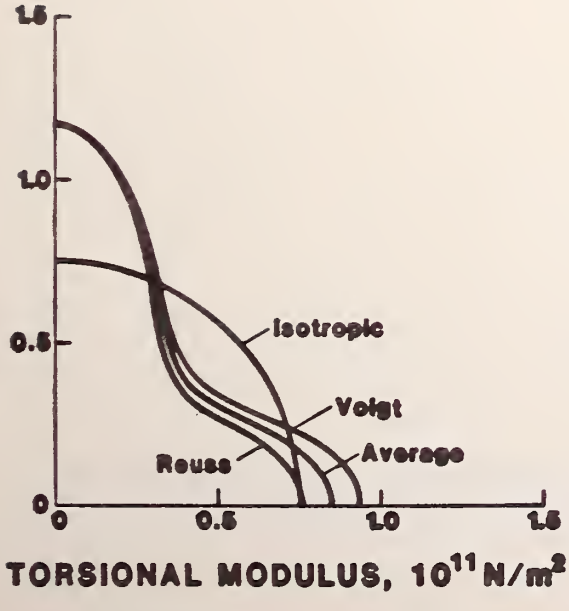

Fig. 3. Angular variation of torsional modulus. See caption 2.

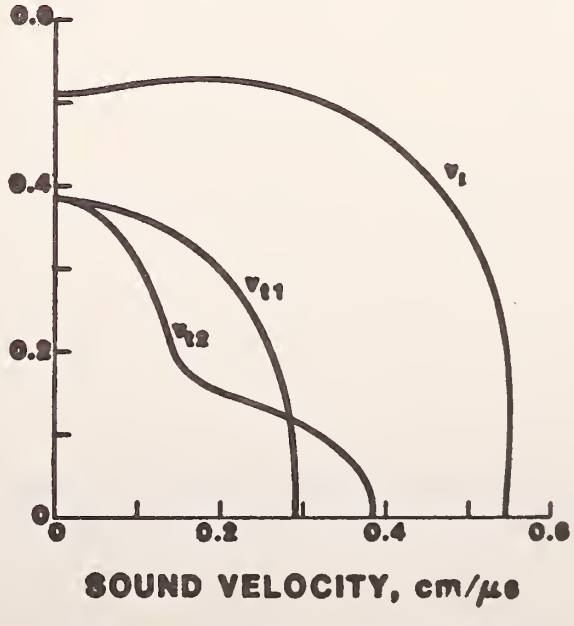

Fig. 4. Angular variation of three sound velocities. See caption 2.

Sound velocity as a texture probe: application to stainless-steel-316 welds

H. M. Ledbetter

Fracture and Deformation Division

National Bureau of Standards

Boulder, Colorado 80303

Texture (nonrandom distribution of crystallites) influences many properties of welds: for example, the optimum direction for propagating an elastic wave with minimum loss. We show theoretically that sound velocity provides a sensitive test for texture. For 316 stainless steel, a face-centered-cubic Fe-Cr-Ni alloy, we calculate elastic stiffnesses (C_{ij}^{H}'s), elastic compliances (S_{ij}^{H}'s), and sound velocities for three ideal fiber textures: <100>, <110>, and <111>. This amounts to modeling the macroscopically hexagonal-symmetry weld in terms of its cubic-symmetry constituents.

Key Words: Elastic-compliance tensor; elastic constants; elastic-stiffness tensor; iron alloy; sound velocity; stainless steel; texture; weld

Introduction

Several recent studies[1-6] emphasize the elastic anisotropy of stainless-steel welds. This anisotropy reflects texture, which arises during welding, probably from strongly directional heat flow.

Absence of macroscopic elastic isotropy affects several weld properties: (1) ultrasonic-wave velocity varies with direction; (2) for a fiber texture, five independent elastic constants are required to characterize the macroscopic material (only two are required for isotropic symmetry); (3) internal friction and ultrasonic-wave-amplitude attenuation also vary with direction; (4) elastic-wave-energy deviations depend strongly on direction; (5) optimum directions exist for propagating an elastic wave with minimum loss. All these properties impact on both the materials science of welds and their nondestructive evaluation.

The present study shows that ultrasonic velocity provides a sensitive test for texture, both qualitatively and quantitatively. For the particular case of stainless-steel-316 welds, we show that <100>, <110>, and <111> fiber textures have fiber-direction shear-wave velocities that differ +26, -6, and -14 percent from the shear-wave velocity of the nontextured random aggregate. Since sound-velocity measurement error seldom exceeds one percent, the amount of <100> texture, for example, is measurable, in principle, to within about four percent. This compares favorably with results of more familiar x-ray diffraction methods for determining texture. It has the advantages of possible in-situ measurements and volume sampling rather than surface sampling.

Theory

One expects that cubic-symmetry crystallites in welds occur either with random orientations or with a single preferred axis parallel to the principal

heat-flow direction, vertical in the figures, denoted x_3. In the x_1-x_2 plane, crystallites are expected to orient themselves randomly because no preferred heat-flow direction occurs in that plane. Thus, an effective fiber texture occurs with x_3 being the fiber axis. Macroscopically, such a material exhibits transverse-isotropic symmetry, with five independent elastic constants. This is equivalent to hexagonal symmetry. In Voigt's contracted C_{ij} notation, the symmetrical elastic-stiffness matrix is:[7]

$$C_{ij}^{H} = \begin{bmatrix} C_{11}^{H} & C_{12}^{H} & C_{13}^{H} & 0 & 0 & 0 \\ & C_{11}^{H} & C_{13}^{H} & 0 & 0 & 0 \\ & & C_{33}^{H} & 0 & 0 & 0 \\ & & & C_{44}^{H} & 0 & 0 \\ & & & & C_{44}^{H} & 0 \\ & & & & & C_{66}^{H} \end{bmatrix} \qquad (1)$$

where $C_{66}^{H} = \frac{1}{2}(C_{11}^{H} - C_{12}^{H})$. Thus, the theoretical problem is to express the five hexagonal-symmetry elastic constants, C_{ij}^{H}, in terms of the three cubic-symmetry elastic constants: C_{11}, C_{12}, and C_{44}.

Present theory does not permit calculation of the elastic constants of textured polycrystalline aggregates of cubic-symmetry crystallites. This is a special and more difficult case of determining the average elastic constants of a random polycrystalline aggregate. For this latter problem, Landau and Lifshitz[8] remind us that "there is ... no general relationship between the moduli of elasticity of a polycrystal and those of a single crystal of the same substance." The fiber-texture case involves a two-dimensional, rather than a three-dimensional, average.

However, elastic-constant bounds can be calculated for textured aggregates. In this study we calculate the Voigt[9] (constant strain) and Reuss[10] (constant stress) bounds and use Hill's[11] suggestion of an arithmetic average to estimate the elastic constants. This approach turns out to be quite reasonable because the Voigt and Reuss bounds do not differ dramatically (a maximum of 37 percent). And for the important <100>-texture case, the bounds coincide for three elastic constants: C_{13}^H, C_{33}^H, and C_{44}^H. Thus, we know these three constants unambiguously. Kröner and Wawra[12] explain the systematics of this bounds coincidence.

Several studies[13-16] derive correctly the relationships for calculating the Voigt bounds of the macroscopic elastic constants of fiber-textured cubic aggregates. We used the form given by Kröner and Wawra:[12]

$$
\begin{aligned}
C_{11}^H &= C_1 + 3\beta C_3 \\
C_{12}^H &= C_2 + \beta C_3 \\
C_{13}^H &= C_2 - 4\beta C_3 \\
C_{33}^H &= C_1 + 8\beta C_3 \\
C_{44}^H &= \tfrac{1}{2}(C_1 - C_2) - 4\beta C_3 \\
C_{66}^H &= \tfrac{1}{2}(C_{11} - C_{12}) + 2\beta C_3
\end{aligned}
\qquad (2)
$$

where

$$
\begin{aligned}
5C_1 &= 3C_{11} + 2C_{12} + 4C_{44} \\
5C_2 &= C_{11} + 4C_{12} - 2C_{44} \\
C_3 &= C_{11} - C_{12} - 2C_{44}
\end{aligned}
\qquad (3)
$$

where β = 1/20, -1/80, and -1/30 for the respective <100>, <110>, and <111> fiber textures.

Apparently, relationships for the S_{ij}'s, which give the Reuss bounds by matrix inversion, do not occur in the literature. These are:

$$
\begin{aligned}
S_{11}^H &= \tfrac{1}{4}(3S_{11} + S_{12} + 8S_{44}) \\
S_{12}^H &= \tfrac{1}{4}(S_{11} - 3S_{12} - 8S_{44}) \\
S_{13}^H &= S_{12} \\
S_{33}^H &= S_{11} \\
S_{44}^H &= 4S_{44} \\
S_{66}^H &= 2(S_{11}^H - S_{12}^H) = S_{11} + 2S_{12} + 8S_{44}
\end{aligned}
\tag{4}
$$

In deriving these relationships, one must remember that the inverse C_{ijkl}^{-1} of a fourth-rank elasticity tensor relates to the inverse $C_{\alpha\beta}^{-1}$ of its associated 6 x 6 matrix by a factor multiplied times C_{ijkl}^{-1}. This factor is 4 if both α and β exceed 3, is 2 if either α or β exceeds 3, and is 1 if neither α nor β exceeds 3.

Results

Input information for the calculations came from the author's previous publications: C_{11} = 2.06, C_{12} = 1.33, C_{44} = $1.19 \cdot 10^{11} N/m^2$, and ρ = 7.958 g/cm^3. Isotropic values in the tables were calculated using Kröner's method.[17] Principal results of the study--elastic stiffness, elastic compliance, and sound velocity--occur in tables 1-3, which show Voigt and Reuss bounds together with their arithmetic average for three ideal fiber textures: <100>, <110>, and <111>. Table 1 shows the C_{ij}^H's, table 2 the S_{ij}^H's, and table 3 the sound velocities based on a mass density of 7.958 g/cm^3. From

these results, the polar plots shown in Figs. 1-4 were determined. For all three textures, these figures give the angular variation of Young's modulus, E, torsional modulus, T, and sound velocities, both longitudinal, v_ℓ, and transverse, v_t. All curves in Figs. 1-4 represent arithmetic averages of Voigt and Reuss bounds.

Discussion

The tables and figures show several interesting, potentially important, results:

1. Texture induces large elastic-constant changes (departures from isotropic values), up to 58 percent.

2. Shear elastic constants, C_{44}^H and C_{66}^H, change more than longitudinal constants, C_{11}^H and C_{33}^H, and more than the off-diagonal constants, C_{12}^H and C_{13}^H.

3. C_{44}^H offers the best opportunity for detecting texture and estimating its amount. C_{44} corresponds to a shear wave propagated along the fiber axis (x_3) and vibrating in the x_1-x_2 plane, which is elastically isotropic.

4. If high attenuation precludes accurate C_{44}^H measurement, C_{33}^H provides a good lower-attenuation alternative. C_{33}^H corresponds to a longitudinal wave propagating along the fiber axis.

5. For the principal crystallographic directions, with one exception, if texture increases v_ℓ it decreases v_t, and vice versa. Hardly surprising, this means simply that stiffening in a particular direction corresponds to softening in transverse directions.

6. For all three textures, the longitudinal constants C_{11}^H and C_{33} either both increase or both decrease. Surprisingly, there is no mixed behavior. In terms of the S_{ij}'s, where the principal-axis Young's moduli are $E_i = S_{ii}^{-1}$, texture decreases E_i for <100> texture but increases E_i for <111> texture.

Figures 1 and 2 show polar plots of Young's modulus and the torsional modulus computed from the S^H_{ij}'s using standard relationships.[18]

7. Elastic constants affected least by texture are C^H_{66} and S^H_{66}. This result, at first surprising since C^H_{66} depends on the difference between C^H_{11} and C^H_{12}, arises presumably because C^H_{66} represents a shear wave both propagated and polarized in the x_1-x_2 plane, an elastically isotropic plane with properties determined, for all textures, by averaging over all directions perpendicular to the fiber axis.

8. Along two directions oblique to x_3, both E(110) and E(111) equal the isotropic value. For these two textures, this amounts effectively to an elastic-constant invariant. Along two different directions, the torsional modulus shows a similar invariance for these two textures. Invariance properties are quite important. For example, isotropic Young's and torsional moduli can be determined directly from anisotropic textured aggregates by making measurements in special directions.

9. The bulk modulus of the fiber-textured cubic-crystallite aggregate equals identically the cubic-symmetry bulk modulus, $(C_{11} + 2C_{12})/3$. It is a scalar. Hydrostatic stress would dilate uniformly the textured aggregate. This contrasts sharply with a microscopically hexagonal material that behaves anisotropically, altering its axial length ratio, in response to hydrostatic stress. This means that welds of cubic-symmetry alloys do not develop pressure-induced internal stresses due to texture. Such stresses would occur, of course, in lower-symmetry-alloy welds.

Acknowledgment

Two agencies supported this study: the DoE Office of Fusion Energy and the NBS Office of Nondestructive Evaluation. J. Dahnke assisted with calculations.

References

1. B. R. Dewey, L. Adler, R. T. King, and K. V. Cook, Measurements of anisotropic elastic constants of type 308 stainless-steel electroslag welds, Exper. Mech. 17, 420-426 (1977).
2. D. S. Kupperman and K. J. Reimann, Ultrasonic wave propagation and anisotropy in austenitic stainless steel weld metal, IEEE Trans. Sonics Ultrason. SU-27, 7-15 (1980).
3. M. G. Silk, B. H. Lidington, and G. F. Hammond, A time domain approach to crack location and sizing in austenitic welds, Brit. J. NDT 22, 55-61 (1980).
4. J. R. Tomlinson, A. R. Wagg, and M. J. Whittle, Ultrasonic inspection of austenitic welds, Brit. J. NDT 22, 119-127 (1980).
5. M. G. Silk, The propagation of ultrasound in anisotropic weldments, Materials Evaluation 39, 462-467 (1981).
6. C. M. Fortunko, Ultrasonic evaluation of austenitic stainless steel welds using shear horizontal waves, Appl. Phys. Lett. 39, 699-700 (1981).
7. J. F. Nye, Physical Properties of Crystals: Their Representation by Tensors and Matrices (Oxford, England, 1957), p. 141.
8. L. D. Landau and E. M. Lifshitz, Theory of Elasticity (Pergamon, Oxford, 1970), p. 42.
9. W. Voigt, Ueber die Beziehung zwischen den beiden Elastizitätsconstanten isotroper Körper, Ann. Phys. 38, 573-587 (1889).
10. A. Reuss, Berechnung der Fliessgrenze von Mischkristallen auf Grund der Plastizitätsbedingung für Einkristalle, Z. Angew. Math. Mech. 9, 49-58 (1929).
11. R. Hill, The elastic behavior of a crystalline aggregate, Proc. Phys. Soc. Long. A65, 349-354 (1952).

12. E. Kröner and H. H. Wawra, Coincidence of bounds for some elastic moduli of polycrystals with fibre texture, Philos. Mag. 38, 433-437 (1978).

13. G. Bradfield and H. Pursey, The role of preferred orientation in elasticity investigations, Philos. Mag. 44, 437-443 (1953).

14. H. Pursey and H. L. Cox, The correction of elasticity measurements on slightly anisotropic materials, Philos. Mag. 45, 295-302 (1954).

15. J. P. Talashkevich and K. S. Aleksandrov, Effect of preferred grain orientations on the elastic properties of polycrystals, Fiz. Metal. Metalloved. 14, 801-805 (1962).

16. G. Kneer, Über die Berechnung der Elastizitätsmoduln vielkristalliner Aggregate mit Textur, Phys. Stat. Solidi 9, 825-838 (1965).

17. E. Kröner, Berechnung der elastischen Konstanten des Vielkristalls aus den Konstanten des Einkristalls, Z. Physik 151, 504-518 (1958).

18. E. Schmid and W. Boas, Plasticity of Crystals (Hughes, London, 1950), p. 21.

Table I. Predicted C_{ij}'s for textured stainless-steel 316, in units of 10^{11} N/m^2

Texture	Bound	C_{11}	C_{12}	C_{13}	C_{33}	C_{44}	C_{66}
[100]	Voigt	2.473	0.926	1.326	2.072	1.174	0.774
	Reuss	2.265	1.133	1.326	2.072	1.174	1.566
	Avg	2.369	1.029	1.326	2.072	1.174	0.670
[110]	Voigt	2.773	1.016	0.926	2.873	0.774	0.874
	Reuss	2.480	1.179	1.065	2.593	0.566	0.650
	Avg	2.626	1.102	0.906	2.733	0.670	1.762
[111]	Voigt	2.873	1.059	0.792	3.140	0.640	0.970
	Reuss	2.650	1.282	0.792	3.140	0.483	0.684
	Avg	2.762	1.170	0.792	3.140	0.561	0.796
Isotropic		2.577	1.073	1.073	1.577	0.752	0.752

Table II. Predicted S_{ij}'s for textured stainless-steel 316, in units of 10^{-11} m^2/N

Texture	Bound	S_{11}	S_{12}	S_{13}	S_{33}	S_{44}	S_{66}
[100]	Voigt	0.617	-0.029	-0.376	0.964	0.852	1.293
	Reuss	0.736	-0.148	-0.376	0.964	0.852	1.766
	Avg	0.676	-0.088	-0.376	0.964	0.852	1.530
[110]	Voigt	0.442	-0.130	-0.101	0.413	1.293	1.145
	Reuss	0.564	-0.205	-0.148	0.507	1.766	1.538
	Avg	0.503	-0.167	-0.124	0.460	1.530	1.341
[111]	Voigt	0.417	-0.134	-0.071	0.355	0.563	1.103
	Reuss	0.507	-0.224	-0.071	0.355	2.071	1.462
	Avg	0.462	-0.179	-0.071	0.355	1.817	1.287
Isotropic		0.514	-0.151	-0.151	0.514	1.330	1.330

Table III. Predicted sound velocities for textured stainless-steel 316, in units of cm/μs.

Texture	Bound	v_{11}	v_{33}	v_{44}	v_{66}
[100]	Voigt	0.5574	0.5103	0.3841	0.3118
	Reuss	0.5335	0.5103	0.3841	0.2667
	Avg	0.5455	0.5103	0.3841	0.2892
[110]	Voigt	0.5903	0.6008	0.3118	0.3313
	Reuss	0.5882	0.5708	0.2667	0.2859
	Avg	0.5742	0.5858	0.2892	0.3086
[111]	Voigt	0.6008	0.6281	0.2836	0.3376
	Reuss	0.5771	0.6281	0.2463	0.2932
	Avg	0.5890	0.6281	0.2649	0.3156
Isotropic		0.5691	0.5691	0.3074	0.3074

List of Figures

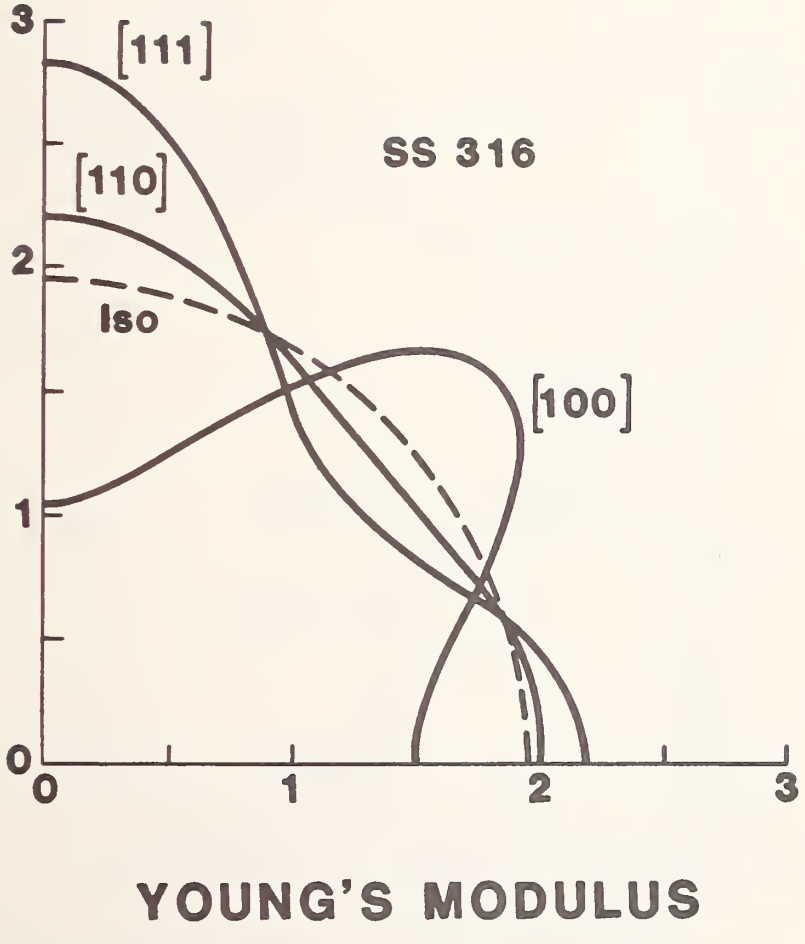

Fig. 1. Angular variation of Young's modulus for three ideal fiber textures. All curves represent arithmetic average of Voigt and Reuss bounds. Units are 10^{11} N/m^2.

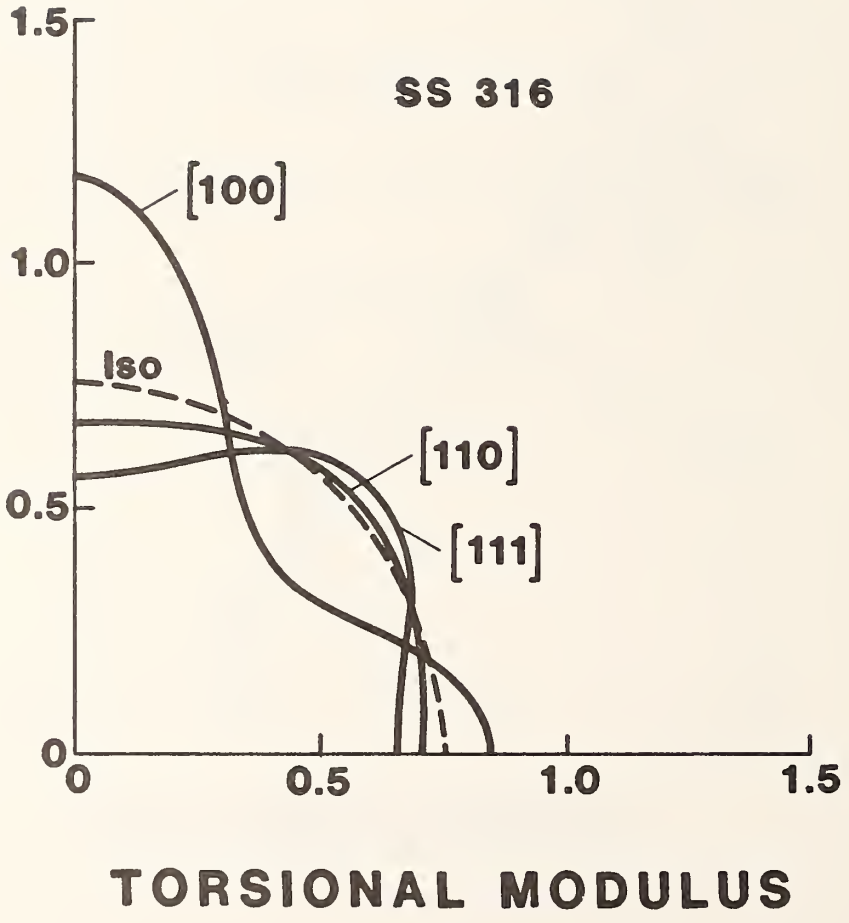

Fig. 2. Angular variation of torsional modulus. Units are 10^{11} N/m^2.

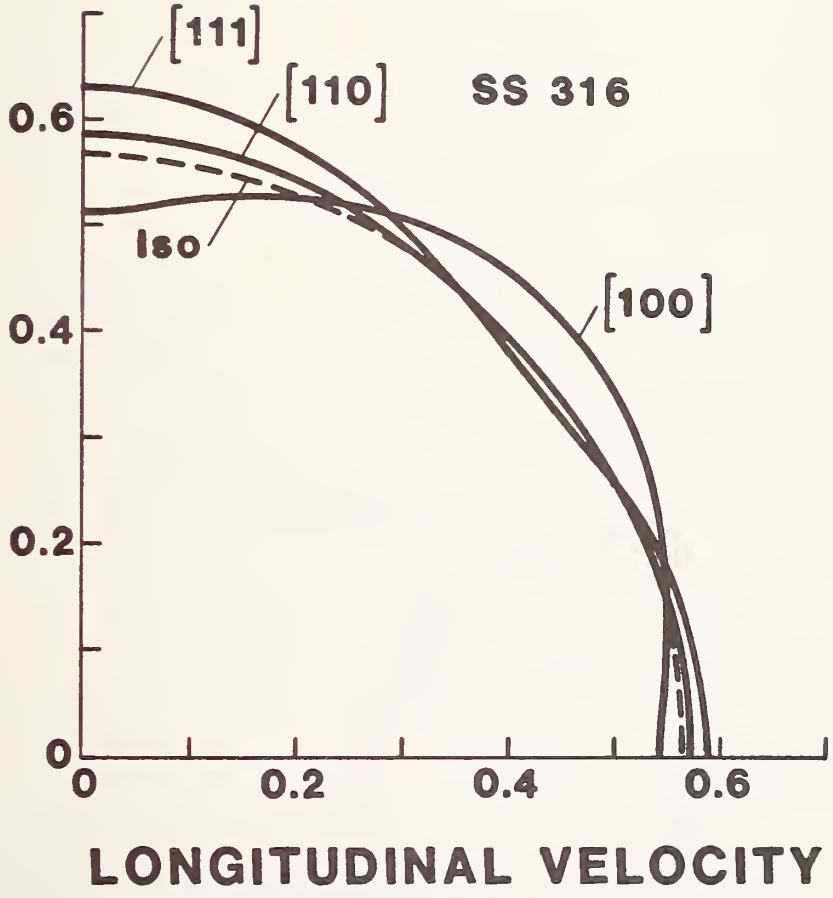

Fig. 3. Angular variation of longitudinal sound velocity. Units are cm/μs.

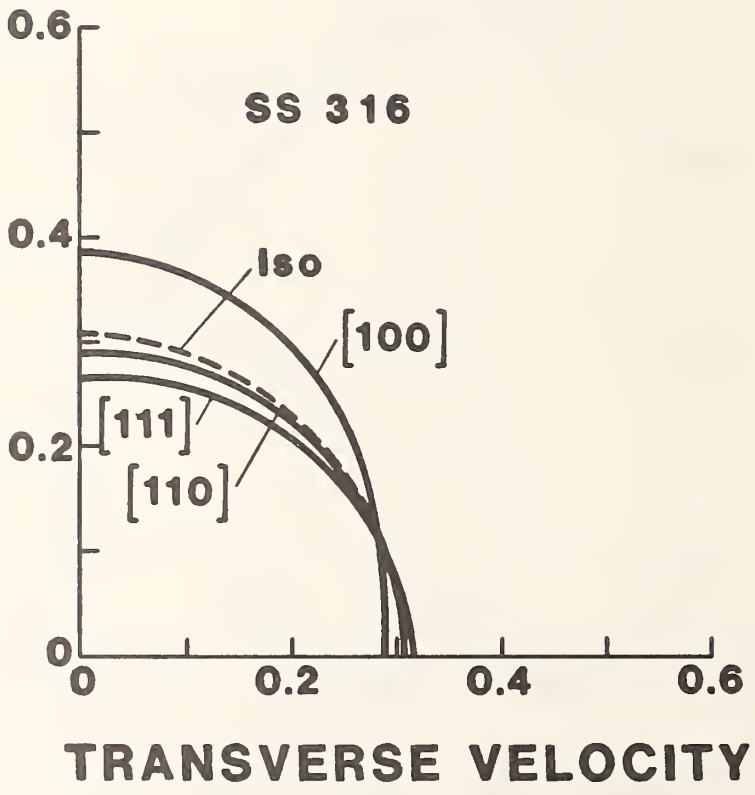

Fig. 4. Angular variation of first transverse sound velocity. Units are cm/μs.

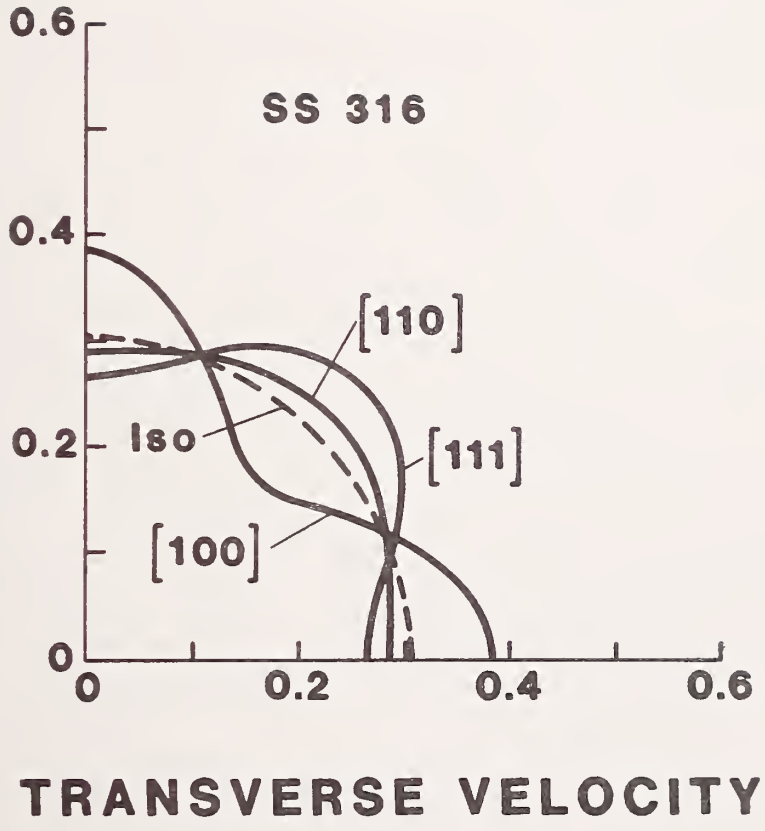

Fig. 5. Angular variation of second transverse sound velocity. Units are cm/μs.

NONMETALLICS

NONMETALLICS PROGRAM

LEADERS: M. B. Kasen, H. M. Ledbetter, NBS
STAFF: M. W. Austin, R. D. Kriz, R. E. Schramm, NBS
CONTRACTS: S. K. Datta, U. Colorado; J. G. Hust, Division 773, NBS

OBJECTIVES:

(1) To measure, model, and understand the properties of composites that enter essentially into the conception, design, construction, operation, and performance of magnetic-fusion-energy equipment.
(2) To cooperate with industry to establish and refine cryogenic-grade specifications for insulating laminates and coding systems for laminates.

RESEARCH PAST YEAR (1981):

(1) Ledbetter. Review of NBS studies of anisotropic elastic constants and internal friction of fiber-reinforced composites.
(2) Datta, Ledbetter, Kinra. Theoretical-experimental study of wave propagation and elastic constants in particulate and fibrous composites.
(3) Datta, Ledbetter. A critical comparison of observation and theory of the elastic constants of fiber-reinforced boron-aluminum.
(4) Kriz. Effects of absorbed moisture on stress-wave propagation in graphite/epoxy.
(5) Kriz. A monitoring device for elastic-stiffness degradation in graphite/epoxy.
(6) Kriz. Ply cracks and fracture strengths of graphite/epoxy laminates at 76 K.
(7) Kasen, Schramm. Measurement of mechanical properties down to 4 K of a polyimide-matrix variant of G-10CR.
(8) Kasen, Schramm. Screening, down to 76 K, of samples of G-10CR produced by two new manufacturers of this product.
(9) Hust. Measurements of thermal conductivity at cryogenic temperatures for two glass-fabric-reinforced epoxy-matrix laminates with different reinforcement-to-resin ratios.

RESEARCH THIS YEAR (1982):

(1) Kriz, Ledbetter. Ultrasonic measurement of the complete nine-component elastic-constant tensor of a woven glass-fiber/epoxy composite.
(2) Kriz. Calculated stress distributions in a woven composite by a finite-element model.
(3) Datta, Ledbetter, Kriz. Predicted elastic constants of transversely isotropic composites containing anisotropic fibers.
(4) Ledbetter, Kriz. Elastic-wave surfaces in fiber-reinforced composites.
(5) Datta, Ledbetter, Austin, Kriz. Longitudinal wave propagation in an elastic composite thin rod.
(6) Kasen. Continuation of a program on the standardization of cryogenic grades of insulating and structural laminates in cooperation with industry.

DISCUSSION:

The following discussion gives some details of the studies listed above.

(1) Kriz, Ledbetter. By inspection, a cloth-reinforced composite has three mutually orthogonal mirror planes and, therefore, orthotropic (or orthorhombic) symmetry. The point group is mm = 2m. Any of the three diad axes formed by intersecting mirror planes could be chosen as the z axis. Since z usually denotes the physically most unique axis, we chose z to be perpendicular to the cloth layers. Materials with this symmetry exhibit nine independent elastic constants. Contracting the fourth-rank tensor, C_{ijkl}, to a two-index (Voigt) notation , C_{ij}, and representing C_{ij} by a 6x6 matrix, we have for orthotropic symmetry and the above coordinate system:

$$C_{ij} = \begin{bmatrix} C_{11} & C_{12} & C_{13} & 0 & 0 & 0 \\ & C_{22} & C_{23} & 0 & 0 & 0 \\ & & C_{33} & 0 & 0 & 0 \\ & & & C_{44} & 0 & 0 \\ & \text{symmetrical} & & & C_{55} & 0 \\ & & & & & C_{66} \end{bmatrix}$$

By ultrasonic methods, we will determine this elastic-stiffness tensor by measuring the elastic compliances, S_{ij}, and using the matrix equation

$$[S_{ij}] = [C_{ij}]^{-1}.$$

No one has done this. The results will provide valuable material characterization, a valid test for any proposed macroscopic-microscopic theory of material properties, and key design information. We intend to study a G-10CR-type material.

(2) Kriz. For the purpose of establishing a universal design system, a plane-weave fiber-reinforced composite can be geometrically modeled as a combination of structural "unit cells." Investigation of the stress distributions within a unit cell when loaded in tension, compression, or shear provides an explanation of fracture, which initiates in high-stress regions. The fracture process in a woven composite can then be modeled as a sequence of related unit-cell

failures. The elastic and fracture behavior of a three-ply fiber-reinforced plate subjected to bending has been modeled by Hirai and Senba [1] using a unit-cell structural model. The approach to be taken in this study is to classify analytically the elastic response and fracture process of a unit cell when loaded in tension shear, or compression, or any combination thereof. This classification will be accomplished by a fine-mesh finite-element model of the unit cell. On the basis of these results, one can construct an idealized, simpler structural unit cell with appropriate elastic and fracture characteristics; this simpler cell can then be used to predict the mechanical response of a woven composite structure. This analysis has high technological consequences and transcends significantly the existing so-called laminate theory.

(3) Datta, Ledbetter, Kriz. We will derive dispersion relationships for waves propagating perpendicular to continuous fibers that are oriented unidirectionally. In the long-wavelength limit we will obtain relationships that predict the composite's effective static moduli. We will compare these relationships with others derived by energy methods to obtain upper and lower bounds of the effective static moduli. We will demonstrate this comparison graphically by plotting for graphite-epoxy the predicted composite moduli over the full range of fiber volume fractions. We will consider the fibers to be anisotropic, but transversely isotropic. We will consider the relationship between our results and the upper and lower bounds of Hashin. The static properties are, of course, special cases of the more general dispersion relationships.

(4) Ledbetter, Kriz. As explained above, one can describe completely the elastic constants of a woven fabric composite by either the $[C_{ij}]$ or the $[S_{ij}]$ matrix. However, for understanding the elastic constants, no substitute exists for graphical representation surfaces of quantities, such as Young's modulus, torsional modulus, Poisson's ratio, linear compressibility, et cetera. This study will develop and interpret these surfaces.

(5) Datta, Ledbetter, Austin, Kriz. Longitudinal wave propagation in a thin, circular, composite rod has many applications. This theoretical-experimental study will start with a Mindlin-Herrmann type of theory to derive the approximate equations of motion. We anticipate solving a seven-unknown eigenvalue problem to determine the variation of phase and group velocities with frequency. The immediate application is to a NbTi/Cu superconductive wire. Longitudinal wave velocity in the wire will be measured by a kHz-region standing-wave method.

[1] Hirai, T. and Senba, T., An Analytical Approach to Interseparation Behavior of Woven-Fabric Reinforced Plastic Subjected to Bending Displacement," in Composite Materials; Mechanics, Mechanical Properties, and Fabrication, Japan Society for Composite Materials, Tokyo (1981).

(6) Kasen, Schramm. The nonmetallic materials characterization program continued with the determination of the cryogenic mechanical performance of a variant of G-10CR that contained a polyimide matrix in place of the conventional epoxy matrix. Studies at the Oak Ridge National Laboratories had shown that this variant had much higher tolerance to gamma irradiation at 5 K than did the conventional laminate. Unfortunately, the NBS studies showed the tensile, compression, and interlaminar shear properties of the polyimide-matrix laminate to be distinctly inferior to the epoxy laminate at all temperatures. These data, combined with the 5-8 times higher cost of the polyimide laminate as compared with that of the epoxy laminate, raise questions as to the viability of the laminate in magnet construction. Fractographic analysis of the failure modes in the polyimide laminate are currently underway to increase our understanding of its poor cryogenic performance. Discussions are also underway with industry to assess ways of improving basic mechanical performance while maintaining radiation resistance. The use of an epoxy-polyimide "alloy" has been suggested. Characterization studies also included screening of the cryogenic performance of G-10CR produced by two new manufacturers. Samples of G-10CR from a third manufacturer have also been received for screening. These studies will be of value in establishing performance variability among manufacturers.

(7) Hust. Studies on factors controlling thermal conductivity of laminates at cryogenic temperature have continued, recognizing the importance of such data to the efficient design of refrigeration systems for superconducting magnets. Measurements were carried out on specimens of G-10 laminate containing different proportions of glass and resin in an attempt to distinguish the contribution of each to conductivity. As discussed elsewhere in this report, the results were somewhat ambiguous, although analysis is not yet complete. The thermal conductivity program also involved characterization of a G-10CR material produced by a different manufacturer to provide information on the variability that might be expected in materials produced to the specification.

(8) Kasen. The nonmetallics program has continued to emphasize development of standard cryogenic grades of insulating and structural laminates. The objective is to provide magnet builders with commercial sources of reliable, characterized materials and to provide the basis for a systematic materials development program in response to the needs of the magnetic fusion industry. As manufacturers worked with the existing specification for the cryogenic grade of glass-fabric reinforced industrial laminate G-10CR, it became apparent that the specification was unnecessarily restrictive in some respects and deficient in specificity in other respects. The specification was therefore revised on the basis of industry recommendations and copies of the revision were submitted to the manufacturers for comment. Primary changes were a provision for utilization of several alternative chemically equivalent epoxy resins and alternative equivalent glass finishes, guidance in establishing the required cure cycle, and a statement of required minimums in mechanical and physical properties.

The standardization program continues to attract the interest of the U.S. laminating industry; two additional corporations have undertaken production of G-10CR. Three manufacturers are already established in the market.

Substantial progress has been made in working with the laboratory of another manufacturer on the development of a standard specification for a discontinuous glass-mat-reinforced epoxy laminate that could perform most of the functions of G-10CR at a substantially reduced cost. It is hoped that this specification will be completed in FY82.

Progress in the standardization program was reviewed in an invited paper "Current Status of Standardized Nonmetallic Cryogenic Laminates" at the ICMC/ICEC conference in San Diego on August 10-14, 1981. The subject was also reviewed in a session on nonmetallics chaired by M. B. Kasen at the NBS-DoE Vail Workshop, October 6-8, 1981.

The subject of nonmetallic materials standardization was also addressed in the context of a committee discussion on Codes and Standards for MFE Low Temperature Materials held as part of the Vail Conference. It was agreed that the initial effort in nonmetallics should be development of standard test methods. A committee was set up for this purpose.

CURRENT STATUS OF STANDARDIZED NONMETALLIC CRYOGENIC LAMINATES*

M. B. Kasen and R. E. Schramm
Fracture and Deformation Division
National Bureau of Standards
Boulder, Colorado

ABSTRACT

The MFE, MHD, and rotating cryogenic machinery technologies are making increasingly severe demands on materials technology. This is particularly acute in nonmetallic structural and insulating materials required for superconducting magnet construction. Unlike metals technology, the available nonmetallic materials have not been standardized, which creates problems in reliability. This paper is a progress report of the efforts to meet the industrial needs for such materials while laying the groundwork for systematic materials development to meet future needs.

*To be published in Advances in Cryogenic Engineering-Materials, Vol. 28, R. P. Reed and A. F. Clark, Eds., Plenum Press, New York (1982).

INTRODUCTION

National Bureau of Standards personnel are continuing to work with magnet fabricators and with representatives of the U.S. laminating industry to establish standard grades of nonmetallic insulator and structural support materials for use in critical parts of magnetic fusion energy (MFE) cryogenic systems. Standardized materials are required for several reasons: (1) excessive variability in the 4-K mechanical properties among nonmetallic laminates purchased to present industrial generic designations, (2) the impracticality of establishing performance specifications for retention of properties after neutron and gamma irradiation at 4 K, and (3) lack of knowledge of the significant elements in a laminate that determine such performance.

The objective of the program is to assist designers in materials selection by establishing commercial sources of standard materials for which a cryogenic data base has been established. Achievement of this objective will simplify communication between designer and laminate producer, enabling a balance to be achieved between performance and cost, and laying a sound foundation for systematic materials development in response to demonstrated need.

This is, of course, an open-ended task--there will always be a desire for better material performance at lower cost and there will always be avenues for improvement. But the program recognizes that designers require assistance in materials selection for current designs as well as improved materials for future designs. The overall approach is illustrated by the flow sheet of Fig. 1. We

*Invited paper.

start by assessing current materials needs and by consulting with industry on existing laminate systems best capable of meeting these needs. A common specification for a high-grade laminate of the defined type is then established by the laminating industry. At this point, the standard laminates differ from those of a generic designation primarily in the restrictions placed on the components used in their manufacture and on the manufacturing procedure. These restrictions are intended to be sufficiently stringent to insure commercially available products whose cryogenic performance can be meaningfully characterized and whose performance variability is minimal. Deficiencies that are subsequently revealed through experience or additional testing can then be systematically addressed since they are associated with defined materials systems.

This paper reviews progress in this effort during the past several years, discusses the present activity, and offers suggestions for future work.

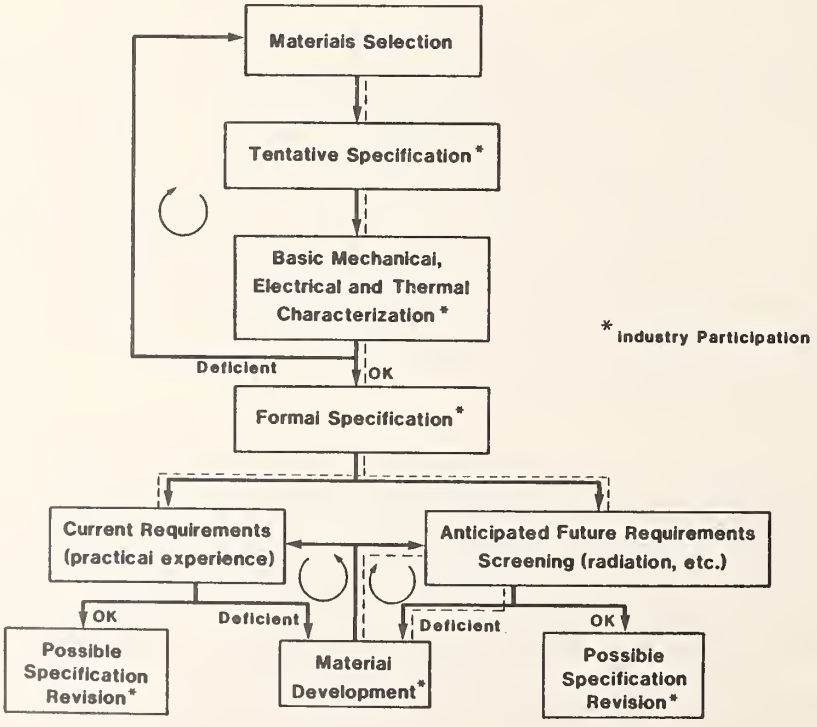

Fig. 1. Flow chart depicting a proposed approach to meeting immediate needs of nonmetallic laminate development for the cryogenic industry. Dashed lines indicate the present state of development of the G-10CR and G-11CR grades of industrial laminates.

PROGRESS TO DATE

A survey of proposed MFE designs[1] revealed that high-pressure glass-cloth-reinforced epoxy laminates of the NEMA G-10 or G-11 type were likely to be widely used for electrical insulation and structural support for superconducting magnet windings. It was known, however, that the cryogenic mechanical properties of such material produced by different manufacturers could differ as much as 40% at 4 K. This stimulated a series of discussions with representatives of the laminating industry, culminating in the establishment of tentative specifications for controlled grades of G-10CR and G-11CR. These materials are currently being manufactured by four U.S. firms and have been well received by the cryogenic industry. The effect of cryogenic temperatures on the mechanical, electrical, and thermal performance of these materials has been reported in the literature,[2] and characterization work is continuing at NBS and other laboratories. The specifications are currently undergoing revision to provide the fabricators with maximum discretion in fabrication while maintaining minimum product variability.

As anticipated, the G-10CR and G-11CR products have served as baseline materials for the study of several variants. An early variant replaced the conventional boron-containing type E glass reinforcement with a boron-free type in expectation of improved radiation resistance; however, no substantial improvement was observed.[3] Another variant, tentatively designated G-10CR-L, replaced the conventional glass reinforcement with a lightweight type having less thickness per layer for the same volume fraction of glass. This variant is useful in fabricating parts with small radii of curvature and thin sections where it is desirable to maximize the number of layers of reinforcement. Cryogenic tests have thus far indicated performance very similar to that of the original CR grade except for some decrease in compressive strength. It is probable that this variant will become a standard grade.

Radiation studies conducted at Oak Ridge National Laboratory[3] have indicated substantial degradation in mechanical properties of G-10CR and G-11CR after exposure to neutron and gamma irradiation at 4 K under fluences at levels expected in the superconducting magnets of working MFE systems. These results led to the investigation of a G-10CR variant in which the epoxy matrix was replaced by a polyimide resin. Subsequent tests at Oak Ridge National Laboratory[4] indicated a much improved radiation resistance for this variant, suggesting that it might be a candidate for insulators and structural supports in MFE magnets.

Unfortunately, the polyimide variant, tentatively designated PG-10CR, has several disadvantages of potential significance. One is high cost--six to eight times that of G-10CR. Another is

relatively low cryogenic mechanical strength compared with that of G-10CR. As illustrated in Figs. 2 and 3, the polyimide variant develops significantly lower tensile, compressive, and interlaminar shear strengths at all temperatures, with the difference increasing notably at cryogenic temperatures. The 30-40% lower interlaminar shear strength of the polyimide variant is potentially the most significant deficit, because many nonmetallic magnet components are loaded in shear. Young's modulus is the only property in which the polyimide variant excells.

POSSIBILITIES FOR THE FUTURE

In the near term, it will be necessary to continue the development of standard laminate grades for use in radiation environments. Results described above suggest that radiation resistance and cost may go hand in hand, in which case it would be desirable to provide designers with a series of laminate types so that material selection could be made on a cost-versus-performance basis. Ideally, the series would include laminates reinforced with glass mat as well as glass fabric and material that could be fabricated by low- as well as high-pressure molding techniques. Discussions are being held to determine the feasibility of such development.

Because so little is known of the factors affecting degradation of laminate propeties due to irradiation at 4 K, the achievement of this goal will require close cooperation between researchers in industry and several scientific disciplines. A successful program must work with extremely well-characterized

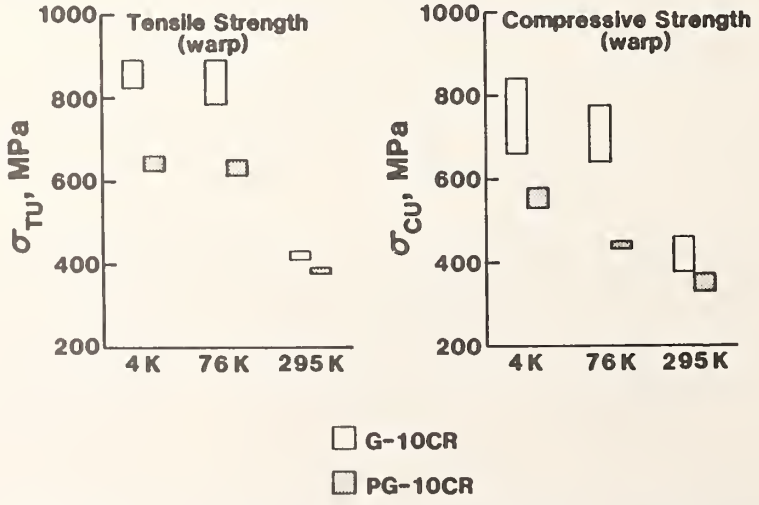

Fig. 2. Comparison of the effect of cryogenic temperature on the tensile and compressive strength of G-10CR and the polyimide-matrix variant tentatively designated PG-10CR. Preliminary data for two PG-10CR specimens of each condition tested edgewise (warp direction).

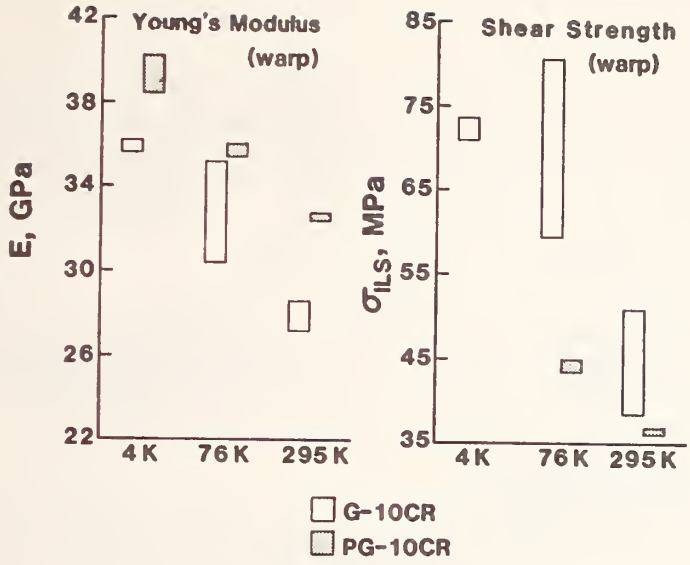

Fig. 3. Comparison of the effect of cryogenic temperature on Young's modulus and interlaminar shear strength (guillotine method) of G-10CR and the polyimide-matrix variant tentatively designated PG-10CR. Preliminary data for two PG-10CR specimens of each condition tested edgewise (warp direction).

materials and would probably require an iterative research cycle of the type illustrated in Fig. 4. As the cryogenic radiation resistance of a polymer is likely to be a strong function of the exact molecular structure,[5] an essential part of the cycle is a correlation of molecular level damage with radiation level and property change. Only in this way will the required scientific basis be established.

The need for standardization largely reflects the absence of a nonmetallic materials classification system in which material performance is associated with a coding system. In the long run, it will be necessary to develop a system for composite laminates that is the equivalent of the systems developed for metals by AISI, the Aluminum Association, and other similar voluntary standard bodies. Although composites are indisputedly more complex than metals, there seems no a priori reason why such an approach would not be feasible for composite laminates, recognizing that the significant engineering properties of a laminate at any temperature are largely defined by a few parameters. For example, the intrinsic mechanical, elastic, thermal, and electrical properties of a high quality laminate should be defined within relatively narrow limits by a numerical classification system that establishes the type and flexibility of the matrix, the type and configuration of the reinforcement, and the reinforcement volume fraction. At the very least, it should be possible to establish meaningful lower bounds

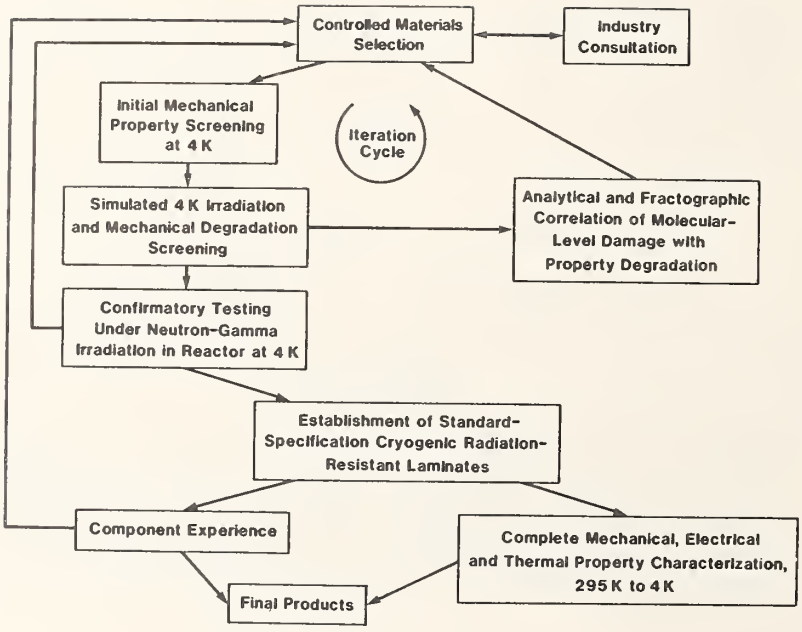

Fig. 4. Proposed flow chart for development of radiation-resistant nonmetallic laminate insulators.

on such properties. The basic elements of such a coding system have been considered in a previous publication.[6]

CONCLUSIONS

The author has reviewed ongoing efforts to provide a commercial supply of standardized, controlled-performance laminates required to meet the short-term needs of the cryogenic industry for critical components in MFE superconducting magnet design and construction. The approach provides a basis for systematic development of material variants and for new materials as required to meet the needs of future designs. The approach recognizes that development of nonmetallic insulators and structural supports in magnets subjected to intense irradiation at 4 K will require a much better understanding of the factors affecting material performance in this environment and that this will be achieved only by an interdisciplinary approach.

The lack of terminology allowing a designer to specify nonmetallic laminate materials by a performance criteria is a

continuing problem. The ongoing standardization effort is designed to meet immediate technical needs; however, a long-range effort to establish an accepted standards notation system for nonmetallics comparable to that used in the metals industry is worthy of consideration.

ACKNOWLEDGMENTS

This work was supported by the Office of Magnet Fusion Energy, United States Department of Energy.

REFERENCES

1. R. P. Reed, F. R. Fickett, M. B. Kasen, and H. I. McHenry, "MFE Low Temperature Materials Program: A Survey," National Bureau of Standards, Institute for Basic Standards, Boulder, Colorado (1977).
2. M. B. Kasen, G. R. MacDonald, D. H. Beekman, and R. E. Schramm, in: Mechanical, electrical, and thermal characterization of G-10CR and G-11CR glass-cloth/epoxy laminates between room temperature and 4 K, in: "Advances in Cryogenic Engineering - Materials," Vol. 26, Plenum Press, New York (1980), p. 235.
3. R. R. Coltman, Jr., C. E. Klabunde, R. H. Kernohan, and C. J. Long, "Radiation Effects on Organic Insulators for Superconducting Magnets," ORNL/TM-7077, Oak Ridge National Laboratory, Oak Ridge, Tennessee (1979).
4. R. R. Coltman, Jr., C. E. Klabunde, and C. J. Long, "The Effect of a 100 MGy (10^{10} Rads) Gamma-Ray Dose at 5 K on the Strength of Polyimide Insulators," Report SSD No. 81-10, Oak Ridge National Laboratory, Oak Ridge, Tennessee (1981).
5. B. S. Brown, Radiation effects in superconducting fusion-magnet materials, J. Nucl. Mater. 98:1 (1981).
6. M. B. Kasen, Standardizing nonmetallic composite materials for cryogenic applications, in: "Fundamentals and Applications of Nonmetallic Materials at Low Temperatures," G. Hartwig and D. Evans, eds., Plenum Press, New York (1981) (in press).

Effect of Cryogenic Temperatures on the Mechanical Performance of Glass-Fabric-Reinforced Laminates

R. E. Schramm and M. B. Kasen
Fracture and Deformation Division
National Bureau of Standards
Boulder, CO 80303

ABSTRACT

This study continues the mechanical testing of glass-fabric/epoxy composites from several producers using the same specifications. In addition to the G-10CR and G-11CR standards, two more variants were made to achieve particular qualities: one contained a lightweight cloth to improve drapability and the second substituted polyimide for the epoxy matrix to achieve greater radiation resistance. From these tests, it appears that: (1) various manufacturers produce a consistent product, (2) the lightweight variant has properties similar to the standards, and (3) the polyimide variant has mechanical properties inferior to its epoxy counterpart.

INTRODUCTION

Previously we reported on the complete mechanical characterization of one manufacturer's CR-grade glass-cloth/epoxy composites and the screening of those from another company.[1-3] This report contains screening data on similar laminates and two variants from two other sources.

MATERIALS

Through NBS-industry cooperation, there are industry-wide specifications for G-10CR and G-11CR. The basis for both laminates is the same glass fabric (style 7628) of silane-finished E glass. It has an unbalanced plain weave with a fiber-bundle density in the warp/fill direction of 42/32 per 25 mm. The G-10CR matrix is a heat-activated, amine-catalyzed, bisphenol-A, solid-type epoxy resin. The G-11CR matrix is an aromatic-amine-hardened, bisphenol-A, liquid-type epoxy resin. Resin weight fraction is 32-36% for G-10CR and 28-33% for G-11CR.[4]

In addition to standard G-10CR and G-11CR, the producers have provided several variants as possible solutions to particular problems. The first ones tested were a G-10CR and a G-11CR made with boron-free glass.[2,3] This report includes two additional variants. One was a G-10CR-type but made with a lightweight glass cloth (style 1165 with thinner fibers and a 60/52 warp/fill ratio) to increase the ability to drape around small-radius curves while still retaining the same glass content; its identification here is G-10CR-L. The other was also a G-10CR type but it had a matrix of aromatic polyimide rather than epoxy;[5,6] its identification here is PG-10CR. Gamma radiation tests on

this composite have shown it retained a substantial portion of its initial strength even after 100 MGy (10^{10} rads) at 5 K.[7]

METHODS

Previous reports have documented our test methods and specimen configurations,[3,8] but a brief summary is in order here. All specimens were cut from flat sheets. Tensile tests used friction grips but no tabs. Specimen gage length was 54-mm (2.125-in) long, 12.7-mm (0.5-in) wide, and 1.27-mm (0.05-in) thick. Tensile measurements included Young's modulus, Poisson's ratio, and strain and strength at failure. Compression specimens had a gage length of 19 mm (0.75 in), a width of 7.9 mm (0.31 in), and a thickness of 3.8 mm (0.15 in). In the guillotine interlaminar shear tests (ASTM D 2733-70), we changed the separation between saw cuts to 9.5 mm (0.375 in). Fracture strength was the only measurement in both compression and shear tests.

The original characterization data were the results of at least three tests at each temperature, 295 K, 76 K, and 4 K (room temperature, in liquid nitrogen, and in liquid helium), and in both of the cloth directions (warp and fill). Our screening process involved only two tests at each of two temperatures, 295 K and 76 K, in the warp direction only. With these values it was possible to check for any major deviations among batches. Since the polyimide matrix represented a major change, we extended its screening to include 4-K measurements and both directions.

Flexural tests are often useful as a method of comparison. We ran a few such tests on three batches of G-10CR at 295 K and 76 K in four-point loading (ASTM D 790-71, Method II, Procedure B). Specimens were nominally 25 mm x 76 mm x 4 mm.

Conditioning of all specimens prior to testing (ASTM D 3039-71) was at least 40 h at 22 ± 2°C and 50 ± 10% relative humidity.

RESULTS

Screening data for several epoxy-matrix laminates are in Table 1. Since the pilot-plant material from Manufacturer A received the most extensive examination,[1,2] all comparisons for the standard composites should look back to this data base. With this reference point, it appears there are no statistically outstanding mechanical variations in the G-10CR from Manufacturer C or D or the G-11CR from Manufacturer D. The inevitable variations that do exist among the six properties measured appear to be randomly positive and negative. Most of them are less than 10%, and a few reach the 20% range--values quite understandable solely on the basis of small sample size.

Comparing Manufacturer C's lightweight variant and standard G-10CR shows that the differences again tend to be minor. There is, however, a possible trend: all of the properties of the variant are somewhat lower at room temperature but at 76 K they are almost the same or slightly greater, except for slightly lower shear strength. To maintain the same glass density, the G-10CR-L contained more layers of cloth per unit thickness and so the epoxy layers between were necessarily thinner. This could possibly allow for some relief of residual stresses caused by cooling. Since the lightweight 1165 cloth is less unbalanced than the 7628 style, it has proportionately less glass oriented in the warp direction and more in the fill direction. This could explain the trend to lower values at 295 K and also amplify the 76-K increase. The change in fiber balance would also lead to more balanced mechanical properties, but we did not test for this.

The PG-10CR data are in Table 2. To determine the effect of changing to a polyimide matrix, it is necessary to compare its test results with those from

the standard laminate. For this purpose, Table 3 lists the average values of both pilot plant and production runs of G-10CR from the same manufacturer.[1,2] Figure 1 shows the range of warp measurements for the two composites, and the mechanical differences due to the matrices are evident. All parameters increased as the temperature decreased, as is usual. Except for the Young's modulus and compressive strength, there was little increase between 76 K and 4 K.

A method of comparing the two composites is to calculate ratios of their properties taken in various pairs. Table 4 collects three sets of such ratios: (1) the value of each PG-10CR parameter divided by the corresponding value for G-10CR, (2) each 4-K parameter divided by the 295-K value, and (3) the fill parameter divided by the warp value.

These room temperature ratios show that all three warp direction strengths, tensile, compressive, and shear, were about 10% lower for the polyimide material. At cryogenic temperatures, the ratio of tensile strengths, dominated by fiber properties but dependent on the matrix for load transfer, underwent about a 25% decrease. However, the ratios of compressive and shear strengths, dominated by matrix properties, dropped a significant 40% at low temperatures. The change in resin also lowered the strain-to-failure ratios about 20-35% throughout the range of test temperatures. For the fill-direction ratios, the tensile and compressive strengths, as well as the failure strain, were less divergent between the two materials. The order of the elastic property ratios, on the other hand, showed a reversal. Poisson's ratio for both was generally the same or possibly somewhat higher for the polyimide composite. The Young's modulus was 10-15% higher for PG-10CR at all temperatures in the warp direction and about 20% higher in the fill direction.

The ratio of cryogenic to room temperature properties indicates that, in almost all circumstances, the PG-10CR was less sensitive to low temperatures than was G-10CR. The one possible exception was the warp direction Poisson's ratio, but this may simply have been the result of scatter in the small number of tests. It is interesting to speculate whether there is any relationship between the polyimide's smaller temperature sensitivity and its greater radiation resistance.

The number of glass fibers in the fill direction is about 75% of that in the warp direction in the glass cloth used in G10-CR and PG-10CR. As a first guess, this would seem to determine the ratio of properties measured along these two main axes. The last section of Table 4 indicates that the fill/warp ratio actually varied considerably from this estimate. These values for all parameters except the tensile strength ran higher than 0.75. Since the interlaminar shear strength is almost totally a function of matrix material and fiber bonding, its ratio was about unity. In most instances, the PG-10CR ratios were greater than those of the G-10CR, indicating less mechanical inhomogeneity in the cloth plane.

The flexural strengths in Table 5 indicate somewhat low values for the fill tests of Manufacturer A, but these are most likely due to statistical fluctuations. The ratio of 76-K to 295-K values ran slightly over two which is similar to the tension and compression strengths; the fill/warp ratio is also very similar. Since flexure involves a complicated mix of tension, compression and shear, the results are not easy to interpret.

CONCLUSIONS

Production standards for G-10CR and G-11CR glass cloth/epoxy laminates are available to all interested U.S. manufacturers. Thus far, five producers have supplied us with one or both composites as well as several variants. After testing material from four of these sources, our mechanical data showed reasonable agreement and the products seemed consistent; this, of course, was the reason for all the effort in establishing and disseminating the specifications.

A G-10CR-L variant made with lightweight cloth offers some possible advantages. Its properties would be somewhat less anisotropic as evidenced by its slightly lower room temperature properties, while its 76-K properties show a possible slight improvement.

A PG-10CR variant with a polyimide matrix rather than epoxy demonstrated a higher stiffness but reduced strength, particularly at low temperatures. This decreased load capacity and its much higher cost necessitate a very careful analysis of its radiation resistance necessary before this composite could be a candidate for large-scale use.

ACKNOWLEDGMENT

We would like to thank Mr. N. J. Armendariz for conducting the flexural tests and analyzing the data.

REFERENCES

1. M. B. Kasen, "Mechanical Properties, Thermal Contraction, and Electrical Properties of G-10CR and G-11CR," in Materials Studies for Magnetic Fusion Energy Applications at Low Temperatures - II, Eds. F. R. Fickett and R. P. Reed, NBSIR 79-1609, National Bureau of Standards, Boulder, Colorado, 407-416 (1979).

2. R. E. Schramm and M. B. Kasen, "Mechanical Properties of G-10CR and G-11CR," in Materials Studies for Magnetic Fusion Energy Applications at Low Temperatures - III, Ed. R. P. Reed, NBSIR 80-1627, National Bureau of Standards, Boulder, Colorado, 335-366 (1980).

3. M. B. Kasen, G. R. MacDonald, D. H. Beekman, Jr., and R. E. Schramm, "Mechanical, Electrical, and Thermal Characterization of G-10CR and G-11CR Glass-Cloth/Epoxy Laminates between Room Temperatures and 4 K," in Advances in Cryogenic Engineering, Vol. 26, Eds. A. F. Clark and R. P. Reed, Plenum Press, New York, 235-244 (1980).

4. J. R. Benzinger, "Manufacturing Capabilities of CR-Grade Laminates," in Advances in Cryogenic Engineering, Vol. 26, Eds. A. F. Clark and R. P. Reed, Plenum Press, New York, 252-258 (1980).

5. J. R. Benzinger, "The Manufacture of Radiation Resistant Laminates" in Materials Studies for Magnetic Fusion Energy Applications at Low Temperatures - IV, Eds. R. P. Reed and N. J. Simon, NBSIR 81-1645, National Bureau of Standards, Boulder, Colorado, 615-638 (1981).

6. R. P. Reed, R. E. Schramm, and A. F. Clark, "Mechanical, Thermal, and Electrical Properties of Selected Polymers," Cryogenics 13, 66-87 (1973).

7. R. R. Coltman, C. E. Klabunde, and C. J. Long, "The Effect of a 100 MGy (10^{10} rads) Gamma-Ray Dose at 5K on the Strength of Polyimide Insulators," Report SSD No. 81-10, Oak Ridge National Laboratory, Oak Ridge, Tennessee (1981).

8. R. E. Schramm and M. B. Kasen, "Cryogenic Mechanical Peoperties of Boron-, Graphite-, and Glass-Reinforced Composites," Mater. Sci. Eng. 30, 197-204 (1977).

LIST OF TABLES

Table 1.

Mechanical Properties of Glass-Cloth/Epoxy Composites

Temperature K	Young's Modulus, E GPa	(Msi)	Poisson's Ratio, ν	Strain to Failure, ε_{Tu}, %	Tensile Strength, σ_{Tu}, MPa	(ksi)	Compressive Strength, σ_{Cu}, MPa	(ksi)	Shear Strength, σ_{ILS}, (Guillotine) MPa	(ksi)
				G-10CR (Manufacturer C - Warp)						
295	26.3	(3.82)	0.146	1.77	410	(59.4)	342	(49.6)	>51*	(>7.4*)
	25.7	(3.73)	0.134	2.47	394	(57.1)	337	(48.8)	>49*	(>7.1*)
Average	26.0	(3.78)	0.140	2.12	402	(58.3)	340	(49.2)		
76	32.9	(4.77)	0.195	2.40	763	(111)	733	(106)	70.3	(10.2)
	29.8	(4.32)	0.147	2.84	721	(105)	665	(96.5)	72.4	(10.5)
Average	31.4	(4.55)	0.171	2.62	742	(108)	699	(101)	71.4	(10.4)
				G-10CR-L (Manufacturer C - Warp)						
295	23.0	(3.33)	0.117	1.93	376	(54.5)	300	(43.5)	>41*	(>6.0*)
	23.4	(3.39)	0.131	1.93	384	(55.6)	342	(49.6)	>47*	(>6.8*)
Average	23.2	(3.36)	0.124	1.93	380	(55.1)	321	(46.6)		
76	32.5	(4.71)	0.192	3.01	732	(107)	737	(107)	60.4	(8.76)
	30.0	(4.35)	0.194	3.36	760	(110)	696	(101)	72.7	(10.5)
Average	31.3	(4.53)	0.193	3.19	746	(109)	717	(104)	66.6	(9.63)
				G-10CR (Manufacturer D - Warp)						
295	29.0	(4.21)	0.174	1.79	454	(65.8)	395	(57.3)	49.2	(7.14)
	29.6	(4.29)	0.151	2.56	477	(69.2)	360	(52.2)	47.7	(6.92)
Average	29.3	(4.25)	0.163	2.18	466	(67.5)	378	(54.8)	48.5	(7.03)
76	33.3	(4.83)	0.218	3.31	877	(127)	698	(101)	73.6	(10.7)
	34.6	(5.02)	0.215	2.91	839	(122)	794	(115)	70.7	(10.3)
Average	34.0	(4.93)	0.217	3.11	858	(125)	746	(108)	72.2	(10.5)
				G-11 CR (Manufacturer D - Warp)						
295	29.1	(4.22)	0.173	1.83	470	(68.1)	320	(46.3)	45.6	(6.05)
	28.3	(4.10)	0.168	1.90	460	(66.7)	379	(54.8)	38.5	(5.58)
Average	28.7	(4.16)	0.171	1.87	465	(67.4)	350	(50.6)	42.1	(5.82)
76	34.7	(5.04)	0.219	3.47	835	(121)	640	(92.8)	48.1	(6.97)
	34.2	(4.95)	0.212	3.06	816	(118)	612	(88.7)	50.9	(7.38)
Average	34.5	(5.00)	0.216	3.27	826	(120)	626	(90.8)	49.5	(7.18)

*Minimum value, specimen broke in tension.

Table 2.

Mechanical Properties of PG-10CR (Manufacturer A)

Temperature K	Young's Modulus, E, GPa	(Msi)	Poisson's Ratio, ν	Strain to Failure, ε_{TU}, %	Tensile Strength, σ_{TU} MPa	(ksi)	Compressive Strength, σ_{Cu} MPa	(ksi)	Shear Strength, σ_{ILS} (Guillotine) MPa	(ksi)
					Warp					
295	32.8	(4.76)	0.164	1.38	386	(56.0)	372	(54.0)	36.9	(5.36)
	32.6	(4.72)	0.169	1.46	384	(55.7)	337	(48.9)	36.9	(5.35)
Average	32.7	(4.74)	0.167	1.42	385	(55.9)	355	(51.5)	36.9	(5.36)
76	35.4	(5.13)	0.195	2.18	617	(89.5)	451	(65.4)	43.7	(6.34)
	36.0	(5.23)	0.225	2.43	648	(94.0)	442	(64.1)	45.3	(6.57)
Average	35.7	(5.18)	0.210	2.31	633	(91.8)	447	(64.8)	44.5	(6.46)
4	40.3	(5.84)	0.236	2.66	654	(94.9)	580	(84.1)	44.9	(6.51)
	38.5	(5.58)	0.251	2.25	622	(90.2)	530	(76.8)	—	—
Average	39.4	(5.71)	0.244	2.46	638	(92.6)	555	(80.5)		
					Fill					
295	28.2	(4.09)	0.150	1.41	271	(39.3)	312	(45.3)	35.6	(5.17)
	28.6	(4.15)	0.152	1.44	259	(37.5)	319	(46.3)	37.4	(5.42)
Average	28.4	(4.12)	0.151	1.43	265	(38.4)	316	(45.8)	36.5	(5.30)
76	31.3	(4.53)	0.175	2.56	382	(55.4)	462	(67.0)	45.2	(6.55)
	33.7	(4.88)	0.198	1.94	375	(54.4)	470	(68.1)	46.2	(6.77)
Average	32.5	(4.71)	0.187	2.25	379	(54.9)	466	(67.6)	45.7	(6.66)
4	34.3	(4.97)	0.169	1.87	396	(57.4)	570	(82.7)	45.0	(6.53)
	34.7	(5.04)	0.189	3.01	407	(59.1)	—	—	—	—
Average	34.5	(5.01)	0.179	2.44	402	(58.3)				

Table 3.

Average Mechanical Properties of G-10CR (Manufacturer A, Pilot Plant and Production)*

Temperature K	Young's Modulus, E, GPa+	Poisson's Ratio, ν	Strain to Failure, ϵ_{TU}, %	Tensile Strength, σ_{TU} MPa+	Compressive Strength, σ_{CU} MPa+	Shear Strength. σ_{ILS} (Guillotine) MPa+
				Warp		
295	28.0	0.160	1.78	419	375	45.2
76	32.0	0.203	3.47	846	778	66.2
4	35.9	0.211	3.65	862	862	72.6
				Fill		
295	22.4	0.143	1.55	257	283	
76	27.0	0.183	2.53	459	557	72.9
4	29.1	0.210	2.70	496	598	78.0

*Calculated from Refs. 1 and 2. Data are the averages of 3-6 tests.

+1 MPa = 145 psi; 1 GPa = 1.45×10^5 psi.

Table 4.

Mechanical Property Ratios*

Temperature, K	E	ν	ε_{TU}	σ_{TU}	σ_{CU}	σ_{ILS}
			PG-10CR/G-10CR			
			Warp			
295	1.17	1.04	0.80	0.92	0.95	0.82
76	1.09	1.03	0.67	0.75	0.57	0.67
4	1.10	1.16	0.67	0.74	0.64	0.62
			Fill			
295	1.27	1.06	0.92	1.03	1.12	-
76	1.20	1.02	0.89	0.83	0.84	0.63
4	1.19	0.85	0.90	0.81	0.95	0.57
			4 K/295 K			
			G-10CR, Warp			
	1.28	1.32	2.05	2.06	2.36	1.61
			G-10CR, Fill			
	1.30	1.47	1.74	1.93	2.11	-
			PG-10CR, Warp			
	1.20	1.46	1.73	1.66	1.56	1.22
			PG-10CR, Fill			
	1.21	1.19	1.71	1.52	1.80	1.23
			Fill/Warp			
			G-10CR			
295	0.80	0.89	0.87	0.61	0.75	-
76	0.82	0.90	0.73	0.54	0.72	1.10
4	0.81	1.00	0.74	0.58	0.69	1.09
			PG-10CR			
295	0.87	0.90	1.01	0.69	0.89	0.99
76	0.91	0.89	0.97	0.60	1.04	1.03
4	0.88	0.73	0.99	0.63	1.03	1.00

*Calculated from average values in Tables 2 and 3.

Table 5.

Flexural Strength of G-10CR

	295 K				76 K			
	Warp		Fill		Warp		Fill	
	MPa	(ksi)	MPa	(ksi)	MPa	(ksi)	MPa	(ksi)
			Manufacturer A (Production Plant)					
	486	(70.7)	283	(41.1)	1120	(163)	745	(108)
	540	(78.3)	333	(48.3)	1100	(159)	745	(108)
Avg	514	(74.5)	308	(44.7)	1110	(161)	745	(108)
			Manufacturer B					
			382	(55.4)			800	(116)
			394	(57.2)			807	(117)
			383	(55.6)			793	(115)
			366	(53.0)			786	(114)
Avg			381	(55.3)			800	(116)
			Manufacturer C					
	512	(74.3	383	(55.5)	1100	(159)	834	(121)
	531	(77.0)	397	(57.6)	1110	(161)	862	(125)
Avg	522	(75.7)	390	(56.6)	1100	(160)	848	(123)

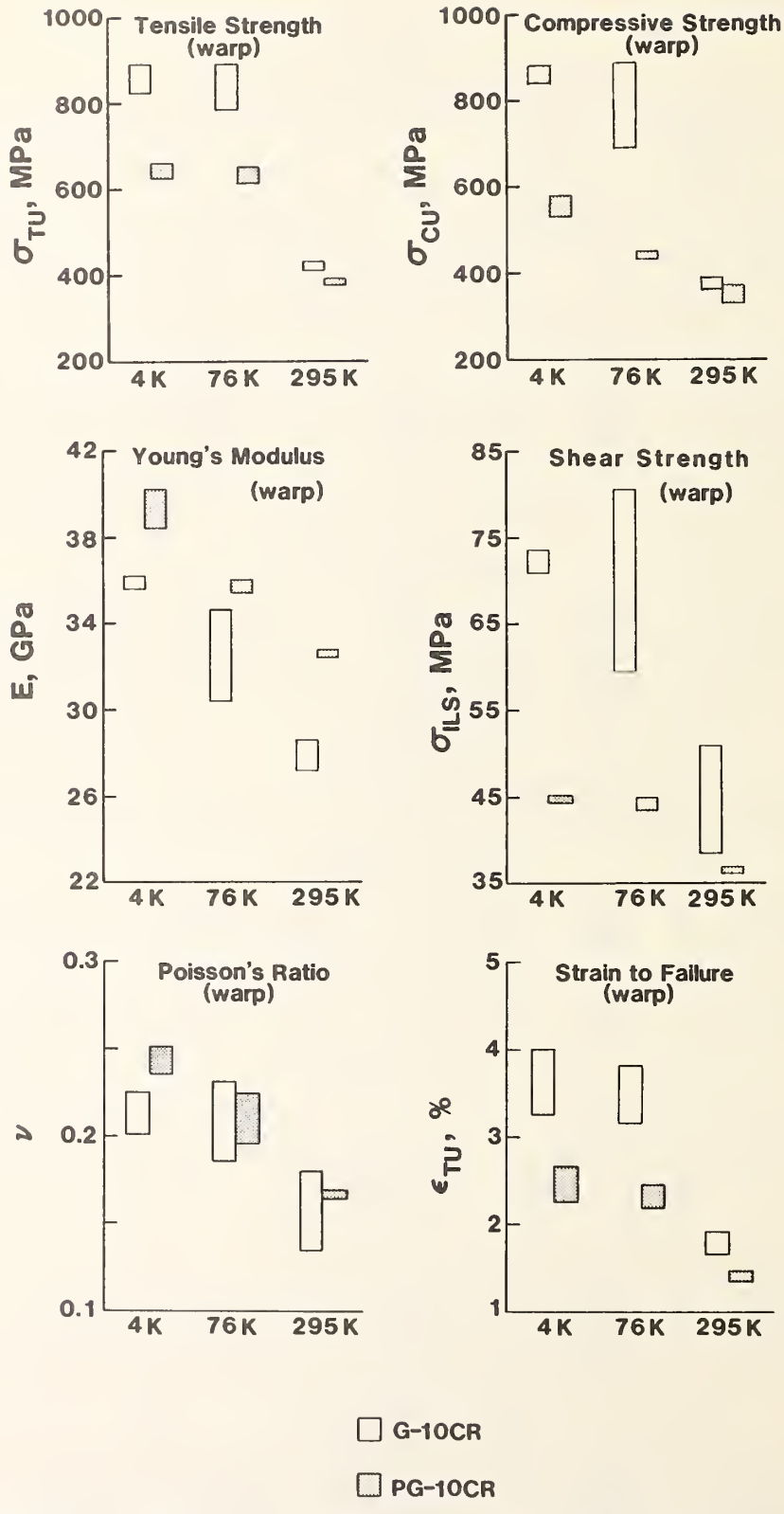

Figure 1. Comparison of the measurements on two glass-cloth composites. The height of the bar indicates the data spread. For the G-10CR there were 3-6 tests and, at most, two for the PG-10CR.

MECHANICAL PROPERTIES OF PLASTIC COMPOSITES UNDER LOW TEMPERATURE CONDITIONS*

M. B. Kasen
Fracture and Deformation Division
National Bureau of Standards
Boulder, Colorado

*Published in Composites, Vol. 12, 107 (1981).

Letters

Mechanical properties of plastic composites under low temperature conditions

Dear Sir,

It was with interest that I noted in a recent issue of your journal a contribution[1] describing the low temperature mechanical properties of plastic composites. The author's conclusion that composites fabricated with a highly flexibilized epoxy matrix provide better cryogenic properties than those fabricated with nonflexibilized systems may be valid for laminates containing 32% by volume reinforcement, but it is not valid for the higher volume fractions typical of laminates in industrial usage. Literature reviews and work in our laboratory[2–4] indicate that residual stresses created by the large thermal contraction of highly flexibilized systems negates any advantage provided by the intrinsically higher strain capability of the matrix when fiber contents approach 50-60% by volume in glass, graphite or aramid laminates. We find, for example, that the flexible Resin 2 formulation[5] decreases the 4 K uniaxial longitudinal tensile strength of an S-901 glass-reinforced laminate to a level about equal to that of a non-flexibilized matrix laminate at 295 K. The transverse strength of a uniaxial graphite-reinforced laminate at 4 K is reduced by about 60% by a higher flexibilized matrix, while the transverse failure strain is reduced by about 90%. When used with aramid fiber, the flexibilized matrix reduces the uniaxial transverse strength to an extent rendering the laminate almost useless for structural applications.

Additionally, the intrinsic weakness of highly flexibilized resin sysytems near room temperature has resulted in the catastrophic failure of several structures designed for cryogenic use but necessarily subjected to moderate stresses at room or slightly elevated temperatures.

The author quite correctly points out the limitation imposed on the effective cryogenic strength of glass-reinforced laminates due to the strain limitations of conventional bisphenol A epoxies at such temperatures (the 'knee point' in the stress/strain curve). But the solution requires a resin system providing reasonably high room temperature strength and reasonably low thermal contraction as well as cryogenic toughness. Possible approaches have been discussed in the recent literature.[6] Until such systems are developed and proven, it appears most prudent to utilize conventional resin systems for cryogenic laminates.

M. B. Kasen

Fracture Deformation Division, National Bureau of Standards, Boulder, CO 80303

REFERENCES

1 **Kadotani, K.** 'Mechanical properties of plastic composites under low temperature conditions' *Composites* 11 (April 1980) pp 87-94

2 **Kasen, M. B.** 'Mechanical and thermal properties of filamentary-reinforced structural composites at cryogenic temperatures' Part I: glass reinforced structural composites, *Cryogenics*, 15 No 6 (June 1975) pp 327-349 Part II: advanced composites, *Cryogenics* 15 No 12 (December 1975) pp 701-719

3 **Kasen, M. B.** 'Cryogenic properties of filamentary-reinforced composites: An update' (In preparation)

4 **Schramm, R. E. and Kasen, M. B.** 'Cryogenic mechanical properties of boron-, graphite-, and glass-reinforced composites' *Mater Sci and Eng* 30 (1977) pp 197-204

5 **Soffer, L. N. and Molho, R.** 'Cryogenic resins for glass-filament-wound composites' *NASA CR-72114* (Final)

6 *Nonmetallic Materials and Composites at low Temperatures* (Plenum Press, 1979)

Author's reply

Dear sir,

I would like to thank Dr Kasen for his interest in my paper[1] and to express general agreement with his comments. However, I would like to enlarge upon the published paper and try to explain further the aims of the work reported. It was my intention to select reinforced-plastics materials for use as electrical insulation in superconducting magnet coils utilized in fusion reactors and rotating machines. For such applications glass-fibre reinforced plastics with low fibre volume are preferred in order to match the thermal contraction characteristics of the copper-clad superconductors and the stainless steel used to fabricate the structural components. The grp components, together with the resin moulded superconducting coils are immersed in liquid helium so that the operating temperature, at which electromagnetic stress is applied is always of the order of 4K. Thus it is not expected that the grp components should have higher mechanical strength at room temperature.

However, assembly of the magnet coils is sometimes carried out at higher temperatures, and resins having adequate (medium) flexibility have been used in these instances. For the manufacture of components such as support rods, pressure vessels and torque tubes, high performance composites such as boron, carbon or aramid fibre-reinforced plastics with higher volume fractions and using conventional resin systems (with Tg in the range 100°C – 200°C) are desirable.

K. Kadotani

Hitachi Research Laboratory, Ibaragi Prefecture, Japan

THERMAL CONDUCTIVITY OF G-10CR AND G-11CR INDUSTRIAL LAMINATES AND THEIR COMPONENT PARTS AT LOW TEMPERATURES

J. G. Hust
Thermophysical Properties Division
Center for Chemical Engineering
National Bureau of Standards
Boulder, Colorado

ABSTRACT

Thermal conductivity measurements and comparisons with literature data are presented on cryogenic grade composites G-10CR and G-11CR and their component parts, resin and glass fibers. The measurements were made in the 2 to 300 K range for heat flow both normal to the fabric and in the warp direction. Material variability from lot-to-lot and the effect of strain is described. The relationship of composite conductivity to the conductivities of the resin and glass components is discussed.

INTRODUCTION

As part of the continuing cryogenic materials program, NBS, in cooperation with the U.S. laminating industry, has arranged for commercial production of component-specified NEMA/ASTM type G-10 and G-11 industrial laminates for cryogenic insulation and structural applications. This action was taken because conventionally produced proprietary G-10 and G-11 laminates did not meet the demanding specifications of superconducting magnets for magnetic fusion energy applications. The cryogenic variability in G-10 and G-11 laminates occurs because the room temperature NEMA specifications can be met by different glass reinforcements, weaves of the fabric, types of epoxy, and cure agents as well as the fabrication procedures. The component-specified laminates investigated are designated as G-10CR and G-11CR.

This report summarizes the thermal conductivity measurements of this project and compares the results with literature data. In addition, the relationship of the composite conductivity to the conductivities of the resin and glass components is discussed.

MATERIAL AND SPECIMEN CHARACTERIZATION

G-10CR and G-11CR are composites of fiberglass fabric and epoxy. The fabric is woven from type E glass threads with 17 threads per cm (43 per in) in the warp direction and 12 threads per cm (32 per in) in the fill direction. The thread is composed of 75 filaments each of 0.00046 cm (0.00018 in) diameter. The density of E glass is 2.58 g/cm^3. G-10CR resin is a heat-activated amine catalyzed bisphenol A, solid type, epoxy resin. G-11CR resin is an aromatic amine bisphenol A liquid type epoxy resin. The G-10CR resin has an uncured density of 1.10 ± 0.01 g/cm^3 and the G-11CR resin has uncured density of 1.04 ± 0.01 g/cm^3. The cured resin density is highly uncertain and is discussed later.

The G-10CR laminate is specified to contain 33-35% resin by weight and the weight fraction of resin in G-11CR is specified to be 27-31% by weight.

The dimensions, weights, and densities at 280 K of the specimens measured are given in table 1. The specimens were generally fabricated from single blocks of the designated material; however, in some instances layered specimens were used.

Specimens G-10C1, G-10C4, G-10C7, and G-11C1 were measured to establish baseline values and to study material variability between manufacturers. Specimen G-10C3 was measured to determine the difference between G-10CR and stock G-10.

The specimen designated as G-10C2 was prepared to study the effect of strain. A thin strip (2-cm wide, 0.4-cm thick, and about 30-cm long) was cut from a sheet and strained in a tensile apparatus to 90% of ultimate (1.44%). This strip was then cut into squares, and the pieces were bonded under pressure to form the thermal conductivity specimen. To obtain a control specimen, G-10C4 was fabricated in the same manner from an unstrained strip.

Table 1. Dimensions, Weights, and Densities of the Thermal Conductivity Specimens. For the composites, the dimension X_1 denotes the direction normal to the fabric, X_2 denotes the warp direction, and X_3 the fill direction. All specimens were cut from single blocks supplied by the manufacturer except as indicated in the footnotes.

Material Designation	Specimen Identification	Specimen Dimensions (cm)			Weight (g)	Density (g/cm^3)
		X_1	X_2	X_3		
G-10CR	G-10C1*	1.910	1.890	1.919	13.188	1.904
	G-10C2+,d	1.913	1.911	1.916	12.767	1.824
	G-10C3**	1.882	1.908	1.873	11.717	1.741
	G-10C4+,d	1.916	1.819	1.824	11.608	1.825
	G-10C5++	0.373	1.951	1.911	2.385	1.71
	G-10C6[a]	0.318	1.808	1.885	2.152	1.98
	G-10C7[c]	0.646	1.910	1.870	3.964	1.72
G-11CR	G-11C1*	1.915	1.913	1.910	13.684	1.956
G-10CR resin	G-10R1	1.915	1.913	1.781	7.698	1.180
	G-10R1A	1.915	0.652	1.781	2.615	1.18
	G-10R1B	1.915	1.041	1.781	4.175	1.18
G-11CR resin	G-11R1	1.915	1.915	1.915	8.620	1.228
E Glass	EGL1	0.955	1.905	1.905	8.924	2.58
Vetronite[b]	VETC1	1.778	0.197	1.765	1.189	1.92
	VETC2[d]	1.780	0.393	1.766	2.328	1.92
	VETC4[d]	1.780	0.792	1.766	4.770	1.91
	VETC12[d]	1.778	2.378	1.765	14.282	1.91
Micarta	MICROD[e]	1.915	2.504			

*-Manufacturer A
**-Fabricated by bonding two 0.952-cm-thick pieces (glue plane parallel to fabric). This is stock G-10 material, not G-10CR.
+-Manufacturer B, G-10C2 measured after 1.44% strain, G-10C4 = control specimen.
++-This material was produced with a higher resin content than normal G-10CR (40% weight fraction resin compared with 34%).
a-This material was produced with a lower resin content (24% weight fraction resin).
b-This is a European glass fiber/epoxy composite.
c-Manufacturer C.
d-These specimens were fabricated by bonding several pieces cut from single sheets.
e-This specimen is a right circular cylinder, X_1 = diameter and X_2 = length.

Specimens G-10C5 and G-10C6 as well as the pure resin and pure glass specimen were measured to determine the variation of conductivity with resin content.

To study thickness effects and inhomogeneities through the thickness of the material, specimen G-10R1 was cut normal to the heat flow direction (after measurement of its thermal conductivity) to produce specimens of approximately one-third and two-thirds the original thickness. The latter specimens are designated as G-10R1A and G-10R2A, respectively.

A sheet of the Vetronite* material, previously measured at CERN [1], was obtained and 12 square specimens were cut from it. These were fabricated by cutting two 1.9-cm-wide strips from the supplied sheet. Each of the two strips were further sectioned into six equal pieces. The 12 resulting pieces were machined to their final dimensions. Measurements were performed on selected groups of these specimens to obtain thermal conductivity values as a function of specimen thickness. These specimens are designated as VETC1 through VETC12. The number in the designation indicates the number of pieces within each specimen. These measurements were performed for comparison with the data reported by CERN along with numerous other data that were suspiciously low.

The Micarta* rod (MICROD) specimen was measured as part of the apparatus calibration procedure.

SPECIMEN DENSITIES

The specimen densities have been measured (see table 1) because they are a useful indication of resin content or void content variations. These variations can significantly affect the thermal conductivity of the specimens.

From the measured bulk resin and glass densities, ρ_r and ρ_g (table 1), and the specified weight fractions, WF, one can calculate the composite density, ρ, using eq (1).

$$\rho^{-1} = \rho_r^{-1} WF_r + \rho_g^{-1} WF_g \qquad (1)$$

These densities are compared with the measured densities in table 2.

The agreement between measured and calculated values is within the specified composition variation except for G-10C1 and G-10C7. It is suspected that G-10C7 is actually a stock G-10 grade, i.e., not the G-10CR grade. The density of G-10C3, which is stock G-10, compares well with G-10C7. The reason for the G-10C1 difference is not known.

It is also noted that the densities of bulk glass and resin may be different from the actual densities within the composites. Void fractions are not known with sufficient accuracy to correct the calculated values. They are estimated to be less than 2%.

*Trade names are used in this report for a proper understanding of the materials investigated. The use of these trade names in no way implies endorsement or disapproval of the product.

Table 2. Comparison of Measured and Calculated Densities for the Indicated Specimens. Density of glass = 2.58 g/cm^3, density of G-10 resin = 1.18 g/cm^3, density of G-11 resin = 1.23 g/cm^3.

Specimen Identification	Weight Fraction Resin	Density (g/cm^3)	
		Measured	Calculated
G-10C1	0.34 ± 0.01	1.904	1.84 ± 0.002
G-10C2	0.34 ± 0.01	1.824	1.84 ± 0.002
G-10C4	0.34 ± 0.01	1.825	1.84 ± 0.002
G-10C5	0.40	1.71	1.75
G-10C6	0.24	1.98	2.01
G-10C7	0.34 ± 0.01	1.72	1.84 ± 0.02
G-11CR	0.29 ± 0.02	1.956	1.92 ± 0.04

EXPERIMENTAL PROCEDURE AND DATA ANALYSIS

The thermal conductivity of the test block is determined in a thermal conductivity integral apparatus. This apparatus, described by Hust and Arvidson [2], can be used to perform measurements at temperatures from 2 to 300 K.

Further details of the experimental setup, the thermal conductivity integral (TCI) method, thermocouple calibration, and the operating procedure are described in the report by Hust and Arvidson [2]. A calibration measurement on a NBS standard reference material is also included in the report. The measurements on the standard reference material (SRM 735) indicate an overall system accuracy of about ± 3% up to 100 K and ± 6% above 100 K. A Micarta rod (along with Vetronite and G-10CR specimens) was used to calibrate the heat leak between the heat source and heat sink in the cell. The uncertainty of this heat leak is ± 10% and is the major source of uncertainty in the final results.

RESULTS AND DISCUSSION

The direct experimental data for each specimen are available from the author. These data were analyzed by both the difference method and the TCI method. The function chosen to represent $\lambda(T)$ in the TCI method is

$$\lambda(T) = \sum_{i+1}^{6} a_i [\ell n(T+1)]^i \qquad (2)$$

Thermal conductivities by the difference method are calculated from eq (3)

$$\bar{\lambda}(T_2,T_1) = Q\Delta x/A(T_2-T_1) \qquad (3)$$

where $\bar{\lambda}(T_2,T_1)$ denotes the average value of $\lambda(T)$ from T_2 to T_1 (the hot and cold faces, respectively), Q is the heat flow through the specimen with cross-sectional area, A, and length, Δx. The value of $\bar{\lambda}(T_2,T_1)$ is normally associated with the mean temperature, $\bar{T} = (T_2 + T_1)/2$, but since large temperature

differences are used here, these values are slightly in error due to the curvature of the $\lambda(T)$ function.

Thermal conductivities by the TCI method are determined by fitting the coefficients in eq (4)

$$TCI_{obs} = \int_{T_1}^{T_2} \lambda dT = \text{integral of eq. (2)} = g(T_2, T_1, a_1, a_2 \ldots a_6) \quad (4)$$

The thermal conductivity integral data for each of the specimens are summarized in table 3. Each of the data sets spanning the range from helium temperatures to room temperature were represented by eqs. (2) and (4). The coefficients, a_i, were determined via a least squares fit of the observed TCI values. The relative rms deviation and the maximum deviation, % Dev. = $(TCI_{obs}-TCI_{calc})100/TCI_{obs}$, of each fit is given in table 3. The coefficients, a_i, for each least squares fit are listed in table 4.

Values of thermal conductivity as calculated from eq (2) for G-10CR and G-11CR are plotted in figure 1. Values obtained for the G-10 high resin content and G-10 low resin content are plotted in figure 2 along with the pure resin and pure glass data. The values for Vetronite and Micarta are plotted in figure 3. The data reported from CERN [1] for Vetronite (same sheet of material) are also shown in figure 3.

From figure 1 it is clear that the values for the warp direction of G-10CR and G-11CR are about 20% greater than the values for the normal direction. This to be expected since the glass fibers represent a parallel high conductivity path through the resin in either the warp or fill direction. However within the material variability, G10-CR and G-11CR for a given direction have equal conductivities. Figure 2 shows that the glass conductivity is about 4 times higher than the resin conductivity. Figure 4 compares available literature data [3-6] on G-10 and G-11 to the values obtained in this research. Comparison of the data in figures 1 and 4 indicates that the CR grade of G-10 has a slightly higher conductivity than the stock G-10 grade. Although material variability data is quite limited, it appears that 10% variability in conductivity should be expected.

The resin conductivities plotted in figure 2 reveal considerable differences. Specimen G-10R1 is the original, approximately 2-cm, cube. Because this specimen is relatively transparent, it was cut into two specimens proportioned approximately one-third and two-thirds of the original thickness, for additional measurements to detect the effect of radiant heat transfer through the specimens. The presence of radiant heat transfer results in a decrease in the apparent conductivity with decreasing thickness. Although a decrease was observed, the magnitude of the decrease was surprisingly large. Further, since the curves are relatively parallel, the difference cannot be caused by radiation. Radiation heat transfer increases with temperature as T^3. The Vetronite results, discussed later, indicate that this thickness dependence is not an apparatus error.

To investigate the possibility of inhomogeneities in the two specimens, due to poor mixing of the ingredients or varying degrees of cure, the glass transition temperature of each piece was measured along with various other

Table 3. Summary of Thermal Conductivity Integral Data and Calculated Value of λ at 280 K for Each Set of Measurements.

Specimen Identification/Heat Flow Direction	Number of Data Points	Temperature Range (K)	Deviation (%)		λ(280 K) ($W \cdot m^{-1} \cdot K^{-1}$)
			RMS	Max.	
G-10C1/Norm	22	2-302	1.4	2.7	0.50
G-10C1/Warp	24	2-302	1.2	3.3	0.79
G-10C2/Warp	17	4-305	1.5	3.1	0.61
G-10C3/Norm	1	288	---	---	0.42
G-10C4/Warp	2	88,282	---	---	0.60
G-10C5/Norm	19	4-308	0.7	1.2	0.37
G-10C6/Norm	17	3-310	0.6	1.1	0.52
G-10C7/Warp	26	4-318	0.4	0.9	0.57
G-11C1/Norm	16	2-297	1.2	2.2	0.53
G-11C1/Warp	15	2-302	1.4	2.1	0.65
G-10R1	21	2-304	1.7	5.0	0.29
G-10R1A	23	4-298	1.6	4.0	0.23
G-10R1B	2	280	---	---	0.24
G-11R1	18	4-304	1.6	4.1	0.27
EGL1	20	4-309	0.5	0.9	1.14
VETC1/Norm	4	289	2.1	6.0	0.44
VETC2/Norm	22	4-308			
VETC4/Norm	22	4-310			
VETC12/Norm	23	4-306			
MICROD/axial	24	2-287	2.7	5.0	0.60

specimens. The results indicate very little difference between the G-10CR resin specimens, T_g = 85 ± 5°C for the thin specimen and 93 ± 5°C for the thick specimen. The T_g of specimen G-10C4 is 97 ± 5°C, which is in reasonable agreement with the resin specimen values. The G-10C5 and G-10C6 specimens had a slightly higher glass transition temperature, 103 ± 5°C. The glass transition temperature of the G-11CR resin specimen was considerably higher, 166 ± 10°C. The above unexplained conductivity dependence on thickness suggests that the effective conductivity of both the resin and the glass, in the normal direction within a composite, will be lower than that measured for the bulk specimens. This is because the distance from fiber-to-fiber within the composite is very small and the fibers themselves are small. In the warp or fill directions, conversely, the effective conductivity of the components should correspond more closely to the measured bulk values.

Figure 2 is plotted to illustrate the progression of conductivities from pure resin to pure glass. Figure 5 is a plot of conductivity as a function of the volume fraction of resin for various temperatures.

The model frequently adopted for heat flow normal to the fabric in a composite is one in which the glass and resin thermal resistances are added in proportion to their volume fractions, VF_g and VF_r. Equation (5) is derived from this model.

Table 4. The Coefficients, a_i from Eq. (2), for Each Set of Measurements.

$a_i \times 10^6$

i	G-10C1/Norm	G-10C1/Warp	G-10C2/Warp	G-10C5/Norm	G-10C6/Norm
1	-103516.92	-41908.943	-169739.97	-152148.13	-230890.44
2	205526.47	97685.284	325116.43	274868.65	369725.03
3	-112281.75	-30664.161	-182492.29	-158528.27	-193542.14
4	29353.211	1025.1003	47592.068	43456.245	48129.142
5	-3503.0441	1119.1669	-5623.2036	-5605.3277	-5578.9960
6	154.74522	-124.32478	245.58291	277.81952	246.05951

$a_i \times 10^6$

i	G-10C7/Warp	G-11C1/Norm	G-11C1/Warp	G-10R1	G-10R1A
1	-160714.93	-52921.090	2506.2012	20818.210	31664.248
2	248829.47	115620.83	109.99048	69419.464	25316.908
3	-107919.63	-53039.929	45194.871	-66383.246	-34696.162
4	19681.969	11279.983	-26205.233	23957.970	14411.594
5	-1148.8081	-894.90446	5593.4980	-3678.6599	-2426.5035
6	-13.425492	11.268249	-400.25814	205.94405	147.08945

$a_i \times 10^6$

i	G-11R1	EGL1	VETC*/Norm	MICROD
1	183281.88	-1354404.2	-35556.453	22175.004
2	-183347.00	2097015.2	60035.153	-13691.739
3	82596.626	-1101425.2	-11965.605	9957.7037
4	-18103.335	267915.51	-2862.1565	-1485.7131
5	2047.0262	-30401.701	1300.5061	300.72406
6	-96.644046	1307.5164	-113.28850	-51.532623

*All of the VETC data were represented with a single fit.

$$\lambda = \frac{\lambda_g \lambda_r}{\lambda_g VF_r + \lambda_r VF_g} \quad (5)$$

where $VF_i = WF_i \rho / \rho_i$.

Using the measured thermal conductivities of the pure resin and glass, λ_r and λ_g, the solid curves in figure 5 were calculated. As can be seen, good agreement between this model and the experimental data exists.

As mentioned earlier, Vetronite was measured as a function of thickness to determine if apparatus errors are dependent on the thickness. A range of thickness covering a factor of 12 was investigated. These results, not shown in figure 3, are plotted in figure 6 for a temperature of 280 K.

Although a slight dependence on thickness in the same direction as for the G-10CR resin specimens is evident in figure 6, it is considerably reduced. The increase for the resin was 25% for a factor of 2 increase in thickness, while for the Vetronite the increase was about 4% for a factor of 12 increase in thickness. Clearly the source of the increase for the resin specimens is not in the apparatus or the method of measurement. Thus the large difference in conductivity between the G-10CR resin specimens remains a mystery.

ACKNOWLEDGMENTS

The author expresses appreciation for the assistance of Rich Boscardin for performing some of the measurements and aiding in the analysis of the data.

REFERENCES

1. K. Dahlerup-Peterson and A. Perrot, "Properties of Organic Composite Materials at Cryogenic Temperatures," ISR-BOM/79-39, CERN, Geneva, Switzerland (1979).
2. J. G. Hust and J. Arvidson, "Thermal Conductivity of Glass Fiber/Epoxy Composite Support Bands for Cryogenic Dewars," Unpublished report available from author, National Bureau of Standards, Boulder, CO (1978).
3. F. J. Walker and A. C. Anderson, "Thermal Conductivity and Specific Heat of a Glass-Epoxy Composite at Temperatures Below 4 K," Review of Scientific Instruments 52(3), 471 (1981).
4. J. A. Barclay, S. S. Rosenblum, and W. A. Steyert, "Low temperature thermal conductivity of some composite materials," Cryogenics 16, 539 (1976), Note: Figures 6 and 8 in this paper are interchanged. The thermal conductivity of G-10 appears in figure 8.
5. M. Kuchnir, "Apparatus to Measure Thermal Conductance," Cryogenics 20, 203 (1980).
6. Y. S. Touloukian and C. Y. Ho, eds., "Thermophysical Properties of Selected Aerospace Materials, Part II. Thermophysical Properties of Seven Materials," Purdue University, TEPIAC/CINDAS, Lafayette, IN (1977).

Figure Captions

Figure 1. Thermal conductivity values of various G-10 and G-11 specimens from this research. Legend:
G-11C1/Norm = ----, G-11C1/Warp = ———,
G-10C1/Norm = ◇, G-10C1/Warp - O,
G-10C2/Warp = •, G-10C3/Norm = □,
G-10C4/Warp = △, G-10C7/Warp = ▽.

Figure 2. Thermal conductivity of pure resins, pure glass and two resin/glass composites of differing resin content.

Figure 3. Thermal conductivity of Micarta and Vetronite. Legend:
MICROD = ———, VETC (all specimens) = ----, VETC (CERN) = O.

Figure 4. Thermal conductivity of G-10 and G-11 as reported in the literature compared with the results of this research. Legend:
G-10CR/Norm (this research) = ———,
G-10CR/Warp (this research) = —— - ——,
G-10/Norm (Kuchnir [5]) = △, G-11/Norm (Kuchnir) = O,
resin/glass composites (Average of values tabulated by Touloukian and Ho [6]) = •, G-10 (Barclay, Rosenblum, and Steyert [4]) = ▽,
G-10CR/parallel to fabric (Walker and Anderson [3]) = ----.

Figure 5. Thermal conductivity variation with resin content of G-10CR normal to the fibers. The circles indicate the experimental values, and the solid curves are calculated from the series resin-glass model.

Figure 6. Observed thermal conductivity of Vetronite at 280 K as a function of thickness.

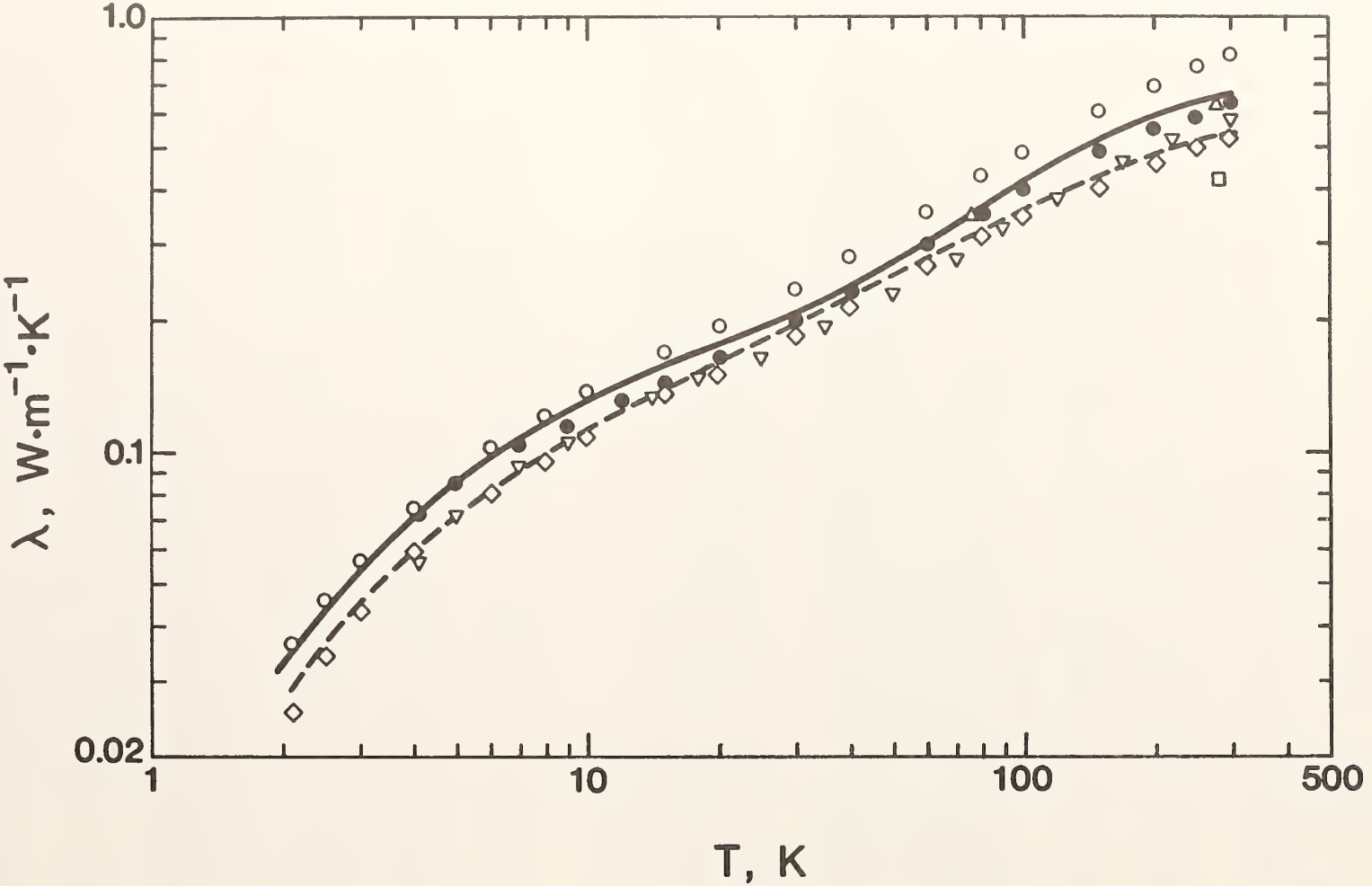

Figure 1. Thermal conductivity values of various G-10 and G-11 specimens from this research. Legend: G-11C1/Norm = ----, G-11C1/Warp = ——, G-10C1/Norm = ◇, G-10C1/Warp - O, G-10C2/Warp = ●, G-10C3/Norm = □, G-10C4/Warp = △, G-10C7/Warp = ▽.

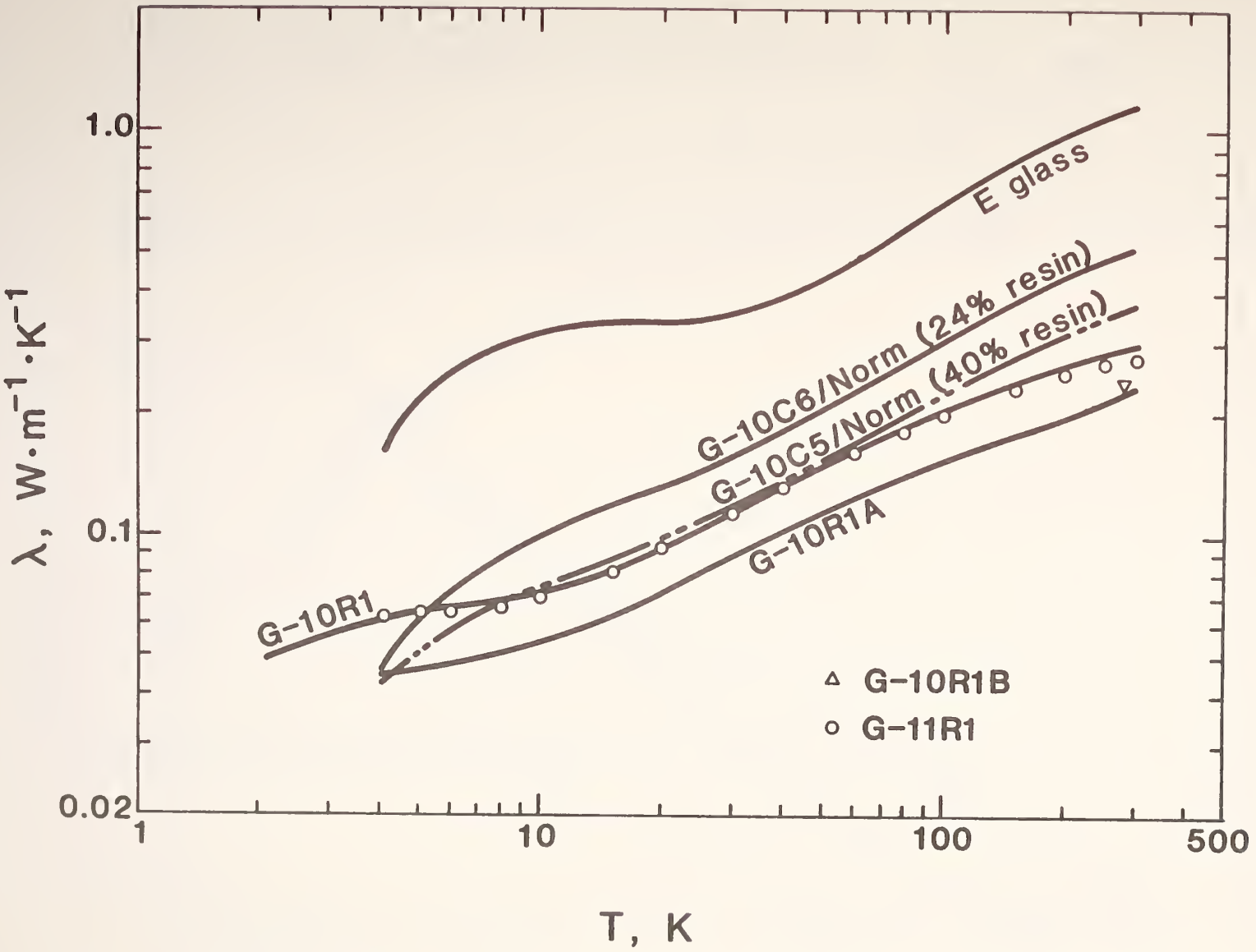

Figure 2. Thermal conductivity of pure resins, pure glass and two resin/glass composites of differing resin content.

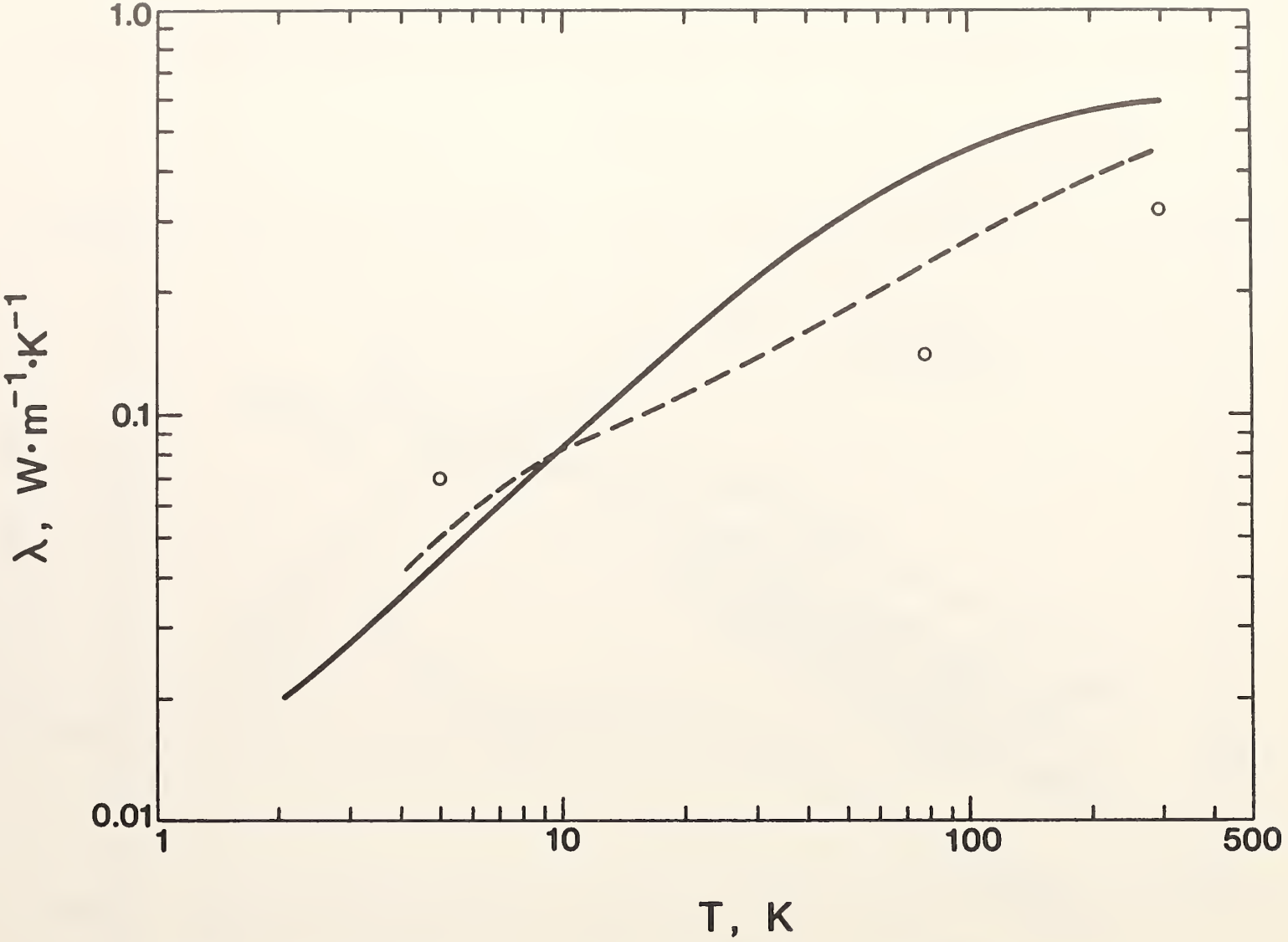

Figure 3. Thermal conductivity of Micarta and Vetronite. Legend: MICROD = ———, VETC (all specimens) = ----, VETC (CERN) = O.

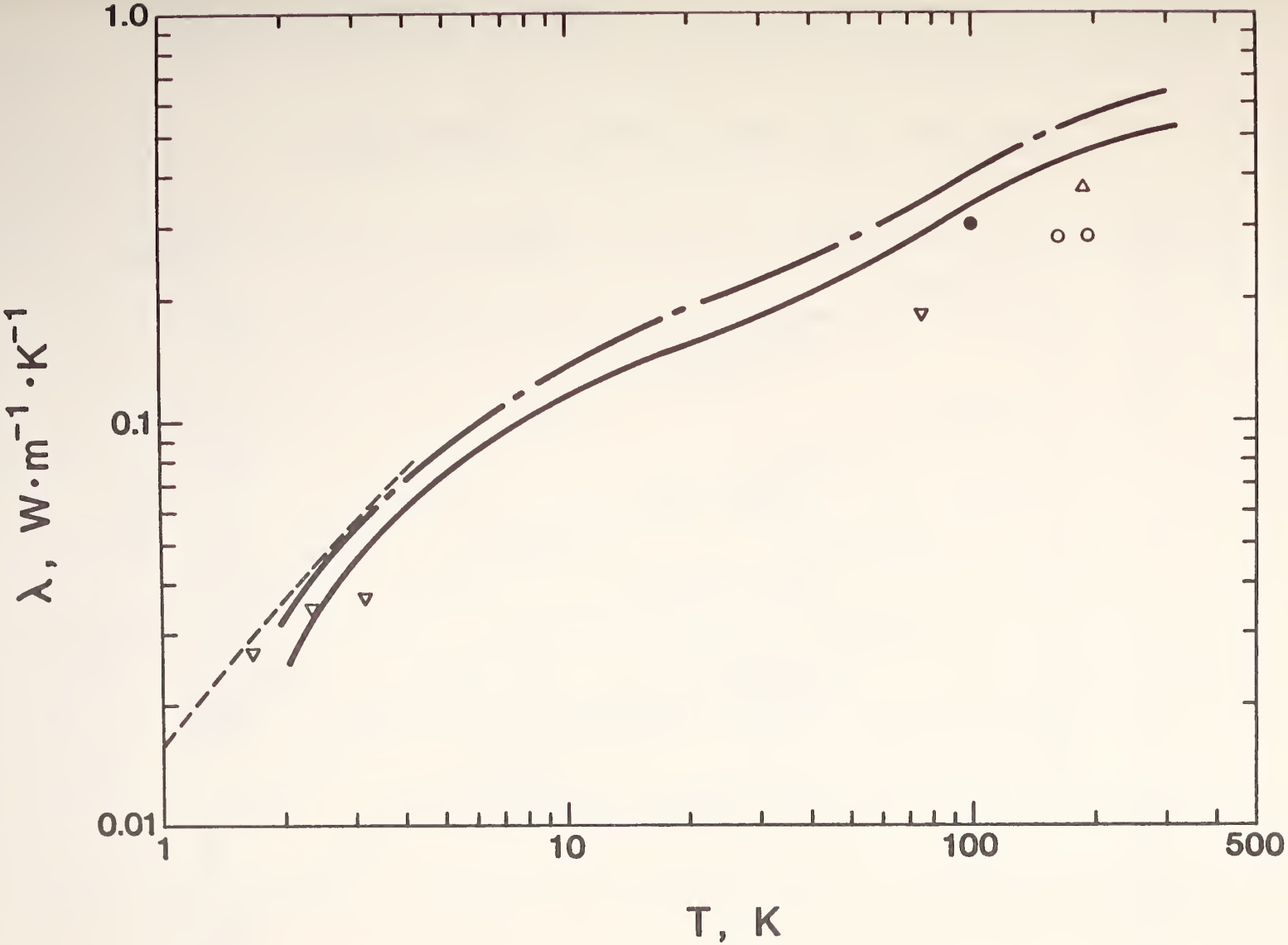

Figure 4. Thermal conductivity of G-10 and G-11 as reported in the literature compared with the results of this research. Legend: G-10CR/Norm (this research) = ———, G-10CR/Warp (this research) = —— - ——, G-10/Norm (Kuchnir [5]) = Δ, G-11/Norm (Kuchnir [5]) = O, resin/glass composites (Average of values tabulated by Touloukian and Ho [6]) = •, G-10 (Barclay, Rosenblum, and Steyert [4]) = ∇, G-10CR/parallel to fabric (Walker and Anderson [3]) = ----.

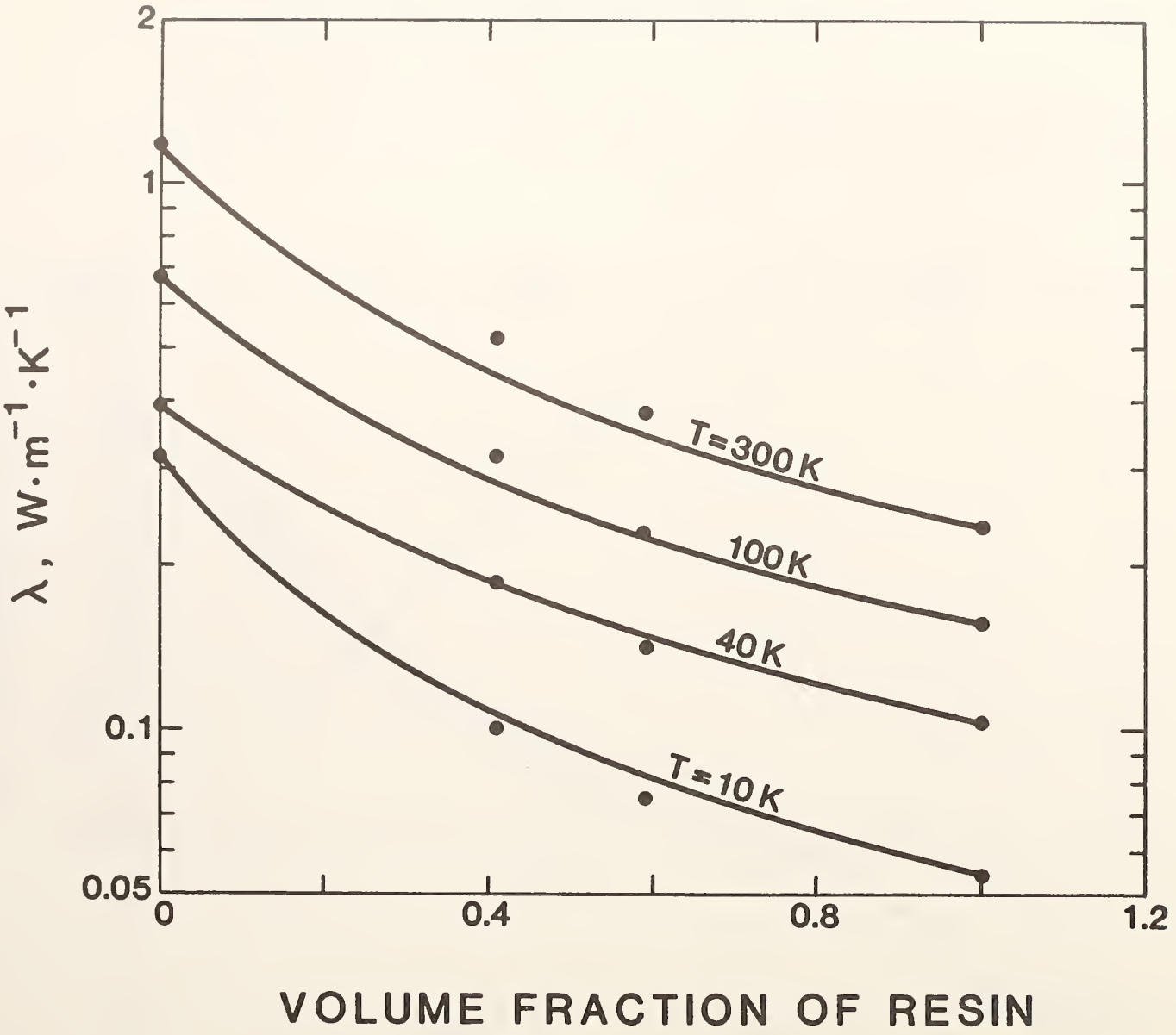

Figure 5. Thermal conductivity variation with resin content of G-10CR normal to the fibers. The circles indicate the experimental values, and the solid curves are calculated from the series resin-glass model.

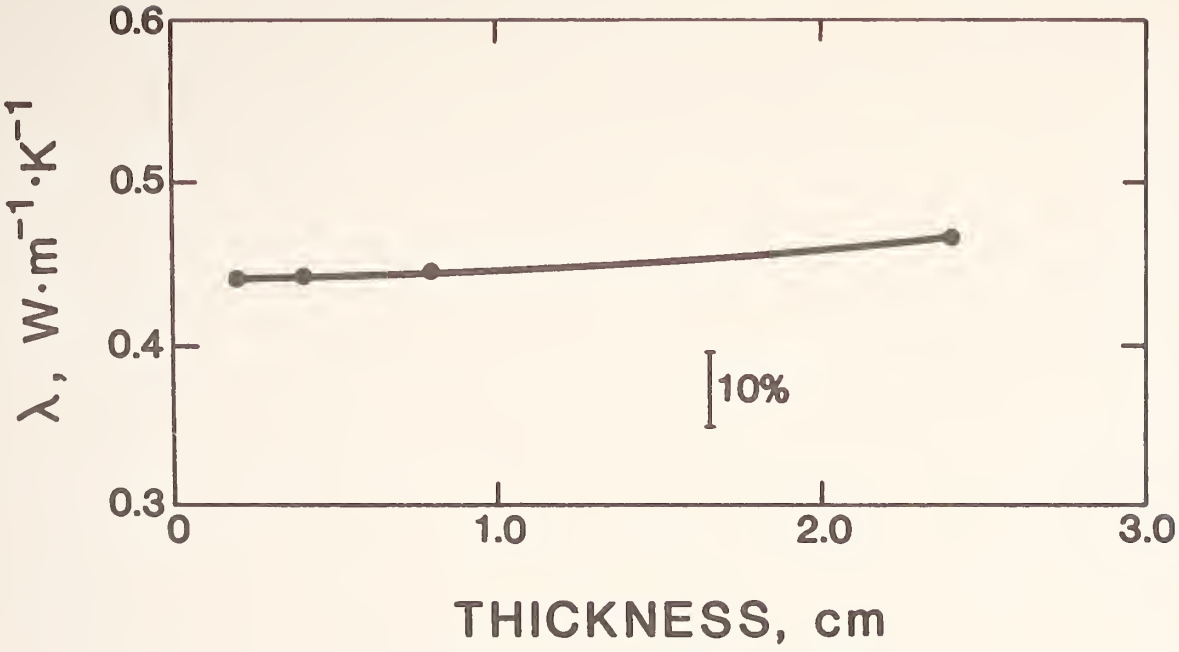

Figure 6. Observed thermal conductivity of Vetronite at 280 K as a function of thickness.

WAVE PROPAGATION AND ELASTIC CONSTANTS IN PARTICULATE AND FIBROUS COMPOSITES*

S. K. Datta and V. K. Kinra
Department of Mechanical Engineering
University of Colorado
Boulder, Colorado

and

H. M. Ledbetter
Fracture and Deformation Division
National Bureau of Standards
Boulder, Colorado

*Published in Composite Materials; Mechanics, Mechanical Properties and Fabrication, Japan-U.S. Conf., Tokyo, 1981, Eds. Kawata, K., Akasaka, T., Japan Society for Composite Materials, Tokyo, Japan (1981).

"Composite Materials," K.Kawata & T.Akasaka, Ed.,
Proc. Japan-U.S. Conference, Tokyo, 1981.

Wave Propagation and Elastic Constants in Particulate and Fibrous Composites

S. K. Datta*, H. M. Ledbetter**, and V. K. Kinra*

* Department of Mechanical Engineering, University of Colorado, Boulder, Colorado 80309, USA.

**Fracture and Deformation Division, National Bureau of Standards, Boulder, Colorado 80303, USA.

ABSTRACT

For two types of composites--particulate and fiber-reinforced--dynamic elastic properties were studied both theoretically and experimentally. The two composites contained, respectively, randomly distributed spherical inclusions and aligned continuous fibers, both in a homogeneous matrix. The theory describes aligned, identical ellipsoidal inclusions. As special cases, the theory comprises both spherical inclusions and short fibers. Bose and Mal presented previously a similar theory for continuous fibers. The theories estimate the effective propagation speed of a plane harmonic wave; the theories average the scattered field by the Waterman-Truell procedure and use the Lax quasi-crystalline approximation. Theory and observation agree quite well. Particulate composites were studied in a through-transmission water-immersion tank, while the fiber composite was studied by both pulse-echo-overlap and resonance methods.

NOMENCLATURE

a	radius of spherical inclusions
$A^{\mu\nu}_{mn}$, $B^{\mu\nu}_{mn}$	coefficients describing coordinate change
$a_{i\mu\nu}$, $c_{i\mu\nu}$	coefficients in wave-function expansions of incident field
A_{imn}, C_{imn}	coefficients in wave-function expansions of scattered field
a, b, c	three principal semiaxes of ellipsoid ($c>b>a$)
$\bar{c}$	volume concentration of ellipsoids
C_1, C_2	longitudinal and shear wave speeds in matrix
$\langle C_1 \rangle$, $\langle C_2 \rangle$	effective principal-axis longitudinal and shear wave speeds
k	wave number
$\underset{\sim}{L}^{(1)}_{imn}(\underset{\sim}{x}, \underset{\sim}{x}_i)$	spherical vector wave function of first kind referred to the center of the ith ellipsoid; a longitudinal wave regular near $\underset{\sim}{x}_i$
$\underset{\sim}{L}^{(3)}_{im}(\underset{\sim}{x}, \underset{\sim}{x}_i)$	spherical vector outlying longitudinal wave function

n, n_o	number density
$N^{(1)}_{imn}(\underset{\sim}{x}, \underset{\sim}{x}_i)$	spherical vector wave function of first kind; represents shear-wave polarization in an individual plane and is regular near $\underset{\sim}{x}_i$
$N^{(3)}_{imn}$	spherical vector outying shear wave function
t	time
T^{mn}_{ij}	transition-matrix coefficients
$\underset{\sim}{u}$	displacement field
V	volume of an ellipsoidal inclusion; $4\pi abc/3$
$\underset{\sim}{x}$	position vector of a point
$\underset{\sim}{x}_i$	position vector of center of ith ellipsoid
x, y, z	Cartesian coordinates of a point measured parallel to a, b, c
α	ω/c_1
β	ω/c_2
δ_{ij}	Kronecker delta
ε	αC, assumed small
ρ	density of matrix
ρ'	density of inclusion
σ	Poisson ratio of matrix
τ	c_1/c_2
ω	angular frequency

INTRODUCTION

Recently, both particulate and fiber-reinforced composites have been studied extensively. Excellent reviews include that of experiment by Bert (1) and of theory by Sendeckyj (2).

In fiber-reinforced composites, two types occur: continuous-fiber and short (chopped)-fiber. The former have been studied extensively, and some recent studies have been reported on the latter (3).

Contrasted with the large literature on fiber composites, few particulate-composite studies have been reported, and most of these focus on spherical inclusions.

Relatively few of the reported theoretical studies consider wave propagation in a composite consisting of a random distribution of either particles or fibers. Most studies consider only the static case.

This paper has three objectives: (1) describe a theory for a composite's effective wave speeds and, therefore, the elastic constants; (2) present some experimental results for particulate and fiber composites; and (3) compare observation and theory. The theory predicts effective wave speeds in a medium containing a random homogenous distribution of aligned ellipsoidal inclusions. Bose and Mal (4) used a similar theory for a random distribution of aligned continuous fibers.

THEORY

The theory of effective wave speeds given here follows closely that of Mal and Bose (5) for spheres and of Datta (6) for ellipsoids, which was confined to very low inclusion concentration. To obtain the effective wave speeds in a com-

posite with random inclusion distribution, one must take the ensemble average of the scattered field due to N ellipsoids with aligned axes and centers at $\underset{\sim}{x}_i$. Suppressing the time factor exp(-iωt), the scattered field is (6):

$$u^{(s)} = \varepsilon^3 \sum_{i=1}^{N} \sum_{n=0}^{2} \sum_{m=-n}^{n} \{A_{imn} \underset{\sim}{L}^{(3)}_{imn}(\underset{\sim}{x},\underset{\sim}{x}_i) + \tau C_{imn} \underset{\sim}{N}^{(3)}_{imn}(\underset{\sim}{x},\underset{\sim}{x}_i)\} + O(\varepsilon^4) \qquad (1)$$

where the A_{imn} and C_{imn} coefficients depend on the material and geometrical properties of each ellipsoid, and on the incident harmonic-wave disturbance. In (1) the Cartesian reference axes are parallel to the ellipsoid's principal axes, and we assume the wavelength is much longer than the ellipsoid.

If the ellipsoids have the same size and properties, then (7)

$$A_{i00} = \frac{iV}{4\pi c^3} T^{\mu'\nu}_{00} (a_{i\mu'\nu} + 3\tau^2 c_{i\mu'\nu}) \qquad \nu = 0,2;\ \mu' = 0,2,-2;\ |\mu'| < \nu \qquad (2)$$

$$A_{ip2} = \frac{iV}{4\pi c^3} T^{\mu'\nu}_{p2} (a_{i\mu'\nu} + 3\tau^2 c_{i\mu'\nu}) \qquad p = 0,2,-2;\ \nu = 0,2;\ \mu' = 0,2,-2;\ |\mu'| < \nu$$

$$= \frac{iV}{4\pi c^3} T^{\mu'2}_{p2} (a_{i\mu'\nu} + 3\tau^2 c_{i\mu'\nu}) \qquad p = -1,1;\ \nu = 2;\ \mu' = -1,1$$

$$A_{i01} = \frac{iV}{4\pi c^3} T^{01}_{01} (a_{i0\nu} + 2\tau c_{i0\nu}) \qquad \nu = 1$$

$$A_{ip1} = \frac{iV}{4\pi c^3} T^{\mu'1}_{p1} (a_{i\mu'\nu} + 2\tau c_{i\mu'\nu}) \qquad p = -1,1;\ \nu = 1;\ \mu' = -1,1$$

where summation is over the repeated indices μ' and ν over the integers indicated. Elements T^{mn}_{ij} are defined in the appendix. Note that

$$C_{i\mu 1} = \tau^2 A_{i\mu 1} \text{ and } C_{i\mu 2} = \tau^3 A_{i\mu 2}/2 \qquad (3)$$

Furthermore, the coefficients $a_{i\mu\nu}$ and $c_{i\mu\nu}$ are the coefficients in the expansion of the exciting field near the ith scatterer, that is,

$$\underset{\sim}{u}^E(\underset{\sim}{x}_i | \underset{\sim}{x}_1;\underset{\sim}{x}_i,\ldots,',\ldots,\underset{\sim}{x}_N) = \sum_{n=0}^{\infty} \sum_{m=-n}^{n} [a_{imn} \underset{\sim}{L}^{(1)}_{imn}(\underset{\sim}{x},\underset{\sim}{x}_i) + \tau c_{imn} \underset{\sim}{N}^{(1)}_{imn}(\underset{\sim}{x},\underset{\sim}{x}_i)] \qquad (4)$$

If a plane wave is incident along one of the ellipsoid axes, say the c axis (= z axis), then

$$a_{imn} = i^{n-1} e^{i\alpha z_i} (2n+1)\delta_{mo} + \varepsilon^3 \sum_{j\neq i} \sum_{\nu=0}^{2} \sum_{\mu=-\nu}^{\nu} A_{j\mu\nu} A^{\mu\nu}_{mn}$$

$$\text{and } c_{imn} = \frac{i^{n-1}(2n+1)}{2n(n+1)} e^{i\beta z_i} (\delta_{m1} - n(n+1)\delta_{m,-1}) + \varepsilon^3 \sum_{j\neq i} \sum_{\nu=0}^{2} \sum_{\mu=-\nu}^{\nu} C_{j\mu\nu} B^{\mu\nu}_{mn} \qquad (5)$$

where $A^{\mu\nu}_{mn}$ and $B^{\mu\nu}_{mn}$ are defined in (5). Note that these depend on the position of the center of the jth ellipsoid relative to that of the ith ellipsoid. Equation (5) assumes that the incident wave is

$$\underset{\sim}{u}^{(i)} = e^{i\alpha z} \underset{\sim}{e}_z + e^{i\beta z} \underset{\sim}{\varepsilon}_x \qquad (6)$$

the sum of a P wave and a shear wave polarized along $\underset{\sim}{x}$, both propagating along $\underset{\sim}{z}$.

To obtain an equation for the averaged field within the composite, we assume a uniform distribution of density n_0. Furthermore, for simplicity, the conditional number density $n(\underset{\sim}{x}_j|\underset{\sim}{x}_i)$ when an ellipsoid is at $\underset{\sim}{x}_i$ will be taken as

$$n(\underset{\sim}{x}_j|\underset{\sim}{x}_i) = n_0 \qquad |\underset{\sim}{x}_j - \underset{\sim}{x}_i| \geq 2c$$
$$= 0 \qquad |\underset{\sim}{x}_j - \underset{\sim}{x}_i| < 2c. \tag{7}$$

Equation (7) means that an ellipsoid is enclosed by a sphere of radius c and the condition of noninterpenetration of spheres is satisfied. From (2) and (5) for an incident P wave,

$$\langle A_{imn}\rangle_i = \frac{iV}{4\pi c^3}\,[T^{\mu\nu}_{mn}\{i^{\nu-1}\,e^{i\alpha z_i}\,(2\nu+1)\delta_{\mu 0} + \varepsilon^3 n_0 \int \langle A_{j\mu'\nu'}\rangle_{ij}\, A^{\mu'\nu'}_{\mu\nu}\, d\underset{\sim}{x}_j\} +$$

$$\delta(n)T^{\mu\nu}_{mn}\{\frac{i^{\nu-1}(2\nu+1)}{2\nu(\nu+1)}(\delta_{\mu 1} - \nu(\nu+1)\,\delta_{\mu,-1}\} + \varepsilon^3\Delta(\nu)n_0\int\langle A_{j\mu'\nu'}\rangle_{ij}\, B^{\mu'\nu'}_{\mu\nu}\, d\underset{\sim}{x}_j] \tag{8}$$

where the integrals are over $|\underset{\sim}{x}_j - \underset{\sim}{x}_i| \geq 2c$. Note that the summations over μ and ν are restricted to the values indicated in (2). Also,

$$\Delta(\nu) = \tau^2; \qquad \nu=1$$
$$= \tau^3/2; \qquad \nu=0,2$$
$$\delta(n) = 3\tau^2; \qquad n=0,2$$
$$= 2\tau; \qquad n=1.$$

One now obtains an integral equation for $\langle A_{imn}\rangle_i$ by assuming

$$\langle A_{j\mu'\nu'}\rangle_{ij} = \langle A_{j\mu'\nu'}\rangle_j \tag{9}$$

which is known as the quasi-crystalline approximation. This integral equation is solved by assuming a plane-wave solution

$$\langle A_{imn}\rangle_i = X_{mn}e^{ikz_i} \tag{10}$$

where k is the effective wave number. After some tedious algebra, it results that for a P wave in the z direction the effective wave speed is

$$\langle C_1\rangle^2/C_1^2 = [1 - \bar{c}\,\{5T^{02}_{02}\,(1 + \bar{c}\,T^{00}_{00}) - T^{02}_{02}\,(1 + 3\beta^2/2\alpha^2) - \tag{11}$$

$$(5T^{02}_{00} + T^{00}_{02} + 5T^{02}_{00}\,T^{00}_{02}\bar{c}\}]/[(1 + 3\bar{c}\,T^{01}_{01})\{(1 + \bar{c}\,T^{00}_{00})(1 + \bar{c}\,T^{02}_{02}(1 + 3\beta^2/2\alpha^2)) -$$

$$\bar{c}^2\,T^{02}_{00}T^{00}_{02}(1 + 3\beta^2/2\alpha^2)\}].$$

For an S wave propagating along $\underset{\sim}{z}$ and polarized along $\underset{\sim}{x}$, the wave speed is

$$\langle C_2\rangle^2/C_2^2 = [1-\bar{c}(T^{12}_{12} + 6T^{-12}_{12})\{(9\beta^2/4\alpha^2) - 1\}]/[(1 + 3\bar{c}\,T^{11}_{11})\{1 + \bar{c}(T^{12}_{12} + 6T^{-12}_{12})$$

$$(1 + 3\beta^2/2\alpha^2)\}]. \tag{12}$$

Expressions for waves moving along $\underset{\sim}{x}$ and $\underset{\sim}{y}$ can be obtained similarly. Effective wave speeds in a continous fiber-reinforced composite can be calculated similarly, as done in (4).

MATERIALS

For the particulate composite, the matrix consisted of an epoxy. The solid spherical inclusions consisted either of glass or lead. For any particular specimen, inclusions of nearly the same diameter (2a) were used: for glass 0.3 mm $\leq$ 2a $\leq$ 3 mm; for lead 0.5 mm $\leq$ 2a $\leq$1.3 mm. The volume fraction of inclusions, c, was varied over the range $0.05 \leq c \leq 0.53$. This range of particle size was chosen to allow examination of all three regions of interest: $\lambda << a$, $\lambda \approx a$, and $\lambda >> a$ where λ is a characteristic wavelength.

The fiber-reinforced composite consisted of 0.14-mm-diameter fibers in an aluminum-alloy-6061 matrix in an F-tempered condition. The composite, containing 48 percent fibers by volume, was fabricated as a 10 x 10 x 1.1 cm plate containing about 70 plies. Mass density measured hydrostatically was 2.534 g/cm^3. Table 1 gives the mass densities and elastic constants of both constituents.

MEASUREMENTS

Through-transmission Water-immersion

All measurements on particulate composites were made in a water-immersion through-transmission ultrasonic apparatus described in detail in (8); only a brief description follows here. The heart of this apparatus is a pair of accurately matched broad-band immersion transducers. A pulse-generator/function-generator combination was used to produce a tone burst (10 to 30 cycles) of desired center frequency, n, where $0.3 \leq n \leq 5$ MHz. A radio-frequency power amplifier was used to boost the signal to about 300 volts peak-to-peak. This signal was applied to the transmitter, a P wave was launched in water, the wave was transmitted through the specimen, and was detected by the receiving transducer; the total time of flight was measured by a universal counter-timer with 1-ns resolution. The phase velocity of the P wave in the specimen, $\langle C_1 \rangle$, was measured as follows. The arrival time of a specific peak at the receiver was measured twice: once with specimen in place and once with specimen removed. Together with the specimen width, this information was enough to calculate $\langle C_1 \rangle$. The shear phase velocity, $\langle C_2 \rangle$, was measured similarly with the following difference: the specimen was inclined to the sound beam at a critical angle at which the amplitude of the mode-converted P wave was minimized. Velocity error was estimated to be one percent.

Pulse-echo-overlap

Elastic stiffness constants, C_{ij}, of the fiber composite were determined from sound velocities, v, and the familiar relationship $C = \rho v^2$, where ρ denotes mass density. Eighteen sound velocities were measured by propagating elastic waves with three polarizations in three <100> and six <110> directions, where [001] denotes the fiber direction and [100] denotes the ply-normal direction. A modified pulse-echo-overlap ultrasonic-velocity system provided the necessary measurement capability (9). Modifications consisted mainly of narrower pulses (0.2 μs, or two cycles at 10 MHz) and wider bandwidths. Echo patterns contained sufficient quality to permit cycle-by-cycle measurements of transit time between leading edges of adjacent echoes. For this we used a dual-delayed-sweep oscilloscope equipped with a microprocessor for precise time-interval measurements (resolution 0.2 ns, typical transit time 5 μs). Other experimental details include: specimen thickness 3-10 mm; opposite specimen faces flat and parallel within 5 μm; quartz piezoelectric transducers 1 cm in diameter, x-cut and ac-cut, rough polished, gold electroplated two sides, 10-MHz fundamental frequencies; phenyl salicylate bonding agent; pulse width near 0.3 μs; pulse height near 20 V.

Resonance

Elastic-compliance constants, S_{ij}, of the fiber composite were determined from standing-wave sound velocities determined by a three-component composite-oscillator resonance technique. A composite oscillator (consisting of a quartz-crystal driver, an identical quartz gage crystal, and a specimen) was resonated by applying a sinusoidal voltage to electrodes plated on the drive crystal. The

resulting oscillation amplitude was monitored by observing the voltage developed between electrodes plated on the gage crystal. The drive-signal frequency was varied until a sharp maximum indicating resonance was observed in the gage voltage amplitude. The elastic constant was computed from the composite-oscillator resonant frequency, the specimen mass, the quartz-crystals' mass, the quartz-crystals' resonant frequency with no specimen attached, and the specimen's mass density and length. By using quartz crystals with orientations and electrode configurations appropriate for extensional oscillation, the Young's modulus of the specimen was measured. Quartz crystals driven in torsional oscillation were used to measure the torsional modulus. Further details and references on this technique are given elsewhere (10, 11). Specimens consisted of cylinders 5 mm in diameter with lengths between 2.5 and 5 cm. Nominal resonance frequency was 60 kHz.

RESULTS AND DISCUSSION

Elastic wave speeds along principal axes were calculated from (11) and (12) and are shown in Figs. 1 and 2 for a particular glass-reinforced epoxy- matrix composite. This composite was modeled as a distribution of thin prolate spheroids (aspect ratio c/a >1) with fibers parallel to the z direction. From symmetry, the composite should behave transversely isotropic. Thus, wave speeds parallel and perpendicular to the fibers (longitudinal and shear) give four of the five independent elastic constants. Figure 1 shows that $\langle C_{33} \rangle$ increases rapidly with increasing fiber volume concentration, c, as well as with increasing aspect ratio, c/a. On the other hand, the $\langle C_{11} \rangle$ elastic-stiffness change with c/a is not rapid. The shear moduli $\langle C_{44} \rangle$ and $\langle C_{66} \rangle$ also change slowly with c/a. Theory predicts a surprising change for $\langle C_{33} \rangle$ that is not immediately understood: $\langle C_{33} \rangle$ becomes infinite at low c, 0.17 for the composite considered here. For all other elastic moduli, the present theory agrees with results of other studies (3).

For spherical (c/a=1) inclusions, present theory predicts bulk and shear moduli that coincide with the lower-bound predictions of Hashin and Shtrikman (12). Figures 3 and 4 compare theory and observation for two particulate composites. Agreement is excellent when wavelength far exceeds the particle size. Interestingly for the lead-epoxy composite, the observed $\langle C_1 \rangle / C_1$ is nearly constant for short wavelengths. To explain this behavior, a model was proposed (13) that considered lead balls as fluid spheres in a matrix with a small shear-wave speed.

Theory outlined in this paper was also used to obtain expressions for the bulk properties of continuous fiber-reinforced composites. These expressions coincide with the lower bounds of (14). Table 2 shows results of theory and observation; agreement is excellent, even for the troublesome, error-prone off-diagonal elastic constants.

From the above observations, we see that the theoretical model considered here predicts accurately the elastic-constant behavior of certain composites. (However, further studies are required on short-fiber composites) The theoretical model considers the scattering of harmonic waves from obstacles; the waves are averaged in the far field by the quasi-crystalline approximation.

ACKNOWLEDGMENTS

The research studies of S.K.D. and V.K.K. reported here were supported in part by grants ENG-76-09613, ENG-76-04328, and CME 78-24179 from the National Science Foundation to the University of Colorado. Principal support for studies by H.M.L. comes from the Department of Defense Office of Fusion Energy and the NBS Office of Nondestructive Evaluation; Defense Advanced Research Projects Agency sponsored the early experimental studies of boron-aluminum.

REFERENCES

1 Bert, C. W., "Experimental Characterization of Composites", Composite Materials, Volume 8, Academic, New York, 1975, pp. 73-133.

2 Sendeckyj, G. P., "Elastic Behavior of Composites", Composite Materials, Volume 2, Academic, New York, 1974, pp. 45-83.

3 Chou, T.-W., Nomura, S., and Taya, M., "A Self-Consistent Approach to the Elastic Stiffness of Short-fiber Composites", Modern Developments in Composite Materials and Structures, Ed. J. R. Vinson, ASME, New York, 1979, pp. 149-164.

4 Bose, S. K. and Mal, A. K., "Elastic Waves in Fiber-reinforced Composites", Journal of the Mechanics and Physics of Solids, Vol. 22, 1974, pp. 217-229.

5 Mal, A. K. and Bose, S. K., "Dynamic Elastic Moduli of a Suspension of Imperfectly Bonded Spheres", Proceedings of the Cambridge Philosophical Society Vol. 76, 1974, pp. 587-600.

6 Datta, S. K., "A Self-consistent Approach to Multiple Scattering by Elastic Ellipsoidal Inclusions", Journal of Applied Mechanics, Vol. 44, 1977, pp. 657-662.

7 Datta, S. K., "Diffraction of Plane Elastic Waves by Ellipsoidal Inclusions", Journal of the Acoustical Society of America, Vol. 61, 1977, pp. 1432-1437.

8 Kinra, V. K., Petraitis, M. S., and Datta, S. K., "Ultrasonic Wave Propagation in a Random Particulate Composite", International Journal of Solids and Structures, Vol. 16, 1980, pp. 301-312.

9 Ledbetter, H. M., Frederick, N. F., and Austin, M. W., "Elastic-Constant Variability in Stainless-steel 304", Journal of Applied Physics, Vol. 51, 1980, pp. 305-309.

10 Weston, W. F., "Low-temperature Elastic Constants of a Superconducting Coil Composite", Journal of Applied Physics, Vol. 46, 1975, pp. 4458-4465.

11 Read, D. T. and Ledbetter, H. M., "Elastic Properties of a Boron-aluminum Composite at Low Temperatures," Journal of Applied Physics, Vol. 48, 1977, pp. 2827-2831.

12 Hashin, Z. and Shtrikman, S., "A Variational Approach to the Theory of the Elastic Behavior of Multiphase Materials", Journal of the Mechanics and Physics of Solids, Vol. 11, 1963, pp. 127-140.

13 Datta, S. K., "Wave Propagation in the Presence of a Random Distribution of Inclusions", to appear in the Proc. 3rd Symposium on Continuum Model of Discrete Systems, Univ. of Waterloo Press, Waterloo, Canada.

14 Hashin, Z. and Rosen, B. W., "The Elastic Moduli of Fiber-reinforced Materials", Journal of Applied Mechanics, Vol. 31, 1964, pp. 223-232.

15 Eshelby, J. D., "The Determination of the Elastic Field of an Ellipsoidal Inclusion and Related Problems," Proceedings of the Royal Society, London, Vol. 241, 1957, pp. 376-396.

APPENDIX

Relevant expressions for $T_{mn}^{\mu\nu}$ needed to calculate $\langle C_1 \rangle$ and $\langle C_2 \rangle$ are:

$$T_{00}^{00} = \frac{1+\sigma}{9(1-\sigma)} \bar{T}_{mmnn}, \quad T_{00}^{02} = \frac{1+\sigma}{45(1-\sigma)}[\bar{T}_{mmnn} - 3\bar{T}_{mm33}], \quad T_{02}^{00} = \frac{1-2\sigma}{9(1-\sigma)}[\bar{T}_{mmnn} - 3\bar{T}_{33nn}],$$

$$T_{01}^{01} = \frac{1}{3}(\rho'/\rho - 1), \quad T_{02}^{02} = \frac{1-2\sigma}{15(1-\sigma)}[\bar{T}_{33nn} - 3\bar{T}_{3333} - \frac{1}{3}(\bar{T}_{mmnn} - 3\bar{T}_{mm33})],$$

$$T_{12}^{12} = \frac{2(1-2\sigma)}{15(1-\sigma)}[\bar{T}_{3131} + \bar{T}_{3232}], \text{ and } T_{12}^{-12} = \frac{(1-2\sigma)}{45(1-\sigma)}[\bar{T}_{3131} - \bar{T}_{3232}]$$

where $\bar{T}_{ijkl}$ is defined by the relationship $e_{ij}^{T} = \bar{T}_{ijkl} e_{kl}^{A}$, where e_{ij}^{T} is the transformation strain in the equivalent ellipsoidal inclusion due to a uniform strain field e_{kl}^{A} at infinity (15).

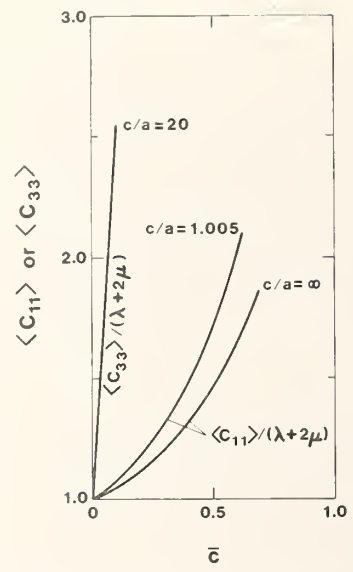

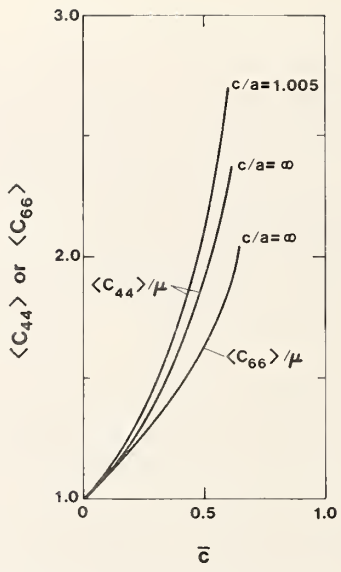

Figs. 1 and 2. Effective elastic constants $\langle C_{11} \rangle$ and $\langle C_{33} \rangle$ and $\langle C_{44} \rangle$ and $\langle C_{66} \rangle$ for short-fiber particulate composites for different aspect ratios.

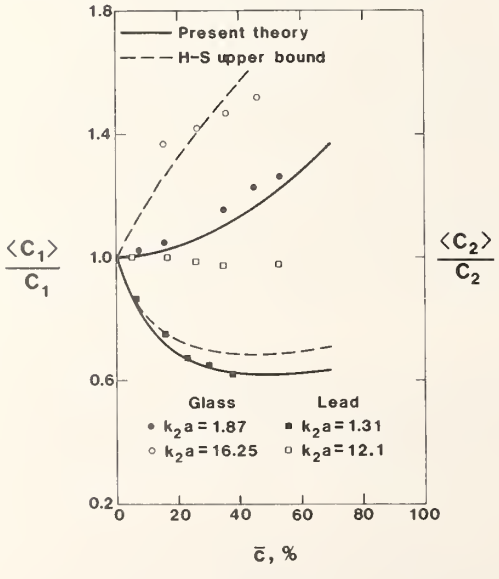

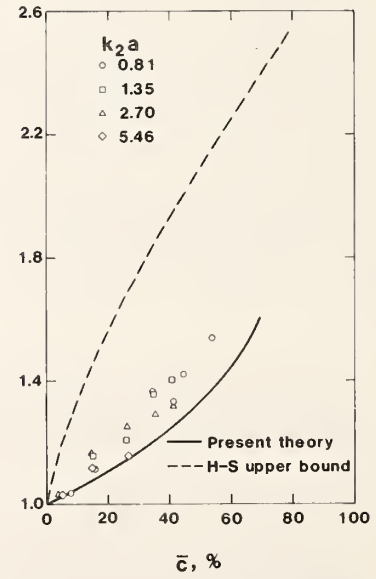

Figs. 3 and 4. Comparisons of theory and observation for longitudinal and shear-wave speeds in spherical-particle composites.

Table 1. Properties of constituent materials.

	ρ (g/cm^3)	E (GPa)	μ (GPa)	B (GPa)	ν -	k (GPa)	λ (GPa)
Boron	2.532	397.9	176.3	178.5	0.129	238.3	59.0
Aluminum alloy	2.702	71.5	26.7	75.1	0.341	84.0	57.3
Epoxy	1.180	4.31	1.57	5.64	0.370	6.16	4.59
Glass	2.492	62.8	26.17	34.85	0.200	43.59	17.42
Epoxy	1.202	4.69	1.71	6.08	0.372	6.65	4.94
Lead	11.300	23.57	8.35	44.32	0.411	47.11	38.76

Table 2. Observed and predicted elastic stiffnesses (C_{ij}) and elastic compliances (S_{ij}) of a boron-aluminum unidirectionally fiber-reinforced composite.

	C_{ij}'s (GPa)		S_{ij}'s (TPa^{-1})		
ij	Observation	Theory	Observation	From C_{ij}'s	Theory
11	185.2	179.0	7.08	6.84	6.99
22	179.7	179.0	7.08	7.07	6.99
33	245.0	256.0	4.38	4.61	4.36
44	56.6	55.9	17.55	17.67	17.88
55	56.9	55.9	17.55	17.57	17.88
66	52.6	52.3	21.23	19.01	19.13
12	77.9	74.5	-3.53	-2.61	-2.58
13	60.6	58.3	-1.06	-1.05	-1.00
23	60.4	58.3	1.06	1.10	1.00

Elastic constants and internal friction of fiber-reinforced composites*

H. M. Ledbetter
Fracture and Deformation Division
National Bureau of Standards
Boulder, Colorado 80303, USA

We review recent experimental studies at NBS on the anisotropic elastic constants and internal friction of fiber-reinforced composites. Materials that were studied include: boron-aluminum, boron-epoxy, graphite-epoxy, glass-epoxy, and aramid-epoxy. In all cases, elastic-constant direction dependence could be described by relationships developed for single crystals of homogeneous materials. Elastic stiffness and internal friction were found to vary inversely.

Key Words: Boron-aluminum; elastic constants; glass-epoxy; graphite-epoxy; internal friction; shear modulus; sound velocity; ultrasonic wave; Young modulus

*Published in "Composite Materials; Mechanics, Mechanical Properties and Fabrication," Proc. Japan - U.S. Conf., Tokyo, 1981, Eds. Kawata, K., Akasaka, T., Japan Society for Composite Materials, Tokyo (1981).

ABSTRACT

We review recent experimental studies at NBS on the anisotropic elastic constants and internal friction of fiber-reinforced composites. Materials that were studied include: boron-aluminum, boron-epoxy, graphite-epoxy, glass-epoxy, and aramid-epoxy. In all cases, elastic-constant direction dependence could be described by relationships developed for single crystals of homogeneous materials. Elastic stiffness and internal friction were found to vary inversely.

NOMENCLATURE

$C_{ij} = C_{ijkl}$	elastic-stiffness tensor
E	Young's modulus
Q^{-1}	internal friction
$S_{ij} = S_{ijkl}$	elastic-compliance tensor
α_{ij}	direction cosines in co-ordinate transformation
ρ	mass density

INTRODUCTION

Here, we highlight recent experimental studies at NBS on the elastic constants and internal friction of several fiber-reinforced composites. Materials that were studied include: boron-aluminum, boron-epoxy, glass-cloth-epoxy, graphite epoxy, and aramid-epoxy. Fiber geometries included: uniaxial, cross-ply, and cloth. Uniaxial materials were studied both parallel and perpendicular to the fibers. In two cases, boron-aluminum and glass-cloth-epoxy, the complete elastic-constant tensor was determined together with the directional dependence of the companion property, internal friction. Internal friction can, of course, be considered as the imaginary elastic modulus, that component ninety degrees out of phase with stress. All studies described here will be described elsewhere in greater detail.

In our laboratory, elastic constants of composites can be measured at low (Hz), moderate (~ kHz), and high (~ MHz) frequencies.

The low-frequency apparatus is a forced-vibration system that has been used so far both in torsion and bending and can be adapted to the extension mode. Internal friction, Q^{-1}, in forced vibration is reflected in the width of a resonance peak. In a free-decay mode, Q^{-1} follows from the exponential time decay of the strain amplitude. For high damping materials, this apparatus gives Q^{-1} as the phase lag of the strain wave behind the harmonic stress wave. Not yet operating, this apparatus has capabilities of determining Q^{-1} from the area of the stress-strain loop. Further details on this apparatus will be described elsewhere (1).

Our middle-frequency apparatus consists of a Marx three-component composite oscillator. Most measurements reported here arose from this apparatus, but, for brevity, we omit details that are given elsewhere (2). This experimental method yields directly the S_{ijkl}'s, the elastic compliances, and was used to study boron-aluminum (3).

At high frequencies we use a pulse-echo-overlap method (4). This technique was used to determine the complete set of C_{ijkl}'s, the elastic-stiffness tensor, for boron-aluminum (5) and NbTi-copper (6).

RESULTS

Room-temperature Young's modulus and internal friction of twelve materials with various fiber orientations are given in Table 1, where they are contrasted with Young's modulus determined statically (7-9). These references also contain material characterizations.

Figure 1 shows the Young modulus versus internal friction for the materials in Table 1.

Figures 2 and 3 show the variation with direction of the Young modulus and internal friction for G-10CR glass-cloth-epoxy.

Figure 4 shows for boron-aluminum the variation with direction of the elastic-wave phase velocity. A companion Figure 5 shows the deviation of the group-velocity vector from the energy-flux vector.

DISCUSSION

Concerning Figure 1, studies on homogeneous materials show an inverse relationship between modulus and damping (10). However, composites could behave differently since modulus and damping may arise from separate properties. Fiber volume fraction may control modulus while fiber-matrix interfacial area may control damping. The preliminary empirical relationship established in Figure 1 clearly needs further study, but it suggests quite useful guidelines for understanding and controlling composite properties. Models should be studied to explain the slope of 0.8, which means a nearly hyperbolic relationship between Young's modulus, E, and internal friction, Q^{-1}.

Figures 2 and 3 show an inverse E-versus-Q^{-1} relationship with direction within a single material, in this case glass-cloth-epoxy. For an arbitrary direction in a material, Young's modulus is

$$1/E' = S'_{11} = S'_{1111} = \alpha_{1i}\,\alpha_{1j}\,\alpha_{1k}\,\alpha_{1\ell}\,S_{ijkl}. \qquad (1)$$

Letting x_1, x_2, and x_3 correspond to warp, fill, and normal directions, respectively, then in the warp-fill, x_1-x_2, plane

$$S'_{11} = \alpha_1^4 S_{11} + \alpha_3^4 S_{33} + \alpha_1^2\alpha_2^2\,(2S_{13} + S_{44}). \qquad (2)$$

The curve in Figure 2 represents a fit to observation of equation (2). The good agreement validates the application to composites of relationships developed nearly a century ago for single crystals of homogeneous materials. And it emphasizes the validity of point-group theory not only for the properties of crystals, but for properties of macroscopic bodies also.

Directional variation of internal friction has been studied only slightly. But we recognize that, like the elastic stiffness, Q^{-1} also has tensor properties because elastic stiffness C_{ij} has two components:

$$\tilde{C}_{ij} = C_{ij} + iC^*_{ij}, \tag{3}$$

one real and one imaginary. The latter, being ninety degrees out of phase with the stress vector, represents internal friction. The symmetry of iC^*_{ij} must relate to that of C_{ij} given by the point group. The same symmetry does not forbid iC^*_{ij} being maximum when C_{ij} is a minimum, and vice versa.

Finally, we discuss Figure 4, which arose from calculations after Musgrave (11) for representation surfaces of phase velocity, slowness, and group velocity together with a determination for the departure of the energy-flux vector from the wave-propagation vector. For input, these calculations require the C_{ij}'s and the mass density, ρ. The smaller shear-wave velocity, denoted T1, is nearly perfectly isotropic. The higher shear-wave velocity, denoted T2, shows maxima at θ (the angle to x_3) of about forty-five degrees. This difference between the two shear waves appears also in Figure 5, which shows that Δ, the angle between energy-propagation and wave-propagation vectors, can be quite large, nearly twenty degrees for the T2 wave. Both the T2 wave and the longitudinal wave, L, behave as pure modes in nonprincipal-axis directions near fifty and seventy degrees, respectively. Other, more-anisotropic composites may show dramatic differences between phase and group velocities arising purely from the elastic constants themselves.

ACKNOWLEDGMENTS

Principal support for this study came from the DoD Office of Fusion Energy and the NBS Office of Nondestructive Evaluation. Defense Advanced Research Projects Agency sponsored the early experimental studies on boron-aluminum.

REFERENCES

1 Austin, M. W., Frederick, N. V., Ledbetter, H. M., and Moulder, J. C., "Low-frequency apparatus for elastic modulus and internal friction of solids", to be published.

2 Ledbetter, H. M., "Dynamic elastic modulus and internal friction in G-10CR and G-11CR fibreglass-cloth-epoxy composites", Cryogenics, Vol. 20, 1980, pp. 637-640.

3 Read, D. T. and Ledbetter, H. M., "Elastic properties of a boron-aluminum composite at low temperatures", Journal of Applied Physics, Vol. 48, 1977, pp. 2827-2831.

4 Ledbetter, H. M., Frederick, N. V., and Austin, M. W., Elastic-constant variability in stainless-steel 304, Journal of Applied Physics, Vol. 51, 1980, pp. 305-309.

5 Ledbetter, H. M., "Orthotropic elastic stiffnesses of a boron-aluminum composite", Journal of Applied Physics, Vol. 50, 1979, pp. 8247-8248.

6 Ledbetter, H. M. and Read, D. T., "Orthorhombic elastic constants of an NbTi/Cu composite superconductor", Journal of Applied Physics, Vol. 48, 1977, pp. 1874-1879.

7 Schramm, R. E. and Kasen, M. B., "Cryogenic mechanical properties of boron-, graphite-, and glass-reinforced composites", Materials Science and Engineering, Vol. 30, 1977, pp. 197-204.

8 Schramm, R. E. and Kasen, M. B., "Static tensile properties of boron-aluminum and boron-epoxy composites at cryogenic temperatures", in Advances in Cryogenic Engineering, Volume 22, Plenum, New York, 1977, pp. 205-213.

9 Kasen, M. B., MacDonald, G. R., Beekman, D. H., and Schramm, R. E., "Mechanical, electrical, and thermal characterization of G-10CR and G-11CR glass-cloth/epoxy laminates between room temperature and 4 K", in Advances in Cryogenic Engineering, Volume 24, Plenum, New York, 1981, pp. 235-244.

10 Read, T. A., "The internal friction of single metal crystals", Physical Review, Vol. 58, 1940, pp. 371-380.

11 Musgrave, M. J. P., Crystal Acoustics, Introduction to the Study of Elastic Waves and Vibrations in Crystals, Holden-Day, San Francisco, 1970.

Table 1. Young's modulus and internal friction of several fibrous composites at room temperature

Material	Fiber orientation, degrees	Static Young's modulus,[a] GPa		Dynamic Young's modulus, GPa	Internal friction, Q^{-1} 10^{-4}	First-harmonic frequency, kHz
		Tension	Compression			
Boron-aluminum	0	200 ± 1	257 ± 51	226.2 ± 0.2	5.6 ± 0.4	50
	90	161 ± 18	148 ± 40	139.2 ± 0.2	17.0 ± 0.5	80
Boron-epoxy	0	231 ± 4	212 ± 42	226 ± 4	17.6 ± 1.4	55
	90	17 ± 1	19 ± 4	22.7 ± 0.2	400.8 ± 20.6	35
	0, ± 45, 0	120 ± 2	102 ± 1	121.4 ± 0.8	79.9 ± 3.3	70
Glass cloth-epoxy 1	woof	26 ± 2	24 ± 1	30.6 ± 0.6	62.1 ± 8.2	40
Glass cloth-epoxy 2	woof	28 ± 1	27 ± 3	29.6 ± 0.2	64.9 ± 7.5	40
Glass cloth-epoxy 3	woof	45 ± 10	---	44.3 ± 0.5	5.4 ± 0.3	30
G-10CR	warp	28.1	---	29.4 ± 1.0	68.7 ± 6.6	40-70
	fill	22.4	---	26.3 ± 1.0	100.1 ± 7.8	45-90
	normal	---	---	14.0[b]	228.6	55
G-11CR	warp	31.8	---	31.4 ± 0.4	114.5 ± 13.9	45-80
	fill	25.5	---	27.7	221.6 ± 85.3	40-70
	normal	---	---	15.6 ± 0.6	406.5	60
Graphite-epoxy 1	0	118 ± 7	129 ± 7	133.5	11.1	90
	90	7.8 ± 1	9.7 ± 1	10.0	164.2	45
	± 45	15.6 ± 2	---			---
Graphite-epoxy 2	0	323 ± 12	368 ± 22	300.5 ± 0.4	17.9 ± 0.4	65
	90	6.7 ± 0.1	7.8 ± 1.0	7.3 ± 0.5	258.8 ± 1.8	45
	± 45	21 ± 0.5	---	---	---	---
	0, ± 45, 90	---	---	120.0 ± 4.0	44.2 ± 4.0	50
Graphite-epoxy 3	0	186 ± 7	---	177 ± 4	15.0 ± 3.8	50
	90	8.6 ± 0.4	---	8.5	218.0 ± 11.7	30
	0, ± 45, 90	---	---	70 ± 1	49.8 ± 2.1	40
Graphite-epoxy 4	0	115 ± 6	---	130.4 ± 1	2.8 ± 0.4	60
Aramid-epoxy	0	71 ± 1	---	66.1 ± 0.5	114.8 ± 6.1	60

[a] All static values are from Schramm and Kasen.[7-9]

[b] Uncertainties are not given for some cases because only one specimen was measured.

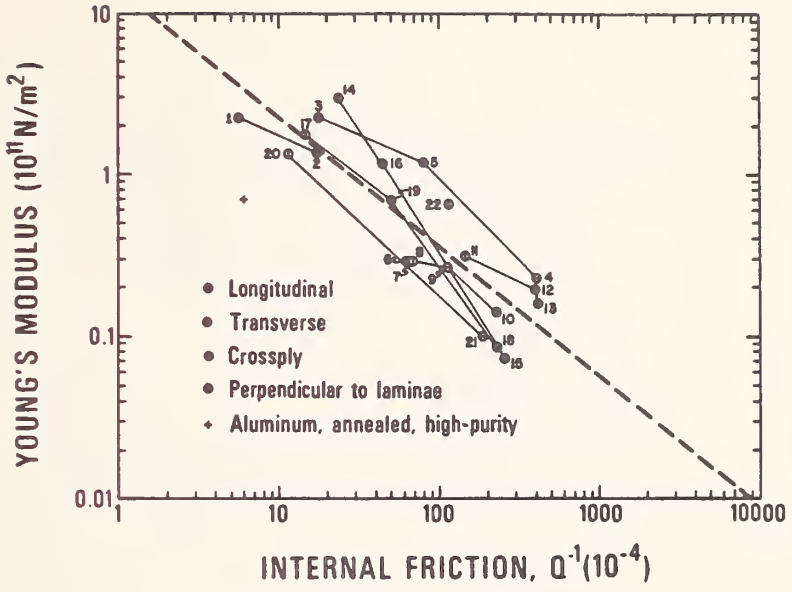

Fig. 1. Young's modulus versus internal friction for materials in Table 1. A least-squares fit to $(Q^{-1})^n E = C$ gives $C = 14.2$ when E is in units 10^{11}N/m^2 and Q^{-1} in units of 10^{-4}.

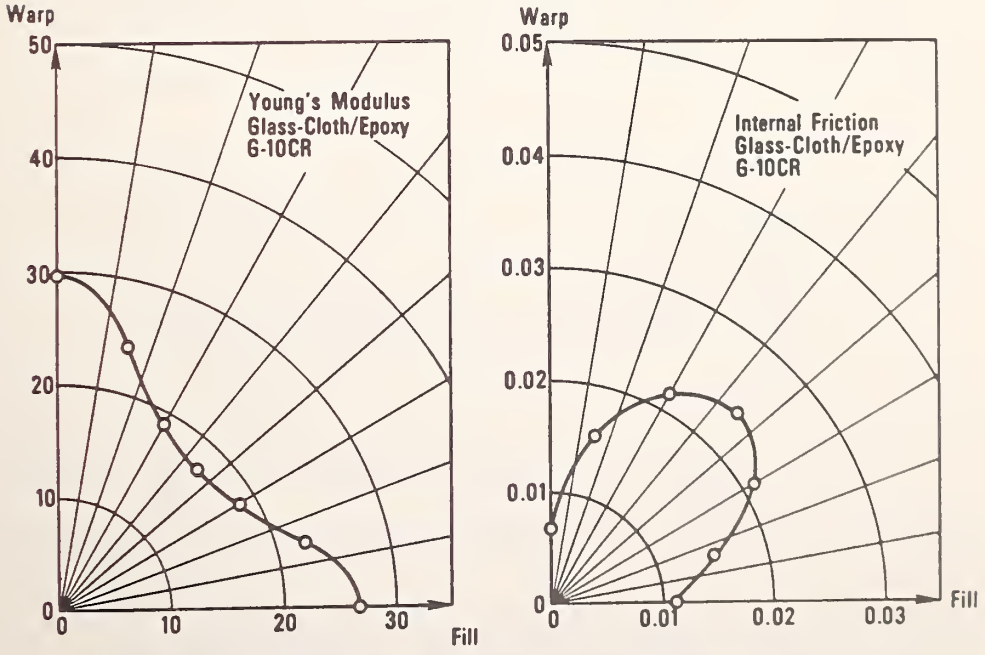

Figs. 2 and 3. Directional variation of Young's modulus and internal friction of G-10CR composite in warp-fill plane, in units of GPa. Curve through points in Fig. 2 represents equation (2).

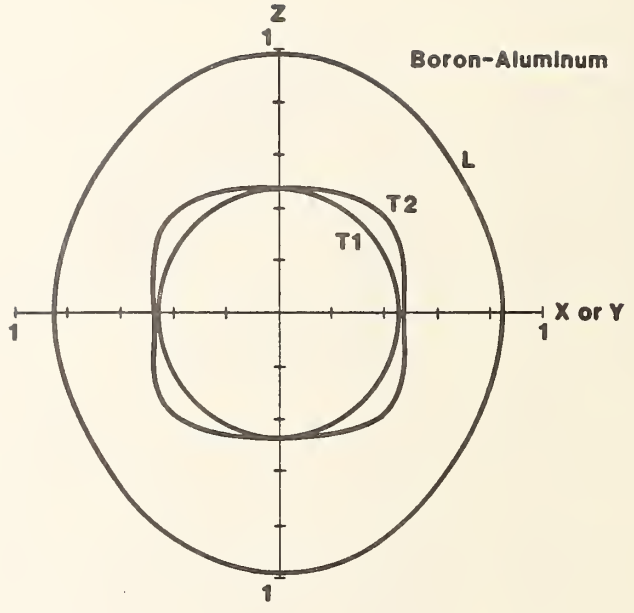

Fig. 4. For boron-aluminum, the directional variation of phase velocity in units of $(C_{44}/\rho)^{1/2}$. Longitudinal (L) and shear (T2 and T1) velocities are shown. For isotropic materials these representation surfaces would be spheres.

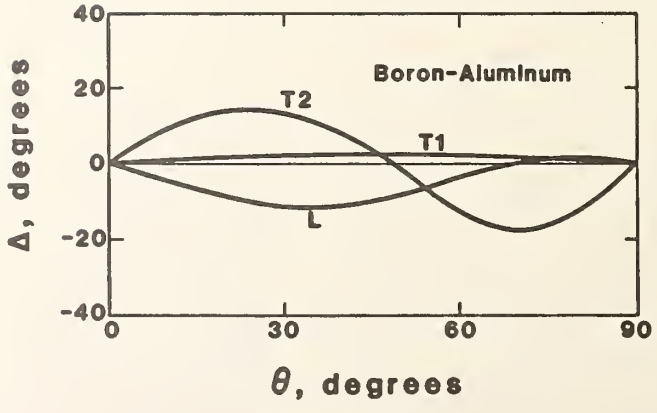

Fig. 5. Angular deviation, Δ, of energy-propagation and wave-propagation vectors. Theta denotes angle between wave vector and fiber direction.

ELASTIC CONSTANTS OF FIBER-REINFORCED BORON-ALUMINUM: A CRITICAL COMPARISON OF OBSERVATION AND THEORY

S. K. Datta

Department of Mechanical Engineering, University of Colorado, Boulder, Colorado, 80309 USA
and Department of Applied Mathematics, University College of Science, 92 Acharya Prafulla Chandra Road, Calcutta 700009, India

H. M. Ledbetter

Fracture and Deformation Division, National Bureau of Standards, Boulder, Colorado, 80303 USA

Abstract

Elastic constants, both the C_{ij}'s and the S_{ij}'s, were measured and calculated for a laminated, uniaxially fiber-reinforced boron-aluminum composite. Three theoretical models were considered: square-array, hexagonal-array, and random-distribution. By combining several existing theoretical studies on randomly distributed fibers, a full set of elastic constants can be predicted for this model. The random-distribution model agrees best with observation, especially for off-diagonal elastic constants. Considering all nine elastic constants, observation and theory differ on the average by six percent. These discrepancies arise from two sources: experimental-error propagation and the limited applicability of a transverse-isotropic model to a laminated composite.

Key Words: Boron-aluminum; composite; elastic constants; fiber reinforcement; sound velocity.

1. Introduction

Fiber-reinforced composites have been studied extensively, both experimentally and theoretically. Recent reviews on this subject include that of experiment by Bert (1975) and of theory by Sendeckyj (1974).

Two types of fiber-reinforced composites occur in practice: continuous-fiber and short (chopped)-fiber. The former type has been studied more thoroughly and constitutes the object of this study.

Boron-fiber-reinforced aluminum, a so-called advanced-technology composite, was the particular material that was studied. The principal purpose of the study was to evaluate various models for predicting the composite's macroscopic elastic constants from those of its constituents. Three models, shown schematically in Fig. 1, were considered: square-array, hexagaonal-array, and random-distribution. The composite's elastic constants were measured two ways: by ultrasonic-velocity measurements, which yield the C_{ij}'s, the elastic stiffnesses; and by standing-wave resonance, which yields the S_{ij}'s, the elastic compliances. These macroscopic elastic constants define for most cases the mechanical response of the composite to an applied force.

2. Material

The studied composite consisted of 0.14-mm-diameter boron fibers in an aluminum-alloy-6061 matrix. The alloy was in the F-tempered condition. The composite, containing 48 percent fibers by volume, was fabricated as a 10 x 10 x 1.1 cm plate containing about seventy plies. Figure 1

is a photomicrograph showing the distribution of fibers in the transverse plane. Cracks in the boron fibers developed during specimen preparation and do not exist in the bulk material. Mass density, measured hydrostatically, was 2.534 g/cm^3.

Throughout this study we adopt the following co-ordinate system: x_3 is the fiber direction, x_1 is normal to the laminae plane, and x_2 is orthogonal to x_1 and x_3 (See Figure 2.). Thus, x_1 and x_2 are equivalent directions from the viewpoint of all three theoretical models considered here.

3. Experimental Methods

Our experimental methods were chosen to provide the advantages of small specimens and low inaccuracy.

For brevity, experimental details are omitted here; they were described previously for both the ultrasonic-velocity method (Ledbetter, Frederick, and Austin, 1980) and the resonance method (Ledbetter, 1979).

Briefly, the ultrasonic-velocity method consisted of a pulse-echo technique using gold-plated piezoelectric crystals at frequencies near 10 MHz with specimen thickness varying from 0.2 to 1.0 cm. Except for an improved velocity-measurement system used in this study, it proceeded similarly to that described by Ledbetter and Read (1977). Reproducibility of measured sound velocities was typically within one to two percent.

The resonance method used a three-component (Marx) oscillator. Specimens were rod-shaped, about 0.4 cm in either circular or square cross section, and 4 to 10 cm long. Frequencies ranged from 30 to 50 kHz.

4. Experimental Results

Results of the experimental studies are given in Table 1 and in Table 2 for the C_{ij}'s and the S_{ij}'s, respectively. The nine C_{ij}'s are based on a least-squares fit to eighteen separate wave-velocity propagation directions and polarizations. For details, see Ledbetter and Read[5]. The five S_{ij}'s are based on extensional-mode and torsional-mode measurements on cylindrical specimens whose axes were in the x_2-x_3 plane, as described by Read and Ledbetter (1977). The plate thickness of the studied material was too short to permit S_{ij} measurements along x_1. Thus, the measured S_{ij}'s are incomplete since they do not reflect the full orthotropic symmetry of the composite. However, as shown in Table 2, except for S_{66} and S_{12}, this incomplete set of S_{ij}'s differs only slightly from those derived from the observed C_{ij}'s, which do contain the full orthotropic symmetry.

Table 3 shows the elastic constants of the constituent materials, both being assumed isotropic. In this Table, ρ denotes mass density, E Young's modulus, μ shear modulus, B bulk modulus (reciprocal compressibility), k plane-strain bulk modulus for lateral dilatation without longitudinal extension, and λ the Lame constant. For aluminum these parameters were determined ultrasonically, as described above, on a bulk specimen; their uncertainty is less than one percent. Boron's elastic constants are less certain, a wide range of values being reported in the literature. The boron values in Table 3 arose from fitting a linear rule-of-mixtures to our observed S_{33} value combined with Gschneidner's (1964) recommended values for boron's bulk modulus.

5. Square-array Model

For a periodic square-lattice array of long, parallel, circular fibers, using a homogeneous continuum model, Achenbach (1976) derived three relationships for plane, harmonic wave-propagation velocities expressed as ρv^2. Simplified and modified for present purposes, and with obvious notational correspondences, these are as follows.

For a longitudinal wave propagating along x_3, parallel to the fibers,

$$\rho v^2 = C_{33} = a_1 - \frac{a_3^2}{a_2}, \tag{1}$$

where

$$a_1 = c(\lambda_f + 2\mu_f) + (1-c)\ (\lambda_m + 2\mu_m),$$

$$a_2 = 4c(\lambda_f + \mu_f), \text{ and}$$

$$a_3 = 2c\lambda_f.$$

For a longitudial wave propagating along x_1, perpendicular to the fibers,

$$\rho v^2 = C_{11} = C_{22} = \mu_m/4M, \tag{2}$$

where

$$M = \frac{c[cD - (1-c)B] + (1-c)[(1-c)A - cB]}{4(AD-B^2)},$$

$$A = a_{22_f} - \frac{(1-c)^2}{c} a_{23_f}^2 \frac{d}{q} \frac{1}{\mu_m},$$

$$B = (1-c) a_{23_f} a_{23_m} \frac{d}{q} \frac{1}{\mu_m},$$

$$D = \left[a_{22_m} - c\, a_{23_m}^2 \frac{d}{q}\right] \frac{1}{\mu_m},$$

$$\frac{d}{q} = \frac{c}{(1-c)^2 a_{22_f} + c^2 a_{22_m}},$$

$$a_{22_f} = c(\lambda_f + 2\mu_f),$$

$$a_{23_f} = c\lambda_f,$$

$$a_{22_m} = (1-c)(\lambda_m + 2\mu_m) + \frac{2}{\pi(4-\pi)} c\, \mu_m + \left[\left(\frac{\pi}{c}\right)^{\frac{1}{2}} - 2\right] \frac{c}{\pi} \mu_m,$$

and

$$a_{23_m} = (1-c)\lambda_m + \frac{4}{\pi(4-\pi)} c\, \mu_m.$$

For a transverse wave propagating along x_3, parallel to the fibers, and polarized along x_1, perpendicular to the fibers,

$$\rho v^2 = C_{55} = C_{44} = a_1 - \frac{a_2^2}{a_3} \tag{3}$$

where

$$a_1 = c\,\mu_f + (1-c)\,\mu_m,$$

$$a_2 = c\,(\mu_f - \mu_m), \text{ and}$$

$$a_3 = c\,\mu_f + \frac{c^2}{1-c}\,\mu_m.$$

The Lamé constants, λ and μ, of the fiber and matrix are denoted by subscripts f and m; c denotes the volume fraction of fibers, 0.48 for the present case, and equals $\pi r^2/d^2$, where r denotes fiber radius and d distance between fiber centers in a square lattice. Clearly, r/d = 0.3909, or d/r = 2.5583. The constants a_1, a_2, a_3, etc. arise from the strain-energy density in Achenbach's derivation.

Results predicted using these relationships based on Achenbach's square-array model are shown in Table 1.

6. Hexagonal-array Model

In calculations similar to Achenbach's, the five independent elastic constants for a composite consisting of parallel fibers arranged

hexagonally were derived by Hlavacek (1975). His relationships, rearranged for present purposes, are as follows.

For a longitudinal wave propagating along x_1, perpendicular to the fibers,

$$\rho v^2 = C_{11} = C_{22} = a_1 - \frac{2a_7a_8a_{23} - a_{22}(a_7^2 + a_8^2)}{a_{22}^2 - a_{23}^2}, \tag{4}$$

where

$$a_1 = (3V + 1)\lambda_m + (7V + 2)\mu_m,$$

$$a_7 = -V(3\lambda_m + 7\mu_m),$$

$$a_8 = -V(\lambda_m + \mu_m),$$

$$a_{22} = -c(\lambda_f + 2\mu_f) - (3V-c)\lambda_m - (7V-2c)\mu_m,$$

$$a_{23} = -c\lambda_f - (V-c)\lambda_m - V\mu_m, \text{ and}$$

$$V = \frac{-c}{8(1-c^{1/2})^2} \ln c.$$

For a longitudinal wave propagating along x_3, parallel to the fibers,

$$\rho v^2 = C_{33} = a_{15} + \frac{2a_{18}^2}{a_{22} + a_{23}}, \tag{5}$$

where

$$a_{15} = c(\lambda_f + 2\mu_f) + (1-c)\ (\lambda_m + 2\mu_m) \text{ and}$$

$$a_{18} = c\ (\lambda_f - \lambda_m).$$

For a transverse wave propagating along x_1, perpendicular to the fibers, and polarized along x_3, parallel to the fibers,

$$\rho v^2 = C_{44} = C_{55} = a_3 + \frac{a_{10}^2}{a_{28}}, \tag{6}$$

where

$$a_3 = c\mu_f + (1-c)\ \mu_m,$$

$$a_{10} = c(\mu_f - \mu_m), \text{ and}$$

$$a_{28} = -c\mu_f - (4V-c)\ \mu_m.$$

For a transverse wave propagating along x_1, perpendicular to the fibers, and polarized along x_2, perpendicular to the fibers,

$$\rho v^2 = C_{66} = -a_2 + \frac{2a_8\, a_9\, a_{26} - a_{25}\,(a_8^2 + a_9^2)}{a_{25}^2 - a_{26}^2}, \tag{7}$$

where

$$a_2 = V\lambda_m + (5V + 1)\,\mu_m,$$

$$a_9 = -V(\lambda_m + 5\mu_m),$$

$$a_{25} = -c\mu_f - V\lambda_m - (5V-c)\,\mu_m, \text{ and}$$

$$a_{26} = -c\mu_f - V\lambda_m - (V-c)\,\mu_m.$$

For the fifth independent elastic constant, Hlavacek derived an expression for $C_{13} + C_{44}$, which is related to the propagation of a transverse wave:

$$C_{13} = \frac{a_5\, a_{28} + a_{10}\, a_{19}}{a_{28}} + \frac{a_{18}\,(a_7 + a_8)}{(a_{22} + a_{23})} - C_{44}, \tag{8}$$

where

$$a_5 = \lambda_m + \mu_m$$

and

$$a_{19} = -4V\mu_m.$$

In Hlavacek's model, the fiber volume concentration, c, equals r_1/r_2, the ratio of the fiber radius to that of the circle radius that equals

the hexagonal "unit-cell" area. Constants a_1, a_2, a_3, etc. arise from Hlavacek's equations of motion.

Results from Hlavacek's hexagonal-array model are shown in Table 1.

7. Random-distribution Model

Considering the propagation of time-harmonic elastic waves in a composite of circular-cross-section, parallel fibers distributed randomly in a matrix, Bose and Mal (1973, 1974) derived expressions for three elastic moduli.

For a longitudial wave propagating along x_1, perpendicular to the fibers,

$$\rho v^2 = C_{11} = C_{22} = \frac{[1 - c\,(1-c^2)\,P_2 - 2c^2\,P_o P_2]\,(\lambda_m + 2\mu_m)}{(1 + cP_o)\,[1 + c\,(1 + c^2)\,P_2]}\ , \tag{9}$$

where $$P_o = \frac{\lambda_m + \mu_m - \lambda_f - \mu_f}{\lambda_f + \mu_f + \mu_m}$$ and

$$P_2 = \frac{\mu_m\,(\mu_m - \mu_f)}{\mu_f\,(\lambda_m + 3\mu_m) + \mu_m\,(\lambda_m + \mu_m)}\ .$$

For a tranverse wave propagating along x_1, perpendicular to the fibers, and polarized along x_3, parallel to the fibers,

$$\rho v^2 = C_{44} = C_{55} = \left[1 + \frac{2c\,(\mu_f - \mu_m)}{\mu_f + \mu_m - c(\mu_f - \mu_m)}\right]\mu_m. \tag{10}$$

For a transverse wave propagating along x_2, perpendicular to the fibers, and polarized along x_1, perpendicular to the fibers,

$$\rho v^2 = C_{66} = \frac{1}{2}(C_{11} - C_{12}) = \left[1 + \frac{2c(\lambda_m + 2\mu_m)(\mu_f - \mu_m)}{2\mu_m(\lambda_m + 2\mu_m) + (1-c)(\lambda_m + 3\mu_m)(\mu_f - \mu_m)}\right]\mu_m \quad (11)$$

Results from the Bose-Mal random-distribution model are shown in Table 1.

8. Full Random-distribution Model

In this section we show that combining the Bose-Mal relationships with previously derived relationships for other elastic constants leads to a full set of five independent elastic constants for the random-distribution case. For this, a new notation (Sendeckyj, 1974) is useful, which will be described as it is introduced.

Hashin and Rosen (1964) derived relationships for the effective moduli of a continuous-fiber-reinforced composite where the fibers are distributed randomly and homogeneously. Hashin (1970) gave these relationships in essentially the form

$$k_T = k_m - \frac{c(k_f - k_m)(k_m + \mu_m)}{k_f + \mu_m - c(k_f - k_m)} \quad (12)$$

and

$$\mu_{LT} = \mu_m + \frac{2c(\mu_f - \mu_m)\mu_m}{\mu_f + \mu_m - c(\mu_f - \mu_m)}. \quad (13)$$

Here, k denotes the two-dimensional, plane-strain bulk modulus, which is $\lambda + \mu$ in an isotropic material. Subscript T denotes deformation in the x_1-x_2 plane, perpendicular to the fibers. Subscript LT denotes shear deformation in any plane containing the x_3 axis, that is, the fiber axis. Equations (12) and (13) were also derived by Hill (1964) for a single fiber placed concentrically in a cylindrical matrix.

Hermans (1967) obtained them also by considering Hill's assembly to be embedded in an unbounded solid having the effective elastic moduli of the composite. In this model, the fiber: matrix-cylinder radius ratio is $r_1/r_2 = c^{1/2}$. In the limit $r_1 = 0$, Hermans' model becomes the "self-consistent" model of Hill (1965).

Knowing k_T, one can derive the Young's modulus E_L (along x_3) and the Poisson's ratio $\nu_{LT} = -\varepsilon_1/\varepsilon_3$, where uniaxial stress is along x_3 and ε denotes strain. This derivation requires some exact relationships given by Hill (1964):

$$\frac{\frac{1}{k_T} - \frac{1}{k_f}}{\nu_{LT} - \nu_f} = \frac{\frac{1}{k_T} - \frac{1}{k_m}}{\nu_{LT} - \nu_m} = \frac{\frac{1}{k_f} - \frac{1}{k_m}}{\nu_f - \nu_m} = \frac{4\,\nu_{LT} - \nu_m - c(\nu_f - \nu_m)}{E_L - E_m - c(E_f - E_m)} \tag{14}$$

Solving for E_L and V_{LT}, using Eq. (12), one finds

$$E_L = (1-c)E_m + cE_f + \frac{4c\,(1-c)(\nu_f - \nu_m)^2}{\frac{1-c}{k_f} + \frac{c}{k_m} + \frac{1}{\mu_m}} \tag{15}$$

and

$$\nu_{LT} = (1-c)\nu_m + c\nu_f + \frac{c(1-c)(\nu_f - \nu_m)(\frac{1}{k_m} - \frac{1}{k_f})}{\frac{(1-c)}{k_f} + \frac{c}{k_m} + \frac{1}{\mu_m}} \tag{16}$$

Of course, both of these relationships represent a simple, linear "rule of mixtures" plus a higher-order correction term. The advantages of Eqs. (12)-(13) are clear: they give simple, explicit relationships for four of the composite's elastic constants in terms of the isotropic

elastic constants of the constituent materials, the fiber and the matrix. On the other hand, self-consistent approaches lead to implicit relationships.

Bose and Mal (1973, 1974) also obtained Eqs. (12) and (13), but by a different approach: by considering the effective velocity for long-wavelength plane waves propagating perpendicular to the fibers, for both a longitudial wave and for a shear wave polarized along x_3, the fiber axis. By a similar approach, examining a shear wave propagating and polarized in a plane transverse to the fibers, Bose and Mal (1973) also derived an expression for the shear modulus μ_{TT}:

$$\mu_{TT} = \mu_m + \frac{2c(k_m + \mu_m)(\mu_f - \mu_m)}{k_m + (\frac{k_m}{\mu_m} + 2)[c\mu_m + (1-c)\mu_f]} \tag{17}$$

Previous studies (Hashin and Rosen, 1964; Hill, 1964) did not obtain this explicit expression, but bounds instead. In fact, Eq. (17) corresponds to their lower bound. Equations (12), (13), (15), and (16) are also identical to the lower-bound results. Thus, the "quasi-cystalline" approximation used by Bose and Mal (1963, 1964) to derive Eqs. (12), (13), and (16) leads to the lower-bound results, which these authors believe to be "nearer to the actual value if correlations are ignored." Equation (17) coincides also with Hermans' (1967) result, which he points out "lies between the bounds derived by Hashin and Rosen." From the above relationships, one obtains for the boron-aluminum composite, using results in Table 3:

$$E_L = 2.292 \cdot 10^{11} \text{ N/m}^2,$$

$$k_T = 1.267 \cdot 10^{11} \text{ N/m}^2,$$

$$\mu_{LT} = 0.559 \cdot 10^{11} \text{ N/m}^2,$$

$$\mu_{TT} = 0.523 \cdot 10^{11} \text{ N/m}^2, \text{ and}$$

$$\nu_{LT} = 0.230 .$$

If the composite behaves transversely isotropic with the unique symmetry axis along x_3, then the C_{ij} elastic-stiffness constants can be computed from

$$C_{11} = C_{22} = k_T + \mu_{TT}, \tag{18}$$

$$C_{33} = E_L + 2\nu_{LT} C_{13}, \tag{19}$$

$$C_{44} = C_{55} = \mu_{LT}, \tag{20}$$

$$C_{66} = \frac{1}{2} (C_{11} - C_{12}) = \mu_{TT}, \tag{21}$$

$$C_{12} = k_T - \mu_{TT}, \text{ and} \tag{22}$$

$$C_{13} = C_{23} = 2\nu_{LT} k_T. \tag{23}$$

These results are given in the final column of Table 1.

9. Discussion

Here we consider principally the correspondence between observed C_{ij}'s and their counterparts predicted by three models: square-array, hexagonal-array, and random-distribution.

C_{33} is predicted reasonably well by all three models, although all are slightly high, perhaps reflecting the slight uncertainty in Young's modulus of the boron fibers.

C_{11} is predicted best by the lattice models, and C_{22} is predicted best by the random model. As shown in Fig. 3, this probably reflects the different imperfections in fiber distributions along the x_1 and x_2 directions.

C_{44} and C_{55}, which represent shears with the force parallel to the fibers, are not predicted accurately by the square-array model; but they are predicted by both the hexagonal-array and the random models. Thus, these elastic constants permit one to distinguish fiber arrays that are transversely anisotropic (tetragonal, orthorhombic) from those that are transversely isotropic (hexagonal, random).

C_{66}, which represents shears with a force perpendicular to the fibers, is predicted well only by the random model. Since C_{66} represents also the velocity of a plane wave both propagated and polarized in the transverse plane, of all elastic constants it should be most sensitive to the fiber distribution. Thus, the different predictions for the hexagonal and random models, both of which are transversely isotropic, are not too surprising. Furthermore, Fig. 1 shows little evidence of either three-fold or six-fold symmetry around the fiber axis.

C_{12}, C_{13}, and C_{23}, the so-called off-diagonal elastic constants, are predicted surprisingly well by the random model. Since these constants are always determined indirectly, whether experimentally or theoretically, one expects larger errors than for the diagonal elastic constants, the C_{ij}'s, discussed above. Absence of large discrepancies between observation and theory for these three elastic constants gives one simultaneous confidences in the experimental measurements and in the random-distribution model for this particular composite.

Finally, we remark that similar observations hold also for the S_{ij}'s, as shown in Table 2. However, these comparisons are less useful because only five S_{ij}'s were determined experimentally, compared with nine C_{ij}'s. Also, the experimental S_{66} is inconsistent with that predicted or that computed by inverting the C_{ij} matrix; this reflects also in the experimental S_{12} value and is believed to be an experimental artifact, related perhaps to impure torsional modes about the x_2 axis. Except for this discrepancy, there are no differences between the 30-kHz S_{ij} results and the 10-MHz C_{ij} results; thus, dispersion does not occur in this material in this frequency range. This absence of dispersion is especially interesting for the higher frequencies where the wavelength is not much larger than the fiber spacing or the fiber diameter.

ACKNOWLEDGMENT

This study was supported by the NBS Office of Nondestructive Evaluation. Most of the sound-velocity measurements were made by M. W. Austin. A first draft of the manuscript was completed while H. M. L. visited the Institute for Theoretical and Applied Physics at the University of Stuttgart. J. Dahnke contributed valuably to constructing the manuscript.

REFERENCES

Achenbach,J. D.	1976	Arch. Mech. 28, 257.
Bert, C. W.	1975	Composite Materials, Volume 8, Ch. 9., Academic, New York.
Bose, S. K. and Mal, A. K.	1973	Int. J. Solids Struct. 9, 1075.
Bose, S. K. and Mal, A. K.	1974	J. Mech. Phys. Solids 22, 217.
Gschneidner, K. A.	1964	Solid State Physics, Volume 16, p.370, Academic, New York.
Hashin, Z.	1970	Mechanics of Composite Materials, p. 201, Pergamon, New York.
Hashin, Z. and Rosen, B. W.	1964	J. Appl. Mech. 31, 223.
Hermans, J. J.	1967	Proc. K. ned. Akad. wet. B70, 1.
Hill, R.	1965	J. Mech. Phys. Solids 13, 189.
Hlavacek, M.	1975	Int. J. Solids Struct. 11, 199.
Ledbetter, H. M.	1979	Nonmetallic Materials and Composites at Low Temperatures, p. 267, Plenum, New York.
Ledbetter, H. M., Frederick, N. V. and Austin, M. W.	1980	J. Appl. Phys., 51, 305.
Ledbetter, H. M. and Read, D. T.	1977	J. Appl. Phys. 48, 1874.
Read, D. T. and Ledbetter, H. M.	1977	J. Appl. Phys. 48, 2827.
Sendeckyj, G. P.	1974	Composite Materials, Volume 2, Ch.3., Academic, New York.

Table 1. Observed and predicted C_{ij} elastic stiffnesses of a boron-aluminum unidirectionally fiber-reinforced composite, in units of 10^{11} N/m^2.

ij	Observed	Square Model[a]	Hexagonal Model[b]	Random Model[c]	Full Random Model
11	1.852	1.856	1.872	1.790	1.790
22	1.797	1.856	1.872	1.790	1.790
33	2.450	2.480	2.551	-	2.560
44	0.566	0.451	0.561	0.559	0.559
55	0.569	0.451	0.561	0.559	0.559
66	0.526	-	0.606	0.523	0.523
12	0.779	-	0.661	-	0.745
13	0.606	-	0.578	-	0.583
23	0.604	-	0.578	-	0.583

[a]After Achenbach (1976).
[b]After Hlavacek (1975).
[c]After Bose and Mal (1974).

Table 2. Observed and predicted S_{ij} elastic compliances of a boron-aluminum unidirectionally fiber-reinforced composite, in units of $10^{-11} m^2/N$.

ij	Observed[a]	From C_{ij}'s[b]	Predicted, Full Random Model
11	0.708	0.684	0.699
22	0.708	0.707	0.699
33	0.438	0.461	0.436
44	1.755	1.767	1.788
55	1.755	1.757	1.788
66	2.123	1.901	1.913
12	-0.353	-0.261	-0.258
13	-0.106	-0.105	-0.100
23	-0.106	-0.110	-0.100

[a]Assumed tranverse-isotropic symmetry.
[b]Based on orthotropic symmetry.

Table 3. Properties of constituent materials.

	ρ (g/cm^3)	E ($10^{11} N/m^2$)	μ ($10^{11} N/m^2$)	B ($10^{11} N/m^2$)	ν	k ($10^{11} N/m^2$)	λ (10^{11}
Boron	2.352	3.979	1.763	1.785	0.129	2.383	0.59
Aluminum alloy	2.702	0.715	0.267	0.751	0.341	0.840	0.57

Figure Captions

Fig. 1. Schematic diagram of fiber distribution for three models considered in this study: square-array, hexagonal-array, and random-distribution. Diagram shows intersection of fibers, parallel to x_3, with x_1-x_2 plane.

Fig. 2. Co-ordinate system adopted in this study. Fibers are parallel to x_3. Laminae lie in the x_2-x_3 plane.

Fig. 3. Photomicrograph showing distribution of 0.14-mm diameter boron fibers in an aluminum alloy matrix. Plane of photo is perpendicular to fibers, which are parallel to x_3 axis.

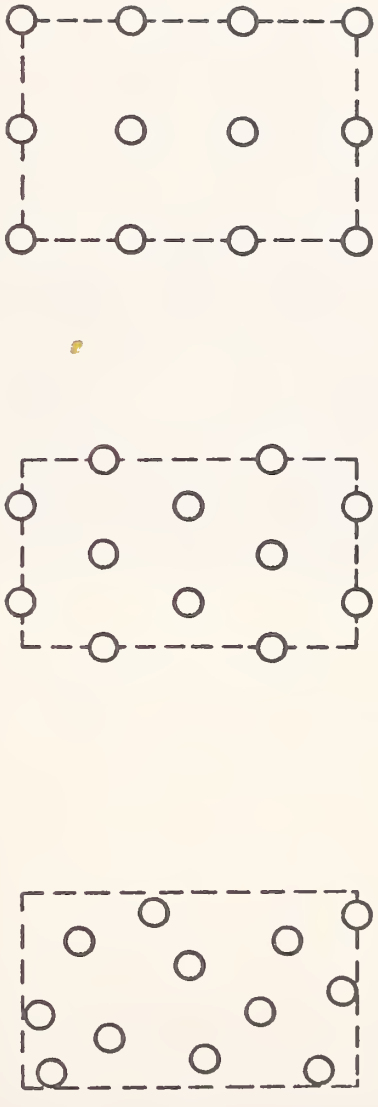

Fig. 1. Schematic diagram of fiber distribution for three models considered in this study: square-array, hexagonal-array, and random-distribution. Diagram shows intersection of fibers, parallel to x_3, with x_1-x_2 plane.

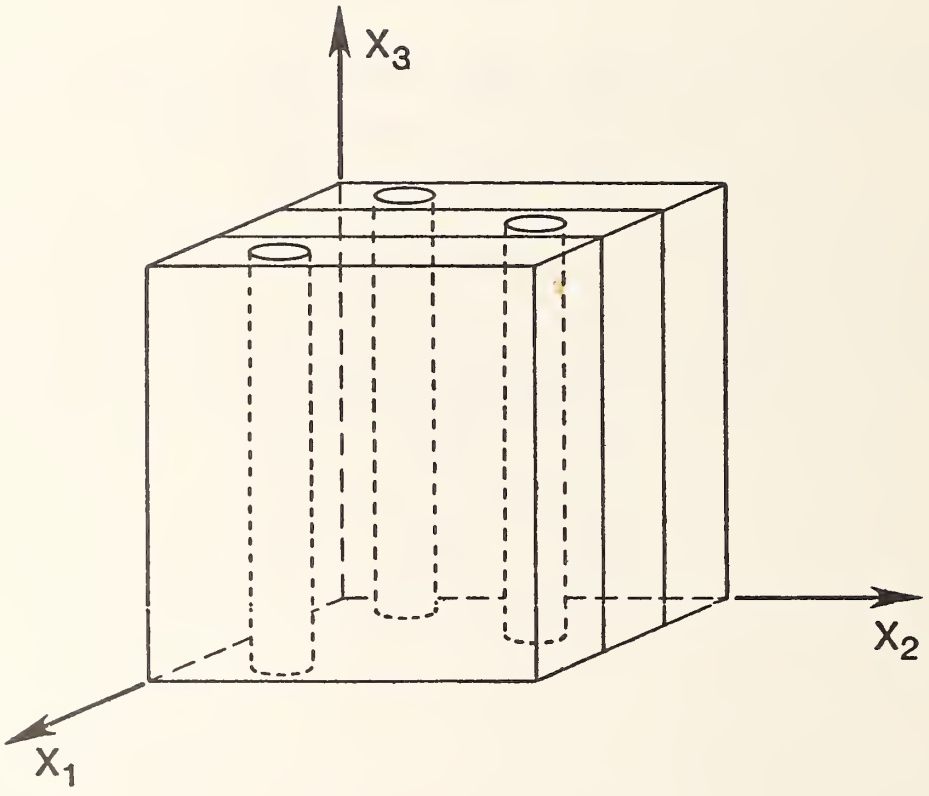

Fig. 2. Co-ordinate system adopted in this study. Fibers are parallel to x_3. Laminae lie in the x_2-x_3 plane.

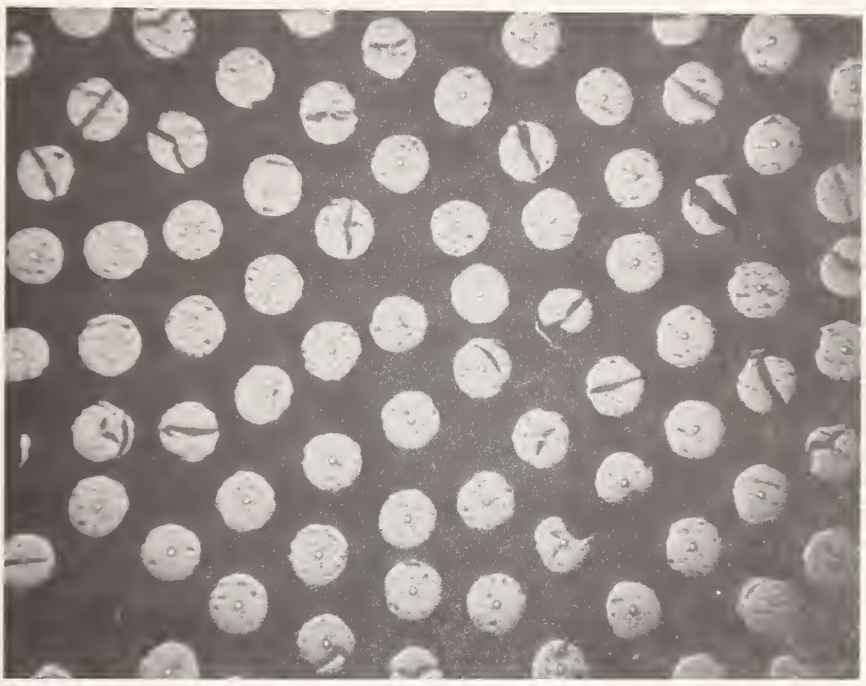

Fig. 3. Photomicrograph showing distribution of 0.14-mm diameter boron fibers in an aluminum alloy matrix. Plane of photo is perpendicular to fibers, which are parallel to x_3 axis.

TECHNOLOGY TRANSFER

TECHNOLOGY TRANSFER PROGRAM

LEADER: N. J. Simon, NBS

OBJECTIVES:

(1) To hold an annual workshop in October of each year. Major topics include design overviews of fusion energy projects with respect to material needs and reviews and data on structural alloys, composites, and weldments.
(2) To produce and distribute an annual report. In addition, monthly reports are furnished to OFE/DoE.
(3) To prepare handbook pages and supporting documentation on low temperature mechanical and physical properties of structural materials for superconducting magnets. The pages are to be distributed to workshop attendees and will form a part of the annual report. The pages will also be presented for inclusion in the Materials Handbook for Fusion Energy Systems.

ACTIVITIES PAST YEAR (1981):

(1) The NBS-DoE Workshop on Materials at Low Temperatures was held October 6-8, 1981 in Vail, Colorado. The program and a description of the topics covered follows.
(2) "Materials Studies for Magnetic Fusion Energy Applications-IV," NBSIR 81-1645, 648 pages (April 1981), Eds. R. P. Reed and N. J. Simon, has been sent to the Technology Information Center, ORNL, and copies have been made available to other interested persons.
(3) Handbook pages and supporting documentation covering mechanical and physical properties of AISI 316 stainless alloys are published as an addendum to this report.

ACTIVITIES THIS YEAR (1982):

(1) Current plans are to hold the annual workshop again in October of 1982.
(2) "Materials Studies for Magnetic Fusion Energy Applications-V," NBSIR 82-1667, 490 pages (1982), Eds. R. P. Reed and N. J. Simon, is the current edition of the annual report.
(3) Production of handbook pages and supporting documentation on mechanical and physical properties of 21-6-9 and AISI 304 stainless steels will be a major effort this year. Also, the AISI 316 handbook pages will go through the review process for the Materials Handbook for Fusion Energy Systems.

NBS-DoE WORKSHOP: MATERIALS AT LOW TEMPERATURES

October 6-8, 1981, Vail, Colorado

N. J. Simon
Fracture and Deformation Division
National Bureau of Standards
Boulder, Colorado

ABSTRACT

A brief summary of the topics discussed at this annual workshop is presented. The program and the list of registered participants follow this summary.

The structural and insulating materials used in the superconducting magnets of fusion energy systems are the subject of this annual workshop. Current methods of plasma confinement for fusion reactors necessitate the use of high-field superconducting magnets that operate at temperatures near 4 K. A major purpose of the workshop is to bring together representatives from the community of users and suppliers of materials for low temperature magnet applications with those engaged in development and characterization of these materials. Participants this year came from industry, the national laboratories, the magnetic fusion energy programs, NBS, DoE, and several universities. The technical presentations were informal, with opportunities for comments and questions. The proceedings of the workshop are not published, but abstracts or short summaries of all the presentations are provided to those who attend. Some highlights of the sessions are given below:

Large Scale Magnet Programs:

Don Beard of the DoE Office of Fusion Energy gave examples of large superconducting magnets that have recently undergone testing as well as a worldwide overview of large scale magnet programs being conducted to support fusion programs. Ed Dalder reported on problems that the Mirror Fusion Test Facility has had with low yield strength and ductility at 4 K of some 304LN stainless steels in 9- to 14-cm-thick plates. Other presentations covered requirements for the Fusion Engineering Device magnets and gave details of Large Coil and other superconducting magnet projects at General Dynamics, Westinghouse, and the Japan Atomic Energy Research Institute.

Inspection of Magnet Systems:

This was the first year that this type of session has been held. M. J. Buckley of Rockwell International reported advances in nondestructive

evaluation (NDE) capabilities and strongly suggested that NDE be considered at the design stage of magnets. D. T. Read of NBS explained the fitness-for-service approach. Fracture mechanics is needed for this type of assessment. C. M. Fortunko of NBS described a new technique for inspecting stainless steel welds using shear waves polarized in the plane of the weldment, generated and detected with noncontacting, electromagnetic-acoustic transducers. Other presentations dealt with the specifics of some NDE systems that have been successfully used in magnet inspection. Committee meetings on the development of codes and standards for superconducting magnet design and construction took place in informal sessions during the conference.

Structural Alloys, Welds and Castings:

R. P. Reed reviewed NBS low-temperature research on alloys, including the inverse relationship found between yield strength and fracture toughness at 4 K. Reprocessing of the alloy can increase both parameters. R. L. Tobler discussed improved mechanical property test methods developed at NBS and recent results for austenitic stainless steels. R. Ogawa of Kobe Steel, Ltd., and H. Masumoto of Nippon Steel considered the new, high-manganese stainless steels that are being developed for cryogenic use because of higher yield strengths and greater austenite stability than the AISI 304 and 316 stainless steels. A progress report on a new handbook effort to collect and disseminate data on structural materials for magnets was given by N. J. Simon of NBS.

Nonmetallics:

The presentation of M. B. Kasen reviewed the NBS/DoE program on cryogenic nonmetallic materials development. Of particular interest were recent measurements of the interlaminar shear strength and other properties of PG-10CR, a polyimide variant of G-10CR. G-10CR is a cryogenic-grade laminate

for which specifications have been established by cooperation between NBS and industry. PG-10CR has shown relatively good resistance to degradation in the radiation environment to which superconducting magnet insulating materials will be exposed, but its mechanical strengths are low. Other proposed cryogenic neutron irradiation studies of various nonmetallics were described by G. F. Hurley of Los Alamos National Laboratory.

The low temperature thermal conductivities of G-10CR, G-10CR variants, and other nonmetallics were reported by L. L. Sparks of NBS for J. G. Hust. H. M. Ledbetter of NBS summarized results of studies that indicate a surprisingly close correspondence between dynamic and static measurements of the Young's modulus of fiber-reinforced composites, in view of theoretically predicted differences.

PROGRAM
NBS/DoE Workshop on Materials at Low Temperatures
October 6-8, 1981
Vail, Colorado

Tuesday, October 6

Session 1 (9:00-12:00 a.m.) Large Scale Magnet Programs
R. P. Reed, Chairman

Introduction	R. P. Reed, NBS
Overview - DoE Office of Fusion Energy	D. S. Beard, DoE
Design and Construction of Mirror Fusion Test Facilities	E.N.C. Dalder LLNL
Large Coil Project (cancelled)	A. J. Moorhead, ORNL
R & D Requirements for the FED Magnet	R. Derby, ORNL
20 MJ Poloidal Magnet Coil	M. Attaar, Westinghouse
Magnet Development at General Dynamics	J. L. Christian, GD

Photograph of the entire group - 12:00 NOON

Session 2 (2:00-5:00 p.m.) Inspection of Magnet Systems
C. M. Fortunko, Chairman

Building in Improved NDE Through Design	M. Buckley, Rockwell
Large Coil Project Solder Bond Inspection System	S. W. Gill, GD-Convair
Stainless Steel Weld Inspection	C. M. Fortunko, NBS
NDE of Magnet and Enclosure	B. W. Maxfield, LLNL
Fitness-for-Service	D. T. Read, NBS
Codes and Standards - Introduction	R. P. Reed, M. B. Kasen NBS

COCKTAIL PARTY 6 - 8 p.m Cabin Lounge

Wednesday, October 7

Session 3 (9:00-12:00 a.m.) Structural Alloys, Welds and Castings
J. W. Morris, Chairman

Review of Structural Alloys	R. P. Reed, NBS
Spontaneous Martensitic Transformations in Type 304 Austenitic Stainless Steels	D. Larbalestier, Univ. of Wisconsin
Deformation and Fracture of Structural Alloys	R. L. Tobler, NBS
High Strength/High Mn Steels for Cryogenic Steels	R. Ogawa, Kobe Steel
Weld Fillers for Austenitic Stainless Steels	K. Crooks, Armco
Cryogenic Research at the Lawrence Berkeley Laboratory	J. W. Morris, Univ. of California
25 Mn Steel	H. Masumoto, Nippon Steel

Wednesday Afternoon FREE FOR ACTIVITIES OR COMMITTEE MEETINGS

Wednesday, October 7

Session 4 (5:00-7:30 p.m.) Nonmetallics
M. B. Kasen, Chairman

Review of Composite Properties	M. B. Kasen, NBS
Radiation Research on Candidate Organic Insulators	G. F. Hurley, LASL
Thermal Conductivities of Composites	J. G. Hust, NBS
Cryogenic Performance of Glass-mat Reinforced Epoxy Laminates	J. Gauchel, Owens-Corning
Dynamic and Static Young's Moduli of Fiber-Reinforced Composites	H. M. Ledbetter, NBS

Thursday, October 8

Session 5 (9:00-11:30 a.m.) Structures and Materials
D. S. Beard, Chairman

Structural Materials for Superconducting Tokamaks	H. Tsuji, JAERI
The Effect of Ferrite on the Mechanical Properties of CF8M Stainless Steel Castings at 4K	T. A. Whipple, NBS
Handbook on Structural Materials for Magnets	N. J. Simon, NBS
Codes and Standards	Committee Discussion

NBS/DOE WORKSHOP

October 6-8, 1981
Vail, Colorado

NAME	AFFILIATION
Albertson, S.	Lawrence Livermore Lab.
Attaar, M.	Westinghouse
Arvidson, J.	National Bureau of Standards
Baysinger, B.	Welk Bros.
Beard, D.	U.S. Department of Energy
Benzinger, J.	Spaulding Fiber Co.
Buckley, M.	Rockwell Science Center
Chow, G.	Brookhaven National Lab.
Christian, J.	General Dynamics Convair
Conder, R.	Beech Aircraft
Crooks, K.	Armco
Dalder, E.	Lawrence Livermore National Lab.
Derby, R.	MIT
Dobson, W.	Teledyne
Fortunko, C.	National Bureau of Standards
Fultz, B.	U.C. Berkeley
Gaines, A.	
Gauchel, J.	Owens Corning Fiberglas
Gill, S.	General Dynamics Convair
Hanson, D.	Welk Bros.
Hassenzahl, W.	Lawrence Berkeley Lab.
Hooper, R.	General Electric
Horvath, J.	General Dynamics Convair
Kasen, M.	National Bureau of Standards
Kim, H.	U.C. Berkeley
Kotecki, D.	Teledyne
Kriz, R.	National Bureau of Standards
Larbalestier, D.	University of Wisconsin
Ledbetter, H.	National Bureau of Standards
Masumoto, H.	Nippon Steel Corp.
Markley, F.	Fermilab
Maxfield, B.	Lawrence Livermore National Lab.
Morris, J.	Lawrence Berkeley Lab.
Ogawa, R.	Kobe Steel
Peters, C.	Lawrence Berkeley Lab.
Read, D.	National Bureau of Standards
Reed, R.	National Bureau of Standards
Rensberger, K.	Cryogenic Energy Co.
Roden, W.	General Dynamics Convair
Shull, G.	Beech Aircraft
Simon, N.	National Bureau of Standards
Tobler, R.	National Bureau of Standards
Tsujo, H.	JAERI
Whipple, T.	National Bureau of Standards
Wille, J.	McDonnell-Douglas
Witherell, C.	Lawrence Livermore National Lab.
Zbasnik, J.	Lawrence Livermore National Lab.

ACKNOWLEDGMENT

The editors wish to express their appreciation to JoAnne Wilken and Carole Montgomery for their work in preparing the manuscript.

Marilyn Stieg removed many of the inconsistencies, grammatical errors, and awkward usages of language. The editors are responsible for those that remain.

NBS-114A (REV. 2-8C)

U.S. DEPT. OF COMM. BIBLIOGRAPHIC DATA SHEET (See instructions)	1. PUBLICATION OR REPORT NO. NBSIR 82-1667	2. Performing Organ. Report No.	3. Publication Date May 1982

4. TITLE AND SUBTITLE

Materials Studies for Magnetic Fusion Energy Applications at Low Temperatures - V

5. AUTHOR(S)
R. P. Reed and N. J. Simon, Editors

6. PERFORMING ORGANIZATION (If joint or other than NBS, see instructions)

NATIONAL BUREAU OF STANDARDS
DEPARTMENT OF COMMERCE
WASHINGTON, D.C. 20234

7. Contract/Grant No.

8. Type of Report & Period Covered

9. SPONSORING ORGANIZATION NAME AND COMPLETE ADDRESS (Street, City, State, ZIP)

Department of Energy
Office of Fusion Energy
Washington, DC 20545

10. SUPPLEMENTARY NOTES

Related earlier reports: NBSIR 81-1645, NBSIR 80-1627, NBSIR 79-1609, NBSIR 78-884

☐ Document describes a computer program; SF-185, FIPS Software Summary, is attached.

11. ABSTRACT (A 200-word or less factual summary of most significant information. If document includes a significant bibliography or literature survey, mention it here) This report contains results of a research program to produce material property data that will facilitate design and development of cryogenic structures for the superconducting magnets of magnetic fusion energy power plants and prototypes. The program was conceived and developed jointly by the staffs of the National Bureau of Standards and the Office of Fusion Energy of the Department of Energy; it is managed by NBS and sponsored by DoE. Research is conducted at NBS and at various other laboratories through subcontracts with NBS.

The reports presented here summarize the fifth year of work on the low temperature materials research program. Highlights of the results are presented first. Research results are given for the four main program areas: structural alloys, weldings and castings, nonmetallics, and technology transfer. Objectives, approaches, and achievements are summarized in an introduction to each program area.

The major portion of the program has been the evaluation of the low temperature mechanical and physical properties of stainless steel base metals, welds, and castings, with particular emphasis on the nitrogen-strengthened stainless steels. Stainless steels with manganese additions and other high manganese steels have also been investigated. Work has been done on the production and standardization of nonmetallics, primarily industrial laminates, for low temperature applications and on the measurement of their properties at cryogenic temperatures. A brief summary is given of the fifth NBS/DoE Vail Workshop held in October 1981.

12. KEY WORDS (Six to twelve entries; alphabetical order; capitalize only proper names; and separate key words by semicolons)

Alloys; castings; composites; cryogenic properties; low temperature; mechanical properties; nonmetallics; physical properties; stainless steels; structural alloys; welding.

13. AVAILABILITY

☒ Unlimited

☐ For Official Distribution. Do Not Release to NTIS

☐ Order From Superintendent of Documents, U.S. Government Printing Office, Washington, D.C. 20402.

☒ Order From National Technical Information Service (NTIS), Springfield, VA. 22161

14. NO. OF PRINTED PAGES
452

15. Price
$33.00

USCOMM-DC 6043-P80

☆ U.S. GOVERNMENT PRINTING OFFICE: 1982—578-925/274 REGION No. 8